

DIGITAL IMAGE PROCESSING OF REMOTELY SENSED DATA FOR LITHOLOGICAL DISCRIMINATION IN RAJASTHAN (INDIA)

*A Thesis Submitted
in Partial Fulfilment of the Requirements
for the Degree of*

DOCTOR OF PHILOSOPHY

by

NILANCHAL PATEL

200911

to the

DEPARTMENT OF CIVIL ENGINEERING
INDIAN INSTITUTE OF TECHNOLOGY KANPUR

AUGUST, 1991

C E R T I F I C A T E

It is certified that the work contained in the thesis entitled "Digital Image Processing of Remotely Sensed Data for Lithological Discrimination in Rajasthan (India)", by Nilanchal Patel, has been carried out under my supervision and that this work has not been submitted elsewhere for a degree.



Dr. K.K. Rampal
Department of Civil Engineering
Indian Institute of Technology
Kanpur

June, 1991



18 OCT 1993/CE

CENTRAL LIBRARY
I. I. T., KANPUR.

Acc. No. A. 116555

CE-1991-D-PAT-DIG.

74
5.52.00
P 272 d

SYNOPSIS

Name of student : Nilanchal Patel Roll No. 8520365
Degree for which submitted : Ph.D. Department : Civil Engineering
Thesis Title : Digital Image Processing of Remotely Sensed Data
for Lithological Discrimination in Rajasthan
(India)
Name of thesis supervisor : K.K. Rampal
Month and Year of Thesis Submission : August, 1991

One of the primary objectives of geologic remote sensing is to discriminate among various rock types. Unfortunately owing to the identical spectral signatures of ^amajority of the minerals and rocks exposed on the earth's surface, it becomes difficult to distinguish them on black and white images and standard false colour composites. This problem can, however, be tackled to a considerable extent through ^{the} application of selective image processing techniques. In the present study, an attempt has been made to carry out lithological discrimination by applying various recently developed image processing techniques. The study area has been purposefully selected in the semi-arid to arid regions of the Aravalli Mountain Ranges in Rajasthan State which provide adequate rock exposures for carrying out research in a satisfactory manner. The study has been carried out in two different areas : "one through the analysis of MSS data from Landsat-2 (i.e., MSS Study area) and the other through the analysis of TM data from Landsat-5 (i.e., TM Study area). The

analysis of MSS data were carried out ^{in the} / DEC-1090 computer system at IIT Kanpur while the TM data were analyzed at ^{the} / Regional Remote Sensing Service Centre at Dehradun. The TM data was analyzed resorting to mainly the digital images generated by applying various image processing techniques in addition to the statistical results and graphical outputs, whereas for the analysis of MSS data, only the statistical results and graphical outputs were used.

The work contained in the thesis is organized into seven chapters. Chapter 1 begins with an introduction of the topic and a review of the geology of the study area followed by a brief description regarding the preprocessing and the data reading techniques adopted in the study. The various methods adopted for analysis of digital data are presented in detail in Chapter 2. These are discussed under the processes of image enhancement and image classification. The various image enhancement techniques employed in the present study are; Contrast Stretching, Multispectral Band Ratioing, Principal Component Analysis (PCA), Inverse Principal Component Analysis, Discriminant Function Analysis, Correspondence Analysis, Greenness and Brightness Components, and False Colour Composites (FCC) of raw band data while ^{the} / supervised Maximum Likelihood Classifier has been employed ^{for image classification.} Chapter 3 covers a discussion on the results of X-ray Diffraction (XRD) studies, microscopic studies and laboratory-derived diffused reflectance spectra (measured in ^{the} / visible and NIR range) of the rock samples collected from the study area.

The analysis of digital data comprises mainly two stages, i.e., firstly, the graphical analysis and secondly, the analysis and interpretation of various digital images. In both kinds of analysis, emphasis has been laid on the effects of brightness variation on the discrimination of the rock types. Since digital images have been generated only for the TM Study area (using TM data), it was possible to identify the illuminated and non-illuminated (shadowed) parts of ^{the} different rock types of only this study area on the digital images. For example, the quartzitic ridges and the rough surface topography of the granites and gneisses cause significant brightness variation in the illuminated and non-illuminated portions of these rocks. Therefore, the illuminated and non-illuminated portions of these two rocks have been represented as two different litho-units in the analysis of digital data.

Chapter 4 is devoted entirely to the results and their interpretation emerging from the two-dimensional graphical analysis of the digital data. The various graphical methods employed in the study comprise coincident spectral plots, plots of extended spectral signatures, histograms of band ratios, two-dimensional (i.e. two band) principal component analysis, and two group discriminant function analysis. The coincident spectral plots depict the ranges of reflectance values of each rock type in ^{the} different bands, whereas the extended spectral signatures plotted for each rock type show the variation of their mean values in ^{the} different bands of ^{the} MSS and TM data. Similarly histograms of ^{the} band ratios have been plotted in order to evaluate the discriminability

among ^{the} different rock types. The objective behind ^{the} two-dimensional principal component analysis is to evaluate the variances accounted for by the principal components in the fields of scatter plots of training samples of ^{the} various rock types. The method of two group discriminant function analysis has been employed for ^{he} various pairs of rocks in order to ascertain the probability of discrimination between the two rock types in each pair in ^{he} different band combinations. This method of analysis has shown that the various rock types of ^{the} MSS area are associated with considerable extent of intermixing or misclassification, whereas many of the rock types in TM area can be fairly discriminated among each other.

Chapter 5 comprises a detailed discussions concerning the multivariate analysis of statistical result and interpretation of the digital images generated by applying various image processing techniques with reference to rock discrimination and delineation of major structural features. As mentioned earlier, digital images have been generated and studied only for the TM Study area while for the MSS Study area, only the statistical results have been used in the multivariate analysis. Examination of the FCCs of raw bands data generated by applying the criteria of Optimum Index Factor reveals three different litho-units on the basis of differences in spectral signature and topography. These are namely the quartzites, phyllites and schists, and granites and gneisses. The black and white images of various spectral band ratios appear tonally homogeneous, whereas their FCCs reveal the various litho-units more conspicuously than the FCCs of raw bands data. A

composite image of the brightness and greenness components highlighted the soil cover and the vegetated areas of the study area. The component images generated by applying the technique of correspondence analysis and the FCCs of the first three correspondence components display, respectively, similar tonal and colour contrast among the various litho-units as the raw bands images and their FCCs; however, the various litho-units are expressed more prominently on the correspondence component images and their FCCs. In the domain of multivariate analysis of digital data, PCA comprises extraction of eigenvalues and eigenvectors of variance-covariance matrices of the training pixels of various rock types in different bands and computation of matrix of factor loadings. An attempt towards supervised classification of principal component images did not yield satisfactory result. Therefore, principal component images were generated using the entire image data of different TM bands since only TM data have been used for image generation. Comparison of various black and white PC images reveals that only the first PC image is useful for lithological discrimination and structural interpretation since all other PC images are associated with significant amount of noise. Examination of the FCC of first three PC images reveals all the five litho-units present in TM study area on the basis of differences in spectral signature and topography. Therefore, this composite image has been used to prepare a lithological map of the TM study area. The FCC of the first three inverse PCs does not provide any additional information relative to other digital images. The various digital images studied show misclassification

among some of the litho-units as revealed by their identical spectral signatures. The misclassification is discussed on the basis of XRD studies, the laboratory derived diffused reflectance spectra of rock samples collected from the field, and the vegetation cover developed on various litho-units. Comparison of the various digital images used in the study reveals that the FCCs of raw bands data display the various structural features of the study area more conspicuously than others.

A thematic digital image of the TM area showing the various litho-units and the agricultural areas has been generated using Maximum Likelihood Classifier and is provided in Chapter 6. In order to account for the brightness variation of the quartzitic and granitic rocks induced by topography, each of them has been represented by two subclasses in the classification - one for the illuminated part and the other subclass for the non-illuminated or shadowed part of the terrain.

Chapter 7 covers the conclusions emerging from the different approaches adopted for the analysis and interpretation of the digital data. Besides, a comparative assessment of the results obtained through application of various image processing techniques is also provided. A geological map prepared from the FCC of first three principal component images (which shows all the five litho-units present in TM study area) and a structural map showing the major geological structures are presented in this chapter. A brief note on the recommendations for future work is provided at the end.

ACKNOWLEDGEMENTS

I wish to express my profound sense of gratitude and reverence to Prof. K.K. Rampal for introducing me to the area, selecting an interesting topic and for his encouraging and constant supervision till the completion of the research.

I am thankful to Dr. K. Subramanya, former Head of Civil Engineering Department, IIT Kanpur for providing me necessary funds to acquire the TM digital data from NRSA, Hyderabad and to carry out the image processing work at Regional Remote Sensing Service Centre (RRSSC), Indian Institute of Remote Sensing (IIRS), Dehradun. My sincere acknowledgements are also due to Prof. S.K. Bhan, Head, RRSSC for permitting me to work at RRSSC.

I am heartily grateful to Dr. R.P. Singh for his constant encouragement and timely assistance throughout the research. I am also thankful to him for providing me necessary help towards my visit to the Netherlands in June, 1990 for presenting a paper at the twenty-eighth COSPAR Plenary Meeting and Associated Activities, 1990 held at the Hague. Thanks are due to Dr. B.C. Raymahasay for permitting me to use the desired facilities at the Engineering Geology Laboratory. I am also extremely thankful to Dr. K.V.G.K. Gokhale for giving me many useful suggestions related to my thesis. I am thankful to the in-charge, X-ray laboratory, IIT Kanpur for permitting me to record X-ray diffractograms of the rock samples.

I am grateful to Dr. P.K. Basudhar, who kindly agreed to act as my administrative supervisor till the oral examination, for his timely assistance and understanding nature. My heartfelt thanks are also due to Mr. N.K. Tripathi for his always friendly attitude during the research.

My sincere acknowledgements are due to Mr. Md. Umar, Senior Geologist, Mines and Geology Department, Sirohi, Rajasthan for providing me necessary instructions in the field work. I also acknowledge the permission received from the Director, DMSRDE, Kanpur and the assistance received from Dr. P.T. Rajagopalan, Scientist, DMSRDE, Kanpur for recording the visible and NIR spectra of the rock samples. I am also thankful to the Director, Petrology Division, G.S.I., Lucknow for kindly giving permission to prepare the thin sections of rock samples. Thanks are due to Mr. K.V. Ravindran, Scientist, RRSSC, Dehradun for giving me useful suggestions in the interpretation of digital images.

Special thanks to Mr. N.B. Venkateswarlu for his invaluable assistance and constant encouragement throughout the research and to Mr. B.K. Panigrahy for providing me timely help in the thin section and XRD studies. I owe a great deal to Messrs Kishore Pahuja, Dukhabandhu Kishan and Dr. C.D. Murty for their whole-hearted cooperation at various stages of my work. My heartfelt thanks are also due to Bhupesh, Dinesh, Pranab, Shanta bhabl and all my colleagues who made my stay at IIT Kanpur pleasant and memorable.

I am thankful to Mr. J.P. Gupta for typing the manuscript neatly and patiently and to Mr. J.C. Verma for drawing the figures neatly in time. I also thankfully acknowledge the assistance received from the staff members of the Survey, Photogrammetry and Remote Sensing Laboratory and Engineering Geology Laboratory at various stages of my work.

Finally, I have no words to express my gratitude to my parents, elder brother and sister-in-law and all other family members for their emotional support and tremendous patience, without which it would have been difficult for me to complete the work smoothly.

(NILANCHAL PATEL)

*To My
Parents,
Elder Brother
and
Sister-in-law.*

CONTENTS

<u>Chapter</u>	<u>Page No.</u>
List of Tables	xvii
List of Figures	xix
1. INTRODUCTION	1
1.1 Remote Sensing in Geology	1
1.2 Objectives of the Study	3
1.3 Selection of Study Area	4
1.3.1 Study Area for MSS Data	5
1.3.2 Study Area for Thematic Mapper Data	5
1.4 Geology of the Study Area	6
1.5 Data Acquisition	12
1.6 Extraction of Digital Data Pertaining to Study Area	13
1.6.1 MSS Study Area	13
1.6.2 TM Study Area	16
1.7 Previous Work	17
1.8 Methodology	20
1.8.1 Reading of Data	20
1.8.2. Preprocessing	21
1.8.3 Development of Software for Image Processing and Pattern Recognition	23
1.9 Organization of the Thesis	25
2. DIGITAL IMAGE PROCESSING TECHNIQUES	27
2.1 Introduction	27
2.2 Characteristics of Remotely Sensed Data Used in the Study	28
2.2.1 Characteristics of MSS Data from Landsat-2	28
2.2.2 Characteristics of Thematic Mapper Data	30

2.3	Image Enhancement	30
2.3.1	Contrast Stretching	32
2.3.1.1	Linear Contrast Enhancement	33
2.3.1.2	Non-linear Contrast Stretch : Gaussian Stretch	33
2.3.2	Multi-image Manipulation	34
2.3.2.1	Band Ratioing	34
2.3.2.2	Principal Component Analysis	35
2.3.2.2.1	Multivariate Extension of Principal Component Analysis	40
2.3.2.2.2	Classification of Principal Component Images	42
2.3.2.3	Inverse Principal Component Analysis	45
2.3.2.4	Discriminant Function Analysis	47
2.3.2.5	Correspondence Analysis	52
2.3.2.6	Empirically-based Image Transforms : Tasselled Cap (Kauth-Thomas) Transformation for Vegetation (Green- ness) and Soil Brightness Indices	54
2.4	Automated Classification of Remotely Sensed Data for Thematic Mapper Extraction	55
2.4.1	General	55
2.4.2	Bayesian Principles of Classification	56
3.	MINERALOGICAL AND SPECTROSCOPIC ANALYSIS OF ROCKS	61
3.1	Introduction	61
3.2	Mineral Identification	63
3.3	Analysis of Laboratory Reflectance Spectra of Rock Samples	76
3.3.1	Analysis, Interpretation and Results	78

4.	GRAPHICAL ANALYSIS OF DIGITAL DATA FOR LITHOLOGICAL DISCRIMINATION	84
4.1	Introduction	84
4.2	Preliminary Analysis of Digital Data	84
4.3	Analysis and Discussion	86
4.3.1	Histograms of Training Data in Different Bands	87
4.3.2	Coincident Spectral Plots	93
4.3.3	Extended Spectral Signature Plots	99
4.3.4	Histograms of Band Ratios	103
4.3.5	Coincident Spectral Plots of Band Ratios	106
4.3.6	Two-dimensional Principal Component Analysis	110
4.3.7	Discriminant Function Analysis	125
4.3.7.1	Discriminant Function Analysis for Rocks of MSS Area	126
4.3.7.2	Discriminant Function Analysis for Rocks of Thematic Mapper Area	132
4.3.7.2.1	Rock Pair : Quartzite-1 - Quartzite-2	133
4.3.7.2.2	Rock Pair : Phyllites - Quartzites	145
4.3.7.2.3	Rock Pair : Phyllites - Granites	146
4.3.7.2.4	Rock Pair : Quartzites - Granites	148
4.3.7.2.5	Rock Pair : Granite-1 - Granite-2	151
5.	DIGITAL IMAGE PROCESSING OF MULTIVARIATE REMOTELY SENSED DATA FOR ROCK DISCRIMINATION	152
5.1	Introduction	152
5.2	Raw Band Images	153
5.3	False Colour Composites (FCCs)	155
5.4	Ratio Images and False Colour Composites of Band Ratios	170
5.4.1	Methodology	170

5.4.2	Analysis and Interpretation	172
5.4.2.1	Black and White Ratio Images	172
5.4.2.2	False Colour Composites of Band Ratios	174
5.5	Colour Composite of the Brightness and Greenness Indices	178
5.6	Multivariate Principal Component Analysis	179
5.6.1	MSS Study Area	179
5.6.2	TM Study Area	186
5.6.3	Image Interpretation and Results	194
5.7	Inverse Principal Component Analysis	199
5.8	Correspondence Analysis	200
5.8.1	Introduction	200
5.8.2	Image Interpretation and Results	203
6.	AUTOMATIC CLASSIFICATION OF THE REMOTELY SENSED DIGITAL DATA	207
6.1	Introduction	207
6.2	Interpretation of Confusion Matrix and Digital Thematic Image	220
7.	SUMMARY AND CONCLUSIONS	226
	REFERENCES	238
	GENERAL REFERENCES	242

LIST OF TABLES

<u>Table No.</u>	<u>Title</u>	<u>Page No.</u>
1.1	Stratigraphic framework of the Aravalli Mountain ranges	8
1.2	Stratigraphy of the study areas	8
1.3	Geographical coordinates, conical orthomorphic coordinates and line numbers and pixel numbers of four corners of MSS scene (160-043)	15
1.4	Transformation coefficients for MSS scene	15
1.5	Geographical coordinates of the MSS study area and corresponding line numbers and pixel numbers	16
2.1	Characteristics of MSS bands	29
2.2	Characteristics of thematic mapper spectral bands	31
3.1	Mineralogical composition of the rock samples of MSS area determined from microscopic and XRD studies	64
3.2	Mineralogical composition of the rock samples of TM area determined from microscopic and XRD studies	65
4.1	Results of discriminant function analysis for rocks of MSS area	127
4.2	Results of discriminant function analysis for rocks of TM area	134

5.1	Entropies and redundancies of Landsat TM imageries of visible and near-infrared range (excluding thermal band 6)	154
5.2	Principal component analysis data sheet for TM data (using the entire digital data of different TM bands)	165
5.3	Optimum index factor (OIF) for six of the TM bands for the TM area	167
5.4	Principal component analysis data sheet for MSS data (using the training sets of rock types used for 2-dimensional PCA of MSS data)	181
5.5	Principal component analysis data sheet for TM data (using the training sets of rock types used for 2-dimensional PCA of TM data)	187
5.6	Correspondence analysis data sheet for thematic mapper data	201
6.1	Description of the training classes used in maximum likelihood classifier	209
6.2	Statistical information for the eight different categories used in the classification of TM data by applying maximum likelihood classifier	211
6.3	Contingency table or confusion matrix of G-Truths	219
6.4	Confusion matrix of training classes, in percentage	221
7.1	Ranking table of various methods employed in the present study for lithological discrimination	237a

LIST OF FIGURES

<u>Figure No.</u>	<u>Title</u>	<u>Page No.</u>
1.1	Study area for the analysis of MSS and TM data	7
1.2	Geological map of the MSS study area	10
1.3	Geological map of the TM study area	11
2.1	Graphical representation of effect of rotation on original scatter plots	36
2.2	Graphical representation for determination of rotation angle ' θ ' and principal components with respect to original axes	36
2.3	Graphical representation of two-dimensional (two group) discriminant function analysis	48
3.1	X-ray diffractogram of Augen gneiss	67
3.2	X-ray diffractogram of Quartzite	68
3.3	X-ray diffractogram of Biotite schist	69
3.4	X-ray diffractogram of Hornblende granite	70
3.5	X-ray diffractogram of Calc gneiss	71
3.6	X-ray diffractogram of Impure limestone	72
3.7	X-ray diffractogram of Tremolite schist	73
3.8	X-ray diffractogram of Hornblende schist	74
3.9	Laboratory derived diffused reflectance spectra of the rocks of MSS area	79
3.10	Laboratory derived diffused reflectance spectra of the rocks of TM area	80
4.1	Histograms of the rocks of MSS area (plotted from their training brightness values)	88
4.2	Histograms of the rocks of TM area (plotted from their training brightness values)	90

4.3	Coincident spectral plots of the rocks of MSS area in different MSS bands	95
4.4	Coincident spectral plots of the rocks of TM area in different TM bands	96
4.5	Extended spectral signatures for the rocks of MSS area	101
4.6	Extended spectral signatures for the rocks of TM area	102
4.7	Histograms of band ratios for the rocks of MSS area	105
4.8	Histograms of band ratios for the rocks of TM area	107
4.9	Coincident spectral plots of the rocks of TM area in different TM band ratios	109
4.10	Scatter diagrams of the training reflectance values of the rocks of MSS area for 2-d principal component analysis in different MSS band pairs	111
4.11	Scatter diagrams of the training reflectance values of the rocks of TM area for 2-d principal component analysis in different TM band pairs	115
4.12	Scatter diagram for discriminant function analysis of Gneiss schist and Quartz mica schist	129
4.13	Scatter diagram for discriminant function analysis of Gneiss schist and Intercalated and cherty quartzite marble phyllite	129
4.14	Scatter diagram for discriminant function analysis of Gneiss schist and Granite	130
4.15	Scatter diagram for discriminant function analysis of Quartz mica schist and Intercalated calc and cherty quartzite marble phyllite	130
4.16	Scatter diagram for discriminant function analysis of Quartz mica schist and Granite	131
4.17	Scatter diagram for discriminant function analysis of Intercalated calc and cherty quartzite marble phyllite and Granite	131

4.18	Scatter diagram for discriminant function analysis of Quartzite-1 and Quartzite-2	137
4.19	Scatter diagram for discriminant function analysis of Quartzite-1 and Phyllite	137
4.20	Scatter diagram for discriminant function analysis of Quartzite-2 and Phyllite	138
4.21	Scatter diagram for discriminant function analysis of Quartzite and Phyllite	138
4.22	Scatter diagram for discriminant function analysis of Phyllite and Granite-1	139
4.23	Scatter diagram for discriminant function analysis of Phyllite and Granite-2	139
4.24	Scatter diagram for discriminant function analysis of Phyllite and Granite	140
4.25	Scatter diagram for discriminant function analysis of Quartzite-1 and Granite-1	140
4.26	Scatter diagram for discriminant function analysis of Quartzite-1 and Granite-2	141
4.27	Scatter diagram for discriminant function analysis of Quartzite-2 and Granite-1	141
4.28	Scatter diagram for discriminant function analysis of Quartzite-2 and Granite-2	142
4.29	Scatter diagram for discriminant function analysis of Quartzite and Granite	142
4.30	Scatter diagram for discriminant function analysis of Granite-1 and Granite-2	143
5.1	Black and white image of TM band 5	156
5.2	False colour composite of TM bands 7,5,& 4 in red, green, and blue colour combination	156
5.3	False colour composite of TM bands 7,4,& 2 in red, green, and blue colour combination	157
5.4	Black and white ratio image of TM bands 3 and 4 (3/4)	157
5.5	Black and white ratio image of TM bands 4 and 5 (4/5)	158

5.6	Black and white ratio image of TM bands 5 and 7 (5/7)	158
5.7	Colour-ratio composite of TM 2/3,3/4, & 4/5 in red, green, and blue colour combination	159
5.8	Colour-ratio composite of TM 3/4,4/5, & 5/7 in red, green, and blue colour combination	159
5.9	Colour composite of brightness and greenness indices in red and green colour combination	160
5.10	Black and white image of first principal component	160
5.11	False colour composite of the first,second, and third principal components in red, green, and blue colour combination	161
5.12	Black and white image of first inverse principal component	161
5.13	False colour composite of the first,second, and third inverse principal components in red, green, and blue colour combination	162
5.14	Black and white image of the first correspondence component	162
5.15	False colour composite of the first,second, and third correspondence components in red, green, and blue colour combination	163
6.1	False colour composite of TM bands 4,3,& 2 in red, green, and blue colour combination with the Ground Truths	208
6.2	Digital thematic image of TM area generated by applying maximum likelihood classifier (using TM bands 1,2,3,4,5, and 7)	208
7.1	Geological map of the TM area prepared from the false colour composite of the principal components -1, -2 and -3 in red,green, and blue colour combination	234
7.2	Structural map of the TM area prepared from the digital images	235

CHAPTER 1

INTRODUCTION

1.1 REMOTE SENSING IN GEOLOGY

Remote sensing has played a very important and significant role in the monitoring and exploration of natural resources of the earth. In the field of mineral prospecting and exploration surveys the technique of remote sensing has contributed a wealth of vital information which could otherwise be greatly difficult to acquire through other conventional means. A good geological map on a suitable scale remains the basic tool for fixing up targets for detailed exploration of minerals. However, due to paucity of outcrops almost in any type of terrain coupled with the inaccessibility of rock exposures in rough and hilly terrain during ground survey, many of the geological maps, to some extent, are built on a considerable quantum of inferences based on random observations or observations along traverses (Ramaswamy, 1983). Remotely sensed data play a unique role in strengthening these inferences by providing relevant information on the continuity of geological interfaces spatially as well as in depth. Most of the information drawn from remote sensing pertains to the surficial exposures of the geological interfaces, both lithological boundaries and structural planes.

One of the main objectives of geologic remote sensing is to discriminate among different rock types and ultimately to identify them thus aiding the mapping process. The role of remote sensing is of paramount importance in the lithological and

structural mapping of a terrain from the following points of view: firstly, the advent of off-nadir viewing capability of the satellite has facilitated the stereoscopic viewing of the imageries of a terrain and secondly, due to the capability of the sensor to detect the radiance in different spectral ranges, and since each material on earth has its characteristic 'unique' response in some specific spectral range, it becomes relatively easy to identify the different litho-units in their characteristic spectral imageries. However, visual interpretation of black and white images and false colour composites (FCCs) generated from raw bands data provides limited scope for identifying various litho-units exposed on the earth's surface. This is because invariably majority of the minerals and rocks exposed on surface are weathered which are mainly composed of the common ingredients namely silicon, aluminium, and oxygen which do not yield spectral features in the visible and near infrared range, thereby imparting similar spectral signatures in the images of different spectral bands (Siegal and Gillespie, 1980). Moreover, due to strong interband correlation caused by similar bulk chemical composition of various rock types, topographical variation and many other obscuring factors such as vegetation growth, a number of ambiguities arise in the process of demarcating different litho-units on the digital images. An effective and practical solution to these problems can be achieved by resorting to the interplay of various digital image processing techniques through which desired and relevant outputs for specific uses can be generated by applying the most suitable

methods. Moreover, in order to optimise the results it is desirable to carry out the conjunctive use of remote sensing techniques with limited ground observations and laboratory reflectance spectra studies of the samples collected from the area of interest.

1.2 OBJECTIVES OF THE STUDY

Spectral response from^a/geological terrain is dependent upon a number of complexly interrelated factors such as soil/vegetation cover, sun-target-sensor geometry, shadow, moisture content and atmospheric effects, as well as rock type and weathering, that make litho-units strongly inhomogeneous and consequently, difficult to classify statistically (Abrams, 1980). Moreover, since the spectral behaviour recorded is the result of interaction of the radiation with the upper few micrometers of the rock surface, it is very difficult to make any direct inference about the underlying lithology. However, in arid and semi-arid environments which are marked by scarcity of vegetation and the consequently favourable exposures of rock surfaces, the spectral reflectance curves of rocks and minerals may be used directly to infer the lithology of the study area.

The present study has been carried out in the semi-arid to arid region in the Aravalli Mountain Ranges of Rajasthan State (India) with the following objectives in mind :

- (1) To discriminate among the different litho-units present in the study areas based on the statistical as well as graphical analyses of the remotely sensed digital data, and

on the digital images generated by employing various image processing techniques,

- (ii) To study the spectral response patterns of the various rocks in relation to the mineralogical composition of the rocks and the laboratory derived diffused reflectance spectra of the rock samples collected from the field,
- (iii) To assess the effect of brightness variation of rocks induced by topography on the digital classification of the rock types, and on the analysis and interpretation of digital images for lithological discrimination,
- (iv) To delineate the major structural features,
- (v) To derive a comparative assessment of the various pattern recognition and image processing techniques for rock discrimination by grossly summarizing the merits and demerits of the various methods employed in the study, and
- (vi) To assess the discrimination capability of the digitally processed images vis-a-vis the available geological map prepared by the Geological Survey of India.

1.3 SELECTION OF STUDY AREAS

The research has been carried out in two phases in two different areas lying in the semi-arid to arid environment in the Aravalli Mountain Ranges, one through the analysis of MSS data (referred to as MSS Study area) and the other through the analysis of thematic mapper (TM) data (referred to as TM Study area) owing to the following reasons. Firstly, the MSS data from Landsat-2 were unable to yield satisfactory results in the discrimination of various litho-units and secondly, the area

studied for MSS data was found to be fairly covered by vegetation growth and also, the area lacks prominent structural features. For these reasons, it was decided to carry out the research in a different area consisting of a number of structural features using TM data from Landsat-5 which provides better scope for lithological discrimination because of its improved spectral, spatial, and radiometric resolutions.

1.3.1 Study Area for MSS Data

An arcuate shaped area located northeast of Sirohi town in Rajasthan State was selected for the analysis of MSS data of Landsat-2. It is bounded between latitudes $N24^{\circ}50'$ to $N25^{\circ}$ and longitudes $72^{\circ}50'$ to 73° and lies in the Survey of India toposheet number 45 $\frac{D}{13}$. The scene constituting the study area covers 285 lines by 386 pixels and is identified on MSS scene number 160-043 on World Reference System (WRS) index map for Landsat-2 and -3. The area comprises numerous closely spaced hillocks and is fairly undulating.

1.3.2 Study Area for Thematic Mapper Data

The area selected for analysis and interpretation of TM data covers a 512×512 (line by pixel) scene within quadrant-1 of TM scene number 148 (path) - 043 (row) with reference to WRS index map for Landsat-4 and -5. The TM area is traversed by three prominent linear ridges trending northeast - southwest and contains little to moderate vegetation in the valleys and on the lower parts of the flanks of the ridges. The area is traversed by numerous dry gullies and streams. Both the MSS and TM areas have

been affected by man made cultivation only at few sites wherever there is supply of water. The TM area lies exactly north of Udaipur city the major part of which falls in Udaipur district and a smaller part in Pali district in Rajasthan. The area is bounded by latitudes $N25^{\circ}01'16''$ to $N25^{\circ}09'53''$ and longitudes $E73^{\circ}28'23''$ to $E73^{\circ}39'20''$ and is covered in the toposheets numbers $45 \frac{G}{8}$ and $45 \frac{G}{12}$ prepared by the Survey of India. The study areas for MSS and TM data are shown in Figure 1.1.

1.4 GEOLOGY OF THE STUDY AREA

As mentioned earlier, the study areas selected for analysis of MSS and TM data belong to the Aravalli Mountain Ranges of early and middle Proterozoic or Precambrian age. Thought to be one of the most ancient mountain ranges in the world, this mountain range runs for more than 700 kms from Delhi in the north to north of Ahmedabad in the south. This orogenic belt which comprises numerous mountains and ridges evolved through the development of a series of basins in which sediments and volcanics were laid down in several successive groups bounded by unconformities. The major units which include the Aravalli Supergroup, the Delhi Supergroup, and the Champaner Group were invaded by hosts of granitic, basic and ultramafic intrusions at different times.

The detailed stratigraphy of the rocks of this mountain range was worked out in detail for the first time by A.M. Heron (1935, 1953) and is given in Table 1.1.

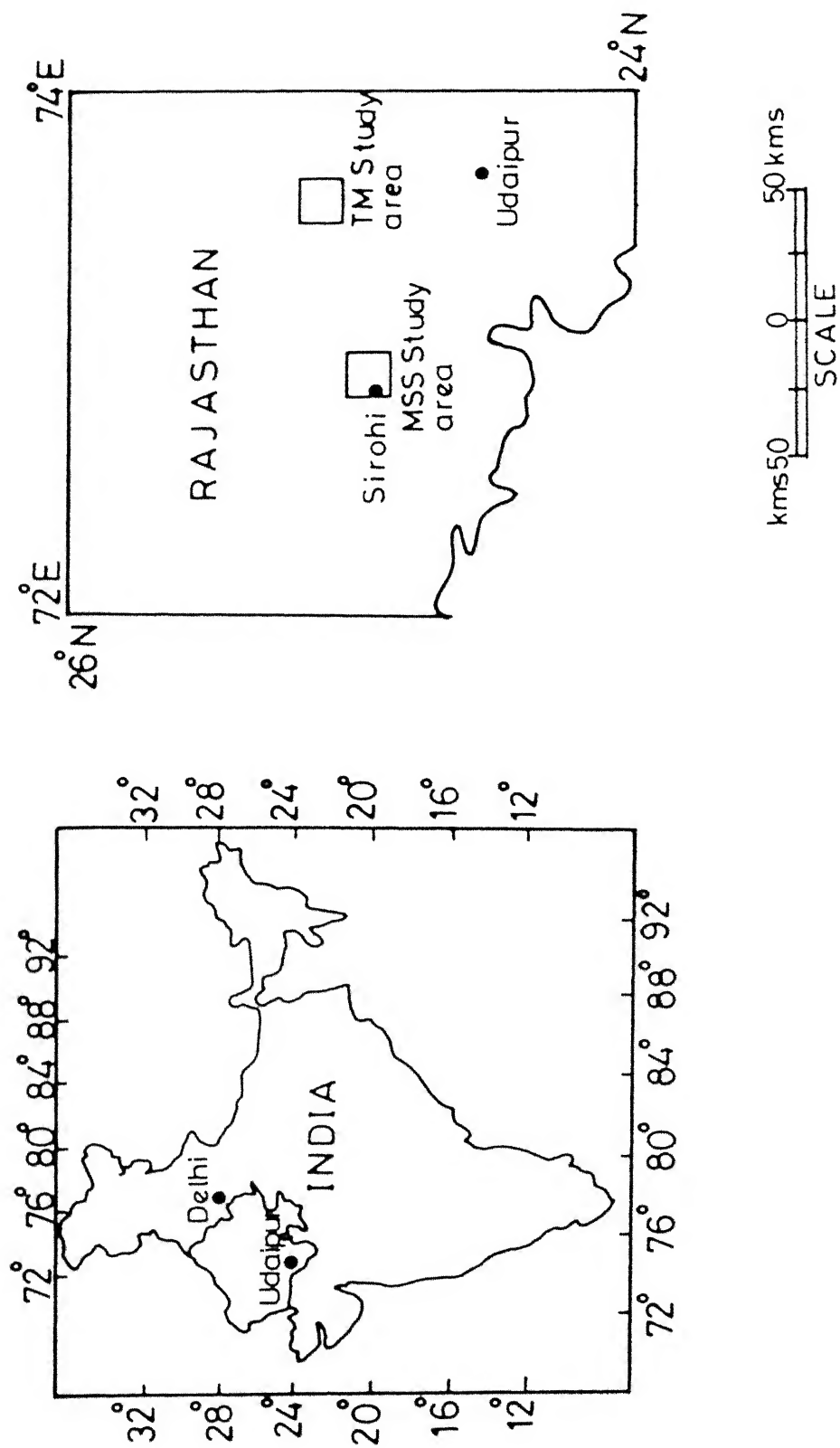


FIGURE 1.1 Study area for the analysis of MSS and TM data.

Table 1.1 Stratigraphic framework of the Aravalli Mountain Ranges
(Based on Heron, 1953)

Erinpura Granite	(900-750 Ma)
Champaner Group	
Post-Delhi Granites	(ca 1450 Ma)
Delhi ^{Super} Group	
Post-Aravalli Granites	(ca 2000 Ma)
Aravalli Supergroup	(ca 2500 Ma)
<hr/>	
Pre-Aravalli granites, gneisses, amphibolites etc.	(> 3000 Ma)
(Mewar Gneiss)	

In the study area, barring the sole Champaner Group, all other rock formations of the Aravalli Mountain Ranges are distributed. The detailed stratigraphy and associated lithology of the various formations modified from the work of Heron (1953) are given in Table 1.2.

Table 1.2 Stratigraphy of the Study Area

(Modified after Heron, 1953; A.B. Roy, 1988)

<u>Formation</u>	<u>Lithology</u>
Recent Alluvium	
Malani Series	Erinpura granites and gneisses, Hornblende schists, Syenites
Delhi Supergroup	
Ajabgarh Series	Upper Phyllites Limestones Biotitic limestones and calc-gneisses Calc schists, biotite schists and composite gneiss

Table contd...

Aravalli Supergroup	Impure Limestones, quartzites, phyllites, biotite schists, composite gneiss Quartzites, grits and local soda- syenites, conglomerates Local amygdaloids and tuffs
---------------------	--

The study area selected for analysis of MSS data comprises rock types belonging to Aravalli Supergroup and Erinpura granites and gneisses as shown in Figure 1.2. The major rock types present are gneiss, schist, phyllite, quartz mica schist, intercalated calc and cherty quartzite, marble, phyllite, calc gneiss, granite and syenite. On the other hand, the area selected for analysis of TM data comprises mainly phyllites, impure limestones, biotitic limestones and calc gneiss, calc schists, and quartzites belonging to Ajabgarh Series of Delhi Supergroup, and Erinpura granites. The geological map of TM area is shown in Figure 1.3. Among the various rock types present in the MSS and TM areas, except the quartzites, all other rocks are weakly weathered at few places only. Surficial coatings resulting from weathering can be clearly noticed at many sites. In the Aravalli Mountains, vegetation differences are controlled by elevation and proximity to surface drainage rather than by the lithofacies (Drury, 1987). The MSS study area lacks prominent structural features, whereas the TM study area comprises a major fold with its axis trending NE-SW and a fault striking NNW-SSE.

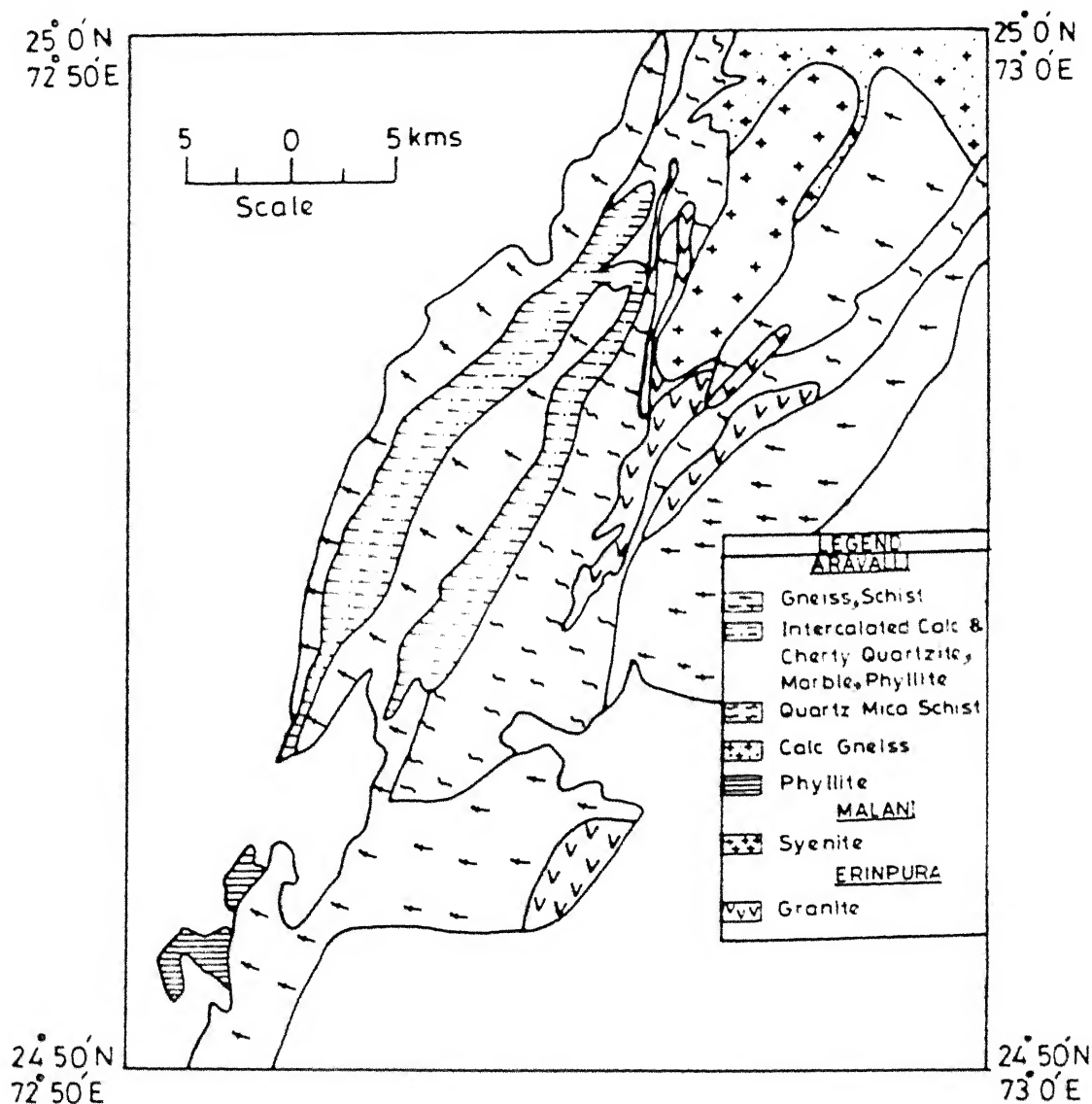


FIGURE 1.2 Geological map of the MSS study area.
(Source: Geological Survey of India Memoirs, Vol.25, 1895 and Geological and Mineral Map of Rajasthan, G.S.I. Publication, 1969).

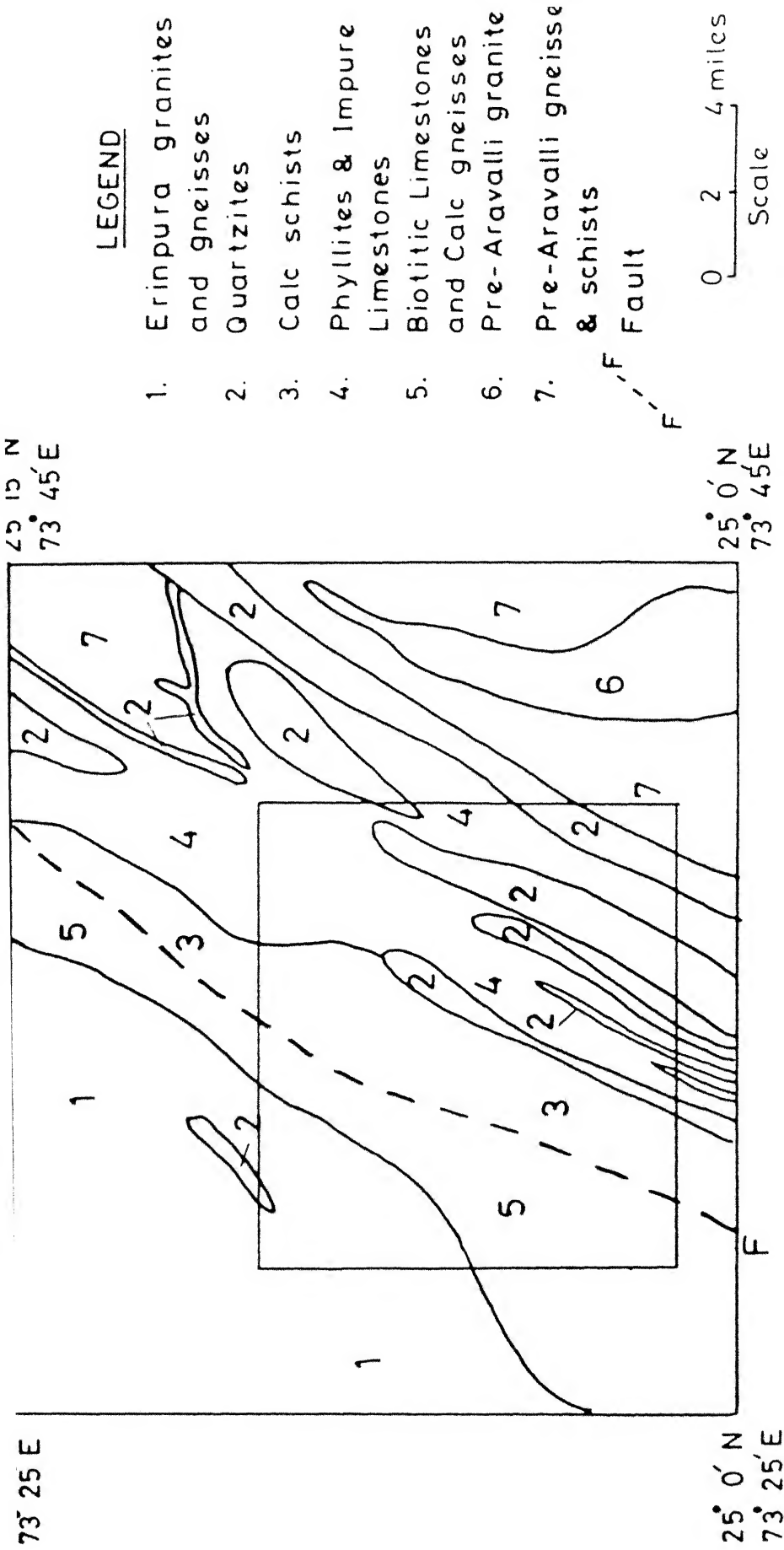


FIGURE 1.3 Geological map of the TM study area; (Modified from Geological Survey of India Memoirs, Vol. 79, Plate 38, 1953); The inner rectangle represents the area actually studied through the analysis of TM digital data.

1.5 DATA ACQUISITION

The following materials were acquired in order to carry out the objectives of the research.

(I) Computer Compatible Tapes (CCTs) :

(i) Two CCTs of MSS data and imageries pertaining to scene number 160-043 of Landsat-2 acquired on 9-10-1978 (Id No. 8286904375500) and procured from EROS Data Centre, Sioux Falls, South Dakota. In addition, four black and white imageries for each band of MSS data on 1:1 million scale identified by scene number E-2 869-043375-5 of June 9, 1977 were acquired from the above organization.

(ii) For TM area, three CCTs and corresponding imageries in bands 5 and 7 of Jan 31, 1988 pertaining to quadrant-1 of scene number 148-043 were procured from National Remote Sensing Agency (NRSA), Hyderabad.

(II) Geological Maps : There is a great paucity of geological maps for the study areas. The study was, therefore, carried out resorting to the following geological maps which are the only ones available at present.

For MSS area, geological map prepared by La Touche on 1:250,000 scale (1895), Geological Survey of India Plate No. 56 (1975) and Geological and Mineral Map of Rajasthan, G.S.I. publication (1969), and for TM area, geological map prepared by A.M. Heron (1953) on the scale of 1 inch to 4 miles. It may be noted that although several modifications and improvements have been made to these the basic

configuration or distribution of the rock formations and structural features have remained unchanged (Roy, 1988).

(III) Toposheets : The following toposheets were acquired for locating training samples and for field observations.

MSS area : $45 \frac{D}{13}$

TM area : $45 \frac{G}{8}$ and $45 \frac{G}{12}$, all being on 1:50,000 scale

1.6 EXTRACTION OF DIGITAL DATA PERTAINING TO STUDY AREAS

The study areas chosen for the analysis of MSS and TM data constitute only small parts of their respective scenes. In the present study, different approaches have been made to extract the digital data pertaining to the two areas in various bands (i.e. bands 4 to 7 of MSS data, and bands 1 to 5, and band 7 of TM data).

1.6.1 MSS Study Area

The study area pertaining to MSS data was demarcated on the basis of the line number and pixel number of the corner points as calculated with reference to those of the scene corners. The exactly similar operation was carried out for extracting the reflectance values at respective training sites.

The determination of line number and pixel number and the corresponding reflectance value at any point on the imagery involves the following steps of operations.

- (i) Precise determination of geographical coordinates (i.e. latitude and longitude) on the imagery or with the help of toposheets

- (ii) Conversion of geographical coordinates to conical orthomorphic coordinates.

This procedure leads to what is called the cartographic projection of geographical coordinates. This is necessary because the Landsat imagery is taken from a curved (geoidal) surface of the earth, whereas the imagery itself is obtained on a plane where the actual measurement of geographical coordinates is carried out. In a country like India having a north-south elongation, conical orthomorphic projection is appropriate.

- (iii) Transformation of conical orthomorphic coordinates to respective line numbers and pixel numbers on Landsat imagery.

- (iv) Reading the computer compatible tapes to obtain reflectance values at given line numbers and pixel numbers.

A detailed description regarding the conversion of geographical coordinates to conical orthomorphic coordinates and in turn, the line numbers and pixel numbers, and the relevant computer programs are given by Rampal (1982). Following the relevant procedure, the conical orthomorphic coordinates of the corners of the MSS scene and the transformation coefficients were determined which are given in Tables 1.3 and 1.4 respectively. Then, using the same coefficients of transformation, the line numbers and pixel numbers of the four corners of the study area were derived which are shown in Table 1.5.

Table 1.5 Geographical Coordinates of the MSS Study Area and Corresponding Line Numbers and Pixel Numbers

Location	Geographical Coordinates		Scene Coordinates	
	Latitude ($^{\circ}$ N)	Longitude ($^{\circ}$ E)	Line No.	Pixel No.
NW Corner	25°	$72^{\circ}50'$	463	2288
NE Corner	25°	73°	424	2582
SW Corner	$24^{\circ}50'$	$72^{\circ}50'$	709	2379
SE Corner	$24^{\circ}50'$	73°	670	2674

It may be seen that the study area selected for analysis of MSS data covers 285 lines by 386 pixels, that is, approximately an area of 495 sq.kms. The MSS study area with its corner coordinates is shown in Figure 1.2. Then the digital data corresponding to different spectral bands in the subscene were extracted from the full scene with reference to the scene coordinates (i.e. line number and pixel number) of the corners of the subscene.

1.6.2 TM Study Area

The area studied by using the TM data was demarcated on the digital image of the entire scene displayed on the colour monitor screen. The area of interest was located on the digital image by matching the features on the image with those on a large scale topographical map of the TM area with reference to the geographical coordinates of the corners of the toposheet. After the study area was demarcated the reflectance values were

extracted by positioning the cursor at selected training sites with the help of a trackball cursor-moving device. The TM study area with its corner coordinates is shown in Figure 1.3.

1.7 PREVIOUS WORK

Ever since the first remote sensing satellite was launched by the United States of America on July 23, 1972 for collecting information about earth resources, a great deal of work has been carried out in the field of geological studies by a number of researchers from all over the world. In the following, ^a few of their notable works are outlined in ^{the} context of the scope and objectives of the present study.

The first systematic study of the principal components of multispectral data specifically intended for a geological study is by Santisteban and Munoz (1978). Their work pertaining to Landsat MSS images has shown that PCA is a very potential technique in eliminating the effect of interband correlation to a considerable extent and consequently, compressing the information content of a n-band image into only a fewer number of components.

Abrams et al. (1983) have carried out a comparative study of the Landsat-4 MSS data and aircraft scanner data simulating the new Landsat-4 TM data to evaluate the spatial and spectral capabilities of both systems for separation of lithologies; discrimination of hydrothermal alteration, and structural mapping. They have reported that Landsat TM data would provide geologists with an improved mapping tool compared to the previous Landsat scanners.

An excellent work pertaining to determination of optimum spectral bands for rock discrimination has been reported by Siegrist et al. (1980) based on aircraft scanner data. Rowan et al. (1987) have successfully applied PCA, band ratioing technique and density slicing technique for digital classification of contact metamorphic rocks in Extremadura, Spain using Landsat thematic mapper data. Lithological discrimination studies using airborne multispectral scanner imagery has also been carried out by Greenbaum (1987) in Central Snowdonia, Great Britain. His research focusses on the utility of optimum index factor (OIF) in evaluating the ranking of possible three band combinations in terms of their uncorrelated spectral data content. D. Evans (1988) has done a comparative study of linear discriminant analysis and supervised classification results based on signatures from Landsat TM, Thermal Infrared Multispectral Scanner (TIMS), and airborne Synthetic Aperture Radar (SAR) for classification of sedimentary rocks in Wind River Basin, Wyoming. A statistical classification of rock types in northern Chile has been attempted by Oldfield and Elgy (1987) using tonal, textural and contextual features of remotely sensed imagery. Their works have shown that contextual filtering can improve the visual appearance of thematic maps produced by computer classification.

An extensive amount of literature is available on the works of Hunt, Salisbury and others (1970, 1976) regarding the visible and near-infrared spectra of a diversity of minerals and rocks determined in the laboratory. Their works suggest that no direct information concerning the bulk chemical composition of

geological materials is available in this range. This is because of the common presence of elements like Al, Si and O which do not possess energy levels such that transitions between them can yield spectral features in visible and near infrared range. In addition, Hunt and Ashley (1974) have proved experimentally that in naturally occurring geological materials most spectral information in these ranges is dominated by the very common presence of iron. However, in short wavelength infrared, features are observed due to presence of hydroxyl molecules and water commonly occurring in clay minerals because of their high fundamental frequencies. Kahle (1984) has presented a comprehensive review concerning the laboratory and field reflectance spectra of minerals and rocks occurring in arid and semi-arid environments. It is reported here that the spectral curves could be used directly in order to infer the lithology of the arid to semi-arid regions owing to scarcity of vegetation and consequently favourable exposures of surfaces.

A scanty amount of literature is available on application of remote sensing methods for rock discrimination studies in the study area. Gupta and Ganesh Raj (1986) have compiled a technical report from the works pertaining to use of remotely sensed data for geological studies in India, in which a very few papers are available pertaining to the study area. Bakliwal et al. (1985) and Ramaswamy et al. (1986) have employed digital enhancement of Landsat MSS data for locating gossans in Rajpura, Dariba and Bhilwara district of Rajasthan. In an area in proximity to the study area chosen for TM data, Gupta and Viswanathan (1983) have

prepared drainage, lithological and structural maps using Landsat-2 MSS data. In the MSS study area, Gupta (1980) has conducted a reconnaissance study on the geology, mineralization and natural resources using raw band imageries of Landsat-2 MSS data.

It is quite apparent from the literatures cited above that digital image processing of remotely sensed data has a fairly reasonable scope for detailed study concerning lithological discrimination and structural mapping in the semi-arid to arid region of the Aravalli Mountain Range. Keeping this point in view, a test area was selected for methodological and thorough treatment of various image processing techniques using Landsat MSS and TM data.

1.8 METHODOLOGY

Keeping in view the objectives of the present study and the constraints involved in the availability of the desired facilities, the following methodology was adopted in order to accomplish the tasks involved in an efficient manner.

1.8.1 Reading of Data

It is the most primary task involved in any kind of research making use of remotely sensed data. The original MSS data from Landsat-2 was recorded in 32 bit configuration (i.e. 1 word = 32 bits) on 800 bpi (bits per inch) density. Therefore, it was necessary to convert these data into 36 bit format recorded on 1600 bpi density tapes in order to make it compatible with the DEC-1090 system existing at IIT Kanpur. This job was carried out

at CMC, Secunderabad by inserting a dummy bite following each word of the original data and copying it later on another tape of 1600 bpi density. The digital data on the original CCTs are recorded in Band Sequential (BSQ) Format.

The thematic mapper (TM) data are recorded in Band Interleaved (BIL) format in which each line consists of seven records, each record representing the digital data of a particular spectral band. The seven records are stored sequentially from band 1 to band 7. However, although the digital data were recorded on 1600 bpi density tapes, the 32-bit recording configuration precluded the possibility of reading the data at any of the computer systems existing at IIT Kanpur at the time of research. Therefore, the desired operations involved in the analysis and interpretation of thematic mapper data were carried out at the VIPS-32 image processing system installed at Regional Remote Sensing Service Centre (RRSSC), Dehradun (U.P.).

1.8.2. Preprocessing

It aims at correcting the original degraded data for radiometric calibration, geometric distortion and removal of noise to create a more faithful representation of the original scene - a process which is also called image rectification and restoration. For the present study, however, since the data used had been already corrected for noise elimination and radiometric calibration, the only operation remained to be performed was to check the data for geometric accuracy. This operation was performed by applying the nearest neighbourhood resampling method.

Image resampling involves the reformation of an image onto a new base. This is achieved by using features that are common to both the image and the new base (Bernstein, 1976). These features which are termed ground control points (GCP) are located on the distorted image by their x and y coordinates and on the new base by their latitudes and longitudes. The functional relationships (f_1 and f_2) between image x and y and latitude and longitude are determined by least squares regression as follows :

$$x = f_1 (\text{lat \& long})$$

$$y = f_2 (\text{lat \& long})$$

where x = image coordinates (rows and columns) and

f_1 & f_2 = transformation functions.

In the present study, ^{the sharp corners of the} water bodies were considered GCPs. Their coordinates (latitudes & longitudes) were measured on the toposheet and then converted to corresponding line numbers and pixel numbers. These were matched with their counterparts on the distorted image where it was observed that the GCPs on the image are misplaced in comparison to their true locations on the ground. In order to correct for this distortion, the digital data recorded in ^{the} form of a matrix were rearranged by shifting each pixel back by ^{the} required margin. This procedure was repeated until a pixel accuracy of +2 to +3 was achieved. This process was preferred because of its computational simplicity as well as its property of retaining the brightness values of the original image unaltered.

.8.3 Development of Software for Image Processing and Pattern Recognition Techniques

In the present study, discrimination of rock types has been carried out employing a number of pattern recognition and image processing techniques. These include Histogram Generation, Contrast Stretching, Band Ratioing, Principal Component Analysis (PCA), Inverse Principal Component Analysis, Correspondence Analysis, Brightness and Greenness Indices, Discriminant Function Analysis, and Maximum Likelihood Classifier. All the techniques mentioned above were applied for the analysis and interpretation of TM data which were read at the image processing system existing at RRSSC, Dehradun. The TM data has been analysed resorting to the statistical and graphical outputs and also, the digital images generated by applying various image processing techniques. However, the MSS data was classified applying only Histogram Generation, Band Ratioing, Discriminant Function Analysis, and Principal Component Analysis. The analysis of MSS data was carried out at DEC-1090 computer system based upon the statistical and graphical outputs since image processing facility was not available with this computer.

The analysis of both MSS and TM data was initiated with the extraction of various multivariate parameters such as mean, variance, covariance and correlation coefficients of different rock types taking into consideration their respective training reflectance values in different bands. This is very important in the sense that these parameters are very useful for determining vital criteria such as interband correlation, and band-component

(principal component) correlation which together or separately, in turn, provide a proper insight to the analysis and interpretation of digital images for rock discrimination studies.

Subsequently, both MSS and TM data were treated for graphical method of Principal Component Analysis. The objective of this approach was to evaluate the potential of different principal components to account for the variance of the system represented by the scatter plots of training data of various classes in two-dimensional spaces defined by different pairs of spectral channels. This was followed by the graphical method of Discriminant Function Analysis. The objective of this method is to ascertain the degree of discrimination between the rock types in various rock pairs on the basis of the number of training brightness values of the rocks present on either side of the line of division in the two-dimensional space. The graphical method of analysis was also supplemented by the generation of histograms from training data sets and their band ratios.

The next step to follow was obviously the multivariate analysis of digital data. In the present study, an attempt has been made to statistically classify the MSS and TM data for discriminating among different rock types on the basis of the decision intervals or confidence limits of rock types estimated for various principal components by considering the training reflectance data of the litho-units. The results of various analysis are presented in statistical form for MSS data and both as statistical outputs and digital images for TM data. For

analysis of digital data, relevant software not available in literature was developed for many of the methods described above.

Following the completion of computational works and generation of digital images, a geological map and a structural map were prepared from the digital images and compared with the one prepared by the Geological Survey of India.

The results obtained through application of various digital image processing techniques were verified vis-a-vis the analysis and interpretation of behaviour of reflectance spectra of the representative rock samples collected from their respective sites in the field. Furthermore, in order to study the reflectance characteristics of the rocks, mineralogical identification studies were carried out by X-ray diffraction analysis of rock powders and optical microscopic studies of thin sections. In order to accomplish these tasks, earlier a field trip was organized for making a reconnaissance check of the terrain and the exposed rock formations besides collecting rock samples from representative locations.

The study was concluded with a summary of results with reference to the potential of various image processing techniques for rock discrimination using remotely sensed data. In addition, a brief note on recommendations and useful suggestions are presented at the end.

1.9 ORGANIZATION OF THE THESIS

The materials contained in the thesis is organized into seven chapters. Chapter 1 begins with an introduction of importance of digital image processing of remotely sensed data

for lithological discrimination. It also comprises a brief description about the geology and terrain characteristics of the study area, objectives, relevant methods and previous research in the field. In Chapter 2, a detailed description of various image processing techniques adopted for the study is presented. Chapter 3 comprises the results and discussions of various experimental methods for rock analysis such as X-ray diffraction studies, thin section studies by optical microscope, and analysis and interpretation of diffused reflectance spectra in the laboratory. Chapter 4 deals with the results and discussions of the graphical analysis of the remotely sensed digital data. In Chapter 5, a detailed description is provided concerning the analysis and interpretation of the statistical results and the digital images generated using the multispectral remotely sensed data. Chapter 6 is devoted exclusively to the supervised classification of the thematic mapper data by maximum likelihood classifier. Chapter 7 comprises summary of the results obtained from various studies. In addition, this chapter also comprises a geological map and a structural map prepared from the digital images, and subsequent comparison of this geological map with the geological map published by the Geological Survey of India. This is followed at the end by a brief note on the useful suggestions and recommendations for future research.

CHAPTER 2

DIGITAL IMAGE PROCESSING TECHNIQUES

2.1 INTRODUCTION

Digital image processing involves the manipulation and interpretation of digital images with the aid of a computer. A digital image is a two-dimensional numeric representation of a sampled field i.e. the reflected and emitted radiance. In actual practice, it consists of a rectangular array of numbers usually stored on magnetic tape or disk. Remotely sensed images can be either continuous (analogue) such as an aerial photograph or digital such as a Landsat MSS image where detail is held in discrete signal units.

All the procedures falling under the domain of digital image processing may be categorized into four broad types of computer assisted operations as mentioned below (Lillesand and Kiefer, 1987):

1. Image rectification and restoration
2. Image Enhancement
3. Image Classification
4. Data Merging or Geographic Information Systems (GIS)

In the present study, except the GIS all forms of image processing techniques have been employed for the analysis of remote data. Image rectification and restoration have been discussed earlier in Section 1.8.2. In the following sections

various enhancement and classification techniques will be dealt with.

2.2. CHARACTERISTICS OF REMOTELY SENSED DATA USED IN THE STUDY

A thorough knowledge regarding the nature and usefulness of remotely sensed data is essential not only for selecting the appropriate methods of digital image processing for specific uses but also for accurate interpretation of the digitally processed images. In the following ^{pages,} a brief description of various characteristics of MSS and TM data is presented.

2.2.1 Characteristics of MSS Data from Landsat-2

The MSS on board Landsat-1, -2 & -3 covered a 185 km swath width in four wavelength bands, two in the visible spectrum of 0.5 to 0.6 μm (green) and 0.6 to 0.7 μm (red), and two in the near infrared at 0.7 to 0.8 μm and 0.8 to 1.1 μm . These bands were designated as bands 4, 5, 6, and 7 respectively. A nominal scene of MSS consists of some 2340 scan lines, with about 3240 pixels per line, each pixel on CCT having a cell size of 56mx79m corresponding to 79mx79m ground resolution cell - the difference being caused by the time lag between the scanning rate and the conversion of continuous electric signal to discrete digital number. The MSS offers a radiometric resolution of 7 bit for bands 4, 5, and 6, and 6 bit for band 7. As a result, the radiance levels or brightness values in bands 4 to 6 are scaled to a range of 0 to 127 and in band 7, they are scaled from 0 to 63. The intended principal application of each spectral band of MSS data is presented in Table 2.1.

Table 2.1 Characteristics of MSS Bands (from Rampal, 1982)

Sl.No.	Band No.		Remarks
1	4	(i)	has the best capability to penetrate water
		(ii)	can be used for study of turbidity in water bodies
		(iii)	distinguishes green vegetation from other surface covers
		(iv)	helps in identifying geologic structures
2	5	(i)	useful for defining cultural (built up), urban and topographic features
		(ii)	useful for classifying different types of green vegetation with full ground cover
3	6	(i)	particularly helpful in land use studies
		(ii)	useful in detecting green biomass in vegetation
4	7	(i)	extremely useful in mapping water bodies (surface)
		(ii)	very effective in delineating land-water boundary and soil-crop contrast

2.2.2 Characteristics of Thematic Mapper (TM) Data

The thematic mapper kept aboard Landsat-4 and -5 is a highly advanced multispectral scanner incorporating a number of spectral, radiometric and geometric design improvements relative to the MSS. Spectral improvements include the acquisition of data in seven bands with new bands in the visible (blue), mid infrared and thermal portions of the spectrum. Also, the wavelength range and location of TM bands are chosen in such a way as to significantly improve the spectral differentiability of major earth surface features.

Radiometrically, the TM records the signal (i.e. the radiance from the earth's surface) over a quantization range of 256 digital numbers (8 bits) which not only permits observation of smaller changes in a given band but also it provides greater sensitivity to changes in relationships with bands. Geometrically, TM offers a spatial resolution of 30 m in bands 1-5 and 7 and 120 m in band 6 which is in thermal range. The application potential of different spectral channels of TM data is listed in Table 2.2.

2.3 IMAGE ENHANCEMENT

Image enhancement aims at improving the visual interpretability of an image by increasing the apparent distinction between the features in the scene. Since the visual interpretability is a subjective measure varying from person to person, there is no simple rule that may be followed to produce the single best image for a specific application. Most enhancement techniques may be categorized as either point or

TABLE 2.2 Characteristics of Thematic Mapper Spectral Bands
(from Lillesand and Kiefer, 1987)

Band	Wavelength (μm)	Nominal spectral location	Principal applications
1	0.45-0.52	Blue	Designed for water body penetration, making it useful for coastal water mapping. Also useful for soil/vegetation discrimination, forest type mapping, and cultural feature identification.
2	0.52-0.60	Green	Designed to measure green reflectance peak of vegetation for vegetation discrimination and vigor assessment. Also useful for cultural feature identification.
3	0.63-0.69	Red	Designed to sense in a chlorophyll absorption region aiding in plant species differentiation. Also useful for cultural feature identification.
4	0.76-0.90	Near-infrared	Useful for determining vegetation types, vigor, and biomass content, for delineating water bodies, and for soil moisture discrimination.
5	1.55-1.75	Mid-infrared	Indicative of vegetation moisture content and soil moisture. Also useful for differentiation of snow from clouds.
6	10.4-12.5	Thermal infrared	Useful in vegetation stress analysis, soil moisture discrimination, and thermal mapping applications.
7	2.08-2.35	Mid-infrared	Useful for discrimination of mineral and rock types. Also sensitive to vegetation moisture content.

local operations. Point operations modify the brightness value of each pixel in an image data set independently, whereas local operations modify the value of each pixel based on neighbouring brightness values.

All the processes of digital enhancement(s) can be broadly categorized into three groups such as contrast manipulation, spatial feature manipulation and multi-image enhancement. The enhancement methods which have been resorted to for the analysis of digital data in the present study are mentioned below under these broad categories.

2.3.1 Contrast Stretching

Remotely sensed satellite images are typically four to display a very narrow range of brightness values probably caused either due to extreme illumination conditions i.e. very poorly or very highly illuminated areas or identical reflectance characteristics of earth's surface materials (Jensen, 1986). As a result of this poor contrast, objects with slightly different brightness values are very difficult to be differentiated from one another. Contrast stretching is a technique that expands the narrow range of brightness values present in the raw image over the entire dynamic range of gray values recorded by the detector, thereby accentuating the contrast between features of interest and making their distinction possible. This is a very useful technique for lithological discrimination.

There are basically two broad types of contrast stretching such as linear and nonlinear.

2.3.1.1 Linear Contrast Enhancement

As the name suggests, this technique involves uniform expansion of the pixel values in the input (raw) image to the full range of the display device (generally 0-255, which is the range of values representable in an 8-bit display device). The linear stretch algorithm (Arlington, 1979) used in the present study is as follows :

$$DN' = \left[\frac{DN - MIN}{MAX - MIN} \right] \times 255 \quad (2.1)$$

where DN' = digital number assigned to pixel in output image

DN = original digital number of pixel in input image

MIN = minimum reflectance value in the scene

MAX = maximum reflectance value in the scene

One major drawback of the linear stretch is that it assigns equal weight to all DNs regardless of their frequency of occurrence. As a result, light tonal areas appear lighter and dark areas appear darker.

2.3.1.2 Nonlinear Contrast Stretch : Gaussian Stretch

It aims at transforming the observed histogram of the original data to a normal or Gaussian histogram. A Gaussian or normal distribution is given by

$$f(x) = Ce^{-ax^2}, \quad (2.2)$$

where $C = (a/\pi)^{0.5}$

The standard deviation, σ , is defined as the range of the variable 'x' (Mather, 1987).

This is carried out by centering the distribution on the range (i.e. 127.5 (or 128) on a 256 grey level scale) and expanding or compressing the distribution using the scale factor 'f' given by the user, so that the two half ranges 0-128 and 128-255 represent 'f' standard deviation i.e. $m-fE$ and $m+fE$, where m = mean and E = standard deviation. The intermediate results are stored in real format, the output values of which, after post-normalization are truncated and stored in output subscene. Algorithm for the intermediate results is :

$$Y'_k(i,j) = a_k \cdot Y_k(i,j) + b_k, \quad (2.3)$$

where $a_k = 128/(fxE_k)$

and $b_k = 128 (1-m_k/fxE_k)$

where m_k = mean and E_k = standard deviation of the k^{th} band in the output scene of the intermediate results.

2.3.2 Multi-image Manipulation

2.3.2.1 Band Ratioing

Band ratioing is a technique in which digital numbers of one band are divided by the corresponding digital numbers of another band. Mathematically, this is expressed as follows :

$$BV_{i,j,r} = \frac{BV_{i,j,k}}{BV_{i,j,l}} \quad (2.4)$$

where $BV_{i,j,r}$ is the output ratio value for the pixel at row i , column j ; $BV_{i,j,k}$ is the brightness value at the same location in band k ; and $BV_{i,j,l}$ is the brightness value in band l at the same location (Jensen, 1986). The resultant ratio data are then

rescaled to fill the dynamic range of the display medium by contrast enhancement technique.

2.3.2.2 Principal Component Analysis

Extensive interband correlation is a problem frequently encountered in the analysis of multispectral image data. That is, images generated by digital data from various wavelength bands often appear similar and convey essentially the same information. Such redundancy in the image data can be eliminated by applying the technique of principal component transformation (Lillesand and Keifer, 1987; Jolliffe, 1986; Morrison, 1976). If it is employed as a preprocessing technique prior to automated classification of the data, the transformation may also increase the computational efficiency of the classification process because this technique attempts to reduce the dimensionality of the original data set. In other words, the information content in an original 'n' channel data set are compressed into a fewer than 'n' new channels (say p, where $p < n$) or components. These principal components are certain linear combination of the original bands obtained by means of Karhunen-Loeve transformation (Moik, 1980; Jensen, 1986).

The objective of ^{the} principal component analysis is to transform the sometimes highly correlated data into an uncorrelated n-dimensional feature space in such a manner that the maximum data variance or information content is redistributed ^a in/descending order in the new transformed axes. The concept involved may be expressed graphically by considering a two-channel image data set as shown in Figure 2.1. It shows an

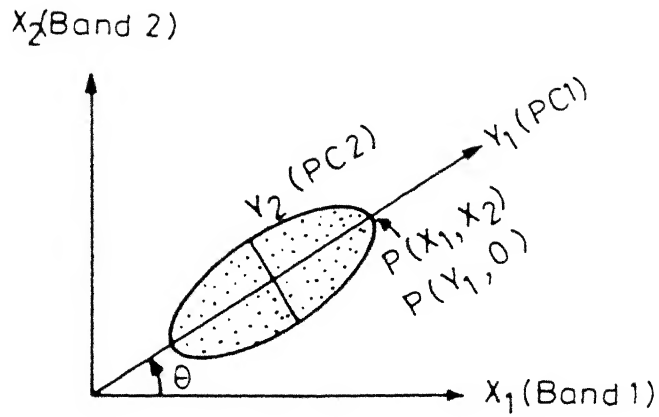


FIGURE 2.1 Graphical representation of effect of rotation on original scatter plots (eg, on a point, P).

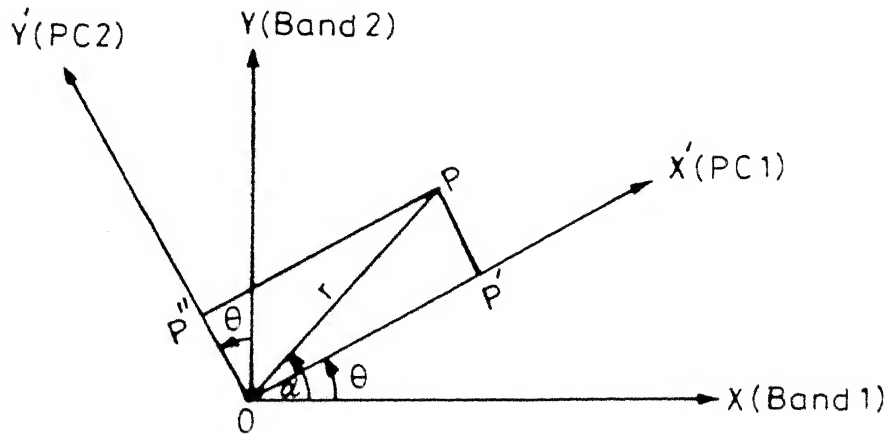


FIGURE 2.2 Graphical representation for determination of rotation angle ' θ ' and principal components with respect to original axes.

elliptical scatter plot of the original brightness values of some features between bands X_1 and X_2 . It is obvious from the figure that a point P in the distribution has almost the same variances with respect to bands X_1 and X_2 , that is, the covariance between bands X_1 and X_2 is too high as a result of their strong correlation. In order to minimise the degree of correlation between the two bands the axes have to be rotated, of course maintaining their orthogonality, in such a way that they represent the major and minor axis of the elliptical scatter plot so that the maximum variance is concentrated in the band (component) representing the major axis while the other band (component) acquires the remaining variance. This is evident with respect to point 'P' whose coordinate changes from (X_1, X_2) to $(Y_1, 0)$.

Algebraically, the transformed axes called the principal components may be expressed in terms of the linear combinations of the original data values. That is,

$$y_1 = a_{11}x_1 + a_{12}x_2 \quad (2.5)$$

$$\text{and } y_2 = a_{21}x_1 + a_{22}x_2 \quad (2.6)$$

or in matrix form,

$$\begin{bmatrix} y_1 \\ y_2 \end{bmatrix} = \begin{bmatrix} a_{11} & a_{12} \\ a_{21} & a_{22} \end{bmatrix} \begin{bmatrix} x_1 \\ x_2 \end{bmatrix} \quad (2.7)$$

The angle of rotation ' θ ' of the transformation is derived as follows. As shown in Figure 2.2, a XY coordinate system representing two spectral bands is rotated by an angle ' θ ' with the same origin so that the transformed coordinates become X'Y'.

A point 'P' representing the original brightness value in XY system and positioned at a distance 'r' from the origin will now have a transformed brightness value in X'Y' system.

Following the basic principles of geometry, we can express

$$\begin{aligned} X' = OP' = PP'' = OP \cos(\alpha - \theta) \\ = r (\cos\alpha \cos\theta + \sin\alpha \sin\theta) \end{aligned} \quad (2.8)$$

where ' α ' is the angle subtended between OP and X axis.

$$\text{Now} \quad r \cos\alpha = X$$

$$\text{and} \quad r \sin\alpha = Y$$

$$\text{Thus} \quad X' = X \cos\theta + Y \sin\theta \quad (2.9)$$

$$\begin{aligned} \text{and} \quad Y' = PP' = OP'' = OP \sin(\alpha - \theta) \\ = r (\sin\alpha \cos\theta - \cos\alpha \sin\theta) \\ = Y \cos\theta - X \sin\theta \end{aligned}$$

$$\text{or} \quad Y' = -X \sin\theta + Y \cos\theta \quad (2.10)$$

The transformed axes, or components, X' and Y' may be expressed in matrix form as

$$\begin{bmatrix} X' \\ Y' \end{bmatrix} = \begin{bmatrix} \cos\theta & \sin\theta \\ -\sin\theta & \cos\theta \end{bmatrix} \begin{bmatrix} X \\ Y \end{bmatrix} \quad (2.11)$$

where $\begin{bmatrix} \cos\theta & \sin\theta \\ -\sin\theta & \cos\theta \end{bmatrix}$ is the rotation matrix denoted by A.

Let σ_X^2 and σ_Y^2 be the variances of measurement in X and Y values. As a result of rotation, it can be shown that the new variances $\sigma_{X'}^2$ and $\sigma_{Y'}^2$ to X' and Y' are given by

$$\begin{bmatrix} \sigma_{X'}^2 \\ \sigma_{Y'}^2 \end{bmatrix} = A \Sigma A^t \quad (2.12)$$

where Σ is the covariance matrix of X and Y and is given in the matrix form by

$$\Sigma = \begin{bmatrix} \sigma_X^2 & \sigma_{XY} \\ \sigma_{XY} & \sigma_Y^2 \end{bmatrix} \quad (2.13)$$

where σ_{XY} is the covariance of X and Y. Substituting for Σ we get,

$$\begin{aligned} \begin{bmatrix} \sigma_{X'}^2 \\ \sigma_{Y'}^2 \end{bmatrix} &= \begin{bmatrix} \cos\theta & \sin\theta \\ -\sin\theta & \cos\theta \end{bmatrix} \begin{bmatrix} \sigma_X^2 & \sigma_{XY} \\ \sigma_{XY} & \sigma_Y^2 \end{bmatrix} \begin{bmatrix} \cos\theta & -\sin\theta \\ \sin\theta & \cos\theta \end{bmatrix} \\ &= \begin{bmatrix} \sigma_{X'}^2 & \sigma_{X',Y'} \\ \sigma_{X',Y'} & \sigma_{Y'}^2 \end{bmatrix} \end{aligned} \quad (2.14)$$

After computation, this leads to following sets of equations :

$$\sigma_{X'}^2 = \sigma_X^2 \cos^2\theta + \sigma_Y^2 \sin^2\theta + 2 \sin\theta \cdot \cos\theta \cdot \sigma_{XY} \quad (2.15)$$

$$\sigma_{Y'}^2 = \sigma_X^2 \sin^2\theta + \sigma_Y^2 \cos^2\theta - 2 \sin\theta \cdot \cos\theta \cdot \sigma_{XY} \quad (2.16)$$

$$\sigma_{X',Y'} = -\sigma_X^2 \sin\theta \cdot \cos\theta + \sigma_Y^2 \sin\theta \cdot \cos\theta - \sigma_{XY} \sin^2\theta + \sigma_{XY} \cos^2\theta \quad (2.17)$$

$$\text{and } \sigma_{Y',X'} = \sigma_{X',Y'}$$

To maximize variances we have to minimize covariances. Thus letting $\sigma_{X',Y'} = 0$ in equation (2.17) leads to

$$\tan 2\theta = - \frac{2\sigma_{XY}}{\sigma_Y^2 - \sigma_X^2} \quad (2.18)$$

where θ = angle of rotation.

In other words, if the axes are rotated through an angle θ given by the above expression, the new variances $\sigma_{X'}^2$, and $\sigma_{Y'}^2$, will be maximized and covariance $\sigma_{X',Y'}$, or $\sigma_{Y',X'}$, will vanish, breaking the correlation between X and Y. This will make X' independent of Y'. These new components viz X' is called the first principal component (PC1) and Y', the second principal component (PC2).

2.3.2.2.1 Multivariate Extension of Principal Component Analysis

The concept of PCA can be extended for multichannel image data using the same procedure as described above. However, since the multicomponent transformation cannot be shown graphically, the objective lies in finding the transformation or rotation matrix rather than the rotation angle. This is achieved by diagonalization of the variance-covariance matrix of the original data. The matrix which diagonalizes the covariance matrix is nothing but the matrix of the eigenvectors of the same. Therefore, principal components are simply the eigenvectors of the covariance matrix and they define the orientation of the latter. Because the covariance matrix is symmetrical, its resulting eigenvectors will be mutually orthogonal. Principal components are therefore orthogonal transformations of the original image data set. The eigenvalues of the new covariance

matrix represent the length or weightage of the principal components. Thus, in matrix form, these may be expressed as a characteristic matrix of the form

$$RV_i = \lambda_i V_i$$

where R is the variance-covariance matrix for which a solution is sought, V_i is the eigenvector to be found and λ_i is the eigenvalue. In the present study, the eigenvalues and eigenvectors have been determined using the standard computer algorithms with the additional facility that the eigenvectors have been normalized to unit length. The variance in different principal components is obtained by

$$\frac{\lambda_{ii}}{\sum_{i=1}^n \lambda_{ii}}$$

where λ_{ii} is the eigenvalue in PC_i . After the eigenvalues and eigenvectors are computed, the original pixel values are transformed onto the principal components as follows :

$$pc_{1ij} = e_{11} \cdot x_{ij1} + e_{12} \cdot x_{ij2} + \dots + e_{1j} \cdot x_{ijm} \quad (2.19)$$

where i = row, j = column and m = band.

In the above equation, pc_{1ij} represents the brightness value of the pixel at row i , column j in the first principal component image; e_{11} to e_{1j} represent the eigenvectors in columns 1 to j of the i th row; and x_{ijk} is the observed pixel value at row i , column j of band k ($k=1,m$). The remaining principal component images are computed in the same way using the appropriate

eigenvector. The factor loadings are derived by multiplying the eigenvectors with a diagonal matrix whose elements are $1/\sqrt{\lambda_{ii}}$, where λ_{ii} is the i th eigenvalue. Of special significance is the determination of band-component relation from which the contribution of each spectral channel to any principal component can be known. This is given by following relation :

$$\text{Degree of correlation, } R_{ij} = \frac{a_{ij}(\lambda_j)^{1/2}}{s_{ii}} \quad (2.20)$$

where R_{ij} is the correlation of each channel i with principal component j ,

a_{ij} = eigenvector for i th row and j th column, in a matrix in which eigenvectors are arranged in columns corresponding to the respective eigenvalues in descending order (that is, the first column represents the eigenvectors of first principal component having the highest eigenvalue),

λ_j = eigenvalue for j th component, and

s_{ii} = standard deviation for i th channel.

2.3.2.2.2 Classification of Principal Component Images

Supervised classification of principal component images can be performed by considering the training samples of various categories on the image and then estimating the statistical confidence intervals (of intensity levels) of these categories in different principal components under the assumption that the transformed brightness values in the components follow normal

distribution. This is carried out using the following steps of operation :

- (i) First, the category-wise means and the category-wise standard deviations are computed for each spectral channel
- (ii) These are then transformed using the following relations, so that the transformed values represent their corresponding values in the respective principal components

$$Y_{(m)ij} = C_{ik} \cdot X_{(m)kj} \quad (2.21)$$

and

$$Y_{(s)ij} = C_{ik} \cdot X_{(s)kj} \quad (2.22)$$

where $Y_{(m)}$ and $Y_{(s)}$ represent respectively the transformed matrices of category-wise means and category-wise standard deviations of the principal components, $X_{(m)}$ and $X_{(s)}$ represent respectively the matrices of category-wise means and category-wise standard deviation of the training samples in the original bands,

C_{ik} is the transformation matrix of factor loadings, and i, j, k stand for principal components, category, and bands respectively.

- (iii) Then, assuming that the brightness values in different categories are normally distributed in various principal component images, the statistical confidence intervals of respective categories are computed separately for different confidence ranges. In the present study, 95% confidence

intervals have been computed for various rock types in order to assess the discrimination capability of different components. The confidence intervals are computed as follows:

For 95% confidence interval

(which means approximately 95% of all pixels fall within the interval from +2 to -2 standard deviations)

$$\text{Lower limit} = Y_m - 1.96 Y_\sigma$$

$$\text{Upper limit} = Y_m + 1.96 Y_\sigma$$

- (iv) A decision tree is then formed taking into consideration the non-overlapping ranges of different categories which can be used for layered classification of principal component images.

When the categories have distinct non-overlapping ranges, the eigenvectors and eigenvalues computed from the variance-covariance matrix of the training samples of the categories may be used to generate images in different principal components. Such images have the additional advantage of enhancing the separation among rock types. Conversely, if the categories have overlapping confidence intervals, the principal component images generated by using the eigenvectors computed from the covariance matrix will result in severe misrepresentation or misclassification of the categories.

2.3.2.3 Inverse Principal Component Analysis

A difficulty with principal components colour display is that there is no longer a one to one mapping between sensor wavelength bands and colours. Rather each colour now represents a linear combination of spectral components, making photointerpretation difficult for many applications. This is true particularly in geological studies where the emphasis lies in discriminating among rock types on the basis of their colour differences. The objective of the inverse principal component analysis is to transform the principal components data back to the original image space. This is achieved by using the inverse of the principal components transformation matrix, that is, the inverse of the matrix of eigenvectors. Since the matrix of eigenvectors is orthogonal, its inverse is simply its transpose.

That is, if (PC1) (PC2) (PC3)

$$\begin{bmatrix} e_{11} & e_{21} & e_{31} \\ e_{12} & e_{22} & e_{32} \\ e_{13} & e_{23} & e_{23} \end{bmatrix}$$

represents the matrix of eigenvectors in columns corresponding to PC1, PC2 and PC3, from a 3-channel image, then the matrix used for inverse principal component analysis is the transposed equivalent of the same, that is,

$$\begin{array}{ccc}
 (\text{IPC1}) & (\text{IPC2}) & (\text{IPC3}) \\
 \left[\begin{array}{ccc}
 e_{11} & e_{12} & e_{13} \\
 e_{21} & e_{22} & e_{23} \\
 e_{31} & e_{32} & e_{33}
 \end{array} \right]
 \end{array}$$

Then the inverse principal component scores for their respective components can be computed as follows :

$$\text{IPC1} = \text{BV}_1 \cdot e_{11} + \text{BV}_2 \cdot e_{21} + \text{BV}_3 \cdot e_{31} \quad (2.23)$$

$$\text{IPC2} = \text{BV}_1 \cdot e_{12} + \text{BV}_2 \cdot e_{22} + \text{BV}_3 \cdot e_{32} \quad (2.24)$$

$$\text{and } \text{IPC3} = \text{BV}_1 \cdot e_{13} + \text{BV}_2 \cdot e_{23} + \text{BV}_3 \cdot e_{33} \quad (2.25)$$

where BV_n s represent the brightness values in band 'n'.

Thus, now it may be seen that each of the inverse principal component images generated by using the inverse of the principal component transformation matrix has contributions from each of the original principal component images. In other words, transforming the principal components data by a rotation matrix formed as a result of the inversion of the principal components transformation matrix will bring about transformation of the spectral signatures of various features as seen on the principal components images back to their original colours. Consequently, such images may sometimes accentuate the contrast between various features, thereby facilitating better discrimination of the rock types.

2.3.2.4 Discriminant Function Analysis

In geological remote sensing, one of the major objectives is to discriminate among various rock types. This task can be accomplished by the technique of discriminant function analysis which aims at deriving a set of linear functions that best separate a set of k groups. This method was introduced by Sir R.A. Fisher (1936) for discriminating the fossil remains into two groups such as homonid and ape.

In a bivariate plot of data from two groups, such a line called linear discriminant function will have an orientation along which the two clusters have the greatest separation while simultaneously each cluster has the least inflation. In other words, a linear discriminant function is one which separates the group means as much as possible and making the variance as small as possible. Thus, discriminant function analysis consists of finding a transform which gives minimum ratio of the difference between a pair of group multivariate means to the within group multivariate variance. A detailed discussion regarding the linear discriminant function analysis is provided by Davis (1986); the two-dimensional approach of the same is presented below.

In the Figure 2.3, it is seen that an adequate separation between groups A and B cannot be made using either variable X_1 or X_2 . However, it is possible to find an orientation on which if the data are projected, will separate the two groups the most while inflating each the least. This line is called the discriminant function line, ab , as shown in Figure 2.3. It may be noticed that a line passing at right angles to the discriminant

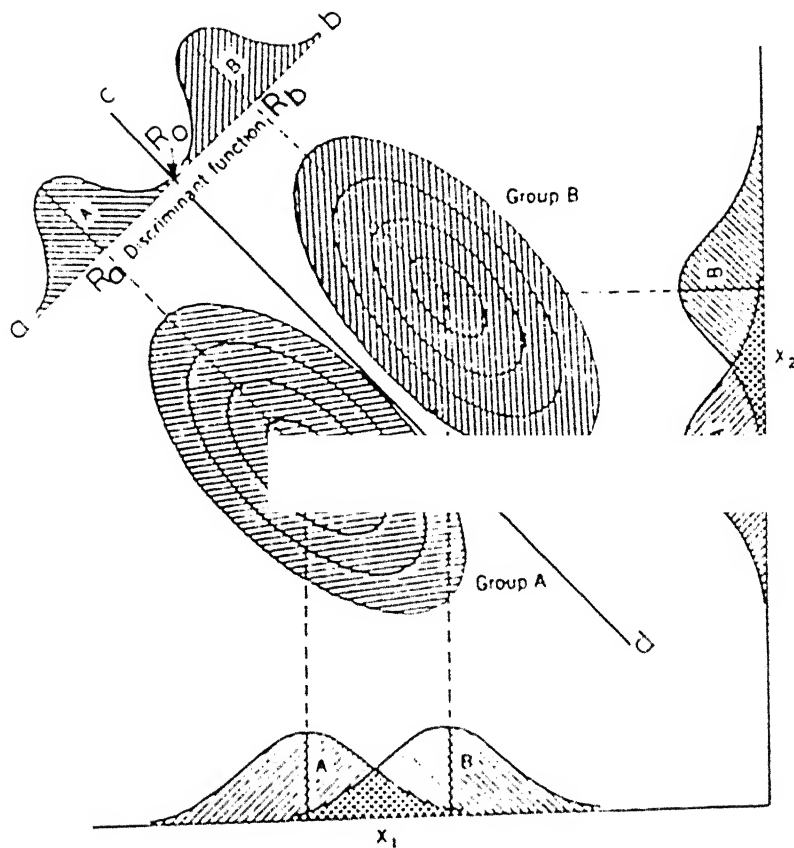


FIGURE 2.3 Plot of two bivariate distributions, showing overlap between groups A and B along both variables x_1 and x_2 . Groups can be distinguished by projecting members of the two groups onto the discriminant function line (ab). cd is line of division. R_a , R_b are the projections of bivariate means of two groups A and B on the discriminant function line. R_0 is the discriminant index, mid-way between R_a and R_b .

The difference between these multivariate means therefore forms a vector

$$\begin{bmatrix} D_j \end{bmatrix} = \begin{bmatrix} \bar{A}_j \end{bmatrix} - \begin{bmatrix} \bar{B}_j \end{bmatrix} \quad (2.27)$$

or in expanded form,

$$\begin{bmatrix} D_1 \\ D_2 \\ \vdots \\ D_m \end{bmatrix} = \begin{bmatrix} \bar{A}_1 \\ \bar{A}_2 \\ \vdots \\ \bar{A}_m \end{bmatrix} - \begin{bmatrix} \bar{B}_1 \\ \bar{B}_2 \\ \vdots \\ \bar{B}_m \end{bmatrix}$$

(ii) The pooled variance-covariance matrix $\begin{bmatrix} S_p^2 \end{bmatrix}$ is determined as follows

$$\begin{aligned} \begin{bmatrix} S_p^2 \end{bmatrix} &= \frac{\sum_{l=1}^G (n_l - 1) \hat{C}_l}{\sum_{l=1}^G n_l - G} \\ &= \frac{(n_1-1)\hat{C}_1 + (n_2-1)\hat{C}_2 + \dots + (n_G-1)\hat{C}_G}{n_1 + n_2 + \dots + n_G - G} \end{aligned} \quad (2.28)$$

where \hat{C}_1 = band variance-covariance matrix of group 1

n_1 = number of observations in group 1

and G = number of groups

This is also called the average within-class covariance matrix. For two groups of observations, this expression simplifies to

$$\begin{bmatrix} S_p^2 \end{bmatrix} = \frac{(n_1-1)\hat{C}_1 + (n_2-1)\hat{C}_2}{n_1+n_2-2} \quad (2.29)$$

Now the augmented matrix with the values of $\begin{bmatrix} S^2 \\ P \end{bmatrix}$ and $\begin{bmatrix} D \end{bmatrix}$ may be solved to determine the coefficients (λ s) of the linear discriminant function. The set of λ coefficients found are entries in the discriminant function equation of the form

$$R = \lambda_1 \psi_1 + \lambda_2 \psi_2 + \dots + \lambda_m \psi_m \quad (2.30)$$

where $\psi_1, \psi_2, \dots, \psi_m$ represent the variables (say, spectral bands) 1, 2, \dots, m respectively. This is a linear function; that is, all the terms are added together to yield a single number, the discriminant score. In two-dimensional case, equation (2.30) simplifies to

$$R = \lambda_1 \psi_1 + \lambda_2 \psi_2 \quad (2.31)$$

From the equation (2.31), the slope, α , of the discriminant function line may be determined as follows :

$$\alpha = - \frac{\lambda_1}{\lambda_2} \quad (2.32)$$

Since the line of division is perpendicular to the discriminant function line, its slope, α' , is given by

$$\alpha' = \frac{\lambda_2}{\lambda_1} \quad (2.33)$$

Both these lines, that is, the line of division and the discriminant function line may be plotted on the scatter diagram of the two original variables.

Now the discrimination potential of the discriminant function analysis can be estimated on the basis of the number of samples of any particular group being classified as the same

CENTRAL LIBRARY
I. I. T. KANPUR
Acc. No. A.116555

group. On the scatter diagram, the classification accuracy of a group is determined by the ^{percentage} of samples or training pixels of this group lying on that side of the line of division where the group in question is represented by the maximum number of its training samples.

The applicability of linear discriminant function analysis is based upon two basic assumptions : firstly, the data in the k classes is normally distributed and secondly, the variance-covariance matrices of the groups are equal in size. In the present study, however, a compromise has been made in overlooking the second assumption.

2.3.2.5 Correspondence Analysis

Correspondence analysis is a technique primarily aimed at analyzing the correspondence between raw bands (Davis, 1986; Legendre and Legendre, 1983). This implements a transformation in the spectral band domain for which a linear combination of the input bands is performed. The method proceeds by operating on a matrix derived from a (MxN) data set where M represents the number of spectral bands and N, number of pixels in each band which has been transformed so that the elements of the data set can be regarded as proportions of the total number of observations or pixels. Because of the nature of transformation, relationship between the original reflectance data in raw bands is maintained even after transformation.

The matrix used for the transformation contains the eigenvalues of the matrix S which is calculated as follows :

$$S = \left[F \right]^T \left[D_k \right]^{-1} F \left[D_n \right]^{-1} \quad (2.34)$$

where F = matrix of all the components of all the pixels in the subscene, each divided by their sum over the complete subscene

D_k = diagonal elements containing the sum of the elements in F per line

D_n = diagonal elements containing the sum of the elements in F per column

T = transpose

and (-1) = inverse operator.

The above matrix S can be estimated in its computational form as follows :

$$S(I,J) = \frac{\sum_{\text{pix}} \left[\text{pix}(I) * \text{pix}(J) / \sum_{k=1, \text{Nband}} (\text{pix}(k)) \right]}{\text{sqrt} [V(I) * V(J)]} \quad (2.35)$$

where $V[I] = \sum_{\text{pix}} [\text{pix}(I)]$

$V[J] = \sum_{\text{pix}} [\text{pix}(J)]$

and Nband = Number of processed bands.

The transformed images generated by considering the eigenvectors of the matrix $[S]$ as coefficients in the linear combination of raw image data, like the operation carried out in Principal Component Analysis, are then processed for Gaussian post-normalization.

Since the elements in matrix S are expressed as proportions of the total, it ensures that the sum of the columns (and of rows) is equal to 1. Therefore, the data set in S is now closed and accordingly, one eigenvalue becomes zero. This means the dimensionality of the data is reduced from M to $M-1$. Since the matrix S is symmetrical, the correspondence axes are orthogonal to each other.

2.3.2.6 Empirically-based Image Transforms : Tasseled Cap (Kauth-Thomas) Transformation for Vegetation (Greenness) and Soil Brightness Indices

This is a technique of multi-image empirical transformation of the original data in all the spectral channels, which aims at highlighting the vegetation and soil areas of the earth on the transformed digital images (Jensen, 1986; Mather, 1987). One solid justification for this type of operation is that the axes will provide a consistent, physically-based coordinate system for the interpretation of images for vegetation and soil mapping regardless of the time of observation. This technique was introduced by Kauth and Thomas (1976) for Landsat MSS data and was later extended by Crist (1983) and Crist and Cicone (1984) for Landsat TM data. The latter group of workers defined three dimensions representing the brightness, greenness and wetness functions associated with reflectance from soil, vegetation and water (moisture content) respectively. These axes are statistically uncorrelated and are orthogonal to each other. In the present study, however, only the brightness and greenness functions transformations have been carried out. The coefficients

for these functions for the TM data as per Crist and Cicone (1984) are as follows :

TM Bands	1	2	3	4	5	7
Brightness	.3318	.3312	.5518	.4251	.4809	.2525
Greenness	-.2472	-.1626	-.4064	.8547	.0549	-.1175

Since the coefficients are empirical and not a-priori, the resulting Tasselled Cap coordinates will not lie in the range 0-255 (for TM data) and will thus not be capable of being displayed on standard image processing equipments. Therefore, the resulting values are rescaled using contrast stretch technique with a check being made for negative scaled values (which are set to zero) or values greater than 255 (which are set to 255).

2.4 AUTOMATIC CLASSIFICATION OF REMOTELY SENSED DATA FOR THEMATIC INFORMATION EXTRACTION

2.4.1 General

Automatic classification aims at categorizing the numerical pixel values of an image into a thematic map on which each class represents a real-world object. The present study has been carried out resorting to supervised classification method which proceeds by categorizing the pixels on the basis of the a-priori knowledge of the various classes already identified, which is acquired from the training samples of each class extracted from their respective homogeneous sites. Thus, it basically involves two stages :

- (i) Training stage
- and (ii) Classification stage

The training stage comprises the task of extracting training samples which must be both representative and complete. In the present study, training samples have been derived through polygons delineated on various classes on the image by using a cursor-control device. Keeping in view the general rule of the theoretical lower limit of the number of pixels for each class (i.e. $n+1$, where n is the number of bands), sufficient number of training samples have been collected in order to improve the estimates of various statistical parameters used in classification.

In the classification stage, the test samples or the entire image itself is classified on the basis of the estimates of the statistical parameters of the training samples. In the present study, Bayesian classifier has been employed for classifying the multispectral Thematic Mapper Data from Landsat-5.

2.4.2 Bayesian Principles of Classification

The Bayesian classification is based on the conditional probability density functions (James, 1985; Jensen, 1986; Moik, 1980; Swain and Davis, 1978). The decision rule assigns each unknown pixel having pattern measurements or features X to the class i whose units are most likely to have given rise to feature vector X . Mathematically, this can be stated as follows :

If there are G groups or classes then according to Bayes' rule, the unknown pixel (X) is assigned to group i when

$$P(G_i|X) > P(G_j|X) \quad \text{for all } i \neq j \quad (2.36)$$

where $P(G_i|X)$ expresses the probability that G_i will occur only if X has already occurred.

Since the features and the groups are closely related (i.e. dependent) in remote sensing measurements, the fact that X has already transpired implies the likelihood that G_i will then occur. The joint probability of X and G_i is given by

$$P(X, G_i) = P(G_i|X) P(X)$$

Conversely, it can be written as

$$P(X, G_i) = P(X|G_i) P(G_i)$$

where $P(G_i)$ is the probability that G will occur.

Equating these two terms, we have

$$P(G_i|X) P(X) = P(X|G_i) P(G_i)$$

which may be rewritten as

$$P(G_i|X) = \frac{P(X|G_i) P(G_i)}{P(X)} \quad (2.37)$$

This relation expresses the Bayes' theorem which is unique because it links the conditional probability with the unconditional probability.

Now the decision rule as mentioned in equation (2.36) can be restated as follows :

Assign X to group G_i if

$$P(X|G_i) P(G_i) > P(X|G_j) P(G_j) \quad \text{for all } i \neq j \quad (2.38)$$

A very important assumption underlying the classification by bayesian principle is that the training data sets for each class are normally distributed (i.e. Gaussian in nature). This assumption is generally reasonable for common spectral response distributions. Under this assumption, the distribution of a category response pattern can be completely described by the mean vector and the covariance matrix. Using these two parameters, we may compute the statistical probability of a given pixel value belonging to a particular group on the basis of the probability density function of each group. Mathematically, the form of conditional probability $P(X|G_i)$ for multivariate normal distribution of the measurement vectors is given by

$$P(X|G_i) = (2\pi)^{-N/2} |\Sigma_i|^{-1/2} \exp \left\{ -\frac{1}{2} (X-m_i)^t \Sigma_i^{-1} (X-m_i) \right\} \quad (2.39)$$

where N = number of bands

m_i = mean of class i

Σ_i = variance-covariance matrix of class i

and $P(G_i)$ = a-priori probability of class i .

Therefore, as already mentioned, estimation of $P(X|G_i)$ necessitates estimation of two parameters, that is, group mean and group covariance matrix. The need of computation of a-priori probability arises when the classes have unequal weights or areal extents in the image subscene so that the anticipated likelihood of occurrence for each class in the scene is different. In the present study, a compromise has been made by assuming equal probability of occurrence of each class. In such case, the

Bayesian Classifier simplifies to a form which is called the Maximum Likelihood Classifier.

Using the normal form of $P(X|G_i)$ the Bayes' decision rule in equation (2.38) can be written as :

Assign X to G_i if

$$P(G_i)(2\pi)^{-N/2} |\Sigma_i|^{-1/2} \exp \left[-\frac{1}{2} (X-m_i)^t \Sigma_i^{-1} (X-m_i) \right] \\ > P(G_j)(2\pi)^{-N/2} |\Sigma_j|^{-1/2} \exp \left[-\frac{1}{2} (X-m_j)^t \Sigma_j^{-1} (X-m_j) \right] \\ \text{for all } i \neq j \quad (2.40)$$

Taking the natural \log_e [ln] of both sides,

$$-\frac{1}{2} N \ln(2\pi) - \frac{1}{2} \ln |\Sigma_i| - \frac{1}{2} (X-m_i)^t \Sigma_i^{-1} (X-m_i) + \ln P(G_i) \\ > -\frac{1}{2} N \ln(2\pi) - \frac{1}{2} \ln |\Sigma_j| - \frac{1}{2} (X-m_j)^t \Sigma_j^{-1} (X-m_j) + \ln P(G_j) \\ \text{for all } i \neq j \quad (2.41)$$

Cancelling common terms occurring on both sides, we have

$$-\ln |\Sigma_i| - (X-m_i)^t \Sigma_i^{-1} (X-m_i) + \ln P(G_i) \\ > -\ln |\Sigma_j| - (X-m_j)^t \Sigma_j^{-1} (X-m_j) + \ln P(G_j) \text{ for all } i \neq j \\ (2.42)$$

Cancelling -ve sign on both sides and consequently changing > sign to < sign, we have,

$$\ln |\Sigma_i| + (X-m_i)^t \Sigma_i^{-1} (X-m_i) - \ln P(G_i) \\ < \ln |\Sigma_j| + (X-m_j)^t \Sigma_j^{-1} (X-m_j) - \ln P(G_j) \text{ for all } i \neq j \quad (2.43)$$

In equation (2.43) the quantity $\ln |\Sigma_i| + (X - m_i)^t \Sigma_i^{-1} (X - m_i) - \ln P(G_i)$ is referred to as the discriminant score and the expression $d_i(x) = \ln |\Sigma_i| + (X - m_i)^t \Sigma_i^{-1} (X - m_i)$ is called "ML Discriminant Function".

As a final rule for Bayesian method of classification, assign the measurement X to the group with the smallest value of $d_i(X) - \ln P(G_i)$. That is, as $d_i(X)$ becomes smaller, the probability of X belonging to group 'i' increases which is opposite to the behaviour of $P(G_i|X)$. In other words, we can set the decision rule as follows :

Assign X to group i if

$$d_i(X) - \ln P(G_i) < d_j(X) - \ln P(G_j) \text{ for all } i \neq j \quad (2.44)$$

where X , the multivariate spectral response pattern is normally distributed in each group. This relation is used for classifying the unknown pixels in the subscene and hence, the computational algorithm is developed based on this expression.

CHAPTER 3

MINERALOGICAL AND SPECTROSCOPIC ANALYSIS OF ROCKS

3.1 INTRODUCTION

Lithological discrimination is carried out based on the differences in the spectral signatures of different rock types. The spectral signature which is a unique characteristic of a material (e.g. a rock) and by which a material is identified on the image, is determined by the spectrum of the material in question. Since rocks are assemblages of minerals, the spectrum of a rock is a composite of the individual spectra of its constituent minerals.

The three important processes contributing to the spectral reflectance of minerals and rocks are the electronic process of charge transfer and crystal field effects, and the vibrational processes; the fourth being the rotational process which occurs only in gases where the molecules are free to rotate. Electronic processes which require more energy than the vibrational processes are confined to lower wavelength ranges which correspond to the visible portion (0.4-1.0 μm) of the spectrum in spectral remote sensing (Kahle, 1984; Goetz et al., 1985). The spectral features produced as a result of electronic processes are due to Fe-O charge transfer in the ultraviolet and blue portions of the spectrum, and since iron is ubiquitous, practically all minerals and rocks have rising reflectances towards longer wavelengths in the visible portion of the

spectrum. The Fe-O transfer band causes rapid fall off in reflectance towards the blue and ultraviolet of the visible spectra, particularly in the spectra of many weathered materials occurring on the surface of the earth.

The second process accounting for spectral features of minerals and rocks is crystal field effects. Electronic transitions in the d-shell electron of the transition elements embedded in the crystal field create absorption features in the visible and near infrared (i.e. 0.4-2.5 μm) range of the spectrum. Again, the most commonly occurring features are related to iron in both Fe^{2+} and Fe^{3+} state.

The spectral signature of terrestrial minerals and rocks in the short or near wavelength infrared (SWIR) region (1.0-2.5 μm) is attributed to vibrational processes or transitions. The spectral features in this portion of the spectrum are caused by the overtones and combination tones involving materials that have very high fundamental frequencies. The most common of these near infrared bands involve the OH stretching mode, and water which yield^a/large number of sharp and unique spectral absorption features. Since most of the common surface materials and the weathering products such as clay minerals comprising kaolinite, montmorillonite, illite etc. contain hydroxyl molecule in their atomic structures, their absorption features could be used as diagnostic criteria for their identification.

From the foregoing discussion, it is now clear that most of the characterizing information concerning identification of naturally occurring geological materials is due to the presence

of iron, and hydroxyl molecules and water in minerals and rocks. In other words, for a proper and thorough understanding of the spectral information of rocks in remotely sensed image data and in turn, for their identification and discrimination, it is essential to determine the complete mineralogy of the rocks in question.

3.2 MINERAL IDENTIFICATION

For the present study, both microscopic and X-ray diffraction (XRD) studies have been carried out for precise determination of constituent minerals in various rock samples collected from the study area. Whereas thin section studies of rock samples were carried out for identification of various minerals, XRD was performed specifically for identification of clay minerals present in the rock samples.

A total number of eight different rock samples were studied for mineralogical identification through microscopic analysis, four each of which pertain to the respective study areas selected for analysis of MSS data from Landsat-2 and TM data from Landsat-5. The various rocks analyzed for MSS area are: augen gneiss, biotite schist, hornblende granite, and quartzite, whereas for TM area, the rocks analyzed are: calc gneiss, tremolite schist, hornblende schist, and impure limestone. The various minerals identified by the thin section studies are presented in Tables 3.1 and 3.2 for rocks of MSS and TM areas respectively. Clay minerals, however, owing to their considerably small crystal lattice dimensions are difficult to be distinguished under a polarizing microscope. Their identification was,

1 Mineralogical Composition of the Rock Samples of MSS Area
Determined from Microscopic and XRD Studies.

c Type	Minerals identi- fied by micro- scopic studies	Minerals identified by XRD studies with the diagnostic peaks in Å shown in brackets	Remarks
n Gneiss	Plagioclase felds- par, Quartz (eye shaped) Biotite, Fe-oxides as impurities	PF (3.196,3.767,2.50) Qtz (3.337,4.295,2.456) Bio (10.042,2.282,2.523) Kao (7.088) AF (3.256) (Figure 3.1)	Partly weathered, Minor amount of Kaolinite and Fe- oxides as impuri- ties present
artzite	Quartz grains altered, Plagio- clase feldspar, lath shaped muscovite	PF (3.189,3.153,3.204) Qtz (3.349,4.298,2.284) Mica (2.85,2.103) (Figure 3.2)	Rock not weather- ed. Clay minerals not found. Minor amount of iron oxides present as impurities
tite ist	Fine grained quar- tz matrix, Biotite, Augite. Minor amount of iron oxides as impurities	Bio (9.854,4.970) PF (3.186,3.667,3.757) Qtz (3.333,4.246,1.192) (Figure 3.3)	Rock not altered and not weather- ed. No clay mine- rals
nblende nite	Large grains of quartz with inclu- sions of hypers- thene (only few grains), Hornblende in minor amount, biotite (only few grains), Plagioclase feldspar dominant, numerous iron oxi- des as impurities	Qtz (3.357,4.253,1.80) PF (3.196,3.663,6.406) Bio (10.1,2.864,2.0) Hb (2.794,2.94) Act (2.956) (Figure 3.4)	Surface altered but rock not wea- thered. Clay minerals not found

Plagioclase feldspar, AF = Alkali feldspar, Qtz = Quartz, Bio = Biotite
Kaolinite, Hb = Hornblende, Act = Actinolite.

1.2 Mineralogical Composition of Rock Samples of TM Area Determined from Microscopic and XRD Studies.

Rock Type	Minerals identified by microscopic studies	Minerals identified by XRD studies with the diagnostic peaks in Å shown in brackets	Remarks
Granitic Gneiss	Calcite with inclusions, Plagioclase feldspar, Microcline with inclusions of quartz grains, Hypersthene. Iron impurities	Cal (3.038, 3.0, 2.284) Dol (4.051, 2.899) Act (3.483, 2.344, 8.522) PF (3.211) AF (3.248, 4.233) Qtz (3.357) (Figure 3.5)	Fresh rock, iron impurities in minor amount. No clay minerals
Impure gneiss	Microcline and quartz dominant, highly altered biotite. Iron impurities	AF (3.241, 3.47, 6.468) Cal (3.025, 2.281) Qtz (3.337, 2.456, 4.266) Bio (9.466, 2.33, 2.567) (Figure 3.6)	Fresh rock. Clay minerals absent
Tremolite schist	Quartz, Tremolite (highly fine grained altered matrix), highly altered biotite. Iron impurities	Qtz (3.341, 2.456, 4.253) PF (3.193, 4.033, 3.474) AF (3.241) Bio (10.004) Trem (2.993, 2.938, 2.159) Kao (7.184) (Figure 3.7)	Intensely weathered rock. Clay minerals present
Hornblende schist	Quartz, Plagioclase feldspar, Biotite, Garnet, Chlorite. Iron impurities	Qtz (3.349, 4.259, 2.128) PF (3.128, 3.218, 3.372) AF (2.517, 3.550, 2.630) Bio (10.868) Chl (7.088, 14.439) Hb (2.016) (Figure 3.8)	Fresh, unaltered rock. No clay minerals

= Plagioclase feldspar, AF = Alkali feldspar, Qtz = Quartz, Bio = Biotite
= Kaolinite, Hb = Hornblende, Act = Actinolite, Cal = Calcite
= Dolomite, Trem = Tremolite, Chl = Chlorite.

therefore, carried out by X-ray diffraction technique which works on the principle of direct interaction of X-ray radiation with the atoms of the substance. In the present study, the XRD studies have been carried using powder method for which the samples were prepared by grinding them to ^{the} desired size. The X-ray radiation used for analysis is Chromium K_{α} radiation having a wavelength of 2.2909 Å. The X-ray spectra were recorded under the following measuring conditions:

Counts per second (CPS)	= monitored between 167 to 833
	depending upon peak intensity
Time constant (TC)	= 10 seconds
Scanning speed (SS)	= 1.2°/minute
Chart speed (CS)	= 1.2 cm/minute
Voltage	= 40 KV
Current	= 30 mA

In the present study, 17 samples were subjected to XRD analysis out of which ten samples pertain to the rocks present in the MSS study area and the rest seven samples pertain to the rocks of the TM study area. The analysis involves identification of various minerals present in the rocks with specific regard to clay minerals. The results of the analysis are presented in Tables 3.1 and 3.2 alongwith the results of microscopic studies. The X-ray diffractograms generated for different rock samples are shown in Figures 3.1 to 3.8, one for each rock type studied.

During field observations and sampling, in general, ^amajority of the rock types in both MSS and TM study areas were found to be unweathered over a large portion of their exposed cover. However,

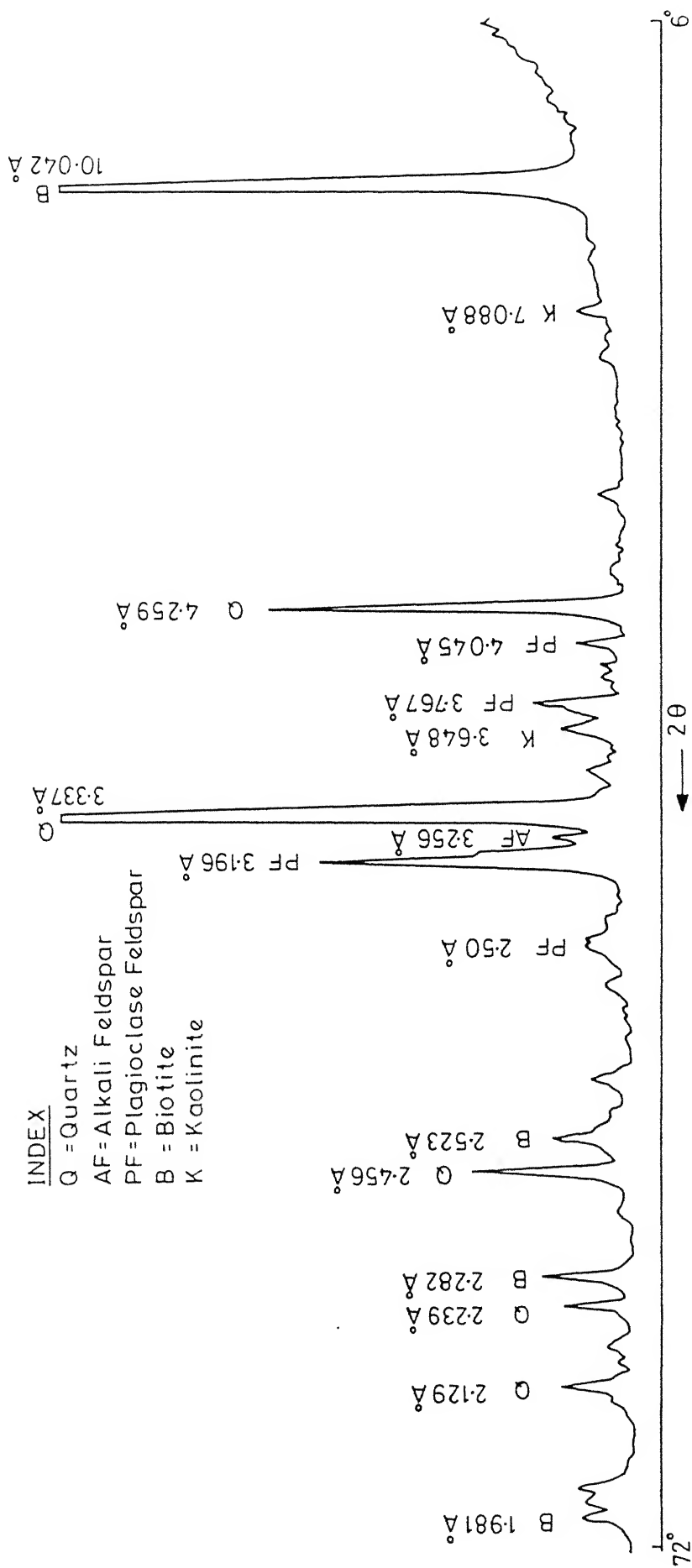


Figure 3.1 X-ray diffractogram of Augen gneiss

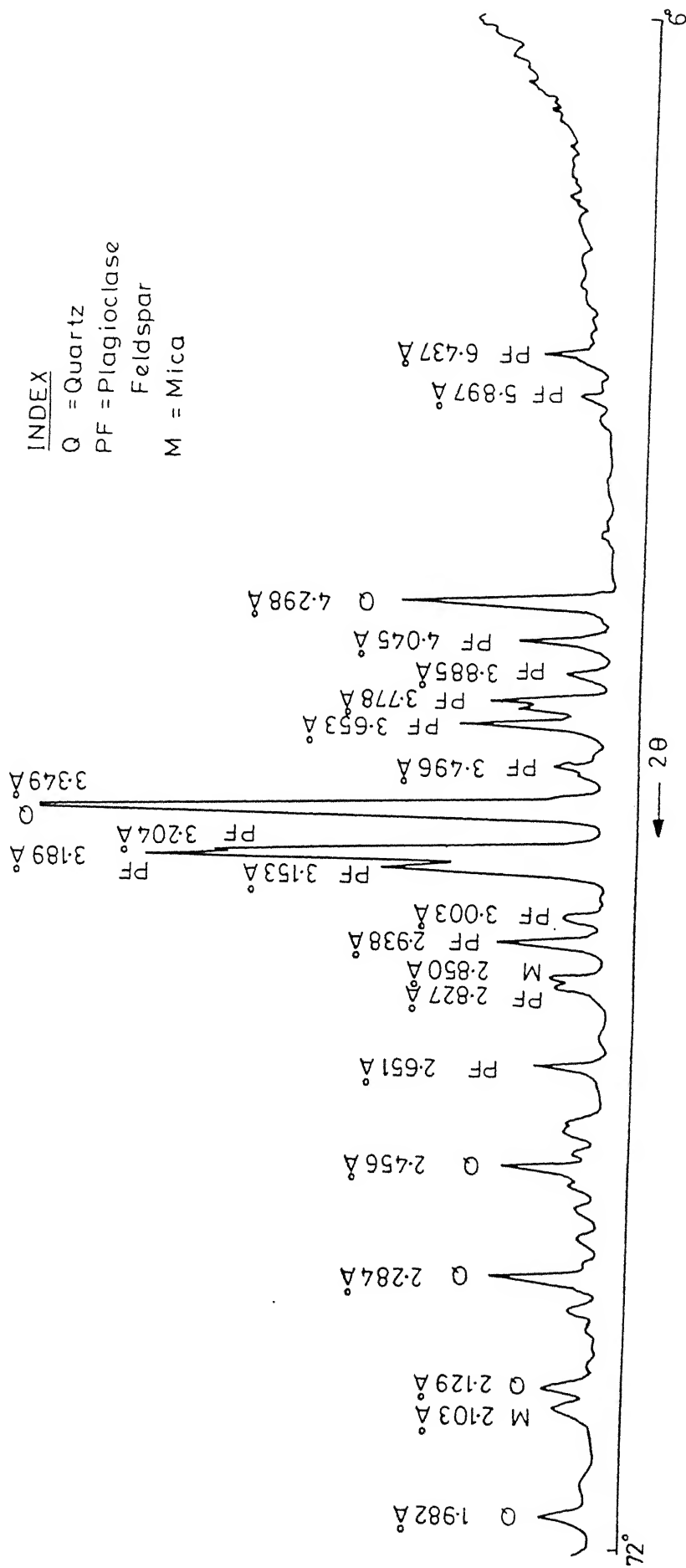


Figure 3.2 X-ray diffractogram of Quartzite

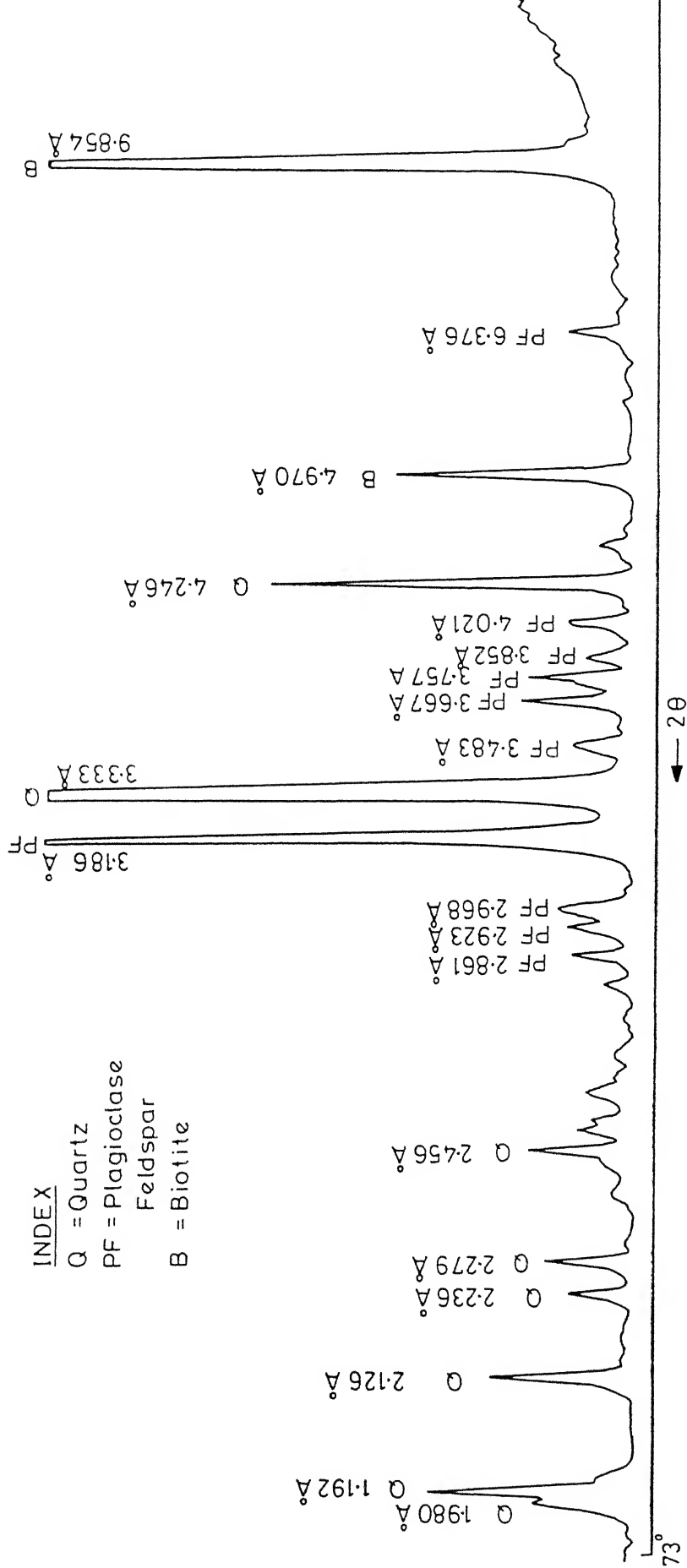


Figure 3.3 X-ray diffractogram of Biotite schist

INDEX

Q = Quartz
 PF = Plagioclase Feldspar
 Act = Actinolite
 B = Biotite
 Hb = Hornblende

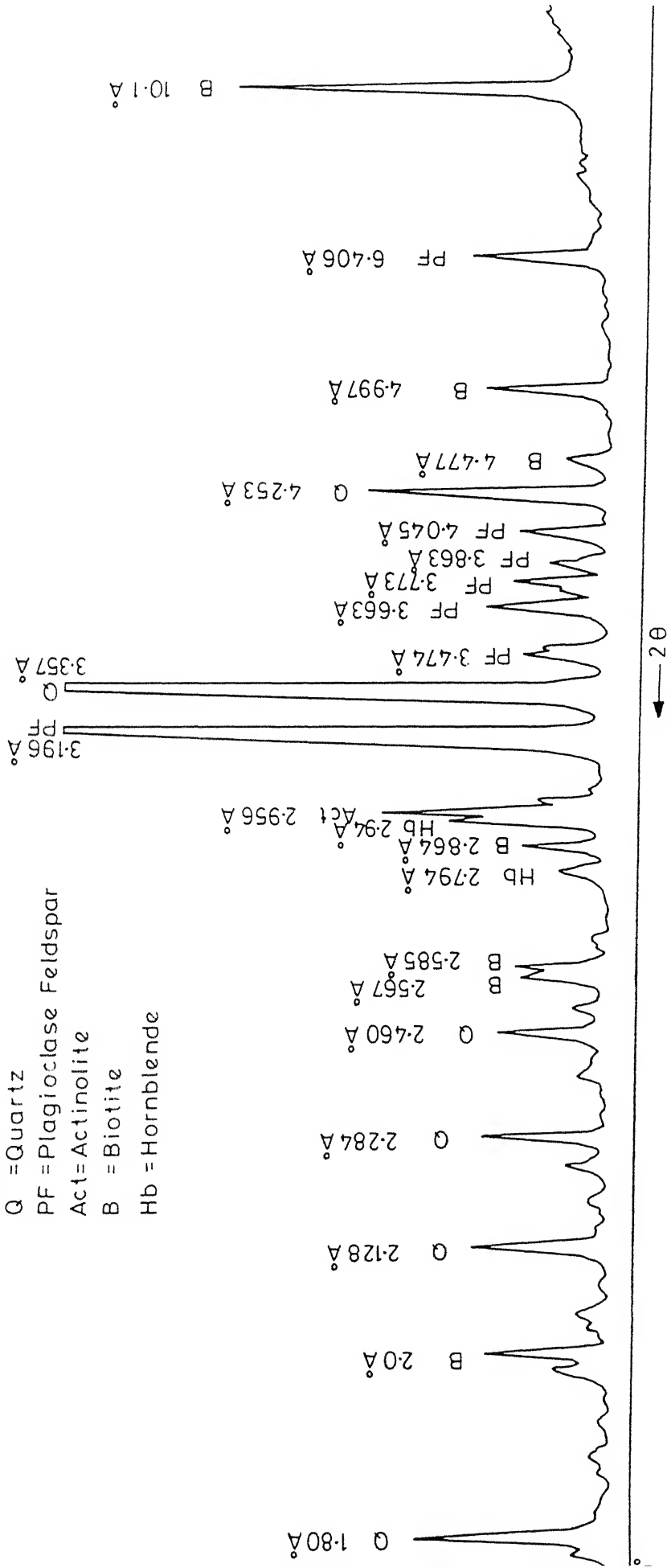


Figure 3.4 X-ray diffractogram of Hornblende granite

INDEX

Cal = Calcite
Dol = Dolomite
Act = Actinolite
Q = Quartz
PF = Plagioclase Feldspar
AF = Alkali Feldspar

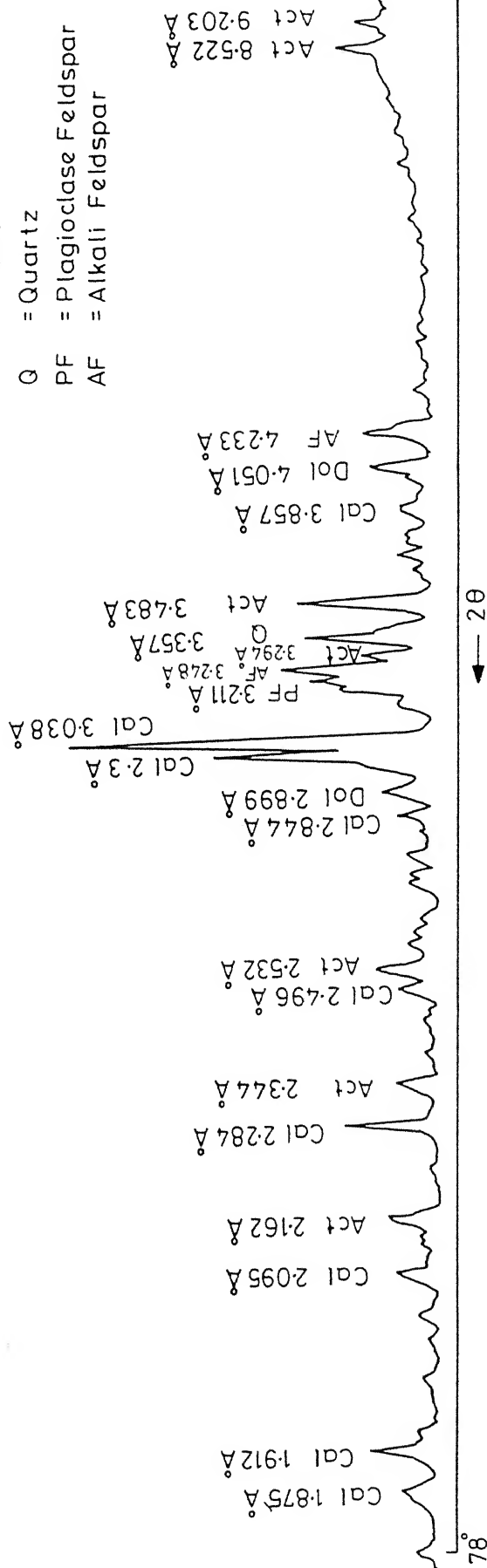


Figure 3.5 X-ray diffractogram of Calc gneiss

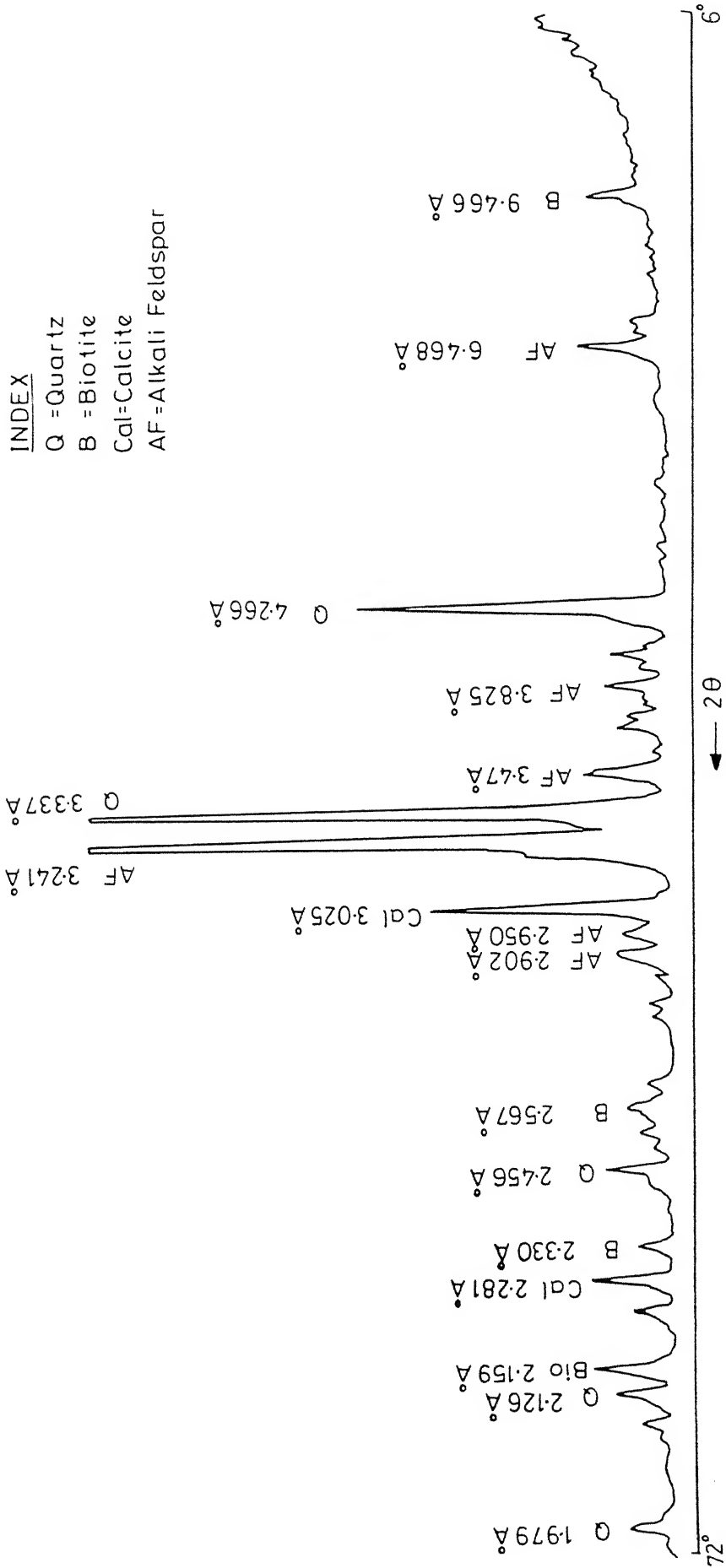


Figure 3.6 X-ray diffractogram of Impure limestone

INDEX

Q = Quartz
 AF = Alkali Feldspar
 PF = Plagioclase Feldspar
 B = Biotite
 Tr = Tremolite
 K = Kaolinite

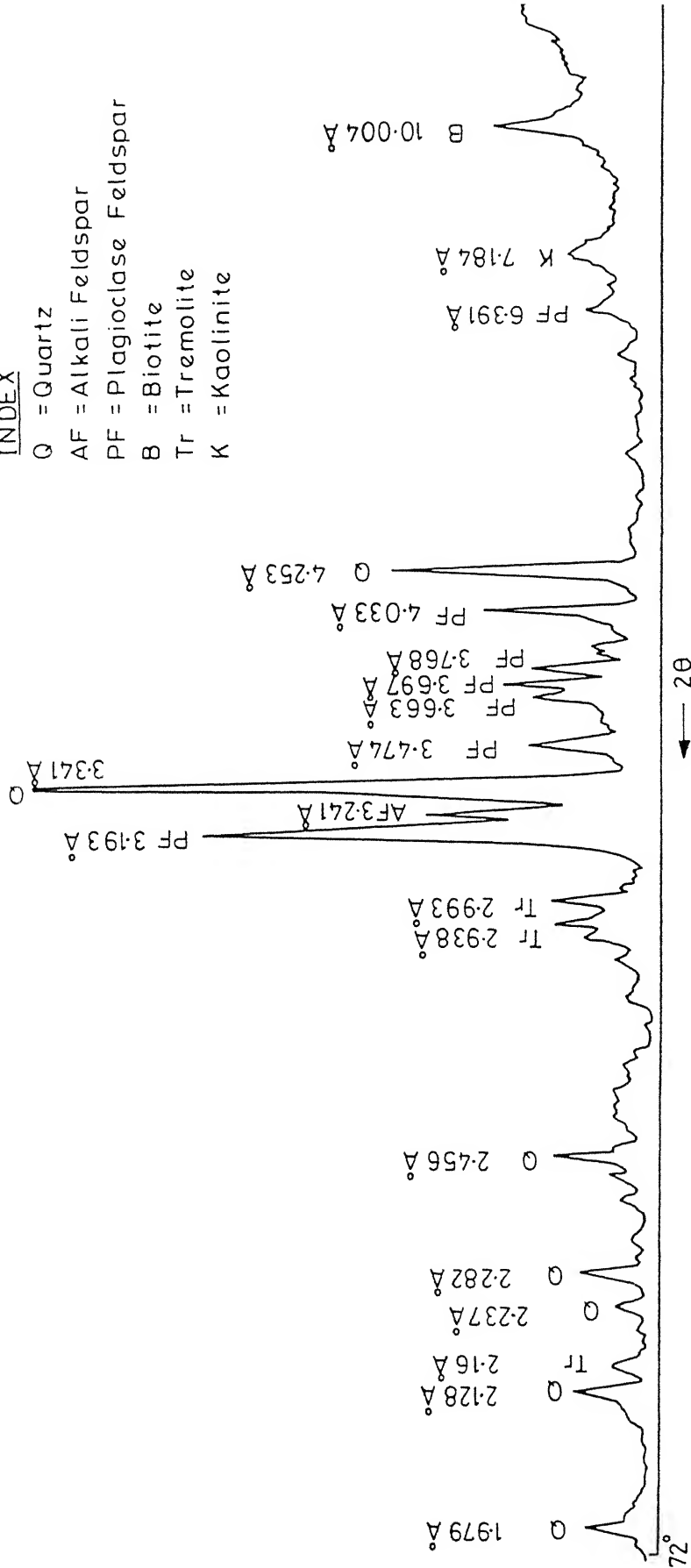


Figure 3.7 X ray-diffractogram of Tremolite schist

INDEX

Q = Quartz
 AF = Alkali Feldspar
 PF = Plagioclase Feldspar
 B = Biotite
 Chl = Chlorite
 Hb = Hornblende

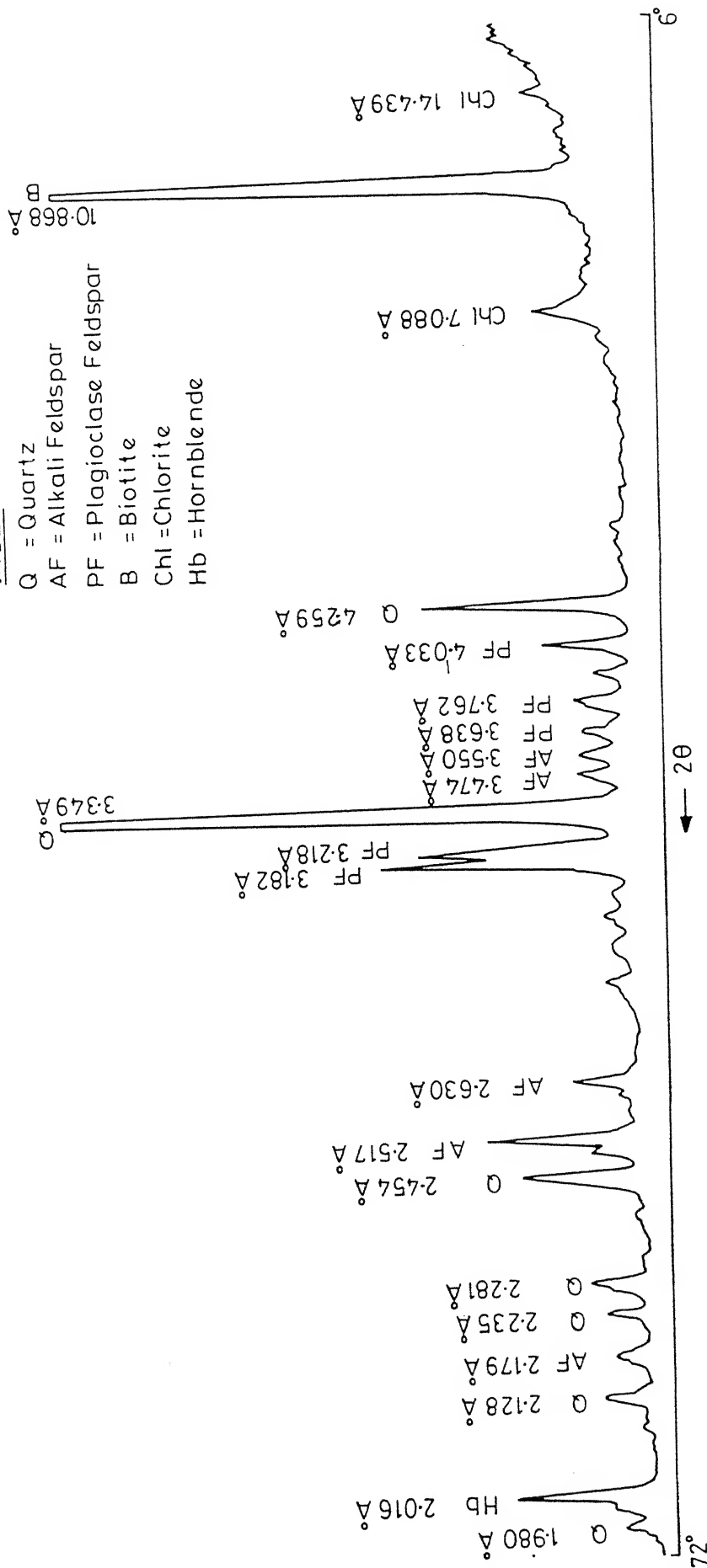


Figure 3.8 X-ray diffractogram of Hornblende schist

deep weathering is observed in tremolite-schist in TM area. Wherever weathering is prevalent in fair intensity, it has led to the formation of clay minerals.

Analyses of samples of different rock types of MSS area show that the rocks are composed mainly of silicates such as quartz, feldspars, pyroxenes, amphiboles, and biotite mica. Iron impurities are common in all the rocks; however, notable amount of it is found in hornblende granite. Out of the four major rock types present in the MSS study area, viz. gneiss, schist, granite, and quartzite, only the gneissic rocks (augen gneiss) being partly weathered shows the presence of clay mineral namely kaolinite. Surficial alteration albeit commonly prevalent in granitic rocks has not led to the formation of any clay mineral.

The TM study area comprises mainly quartzites, calc schists, impure limestones, calc gneiss, tremolite schists and hornblende schists. Microscopic and XRD analyses of samples of these rocks collected from the study area show that the rocks contain, in majority, the silicate minerals such as quartz, feldspar, biotite, hypersthene, garnet, and hornblende. However, in addition to the above minerals, appreciable amounts of carbonate minerals such as calcite and dolomite have been observed in calc gneiss and impure limestone. Tremolite schist is found to contain a reasonable amount of tremolite, whereas hornblende schist shows the presence of chlorite in both microscopic and XRD analyses. Barring the sole rock type viz. tremolite schist, all other rocks have remained practically unaffected by weathering and therefore, they do not contain any clay mineral; however, XRD

analysis reveals the presence of kaolinite in tremolite schist. Moreover, microscopic studies of thin sections of samples of different rock types reveal the presence of iron impurities in all rocks.

3.3 ANALYSIS OF LABORATORY REFLECTANCE SPECTRA OF ROCK SAMPLES

Spectral remote sensing is based upon recording at certain range of wavelength, of electromagnetic radiation (EMR) reflected and/or emitted from the objects on the surface of the earth. The EMR received by the sensor is recorded as digital numbers (DN) which are proportionate to the intensity of the reflected/emitted EMR. The smallest possible area on the surface of the earth which every DN corresponds to is equal to the spatial resolution of the sensor which for MSS is 79m x 59m and for TM, 30m x 30m (excluding the thermal band). This implies that a DN accounts for the gross reflectance from the area as a result of interaction of the incident EMR with every feature occurring in the area. Since the area sensed for every DN is sufficient to contain a mixture of vegetation cover and soil, the DN might not represent the true reflectance of the rock alone lying beneath. Therefore, in order to understand the relationship between the mineralogy and the reflectance of the rocks, it is pertinent to acquire reflectance spectra of the rock samples in the laboratory. Moreover, the results of laboratory investigations provide the optimum intrinsic information available concerning a particular material, and clearly delineate the spectral regions that offer the best remote sensing potential (Siegal and Gillespie, 1980).

In the present study, diffused reflectance spectra of rock samples have been acquired in the laboratory at Defence Materials and Stores, Research and Development Establishment (DMSRDE), Kanpur. The instrument used for measuring diffused reflectance spectra is of the type Varian Cary 2390 UV-VIS-NIR (ultraviolet-visible-near infrared) spectrometer; attached to it is a diffused reflectance accessory of integrating sphere type which can measure reflectance from 400 nm upto 2200 nm. However, due to instrumental problems, reflectance spectra upto 1.5 μm (1500 nm) only could be recorded correctly. The range of 0.4 to 1.5 μm satisfactorily covers all the spectral channels of MSS but takes into account only the first four channels of TM of Landsat-5 (i.e. TM band 1 to band 4). Therefore, it precludes the possibility of studying the relationship of mineralogy with the spectral response in TM band 5 and in particular, in band 7 (2.08-2.35 μm) which offers the best potential for good geological discrimination.

The measurement of diffused reflectance spectra of samples was carried out separately at two different spectral ranges resorting to different detectors. For example, in ^{the} 400-900 nm range, ^aphotomultiplier detector was used while in ^{the} 900-1500 nm range, ^aPbS detector was used, in both cases the reference of measurement used being MgO. The reflectance is determined from the following relation :

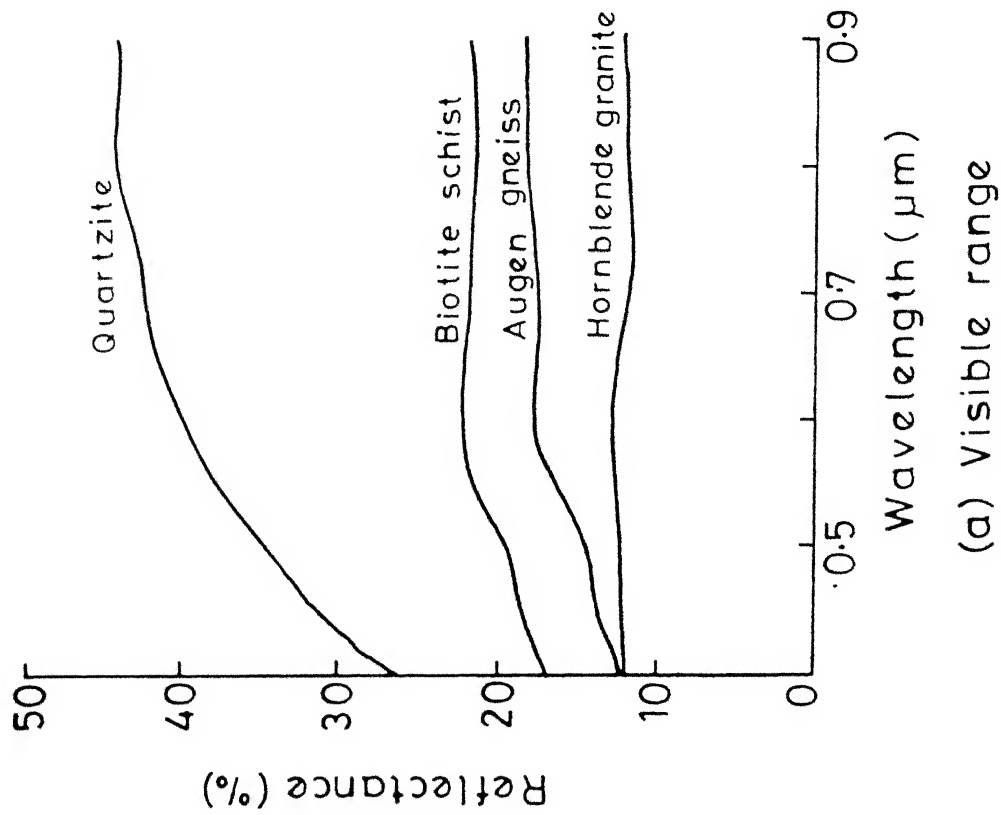
$$\text{reflectance (in percent)} = \frac{R_S}{R_R} \times 100$$

where R_S and R_R denote reflectance from the sample and the reference respectively.

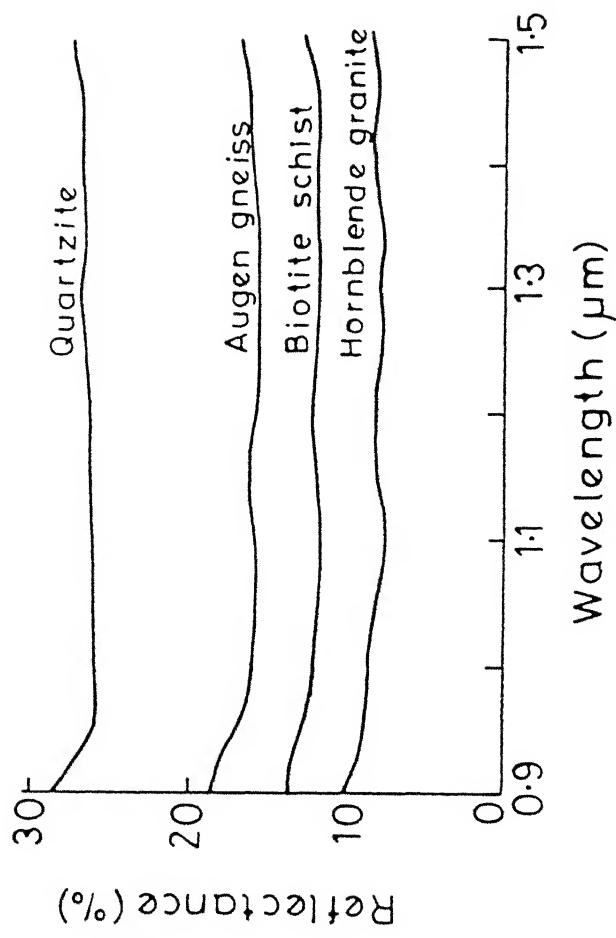
3.3.1 ANALYSIS, INTERPRETATION AND RESULTS

Reflectance spectra were acquired for all the rock samples which were used for mineral identification through microscopic and XRD analyses. As such, spectral measurements were carried out for a total number of eight samples, one each for different kind of rocks exposed in MSS and TM study areas. The spectral curves of the rocks occurring in MSS area are shown in Figures 3.9(a) and 3.9(b) for the spectral range of 0.4-0.9 μm (visible) and 0.9-1.5 μm (Short wavelength infrared, SWIR) respectively. Similarly, the spectral curves of the rocks occurring in TM area are shown in Figures 3.10(a) and 3.10(b) for 0.4-0.9 μm and 0.9-1.5 μm respectively.

A close observation of the spectral curves of the respective rock types occurring in both MSS and TM areas reveals significantly a sudden fall in the reflectance at 0.9 μm wavelength region in the spectral curves of the SWIR range (0.9-1.5 μm) (Figures 3.9(b) and 3.10(b)). This steep fall in the reflectance or the sharp break in the continuity of the spectral curves at 0.9 μm region could be attributed to the different kinds of detectors used in the SWIR range (PbS detector) and in the visible range (photomultiplier detector). Besides, probably due to the same reason, the spectral curves in the SWIR range depict an overall decrease in the reflectance. It may also be observed that the spectral reflectance curves of majority of the rock types show a rising trend towards the longer wavelength of the visible range, that is, a steep fall-off of reflectance towards the ultraviolet while these are almost consistently flat

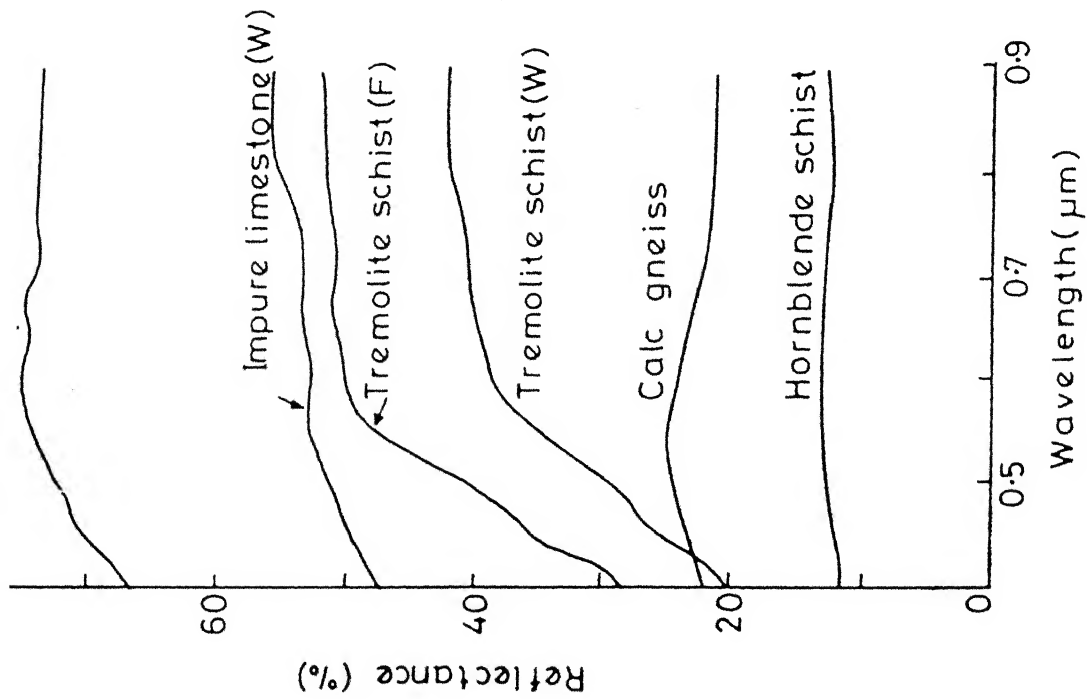


(a) Visible range

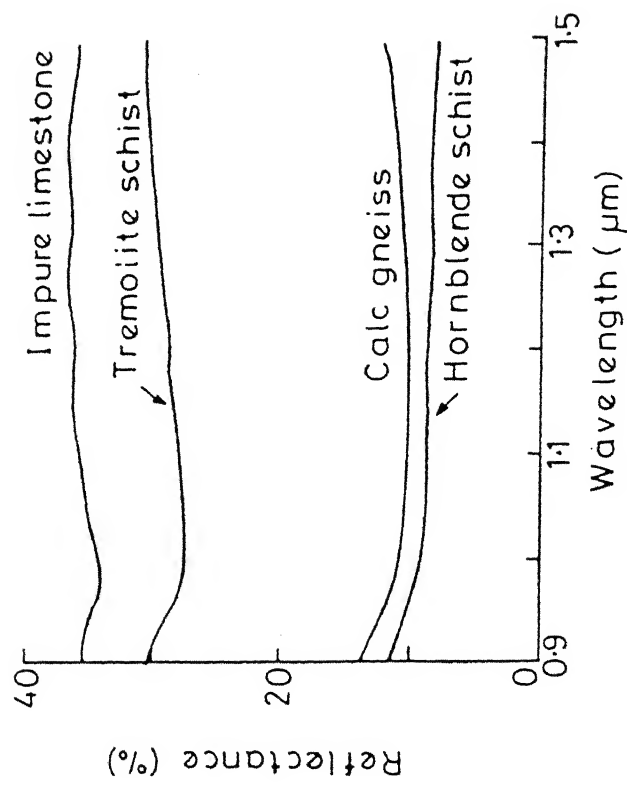


(b) Short wavelength infrared (SWIR) range

FIGURE 3.9 Laboratory derived diffused reflectance spectra of the rocks of MSS area.



(a) Visible range



(b) Short wavelength infrared (SWIR) range

FIGURE 3.10 Laboratory derived diffused reflectance spectra of the rocks of TM area.

throughout the SWIR range (1.1-1.5 μm). This is probably due to the spectrally inert nature of the various rock types to the incident radiation in the SWIR range. Moreover, the spectral curves of all the rock types show a distinct gradual decline in their trend from 0.9 μm to 1.0 μm as seen in Figures 3.9(b) and 3.10(b). The spectral features occurring in the visible portion have been found to be caused by the Fe^{3+} electronic transition (Goetz et al., 1985; Goetz et al., 1981; Kahle, 1984). Therefore, these may be attributed to the ubiquitous presence of iron oxides as impurities as observed from the microscopic studies of thin sections of the various rock types.

As seen from the spectral curves concerning the visible portion of ^{the}/electromagnetic spectrum, of rocks present in MSS area (Figure 3.9a), the quartzites depict remarkably very high reflectance followed by biotite schist, augen gneiss and hornblende granite in decreasing order. However, in the short wavelength infrared portion (Figure 3.9b) the order of spectral reflectance curves of biotite schist and augen gneiss is reversed in the visible portion while the general order remains ^{the}/same. At this stage, it is difficult to ascertain the exact reason of this reversal in the order. The spectral curve of quartzite, in particular, shows a sudden rise in the range 0.4-0.7 μm corresponding to bands 4 and 5 of ^{the}/MSS data and subsequently,

tends to become consistent till the end of SWIR range. This implies that quartzitic rocks in this area do not show much variation in their spectral signature in bands 6 and 7 of MSS data as well as in the first four bands of TM data. The

reflectance spectra of ^{the} other rock types such as biotite schist, augen gneiss and hornblende schist are almost even consistently throughout the visible and SWIR ranges; however, they also depict a steep fall off towards blue. Of special significance to the present study of lithological discrimination is that ^{the} different rock types have strikingly different albedos, but similar reflectance spectra, that is, there is no variation in the slopes of the spectral reflectance curves for ^{the} different rock types at ^{the} corresponding wavelengths.

As mentioned earlier, the spectral pattern of ^{the} various rocks occurring in ^{the} TM area is analogous to that of the rocks of MSS area. Therefore, the same reasons ascribed to the spectra of the rocks of ^{the} MSS area may be considered as being accountable to ^{the} the corresponding features comprising the spectra of the rocks of ^{the} TM area. In order of their increasing reflectance, the rocks may be arranged as hornblende schist, calc gneiss, tremolite schist and impure limestone. It may be seen from Figure 3.10(a) that the reflectance spectra of the weathered portions of the samples of impure limestone and tremolite schist follow the same trends as their fresh or unweathered counterparts; however, as expected, the reflectance of the weathered rocks is lower than their unweathered or fresh counterparts.

From a thorough analysis and interpretation of the visible and SWIR spectra of ^{the} rock samples of both ^{the} MSS and ^{the} TM study areas, the following conclusions may be derived.

- (i) In order of their increasing reflectance, the various rocks may be arranged in the following sequence : granite, phyllite and schist, gneiss, quartzite and limestone.
- (ii) Since spectral measurement has not been carried out beyond 2.0 μm , the effect of clay minerals with regard to their hydroxyl constituents on the spectral pattern cannot be studied.
- (iii) Interpretations derived from the features comprising the laboratory reflectance spectra will be utilized in understanding the spectral signatures of ^{the} different rock types as to their discriminability from ^{one} / another on the various digital images used in the study.
- (iv) Field spectral measurements provide more realistic information in the analysis and interpretation of satellite multispectral scanner data of natural surface materials. However, the present study has been carried out based upon ^{the} / analysis of only the laboratory derived reflectance spectra due to the non-availability of relevant field instruments.

CHAPTER 4

GRAPHICAL ANALYSIS OF DIGITAL DATA FOR LITHOLOGICAL DISCRIMINATION

4.1 INTRODUCTION

As mentioned earlier, the objective of the present study is to discriminate among different rock types in the study area based on the results obtained through application of various digital image processing techniques and subsequently, to evaluate each method in terms of its relative discrimination potential. The analytical results of various digital image processing techniques used in this study have been presented both in graphical form as well as in image form. The two-dimensional graphical representation of the statistical results provides a better picture concerning the discriminability between any two rock types. Moreover, they document many valuable information desired in the understanding and interpretation of the digital images. In this chapter, an elaborate discussion concerning the analysis and interpretation of the graphical outputs of the digital data is provided.

4.2 PRELIMINARY ANALYSIS OF DIGITAL DATA

The area studied by using ^{the}MSS data from ^{the}Landsat-2 comprises mainly seven litho-units viz. (i) gneiss, schist (GNSC), (ii) quartz mica schist (QMS), (iii) intercalated calc and cherty quartzite, marble, phyllite (ICCQMP), (iv) calc gneiss, (v) phyllite, (vi) syenite and (vii) granite as shown in the

geological map (Figure 1.2). However, out of seven only four rock types have been considered for analysis such as (i) GNSC, (ii) QMS, (iii) ICCQMP^{and}/(iv) granites since these four units cover more than eighty percent of the study area and all other litho-units are too small in area to be result through the statistical and graphical analyses of digital data.

Training reflectance values were extracted at different representative sites for each of these four litho-units on a regular grid pattern. Owing to unequal areal extent of the litho-units, proportionate weightage was given while training each rock type. As such,^a/number of training pixels derived for different litho-units are as follows : GNSC = 59, QMS = 49, ICCQMP = 41, Granite = 35.

On the other hand, the study area selected for analysis of TM data of Landsat-5 for lithological discrimination consists of five rock units namely (i) Erinpura granites and gneisses, (ii) quartzites, (iii) calc schists, (iv) phyllites and impure limestones, and (v) biotitic limestones and calc gneiss as shown in the geological map (Figure 1.3). However, only three prominent litho-units can be identified conspicuously on the basis of their colours and textures on the false colour composites and other digital images. These three major litho-units considered for analysis are : (i) granites and gneisses, (ii) schists and phyllites, and (iii) quartzites.

Owing to varying illumination conditions prevailing on the two litho-units namely the granites and gneisses, and the quartzites induced by topography as seen on the FCCs and other digital images, each of these two litho-units has been further

subgrouped into two separate litho-units, one representing the illuminated or bright portion and the other, the non-illuminated or shadowed portion. As a result of this subgrouping, five main litho-units emerge such as (i) quartzite-1, (ii) quartzite-2, (iii) phyllites and schists, (iv) granite-1, and (v) granite-2 in which the suffixes 1 and 2 represent the illuminated or bright portion and non-illuminated or shadowed portion respectively. Training reflectances have been extracted for different litho-units in proportion to their areal extent. For example, quartzite-1, phyllites and schists and granite-1 each has been represented by 25 training pixels, whereas for quartzite-2 and granite-2 only 15 training pixels were extracted owing to their comparatively small areal extent as seen on the false colour composites.

4.3 ANALYSIS AND DISCUSSION

In order to evaluate the degree of discrimination among the litho-units, a series of conceptually straightforward digital graphical techniques were applied to the subscenes pertaining to the respective study areas for MSS and TM data. These include

- (i) histograms of training data in different bands
- (ii) coincident spectral plots
- (iii) extended spectral signature plots
- (iv) histograms and coincident spectral plots of band ratios
- (v) two-dimensional (i.e. two band) principal component analysis (PCA)
- and (vi) discriminant function analysis (DFA).

4.3.1 Histograms of Training Data in Different Bands

In order to assess the quality of the original digital data, histograms for the various rock types present in the study area have been plotted in different bands from the training reflectance values of the rocks. Since a small number of training pixels have been extracted for each rock type in different bands, the frequency of any particular brightness value is expectedly low. Therefore, in the present study, the histograms have been plotted by taking into consideration the frequency determined for continuous and suitable class intervals of brightness values.

The histograms of the various rocks of MSS area namely GNSC, QMS, ICCQMP and Granite in different MSS bands are shown in Figures 4.1(a)-(d) respectively. Similarly, the histograms of the rocks of TM area such as quartzite-1, quartzite-2, phyllite, granite-1 and granite-2 in different TM bands (excluding band 6, thermal band) are shown respectively in Figures 4.2(a)-(e). Examination of the histograms for various rocks in the respective bands shows that the training data sets of the rocks are multimodal in nature. This indicates that the rocks comprise as many subclasses as the number of modes or peaks observed in their respective histograms. Since at least 2 to 3 distinct peaks are present in the histograms of each rock type in different bands, it implies that each rock of both MSS and TM areas is associated with the spectral characteristics of the other rock types present in the respective study areas. In other words, the various rocks are very strongly identical in terms of their spectral property. This very aspect of the rocks makes it difficult to discriminate them statistically as will be discussed in the following chapter.

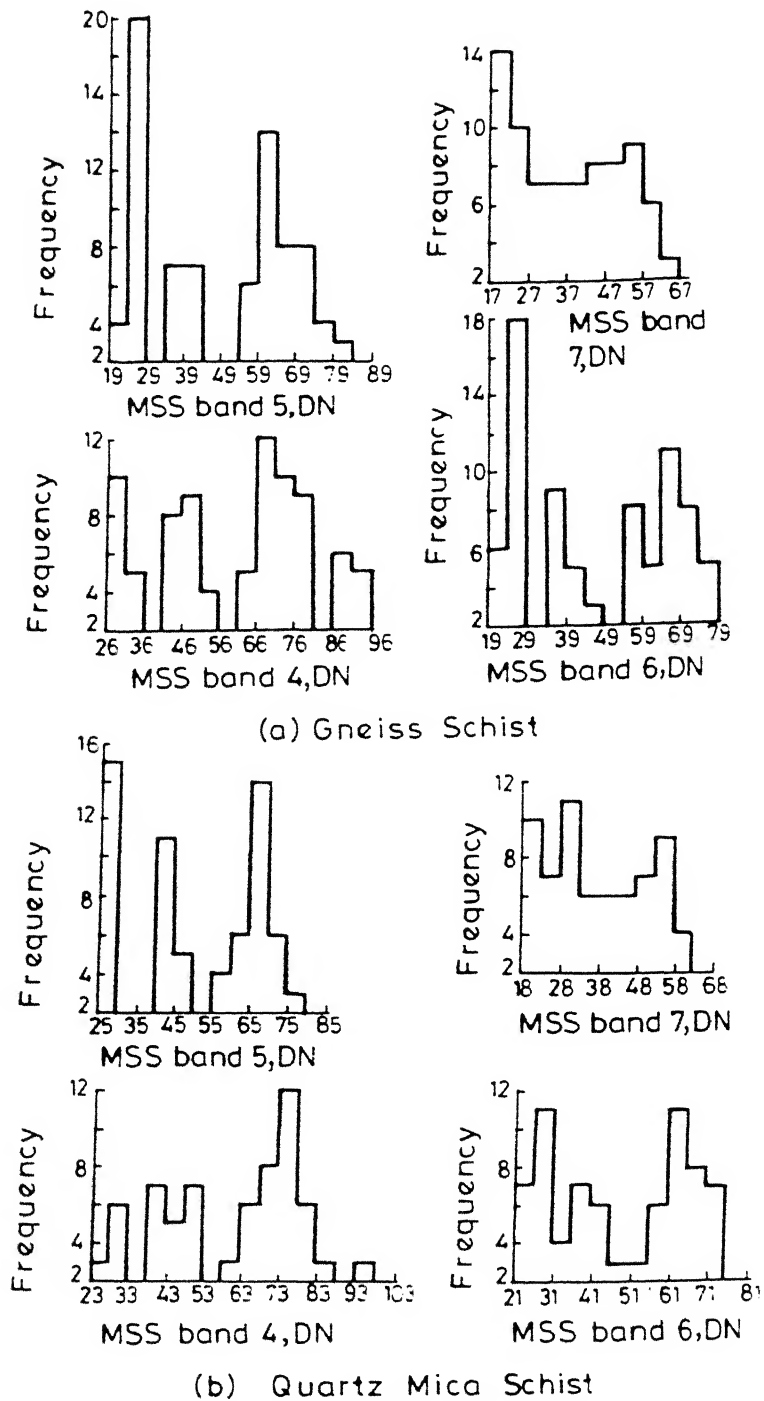
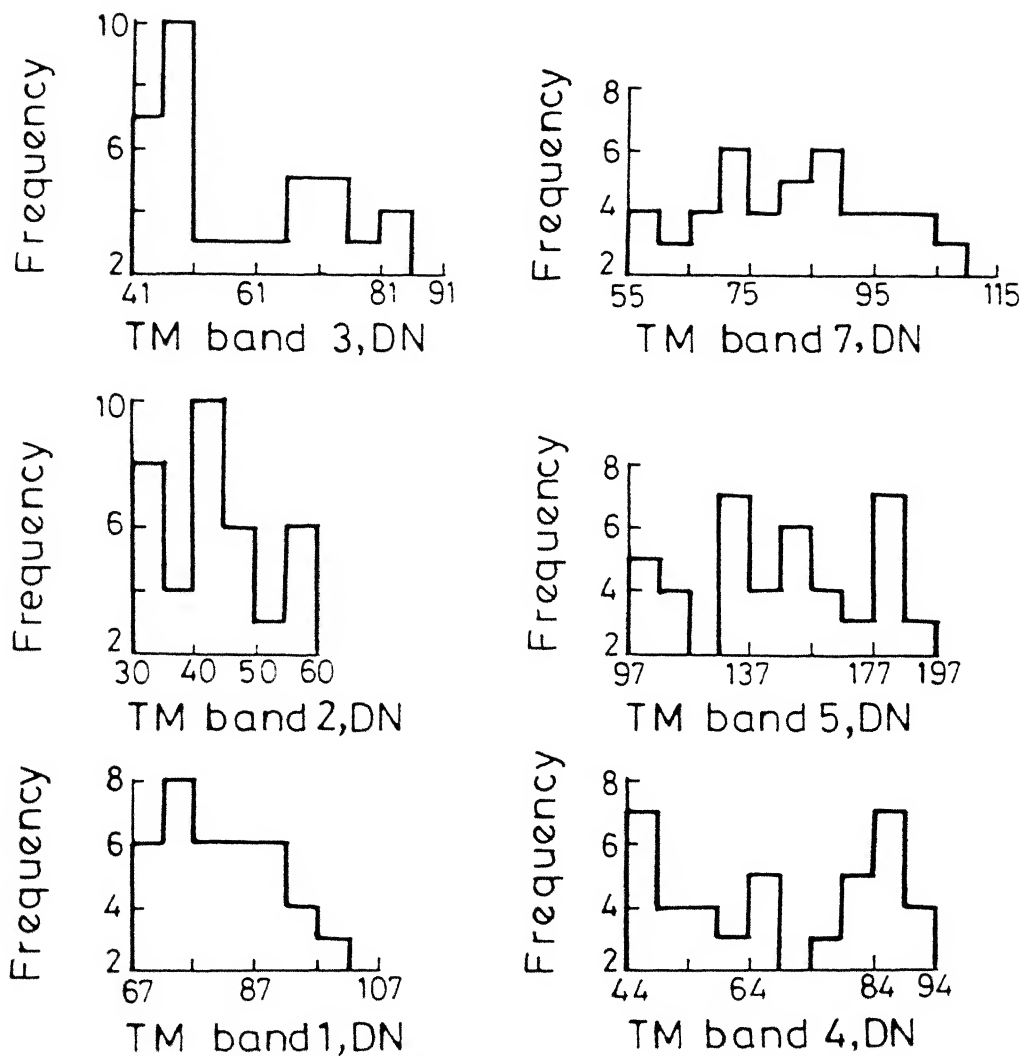
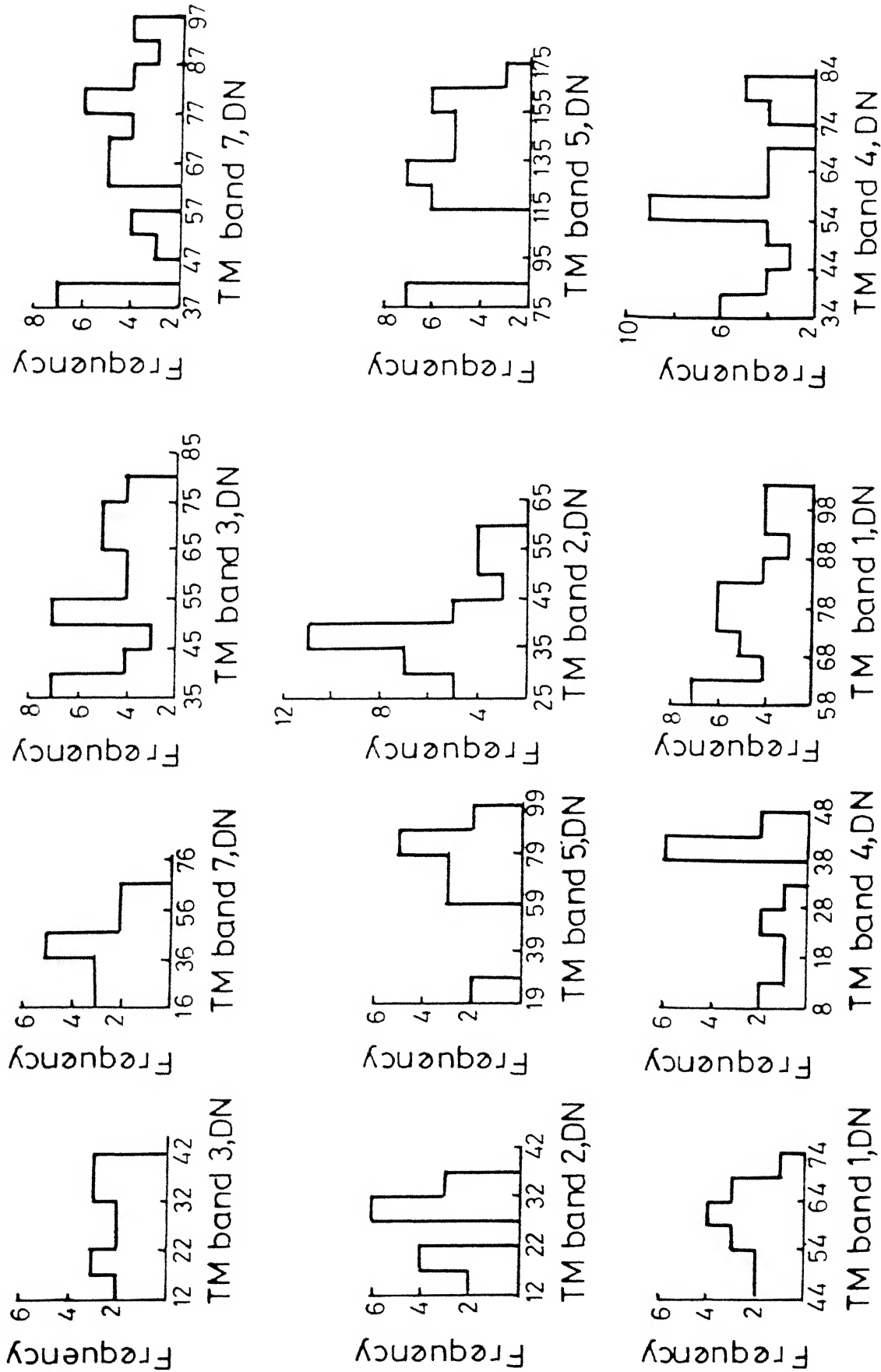


FIGURE 4.1 Histograms of the rocks of MSS area.
(plotted from their training brightness values)



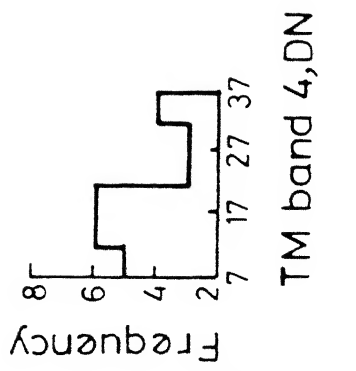
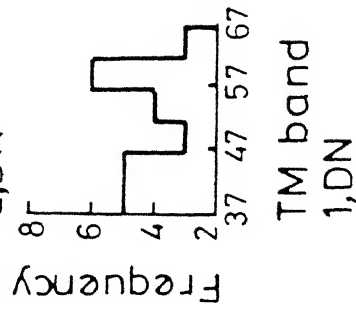
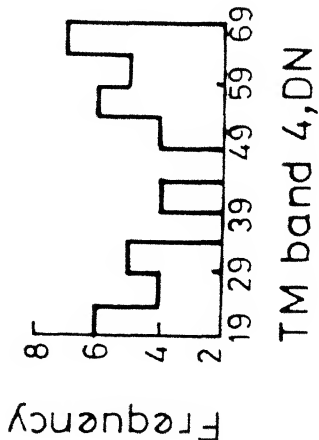
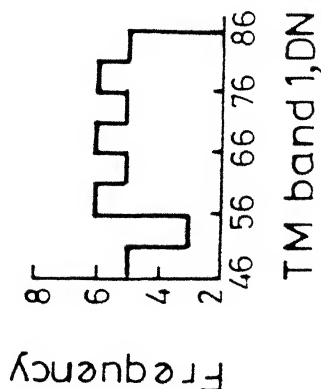
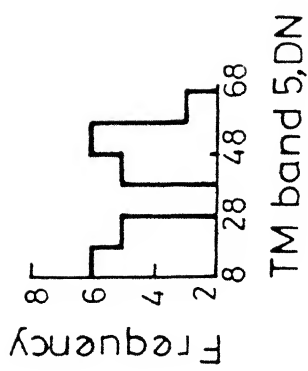
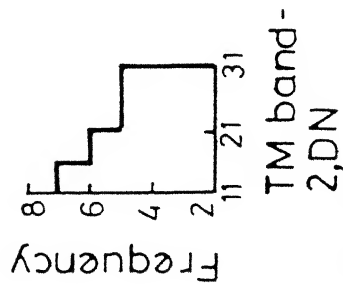
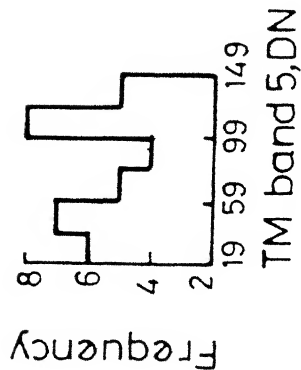
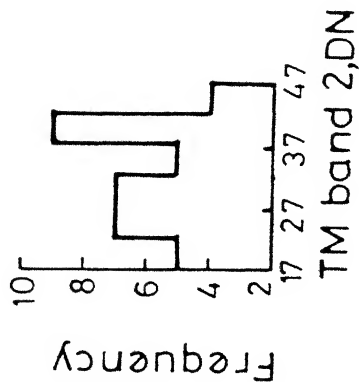
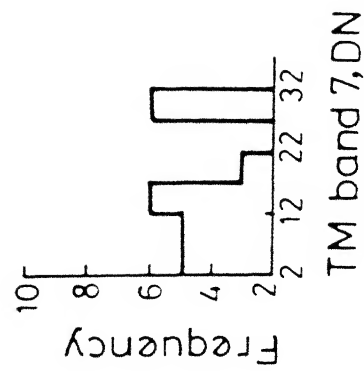
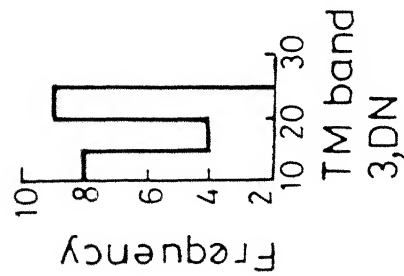
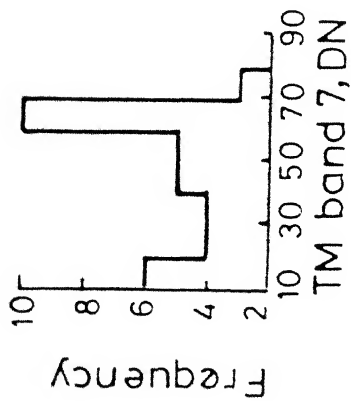
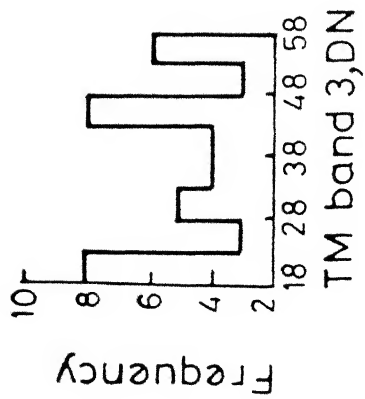
(a) Quartzite -1

FIGURE 4.2 Histograms of the rocks of TM area.
(plotted from their training brightness values)



(b) Quartzite-2

(c) Phyllite



(d) Granite-1

(e) Granite-2

FIGURE 4.2 (continued)

In the present case, the discontinuity of the bars of the histograms could be due to the less number of training data used for analysis.

As compared to the full dynamic range of MSS data of Landsat-2 (0-127), the brightness values cover over fifty percent of this range suggesting that the histograms are of moderate to high contrast. An image with good contrast provides better discrimination among various categories but in the present case, this attribute of MSS data is greatly handicapped by the multimodal nature of the training data sets. Similarly, it may be seen that except in TM band 5, the training brightness values of rocks of TM area are compressed to less than one-fourth of the full dynamic range (0-255) of TM data indicating that the corresponding histograms are of poor contrast. In the histograms of quartzite-2 in bands 1, 5 and 7 and in that of phyllites in band 2, the distribution of the training pixels may be regarded as being poorly Gaussian in nature.

4.3.2 Coincident Spectral Plots

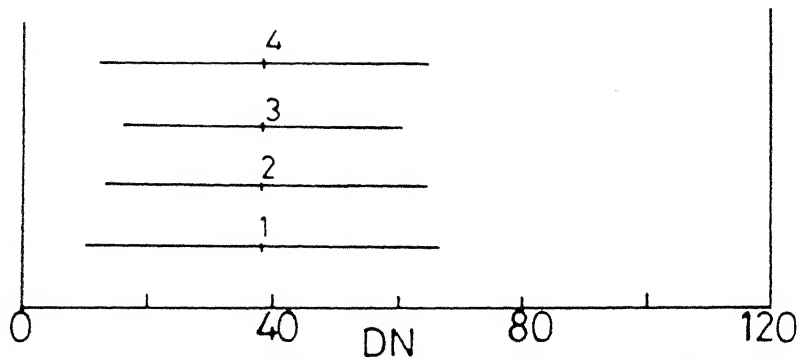
Histograms illustrate the distributions of individual categories very well, yet do not facilitate comparisons between different category types. One of the simplest methods to evaluate the spectral separation between categories is the coincident spectral plot which illustrates, in each spectral band, the mean spectral response of each category and the variance of the distribution. In actual practice, the plots represent the statistical confidence intervals of the training data sets of the rock types in different bands. The magnitude of the confidence interval to be displayed depends upon the level of accuracy the

analyst desires in the discrimination of different categories. In the present study, the degree of separation between rock types has been evaluated at 95% confidence intervals and accordingly, mean ± 1.96 standard deviations of each rock type have been represented in the plots for different bands. The coincident spectral plots for various rocks of MSS and TM areas are shown in Figures 4.3 and 4.4 respectively.

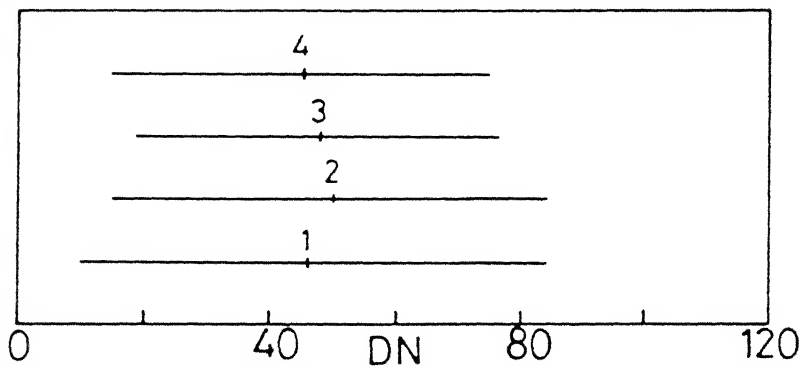
The coincident spectral plots of rocks of MSS area (Figure 4.3) depict considerable overlap between various rocks in all the spectral channels. This observation is in close agreement with the results of the histogram analysis as described in the preceding section in the sense that there exists significantly strong spectral resemblance between rock types in the latter. However, the strong similarity in the spectral property of the rocks may also be, in part, attributed to the method adopted for extraction of training data sets from MSS tapes. It may be recalled that the training reflectances were extracted from the MSS scene with reference to their line numbers and pixel numbers corresponding to the geographical coordinates determined on the geological map, giving no consideration to the factor of brightness variation induced by topography.

On the other hand, in TM area, the rocks marked by rough topography have been represented each by two separate litho-units corresponding to their bright or illuminated portion and the shadowed or non-illuminated portion. As a result, the coincident spectral plots facilitate better representation and comparison of the spectral response pattern distributions of the

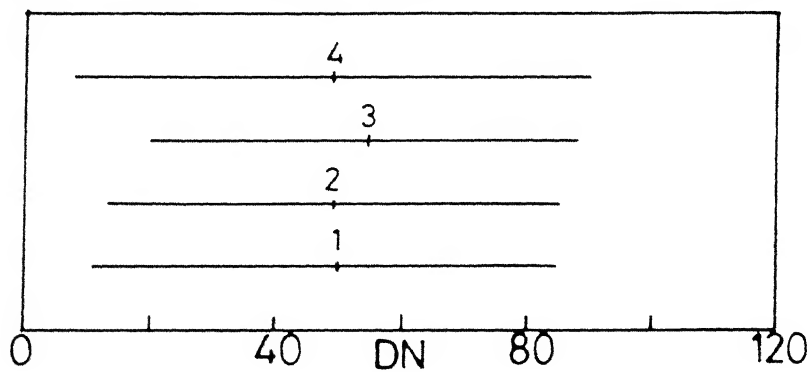
and 7
(d)



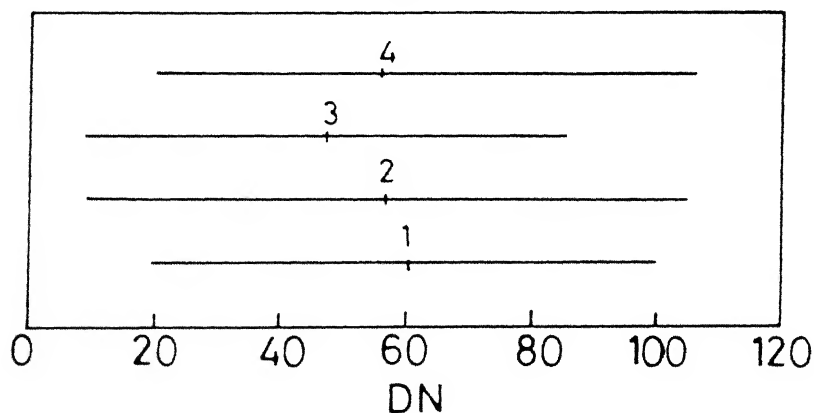
and 6
(c)



and 5
(b)



and 4
(a)



LEGEND

- 1 = Gneiss schist
- 2 = Quartz mica schist
- 3 = Intercalated calc & cherty quartzite marble phyllite
- 4 = Granite

FIGURE 4.3 Coincident spectral plots of the rocks of MSS area in different MSS bands.

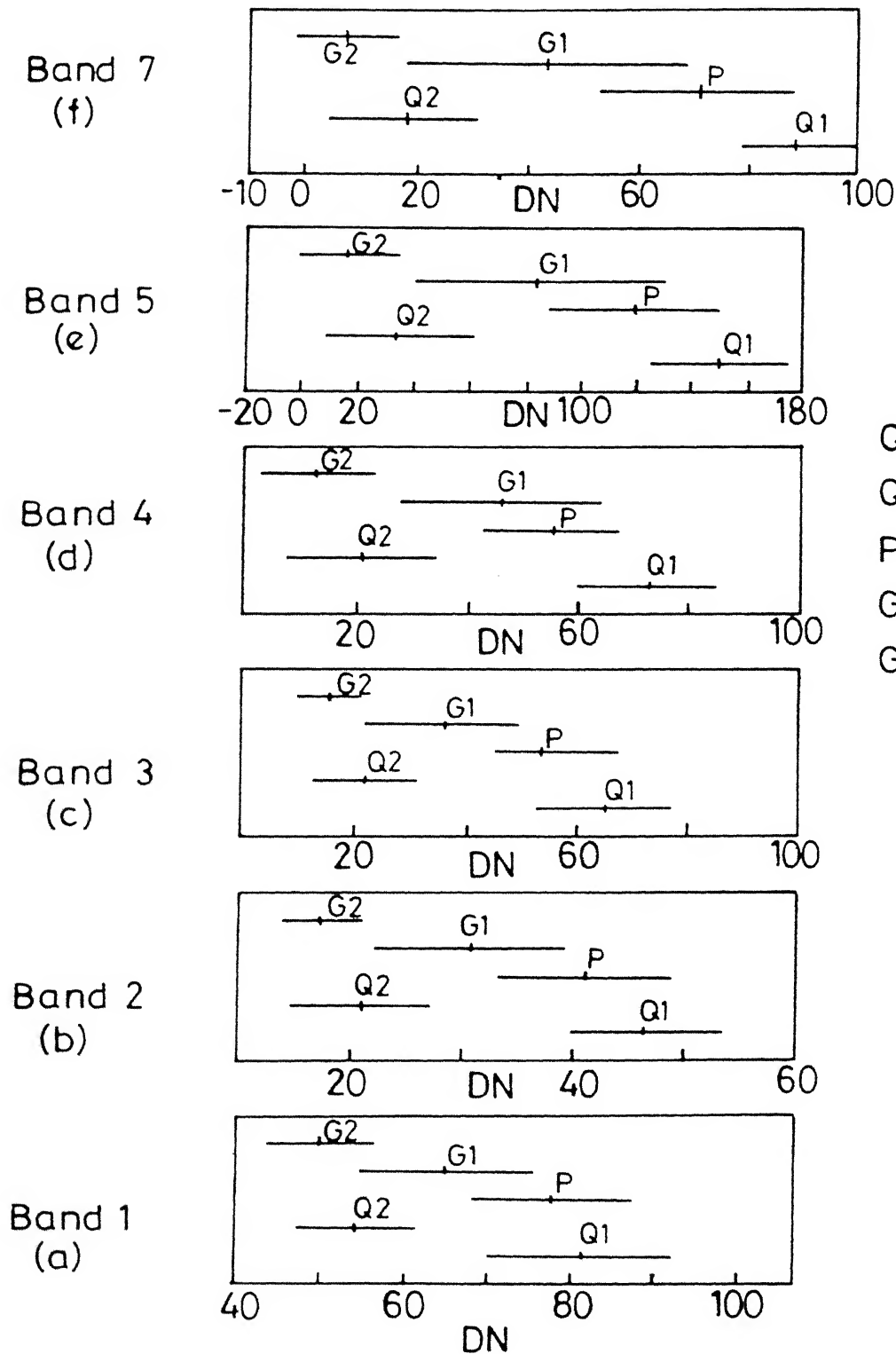


FIGURE 4.4 Coincident spectral plots of the rocks of TM area in different TM bands.

rocks of TM area in different TM spectral channels (Figure 4.4). As expected, the illuminated and non-illuminated parts of each of the quartzitic and the granitic rocks (that is, the pairs quartzite-1 - quartzite-2 and granite-1 - granite-2) are distinctly separated on the coincident spectral plots of all TM bands indicating no misclassification in any band. This results due to the contrastingly different brightness values of the illuminated and non-illuminated portions of each of the quartzitic and granitic rocks despite the fact that both portions of the respective rocks have identical mineralogical composition.

Owing to even nature of the phyllitic terrain resulting in uniform illumination condition, it has been represented as a single litho-unit. The spectral response patterns of the phyllitic rocks depict an overlap of nearly 50 percent of their spectral confidence range with granite-1 (illuminated) in all the bands; however, there is distinct and considerable separation in the spectral response patterns of the phyllites and the granite-2 (shadowed). Similarly, while the spectral response patterns of the phyllites and the quartzite-1 (illuminated) overlap almost by the same extent as the phyllites and the granite-1 in all TM bands except band 1, phyllite and granite-2 response patterns are largely separated in all TM bands. These observations indicate that there is absolutely no chance of misclassification between the phyllitic rocks and the shadowed parts of the quartzites and the granites in any of the TM bands; however, reasonable amount of intermixing is anticipated between the phyllites and the

illuminated parts of the quartzites and the granites in all TM bands.

The spectral response pattern distributions of the quartzitic and the granitic rocks depict considerably large separation between the bright part of the former (i.e. quartzite-1) and the shadowed part of the latter (i.e. granite-2) in all bands of TM data. On the other hand, the non-illuminated or shadowed parts of these rock types (i.e. quartzite-2 and granite-2) exhibit almost complete overlap of their spectral response patterns in each TM band. Similarly, the spectral response patterns of the illuminated parts of the quartzites and the granites (i.e. quartzite-1 and granite-1 respectively) are just separated in TM bands 2, 3, 5 and 7 while they exhibit only little overlap in the other TM bands, that is bands 1 and 4. The spectral response patterns of quartzite-2 (non-illuminated) and granite-1 (illuminated) depict partial overlap in all TM bands. The close separation between the spectral response patterns of quartzite-1 and granite-1 is due probably to reasonably different spectral characteristics of the quartzites and the granites. The considerably large separation between the spectral response patterns of quartzite-1 and granite-2 may therefore be attributed to generally higher reflectance of the quartzites relative to the granites as observed from their laboratory derived diffused reflectance spectra (Figures 3.9 and 3.10) and also, to the prevalence of different illumination conditions in their terrains. On the other hand, the considerable overlap between

quartzite-2 and granite-2 is possibly brought about by similar illumination conditions prevailing on them.

In the analysis of coincident spectral plots for discrimination of rock types, it must be realised that these plots depict between-category overlap or separation on any single MSS or TM band only. Therefore, the results of this analysis should not be used as diagnostic criteria for evaluating the discrimination among various rocks on images that have been generated by using two or more number of bands. The effect of multivariate analysis of digital data on the discrimination of rock types will be discussed under Discriminant Function Analysis in section 4.3.7.

4.3.3 Extended Spectral Signature Plots

As discussed in the preceding two sections, the distributions and the spectral contrast of individual categories in different bands are best illustrated by their respective histograms generated from the training data sets, whereas the spectral overlap or separation between different rock types on different bands can be determined from their coincident spectral plots. However, none of these techniques provides information about the changes in spectral variability of individual categories in different bands together. In order to perform a comparative study of the spectral variability of individual categories in different bands together, it is convenient to plot the means and ± 1 standard deviations for the individual categories or rock types which is also called "extended spectral signature" (Evans, 1988; Lillesand and Kelfer, 1987).

Figure 4.5 shows the extended spectral signatures of various rock types of MSS area. It may be observed that all the rock types namely GNSC, QMS, ICCQMP and Granite depict similar trends of their mean training brightness values, which progressively declines from MSS band 4 to band 7 except the sole occurrence of a reversal in the trend of ICCQMP from band 4 to 5. Moreover, the spectra show that the difference in the mean brightness values of individual rock types in different bands is negligible and this difference is comparable between different rock types. The substantially large standard deviations indicate large variability within the training data set of the various rock types which makes it difficult to discriminate the rock types statistically as well as visually on the digital images.

The mean digital numbers and ± 1 standard deviations for the six visible and near-infrared wavelength TM channels for the five rock types of TM area are shown in Figure 4.6. The training data sets used for calculating means and standard deviations are those used for classification of rock types by maximum likelihood classifier. A comparative study of the extended spectral signatures reveals that the three main rock types namely quartzite-1, phyllites and granite-1 exhibit strong variation of mean values in different TM bands, whereas the other two rock types viz. quartzite-2 and granite-2 are marked by little variation of their mean brightness values. In addition, the illuminated part of the quartzites (i.e. quartzite-1) has highest mean reflectance followed by phyllites, granite-1, quartzite-2 and granite-2 in decreasing order. Invariably all the rock types

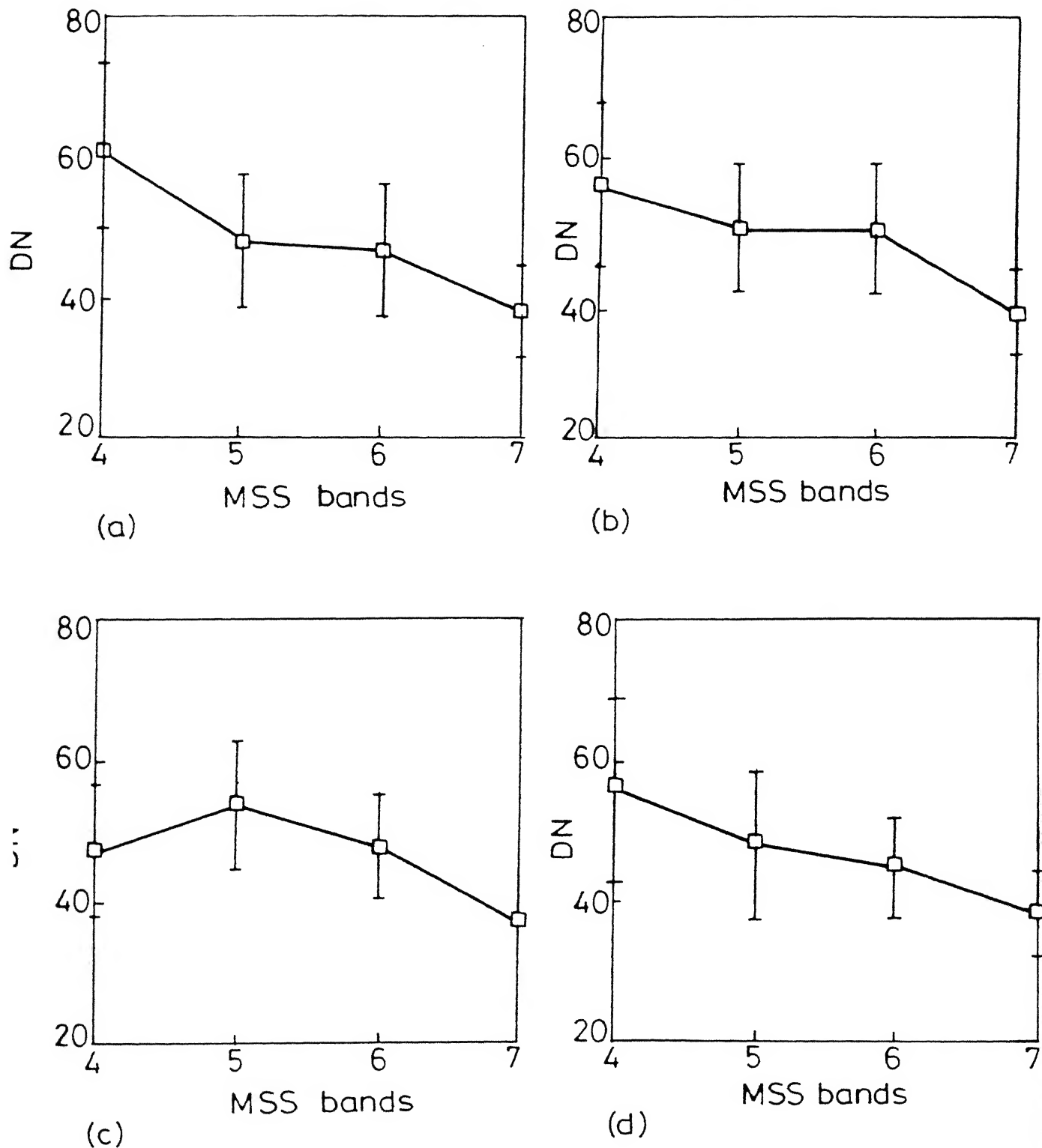


FIGURE 4.5 Extended spectral signatures for the rocks of MSS area. (a) Gneiss schist, (b) Quartz mica schist, (c) Intercalated calc and cherty quartzite marble phyllite, and (d) Granite.

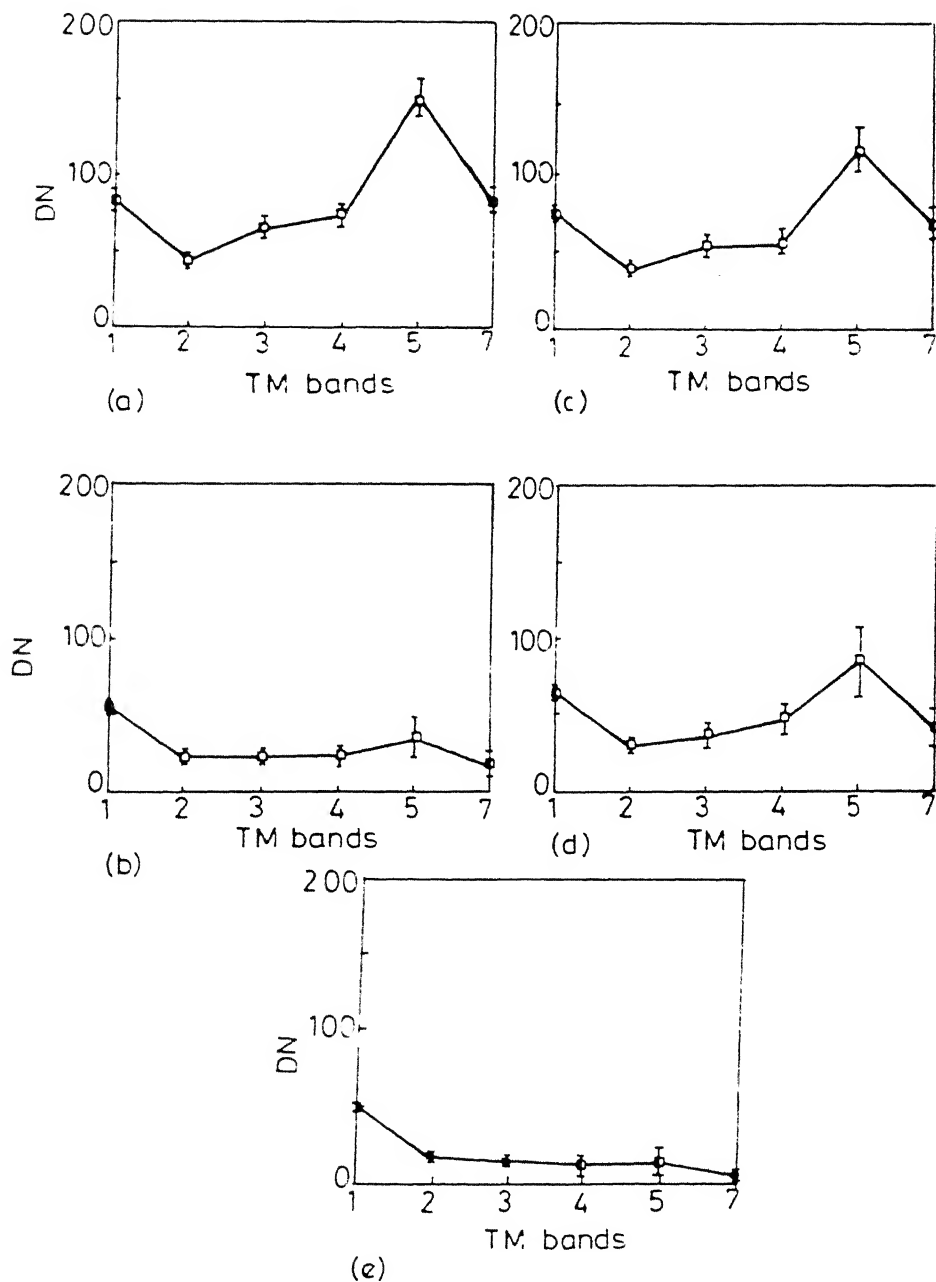


FIGURE 4.6 Extended spectral signature of the rocks of TM area. (a) Quartzite-1 (Illuminated), (b) Quartzite-2 (Non-illuminated), (c) Phyllite, (d) Granite-1 (Illuminated), and (e) Granite-2 (Non-illuminated).

show significantly larger standard deviations in band 5 than in other five channels indicating large variability of the training brightness values of band 5. The smaller standard deviations of rocks in the other bands signify little variability indicating that the discrimination of rock types could be carried out more efficiently in these bands. Besides, due to the appreciably high reflectance in band 5 as compared to band 7, a band ratio image of these two bands ($B5/B7$) could provide many useful information about the spectral characteristics of rock types. However, as seen from the plots of extended spectral signatures, the large variances of brightness values in these bands would considerably reduce the usefulness of this ratio image.

4.3.4 Histograms of Band Ratios

It has been determined from analysis of extended spectral signature plots and coincident spectral plots that brightness variations induced by slope bring about significant amount of spectral resemblance between different rock types. As mentioned earlier in section 2.3.2.1, ratioing of spectral channels is a uniquely potential technique to minimize the redundant and ambiguous information associated with the digital data as a result of brightness variations. To evaluate the improvement, if any, achieved through band ratioing technique, one of the simplest and convenient ways is to represent the ratio values of different bands as histograms and coincident spectral plots.

For the histogram analysis, only selected band ratios have been considered both for MSS and TM digital data. The band

ratios used for the histograms of MSS data have been selected on the basis of the presence of distinct clusters of training data in various two-dimensional scatter diagrams as shown under principal component analysis in the following section. It may be observed that the scatter diagrams of bands 4-5, 5-6, 5-7 and 6-7 (Figures 4.10a,d-f) each exhibits at least three distinct clusters of data points indicating that these band combinations could offer ^a fair chance of discrimination of ^{the} different rock types. Therefore, their respective ratios, that is, 4/5, 5/6, 5/7 and 6/7 have been considered for histogram analysis and are shown in Figure 4.7. As seen in these figures, the ratio values of the rock types follow nearly Gaussian distribution in contrast to the training brightness values. Each of these histograms except that of band 4/5 is unimodal in nature. Besides, the analysis reveals that the highest frequency bar in each histogram comprises almost equal relative frequency (in percent) of different rock types indicating that each of the ratio images will be capable of displaying the various rock types with equal conspicuity.

On the other hand, in general, none of the two-dimensional scatter diagrams of TM bands (Figures 4.11a-o) depicts formation of clusters of training brightness values. Therefore, only the proven and widely used TM band ratios with regard to their usefulness for rock discrimination have been employed for the histogram analysis for rock types of TM area. The various ratios used in the present study are TM 2/3, 3/4, 4/5 and 5/7.

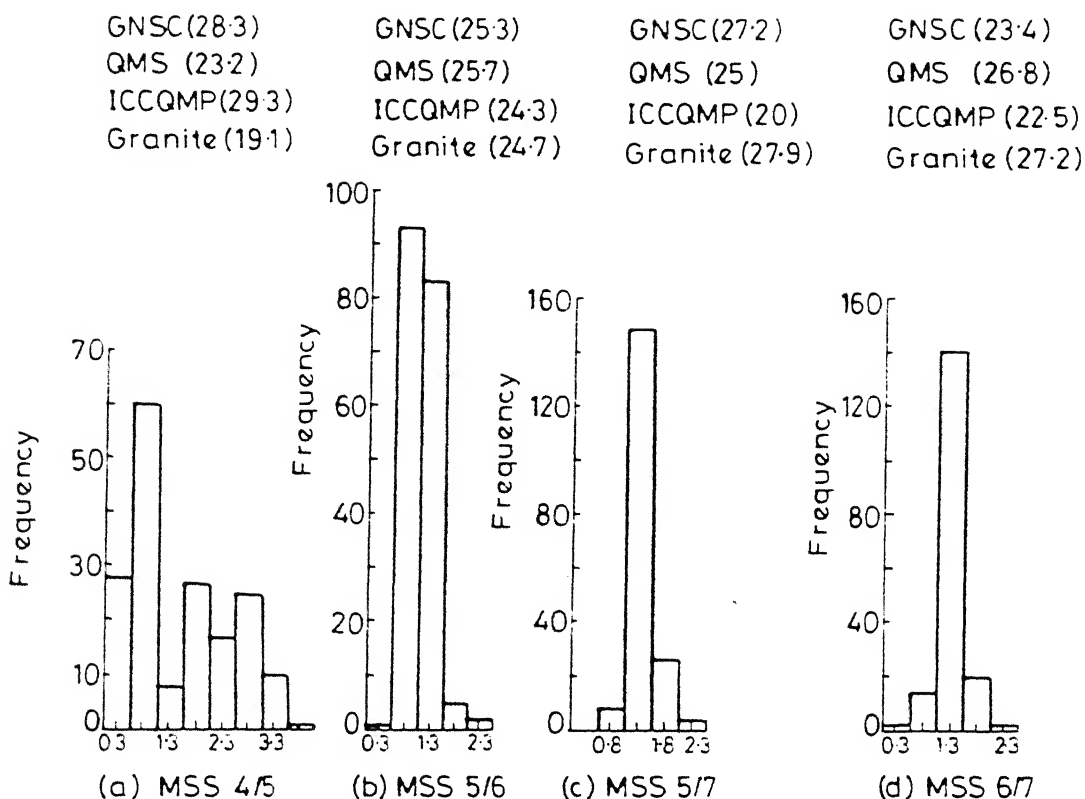


FIGURE 4.7 Histograms of band ratios for the rocks of MSS area. The figures in brackets represent the relative frequency (in percent) of different rocks in the highest bar of the corresponding histogram. In the case of MSS 5/6, these values represent both the dominant bars. GNSC = Gneiss schist, QMS = Quartz mica schist, and ICCQMP = Intercalated calc and cherty quartzite marble phyllite. The relative frequency in each band ratio histogram has been determined as follows. For example, in the histogram of MSS 6/7 :

	ROCKS			
	GNSC	QMS	ICCGMP	Granite
i) No. of training pixels in highest frequency bar (X)	42	40	28	29
ii) Total number of pixels (Y)	59	49	41	35
iii) Actual χ (Z), $Z = X/Y$	71.18	81.6	68.29	82.86
iv) Sum (S), $S = \sum Z$	71.18+81.6+68.29+82.86 = 303.93			
v) Relative frequency (in percent) = Z_i/S	23.4	26.8	22.5	27.2

It may be observed that like the MSS band ratios, the distributions of TM ratio values follow unimodal and nearly Gaussian nature in various ratio histograms shown in Figure 4.8 which is in sharp contrast to the behaviour of the original training brightness values. The analysis of relative frequency of the various rocks estimated for the highest frequency bar in different histograms reveals that the ratio image of TM 2/3 would provide better discrimination up quartzite-1, quartzite-2 and granite-1 because of the relatively high frequency of these rocks in the highest frequency bar. Similarly, ratio images of TM 3/4 and 4/5 would provide reasonably good discrimination of quartzite-1 and granite-1 since all other rocks are represented by considerably low frequency of their ratio values in the highest frequency bar. The histogram of ratio of TM bands 5 and 7 (5/7), however, exhibits, in the highest frequency bar, nearly equal frequency of four of the five litho-units considered for the present study implying that all the rocks will be represented by uniform spectral signature on the ratio image. The inferences derived from the analysis of histograms of different band ratios will be verified vis-a-vis the analysis and interpretation of the ratio images and their false colour composites as discussed in Chapter 5.

4.3.5. Coincident Spectral Plots of Band Ratios

The effects of ratioing of the corresponding brightness values of different channels on the quality of the resulting ratio images can also be fairly understood from the analysis of the coincident spectral plots of the ratio values in different

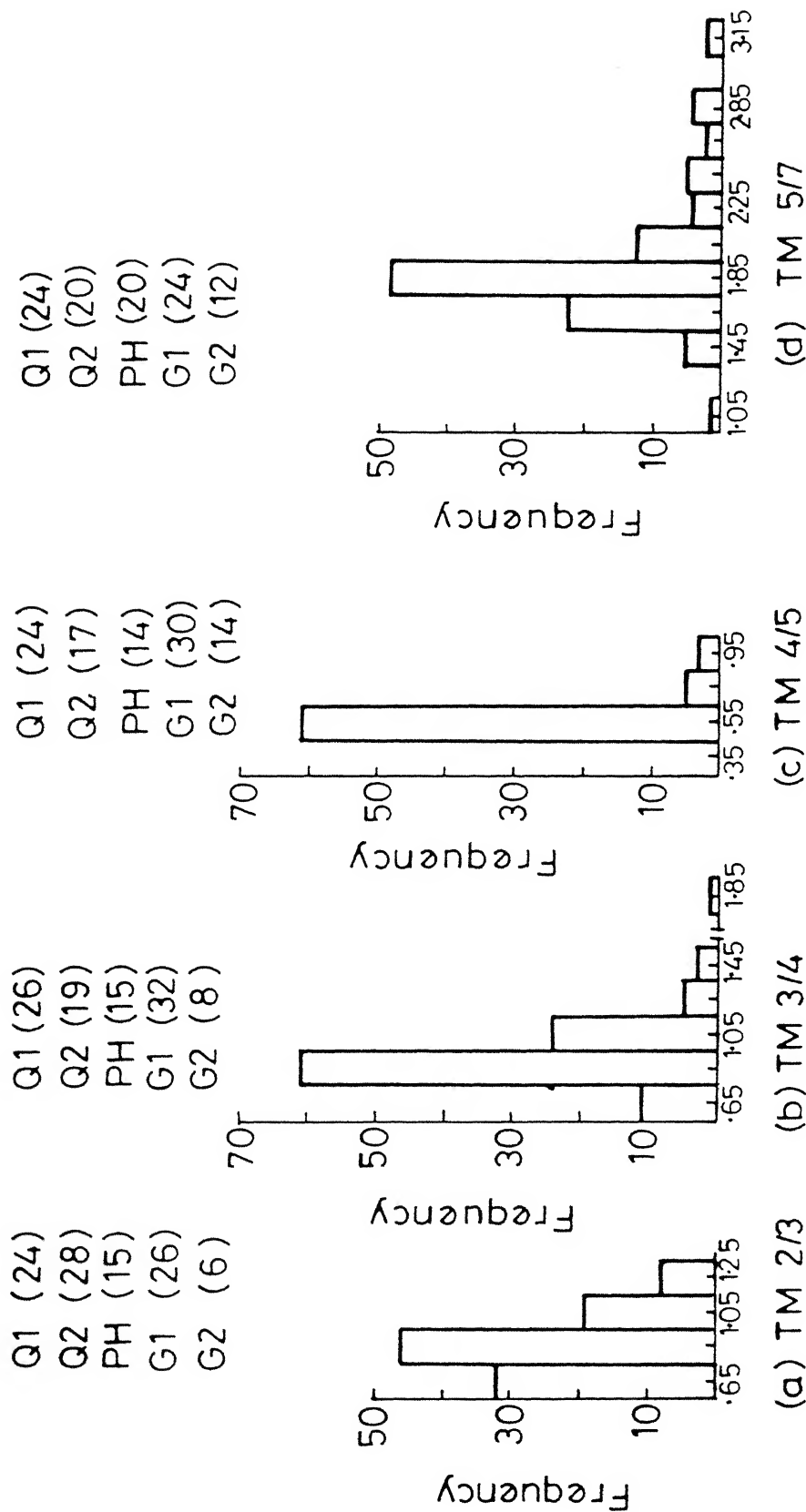
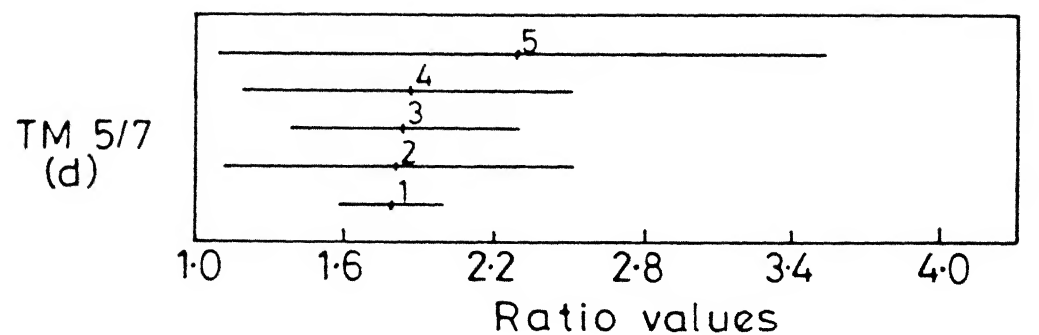


FIGURE 4.8 Histograms of band ratios for the rocks of TM area. Figures in brackets represent the relative frequency (in percent) of different rocks in the highest bar of the corresponding histogram. Q1 = Quartzite-1, Q2 = Quartzite-2, P = Phyllite, G1 = Granite-1, and G2 = Granite-2. For explanation of relative frequency, see Figure 4.7.

band ratios. The coincident spectral plots of ratio values illustrate the 95% confidence intervals of each category which is determined from the formula $\mu \pm 1.96 \sigma$ where μ and σ represent respectively the mean and standard deviation of the ratio values of individual rocks in ratios of different TM channels.

In the present study, since only the TM data have been used for generation of ratio images, coincident spectral plots have been derived by using the band ratios of TM data alone, which are shown in Figure 4.9. It may be observed that all the rock types present in TM area exhibit considerable overlap in the coincident spectral plots of different band ratios. Even the illuminated and non-illuminated portions of the quartzitic and the granitic rocks, despite their strongly contrasting reflectance characteristics, are characterised by a substantial amount of spectral overlap. The coincident spectral plots for each of TM band ratios 3/4 and 5/7 depict ^{the} largest spectral ranges for granite-2 (shadowed), thereby covering the spectral ranges of all other litho-units. The results of the analysis of coincident spectral plots of ratio values do not tally with the results of the analysis of histograms of corresponding band ratios. It may also be noted that the coincident spectral plots of ratio values are in sharp contrast to the coincident spectral plots of the training brightness values in different TM channels in the sense that the latter depict spectral separation of at least some rock types. This study has indicated that spectral ratioing will give rise to ^a considerable amount of redundancy and ambiguity in the identification of various categories on the digital image.



LEGEND

1=Quartzite-1

2=Quartzite-2

3=Phyllite

4=Granite-1

5=Granite-2

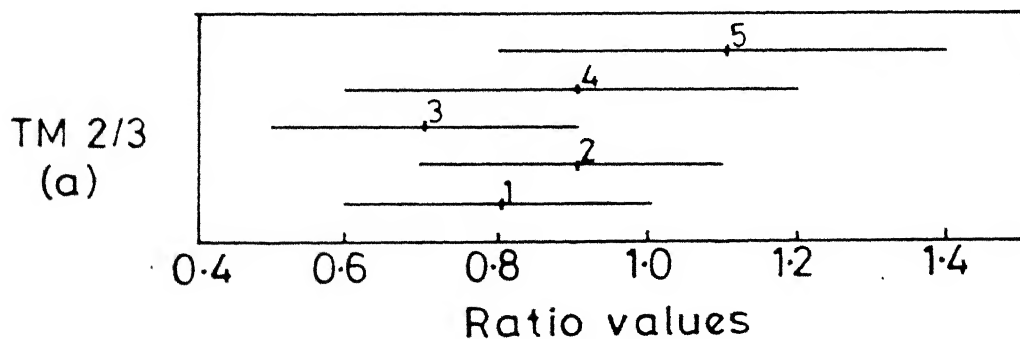
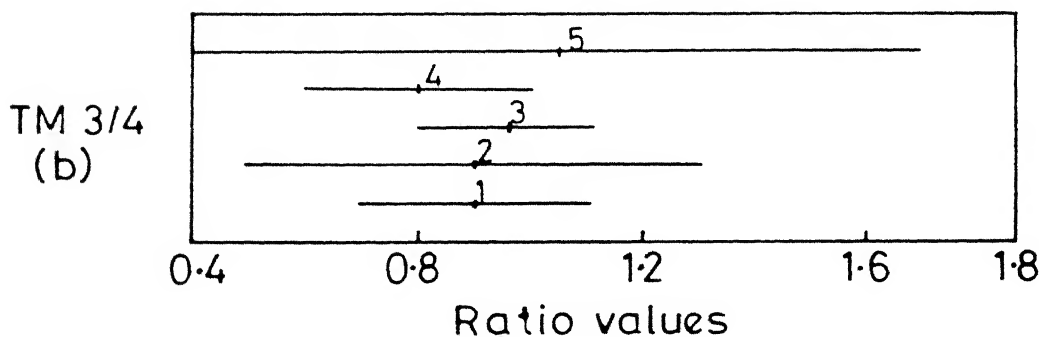
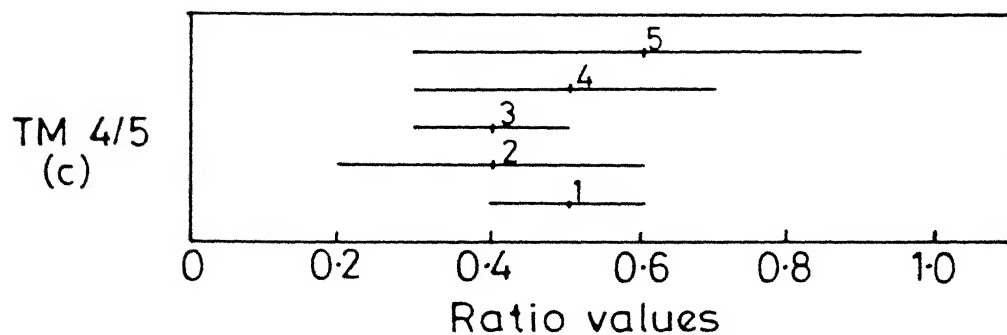


FIGURE 4.9 Coincident spectral plots of the rocks and TM area in different TM band ratios.

The occurrence of the significant amount of spectral overlap of ratio values in the coincident spectral plots for different band ratios could be attributed to strong interband correlation of TM data. Ratio values are dependent both upon the denominator and numerator; therefore, a mutual interchange of these would result in ^a/large difference between the minimum and maximum ratio values.

4.3.6 Two-dimensional Principal Component Analysis (PCA)

The graphical or two-dimensional approach of PCA has been described in detail in Chapter 2. The main objective of this method is to graphically evaluate the potential of the pair of the transformed axes, usually called the principal component (PC) axes for eliminating the interband correlation of the training data sets of various rock types. To perform this task, the training reflectance values of the rock types of MSS and TM area have been plotted in the respective two-dimensional cartesian fields of all possible pairs of MSS and TM bands, which results in the formation of six band pairs for MSS data and 15 band pairs for TM data. The scatter plots of training reflectance values in the fields defined by these spectral pairs are shown in Figures 4.10(a)-(f) for MSS data and in Figures 4.11(a)-(o) for TM data. The angle of rotation ' θ ' for different band pairs has been calculated by using equation (2.18) and is shown along with the resulting two principal components in the respective scatter plots. The band means and variance-covariance matrix used in the estimation of the rotation angle θ and for finding the centroid

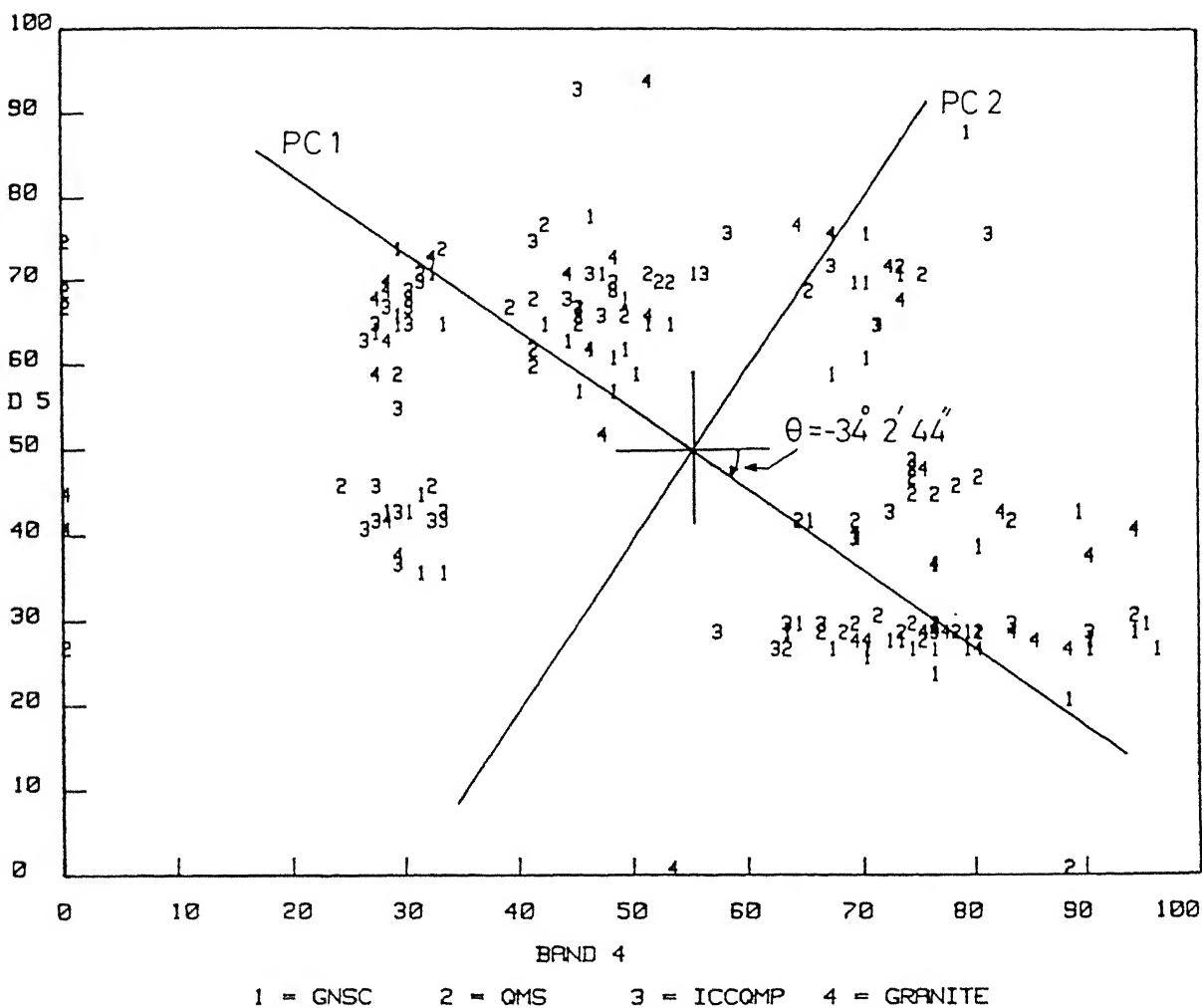
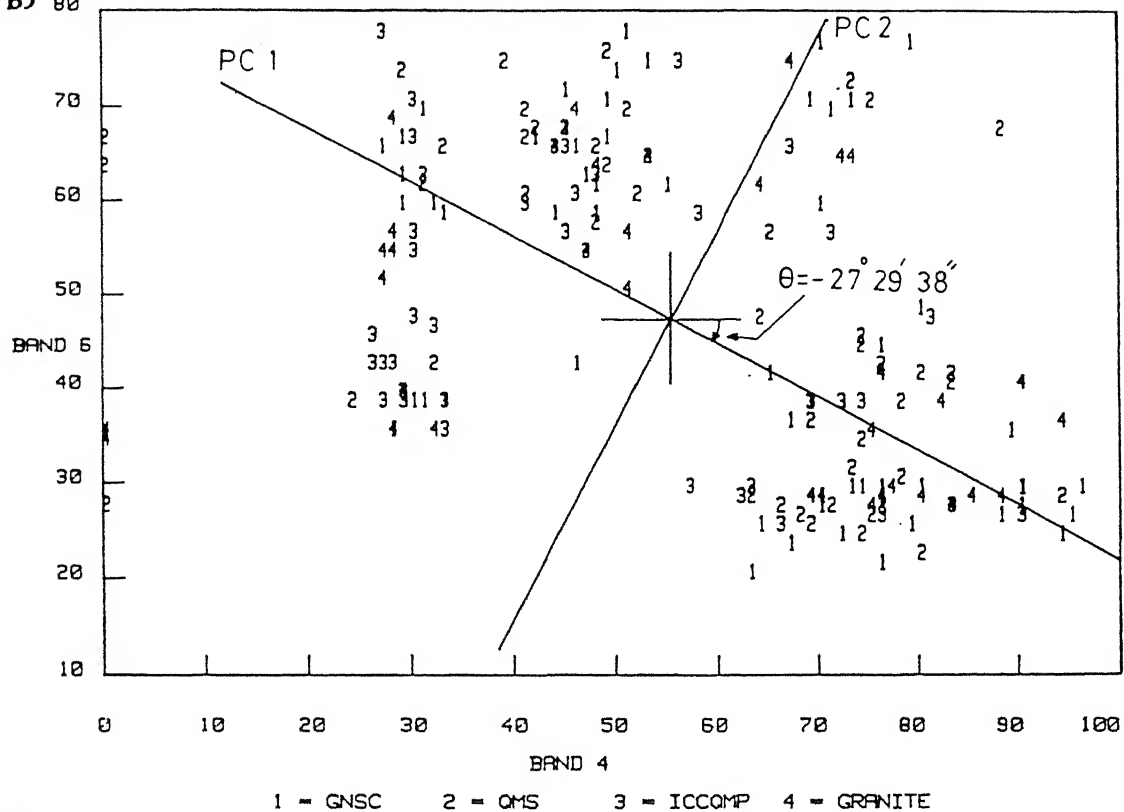


FIGURE 4.10 Scatter diagrams of the training reflectance values of the rocks of MSS area for 2-d principal component analysis in different MSS band pairs. In each scatter diagram, PC1 = Principal Component-1 and PC2 = Principal Component-2.

(b)



(c)

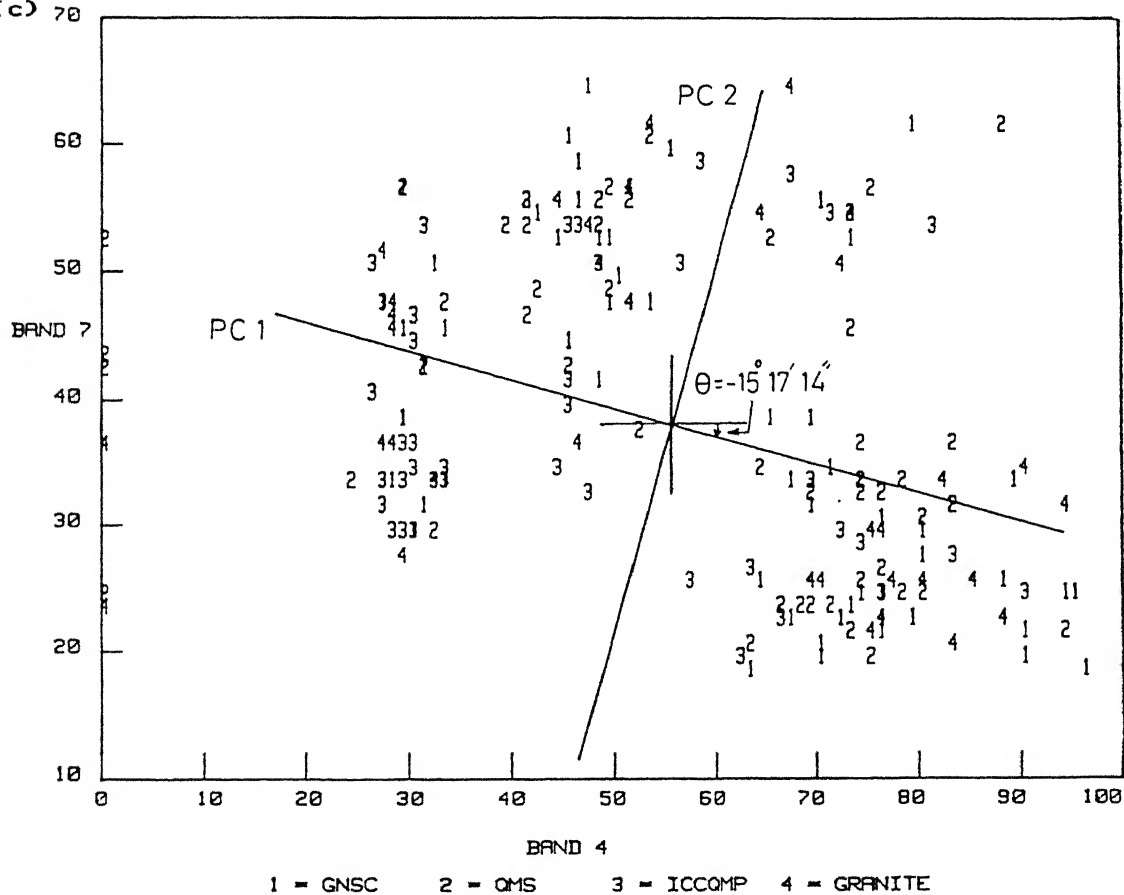


FIGURE 4.10 (continued)

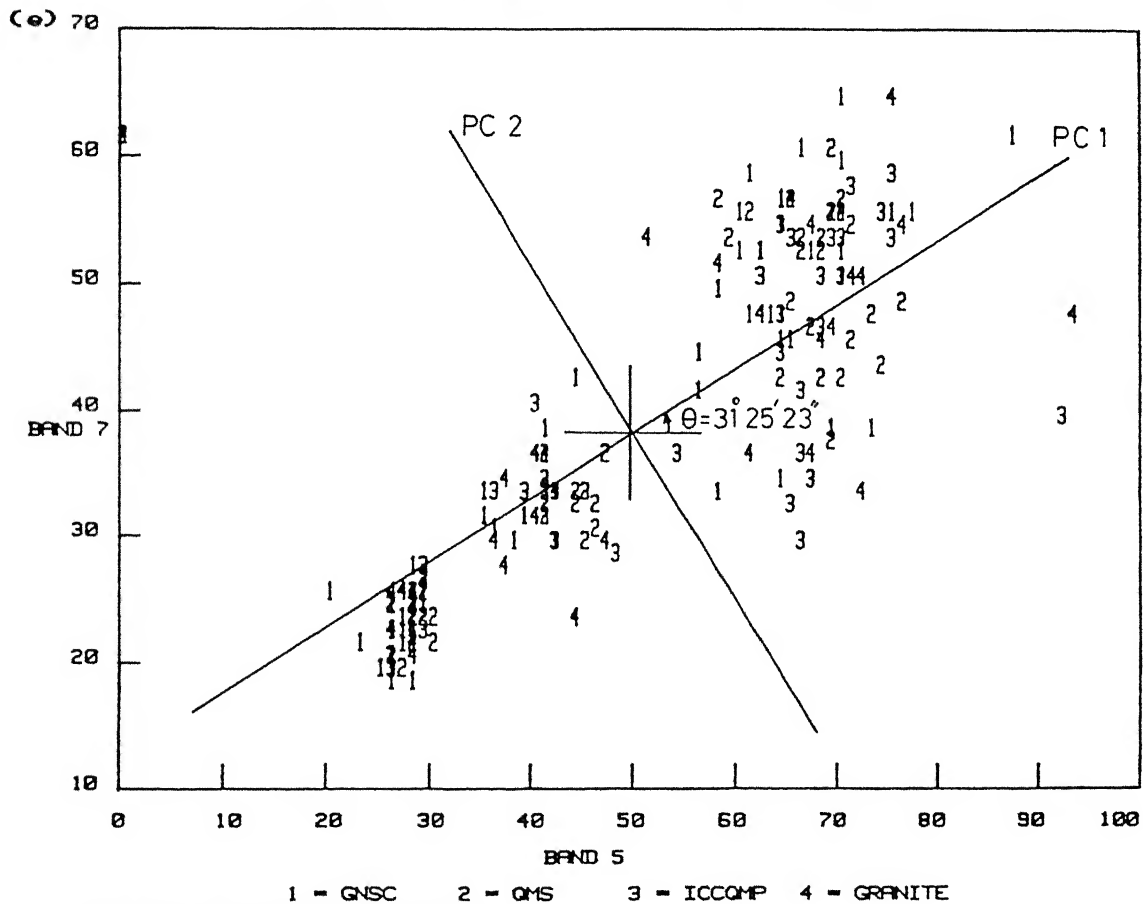
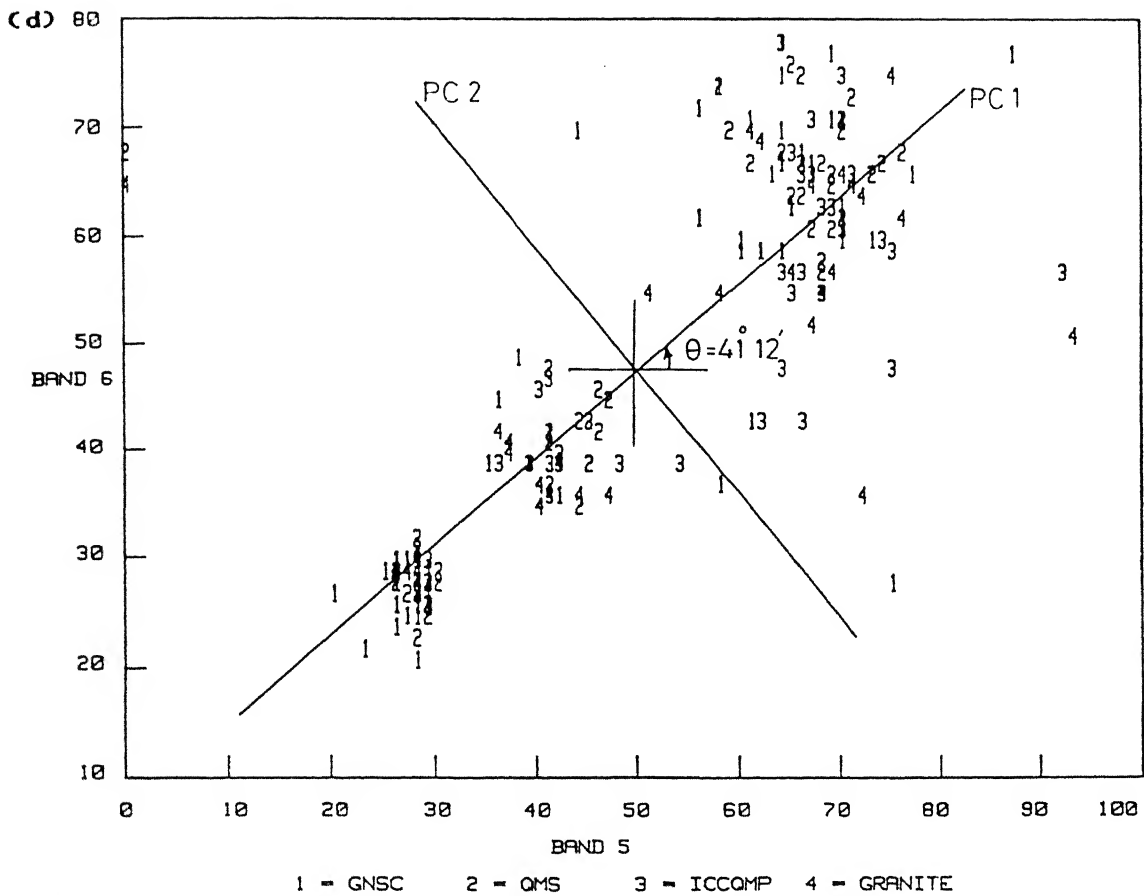


FIGURE 4.10 (continued)

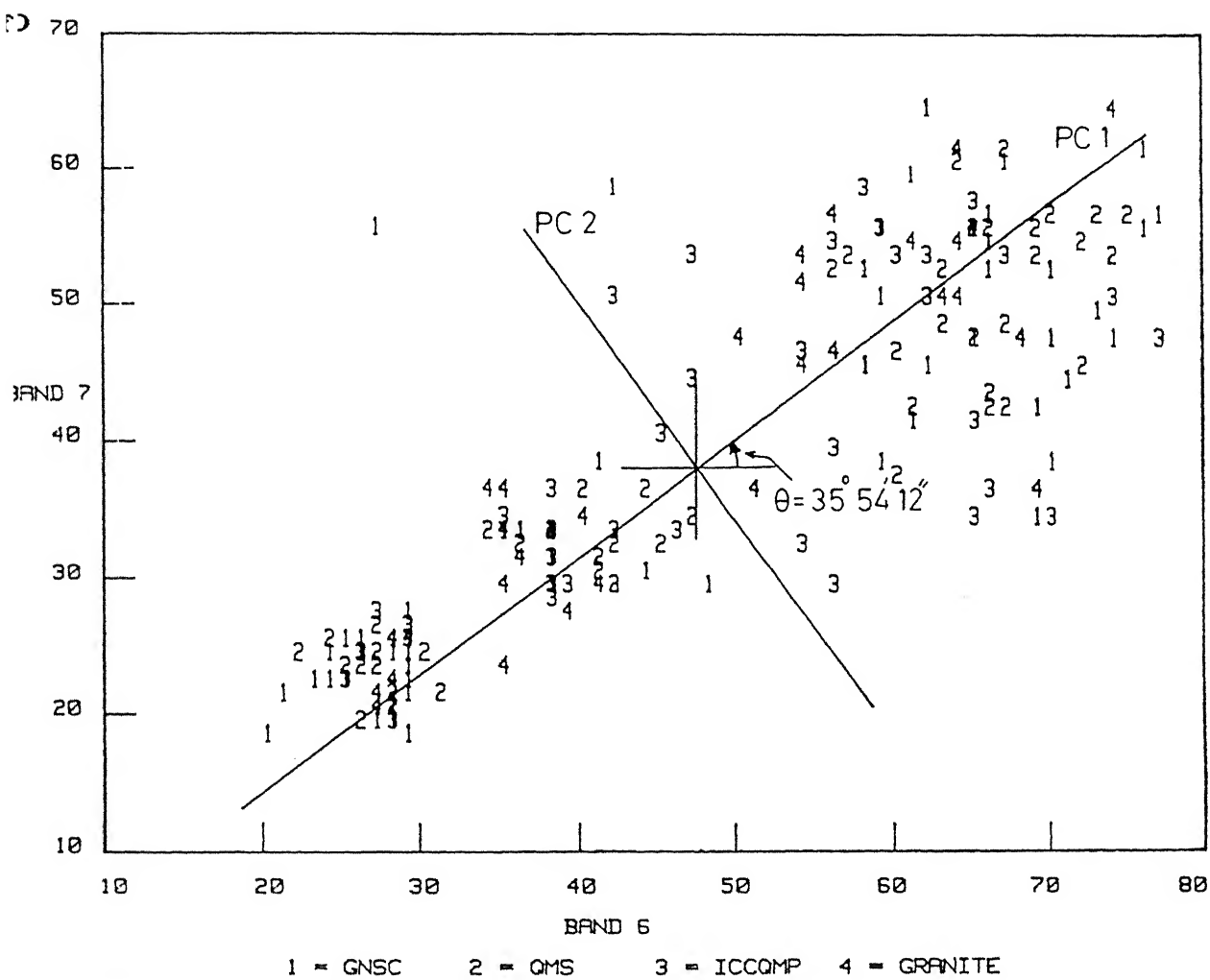


FIGURE 4.10 (continued)

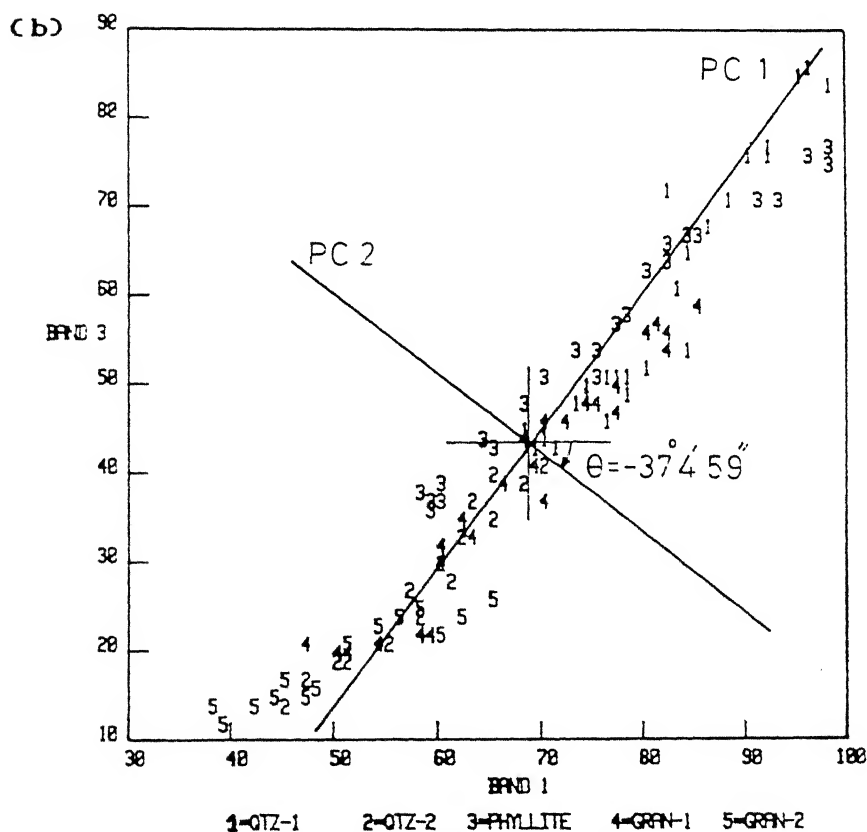
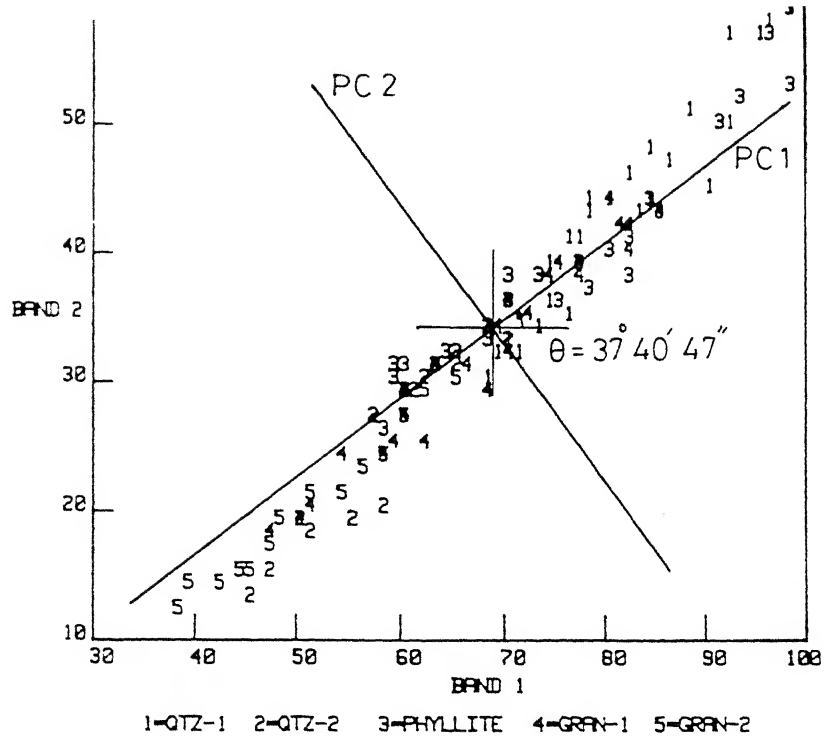


FIGURE 4.11 Scatter diagrams of the training reflectance values of the rocks of TM area for 2-d principal component analysis in different TM band pairs. In each scatter diagram, PC1 = Principal Component-1 and PC2 = Principal Component-2.

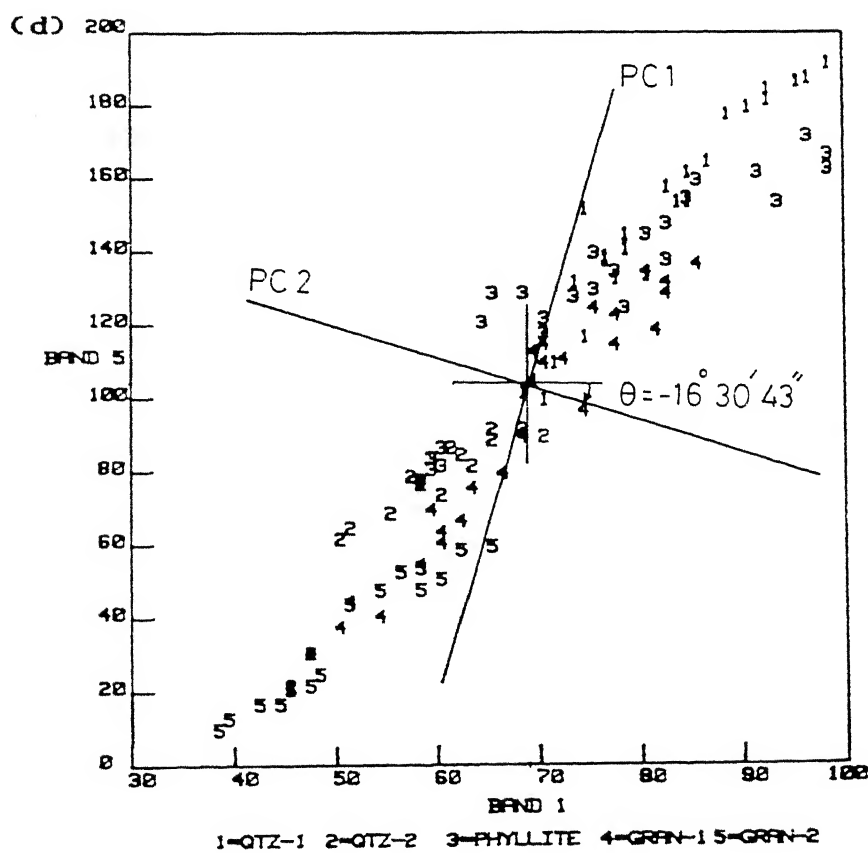
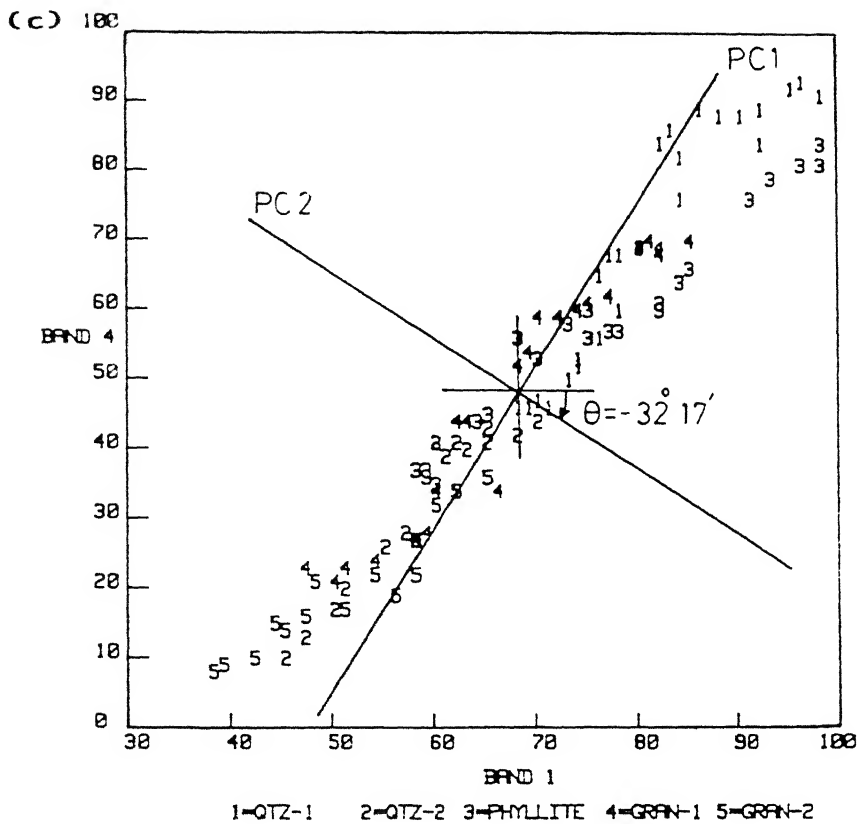


FIGURE 4.11 (continued)

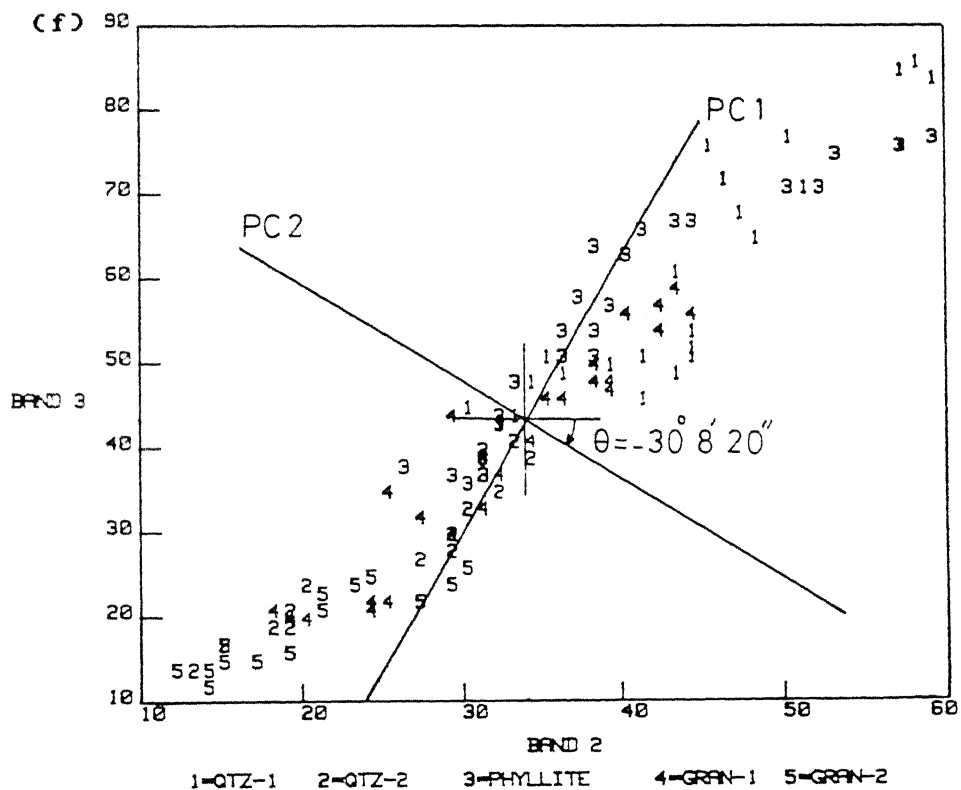
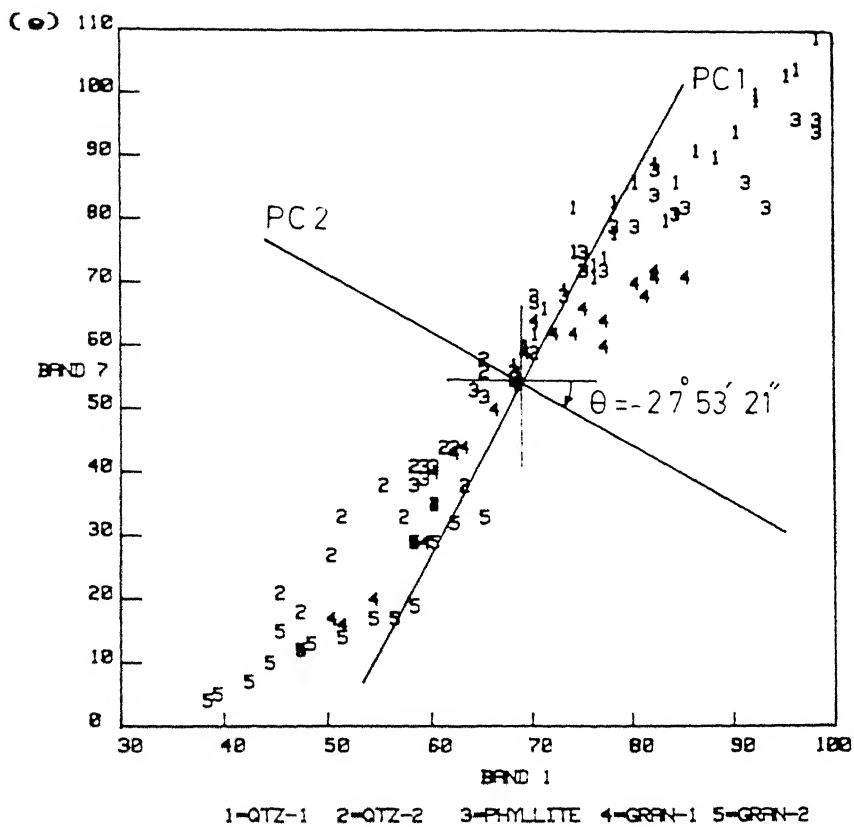


FIGURE 4.11 (continued)

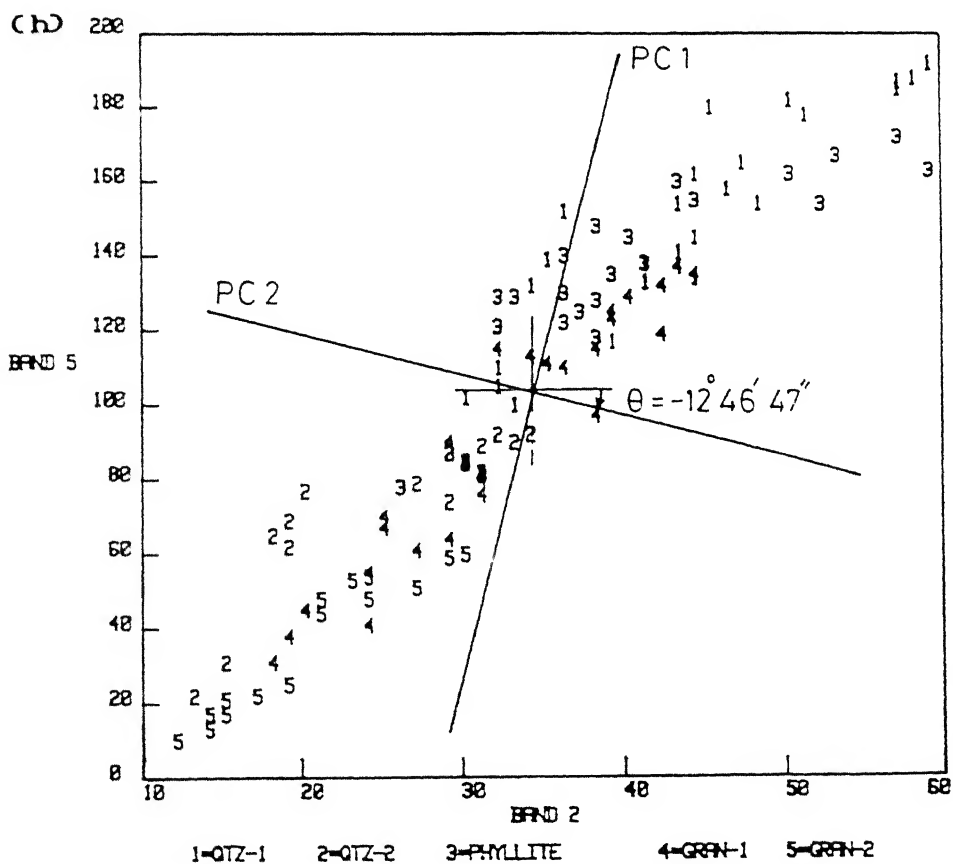
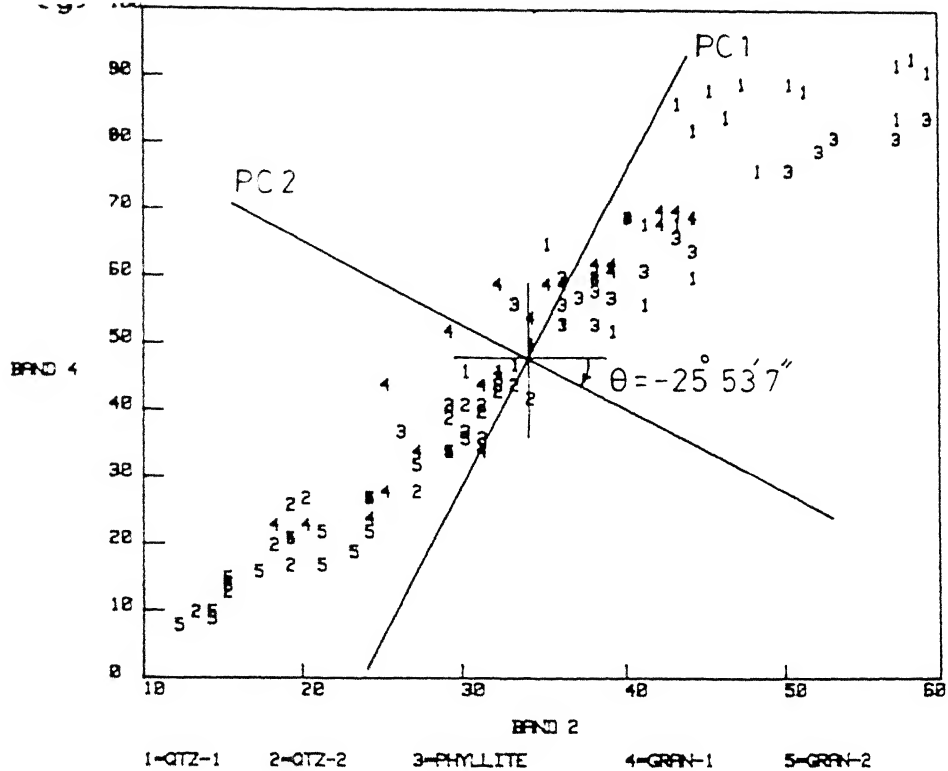


FIGURE 4.11 (continued)

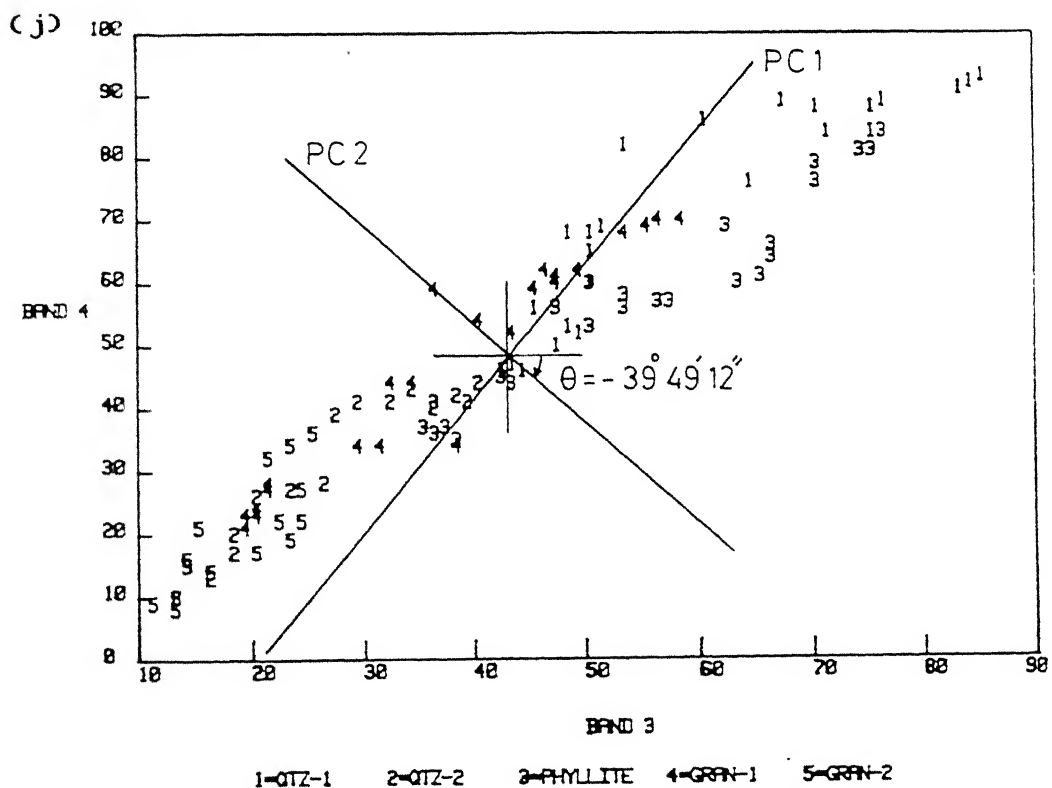
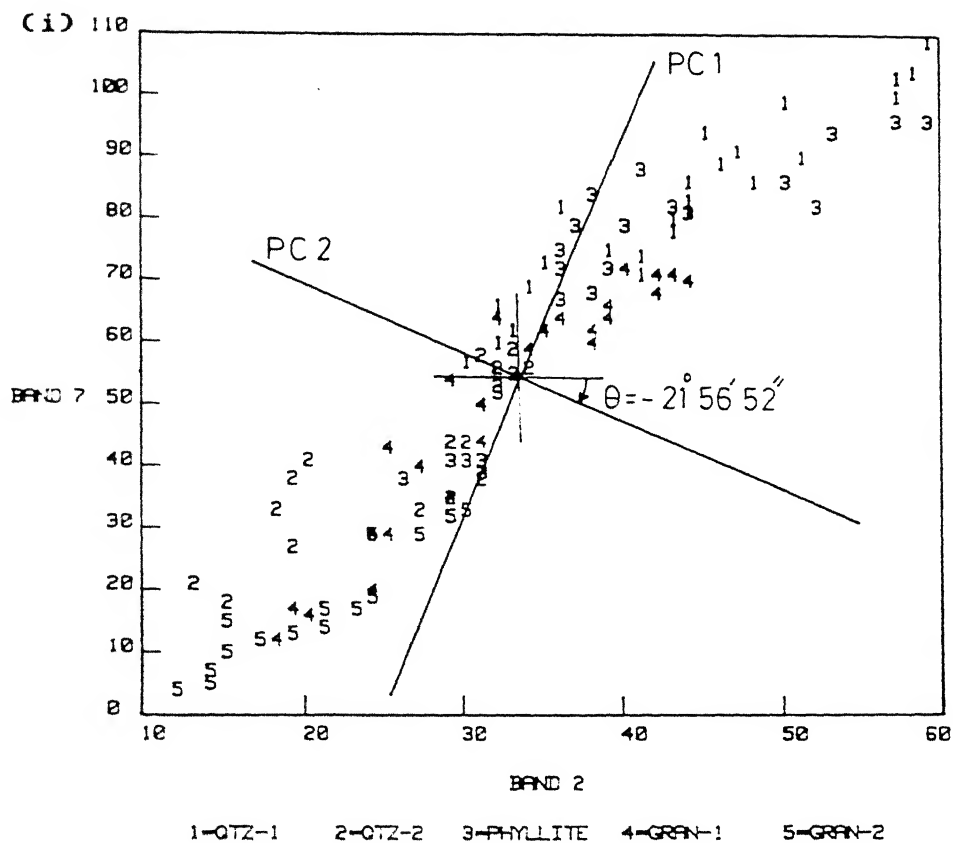


FIGURE 4.11 (continued)

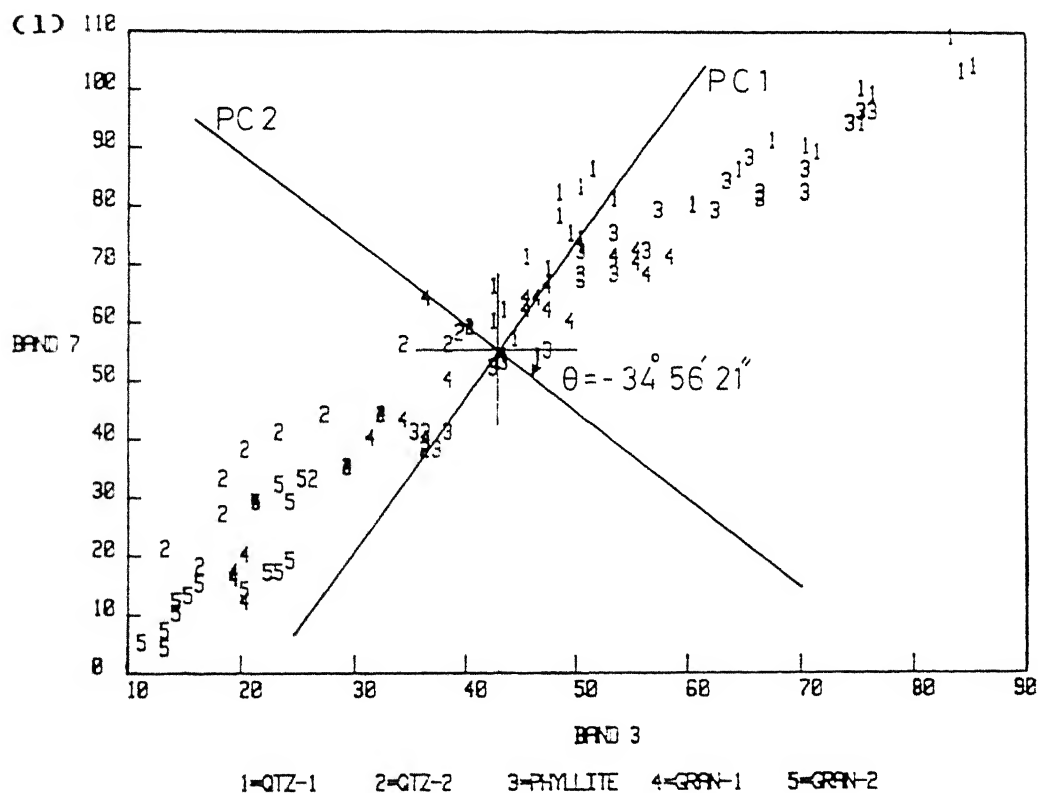
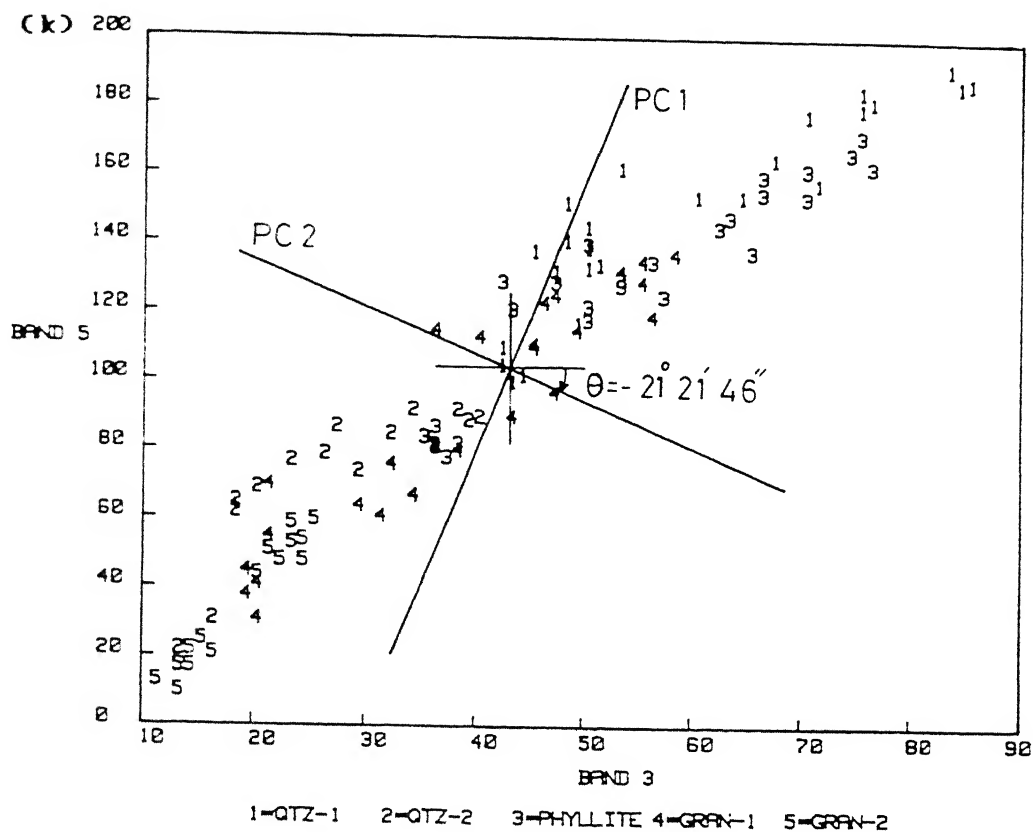


FIGURE 4.11 (continued)

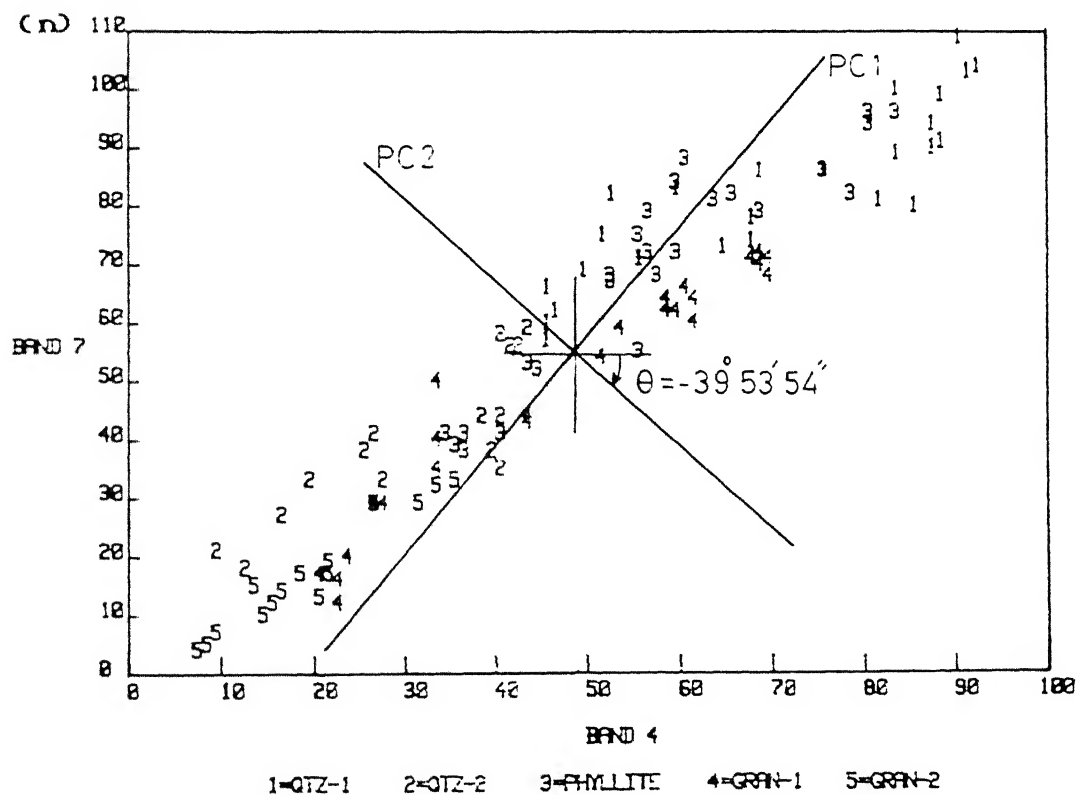
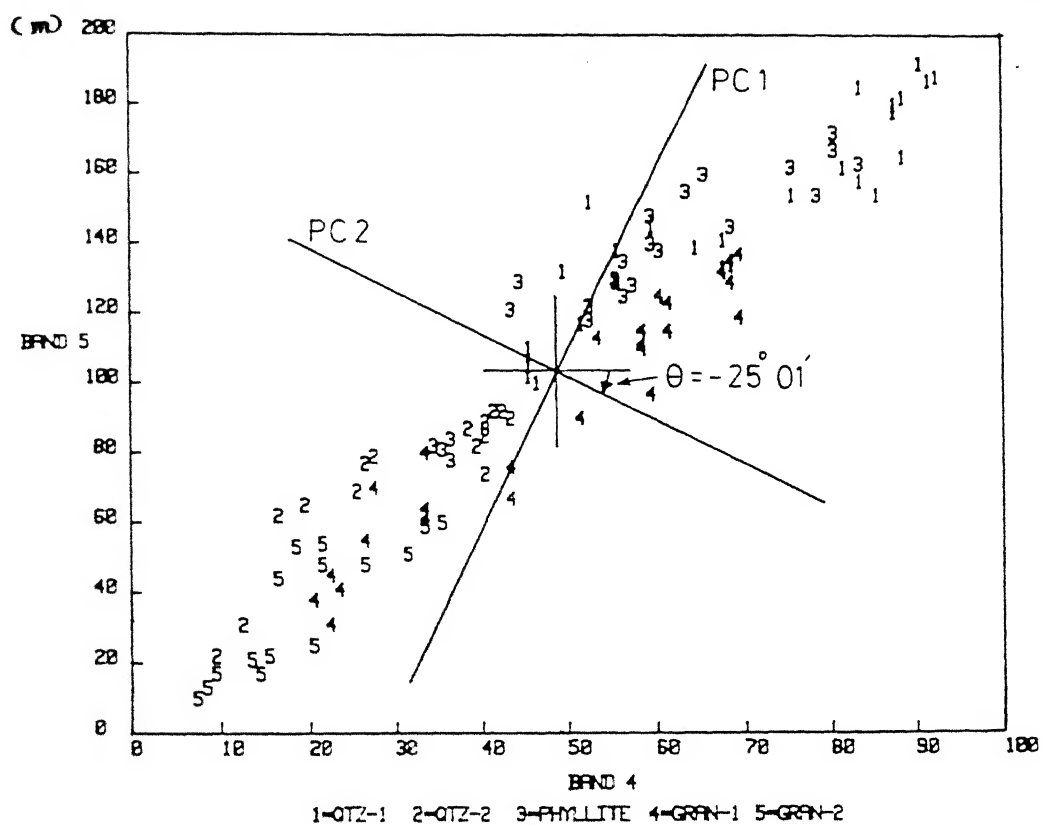


FIGURE 4.11 (continued)

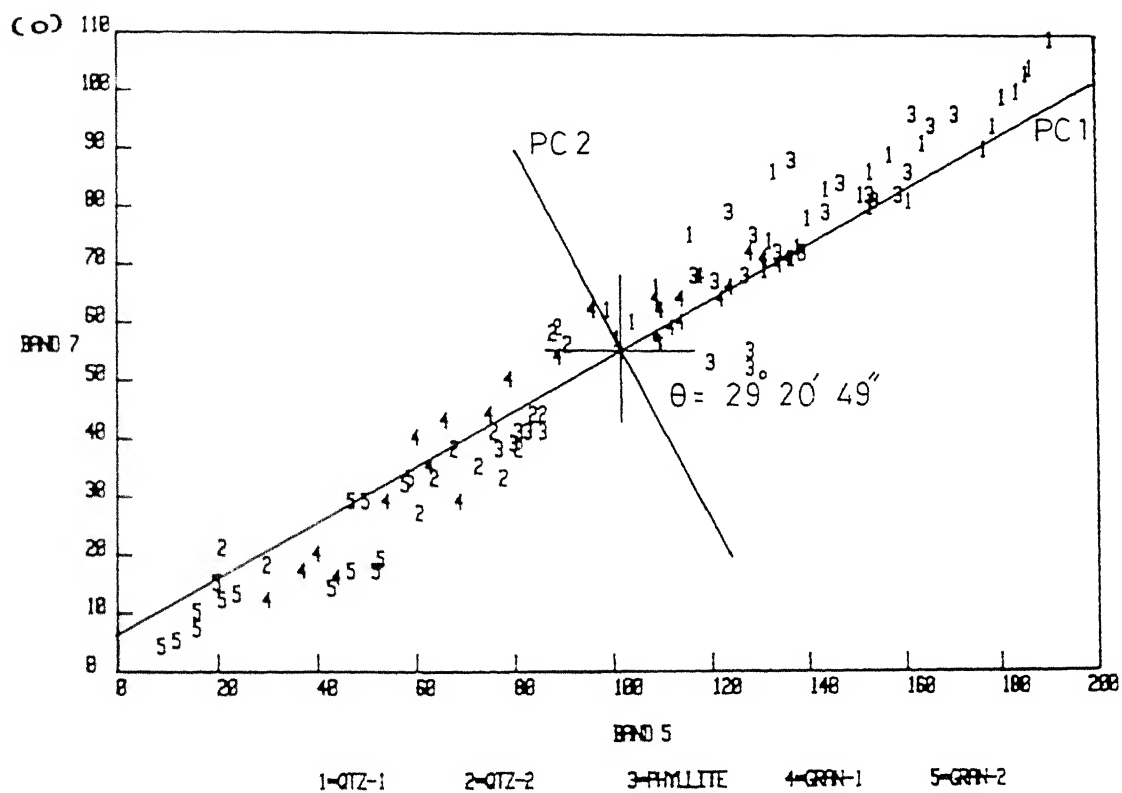


FIGURE 4.11 (continued)

of the scatter plots have been taken from Tables 5.4 and 5.5 for MSS and TM data respectively.

It may be observed that there is formation of distinct and well-defined clusters of the training pixels of the rocks of MSS area in the scatter plots of band pairs 4-5, 5-6, 5-7 and 6-7, whereas in the other two scatter diagrams defined by band pairs 4-6 and 4-7, the training data are distributed almost uniformly throughout the field. However, analysis of the clusters formed in the spectral pairs mentioned above reveals that none of them either represents or is clearly dominated by the training data of any particular rock type and instead, all of them are characterised preferably by nearly equal concentration of training pixels of invariably all the rock types. This situation signifies considerable spectral similarities of the rock types and hence, strong interband correlation. Moreover, examination of the scatter plots of band pairs 4-5, 5-6, 5-7 and 6-7, each of which comprises distinct and well-defined clusters, reveals that the PC1 in each of these plots passes through maximum number of clusters while PC2 lying orthogonal to PC1 passes through the least number of clusters. This observation indicates that PC1 accounts for the maximum variance of the distribution of training data sets while PC2, the minimum.

In contrast to the scatter plots of MSS data, the training data of rocks of TM area are elliptically distributed along the longer diagonal in the fields of invariably all pairs of TM spectral channels suggesting strong interband correlation (Figures 4.11a-o). Moreover, it may be seen that the training

data sets of different rock types do not form clusters in any of the scatter plots which is indicative of large variability of the rock types in different spectral pairs. However, unlike the scatter plots of MSS data which show random distribution of the training pixels of various rock types in the clusters, the TM training data of different rock types occupy definite sites in the elliptical scatters. For example, the training pixels of the illuminated portions of the quartzites (quartzite-1) are found to be distributed around the upper parts of the elliptical plots of all spectral pairs. In contrast, the non-illuminated portions of the quartzites and granites (i.e. quartzite-2 and granite-2 respectively) represent the lower portion of the plots because of their relatively low reflectance values.

Examination of the scatter diagrams also reveals that PC1 passes through the major axis of the elliptical plot in the scatter diagrams of bands 1-2 and 5-7, whereas in the scatter plots defined by other pairs of spectral channels, PC1 passes across the elliptical plot. The reversal in the orientation of PC1 with respect to the elliptical distribution of the training sets could be attributed to the negative angle of rotation in the scatter diagrams of the 13 pairs of spectral bands as against positive angles of rotation in the scatter fields of bands 1-2 and 5-7. In the present case, multivariate Principal Component Analysis (Table 5.5) shows that PC1 is accounted for by the maximum variance of the distribution as evident from its highest eigenvalue. Therefore, in order to represent the maximum variability of the distribution by PC1 on the scatter plots of

the training data sets, the two principal components have been mutually rotated so that PC1 occupies the original orientation of PC2 and vice versa. This also helps in preserving the symmetry of the components and the data set which is facilitated by the orthogonality of the two PCs. As a result, the PC1 passes very closely through the major axis of the elliptical plots in the scatter diagrams of band pairs 1-2, 1-3, 1-4, 3-4, 4-7 and 5-7, whereas in the scatter plots of the other TM band pairs, it significantly deviates from the major axis. This situation implies that in the scatter plots of the band pairs 1-2, 1-3, 1-4, 3-4, 4-7 and 5-7, PC1 accounts for considerable proportion of the total variability of the data set as a result of significant degree of interband decorrelation. In contrast, owing to weak interband decorrelation in the other pairs of TM spectral bands, the PC1 of the scatter plots of these band pairs may be regarded as being accountable to significantly very small variance of the distribution of the training data sets.

4.3.7 Discriminant Function Analysis (DFA)

The objective of Discriminant Function Analysis (DFA) is to define a line of division on the two-dimensional (i.e. 2 band) scatter diagram of the training samples of the two rock types in such an orientation that the field on one side of this line comprises most of the training pixels of any one rock type, whereas the field on other side of the line consists of most of the training pixels of the other rock type. The detailed procedure concerning the derivation of the orientation of this line is provided in section 2.3.2.4. Here is provided a thorough

discussion regarding the analysis and interpretation of the results of DFA of the rock types of MSS and TM areas. The scatter diagrams representing the least misclassification of the rocks in each rock pair of MSS area are shown in Figures 4.12-4.17 and for the rocks of TM area are shown in Figures 4.18-4.30. In each scatter diagram, also shown are the discriminant function (DF) line and the line of division. The bivariate means of the rock types, and the means and within-category variance-covariance matrix used in the estimation of ' α ' (that is, the slope of DF line) have been taken from Tables 5.4 and 5.5 for MSS and TM data respectively.

4.3.7.1 Discriminant Function Analysis for Rocks of MSS Area

A total of four pairs of spectral channels have been chosen for DFA of the rocks of MSS area on the basis of the observation of presence of distinct and well-defined clusters in the scatter diagrams of Principal Component Analysis (Figures 4.10a-f). The spectral pairs selected for analysis are MSS bands 4-5, 5-6, 5-7, and 6-7. However, in order to acquire a thorough understanding about the degree of discrimination among the various rock types, all possible pairs of rock types have been considered for analysis, namely GNSC-QMS, GNSC-ICCQMP, GNSC-Granite, QMS-ICCQMP, QMS-Granite, and ICCQMP-Granite.

The results of discriminant function analysis for the various rock pairs of MSS area are presented in Table 4.1. It may be observed from this table that the rocks of MSS area have comparably equal pixel concentration (i.e. percentage of training pixels of each rock is equal) on either side of the line of

Table 4.1 (Contd.)

N. B. :

- (a) These represent the pixel concentration of respective rocks on that side of the line of division where at least one rock type is dominant.
- (b) The probability of intermixing or misclassification of both the rock types has been determined by taking the average of their pixel percentages when both rocks dominate on the same side of the line of division. However, when only one rock type is dominant on one side and the other on the other side, the probability of intermixing is determined by estimating the probability of misclassification of the less dominant rock in the field of the more dominant rock, on both sides of the line of division and then averaging the sum of their probabilities. For example, in the scatter diagram of GNSC-ICCQMP in the field of bands 4 and 5, ICCQMP has 63 percent of its observations in association with 49 percent of observations of GNSC on one side of line of division. Since in this case, each of these two rocks dominates on different sides of line of division, the probability that GNSC samples will be misclassified as ICCQMP on the side where the latter dominates is equal to 49 percent, whereas on the other side of the line of division the probability that ICCQMP is misclassified as GNSC is equal to 37 percent ($100-63=37$). Hence the average probability of their intermixing or misclassification will be $(49+37)/2$ or 43 percent.

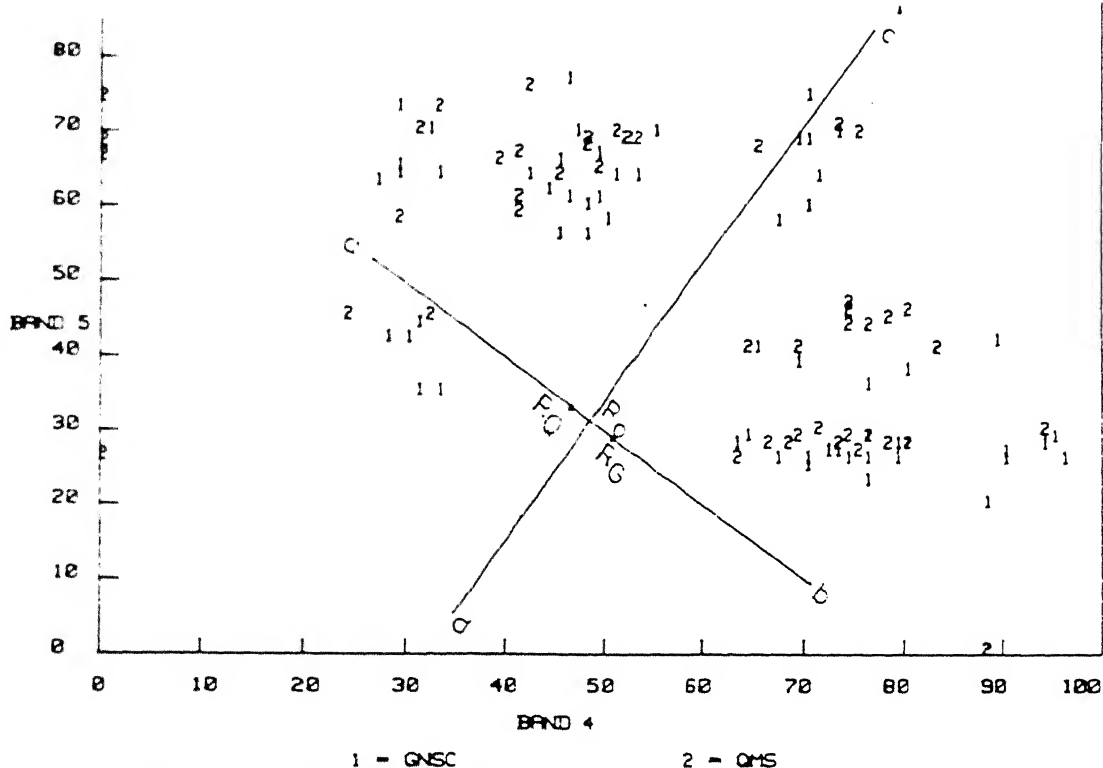


FIGURE 4.12 Scatter diagram for discriminant function analysis of Gneiss schist (GNSC) and Quartz mica schist (QMS). ab = discriminant function (DF) line, cd = line of division, R_G , R_Q = projections of bivariate means of GNSC and QMS on DF line respectively. R_0 = discriminant index, half way between R_G and R_Q .

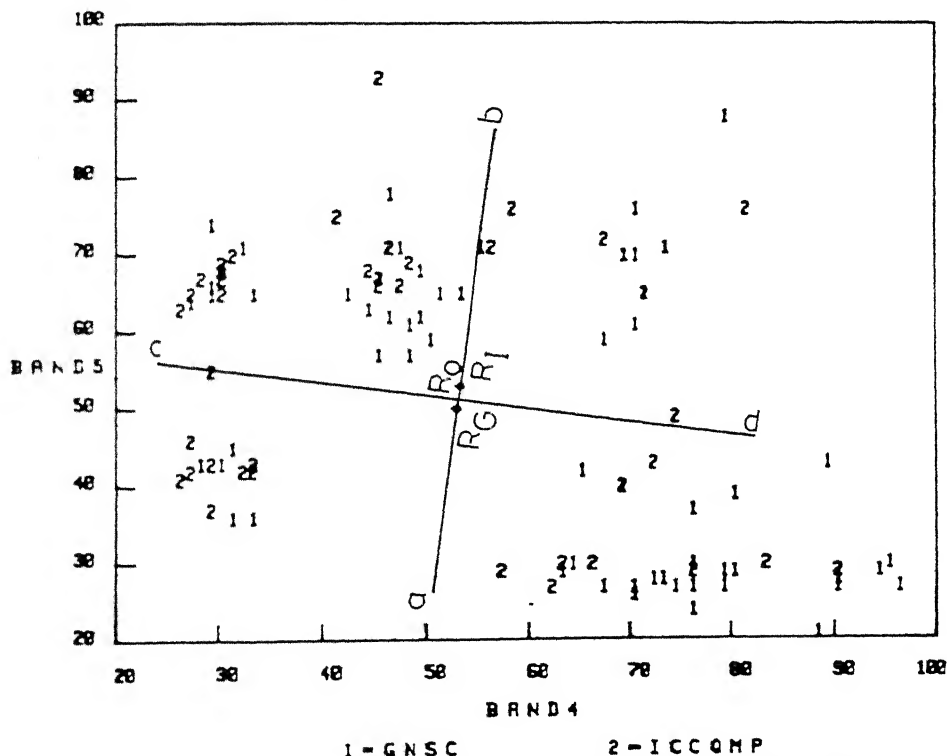
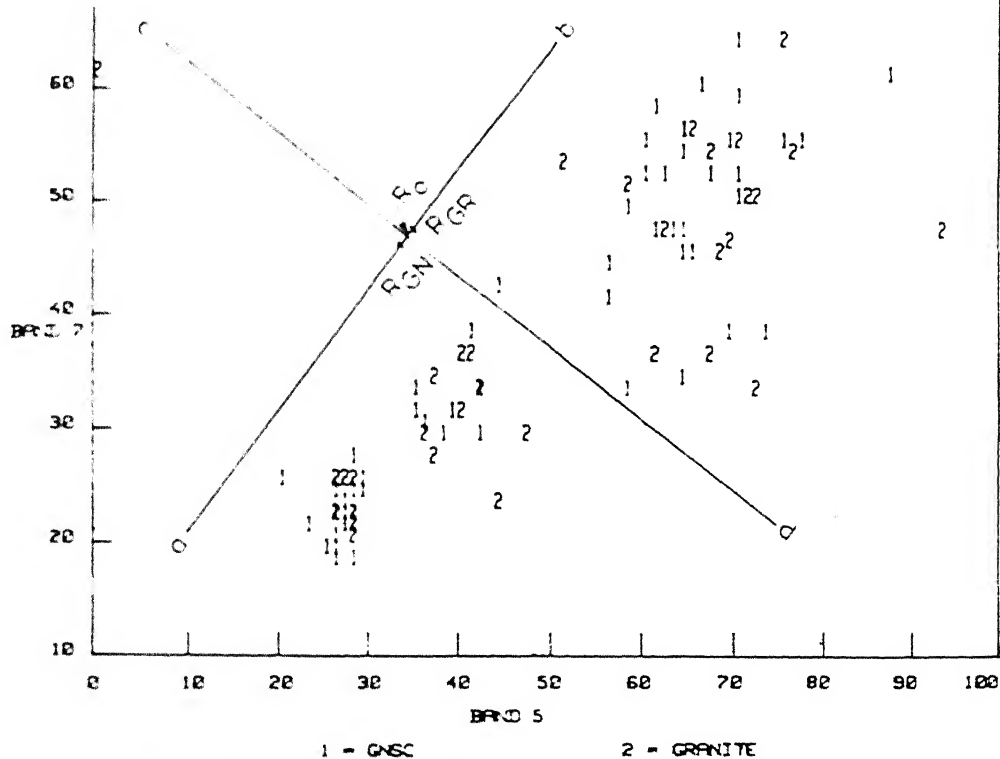
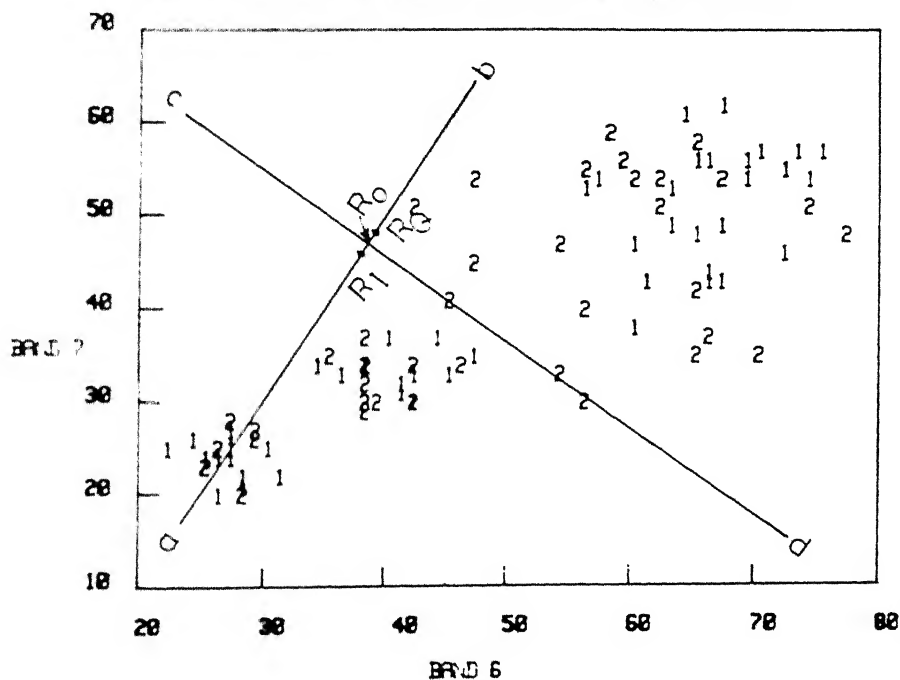


FIGURE 4.13 Scatter diagram for discriminant function analysis of Gneiss schist (GNSC) and Intercalated calc and cherty quartzite marble phyllite (ICCOMP). ab = discriminant function (DF) line, cd = line of division, R_G , R_I = projections of bivariate means of GNSC and ICCOMP on DF line respectively. R_0 = discriminant index, half way between R_G and R_I .



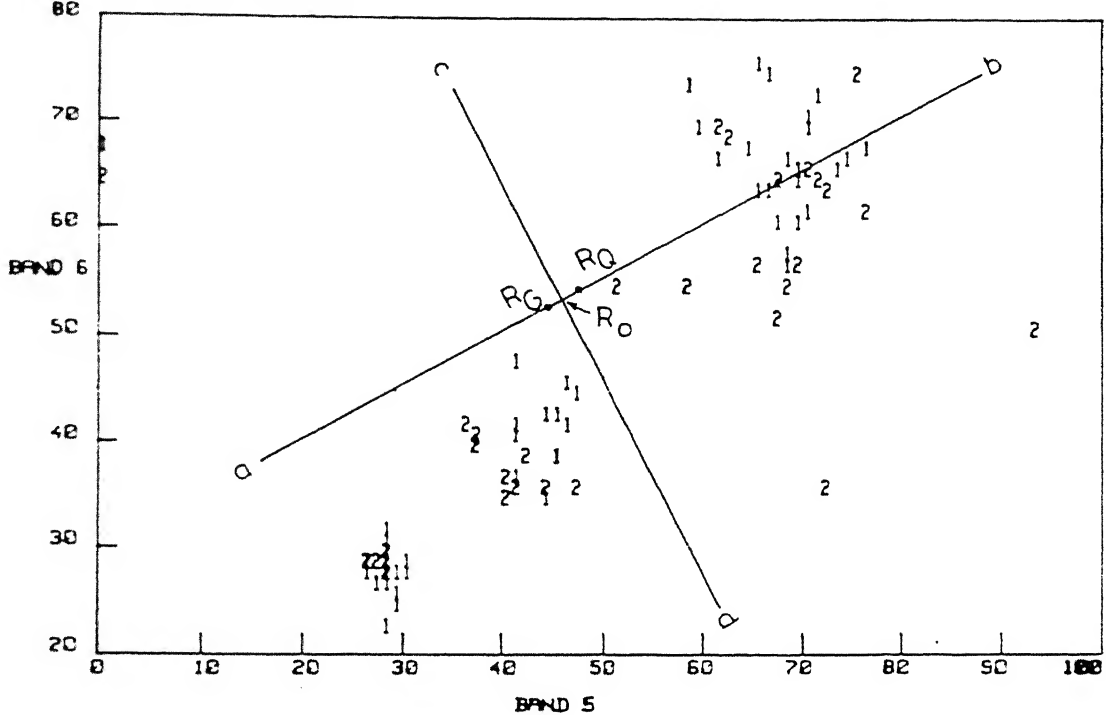
1 - GNSC 2 - GRANITE

FIGURE 4.14 Scatter diagram for discriminant function analysis of Gneiss schist (GNSC) and Granite. ab = discriminant function (DF) line, cd = line of division, R_{GN} , R_{GR} = projections of bivariate means of GNSC and Granite on DF line respectively. R_0 = discriminant index, half way between R_{GN} and R_{GR} .



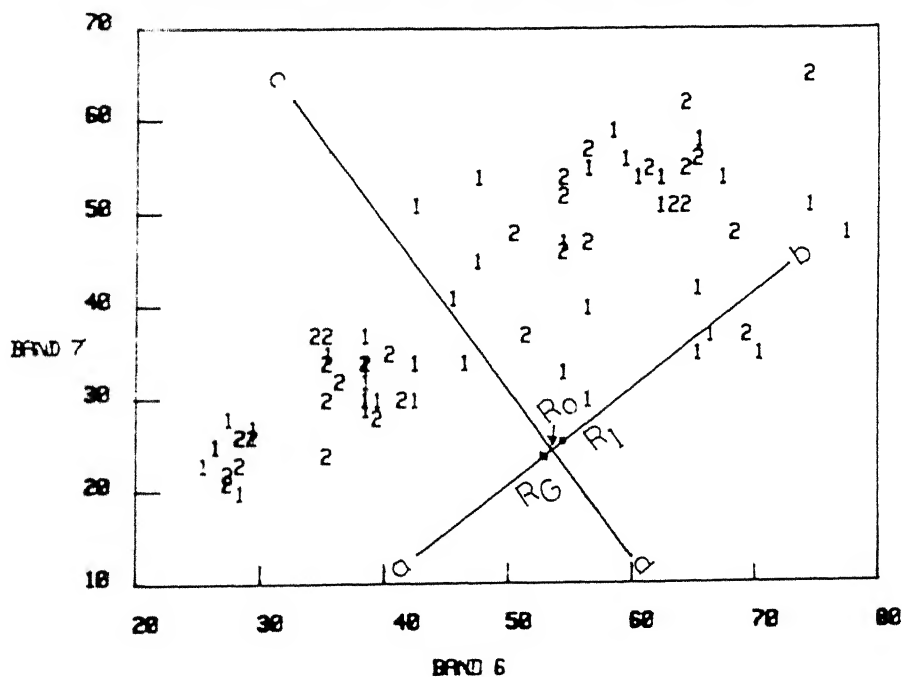
1 - QMS 2 - ICCOMP

FIGURE 4.15 Scatter diagram for discriminant function analysis of Quartz mica schist (QMS) and Intercalated calc and cherty quartzite marble phyllite (ICCOMP). ab = discriminant function (DF) line, cd = line of division, R_Q , R_I = projections of bivariate means of GNSC and ICCOMP on DF line respectively. R_0 = discriminant index, half way between R_Q and R_I .



1 = QMS 2 = GRANITE

FIGURE 4.16 Scatter diagram for discriminant function analysis of Quartz mica schist (QMS) and Granite. ab=discriminant function (DF) line, cd = line of division, R_Q , R_G = projections of bivariate means of QMS and Granite on DF line respectively. R_0 = discriminant index, half way between R_G and R_Q .



1 = ICCOMP 2 = GRANITE

FIGURE 4.17 Scatter diagram for discriminant function analysis of Intercalated calc and cherty quartzite marble phyllite (ICCOMP) and Granite. ab = discriminant function (DF) line, cd = line of division, R_I , R_G = projections of bivariate means of ICCOMP and Granite on DF line respectively. R_0 = discriminant index, half way between R_I and R_G .

division. This observation is significantly in contrast to the objective of DFA as mentioned earlier. The results obtained from the present analysis therefore signify^a considerable extent of intermixing or misclassification of the various rock types of MSS area.

The considerable degree of misclassification or intermixing of the rock types of the MSS area is found to be in close agreement with the inferences made from the coincident spectral plots of the rocks in the sense that the latter also depict^a significant amount of spectral overlap of the rocks in different MSS bands as shown in Figure 4.3. The misclassification of the rocks may be explained by the occurrence of identical spectral slopes in the laboratory-derived diffused reflectance spectra of their respective rock samples as discussed earlier in Chapter 3. The misclassification could also be attributed to the high interband correlation induced, to a considerable extent, by selecting the training pixels of the rock types without giving any consideration to the spatial variation of their reflectance as a result of variation in illumination conditions induced by topography.

4.3.7.2 Discriminant Function Analysis for Rocks of Thematic Mapper Area

The discriminant function analysis for the rocks of Thematic Mapper area has been carried out by taking into consideration the brightness variation of rocks induced by the rough surface topography of the study area. As mentioned earlier in section 4.2, owing to ridge-like outcrop pattern of the

quartzitic rocks and uneven nature of the granitic terrain, each of these two litho-units has been represented as two different and separate litho-units corresponding to their illuminated and non-illuminated portions. As a result, the five litho-units that are finally considered for analysis are : (i) quartzite-1, (ii) quartzite-2, (iii) phyllites, (iv) granite-1, and (v) granite-2 where the suffixes 1 and 2 represent the illuminated and non-illuminated portions respectively.

In the scatter plots for discriminant function analysis, quartzite-1, granite-1 and phyllites have been represented each by 25 training samples, whereas quartzite-2 and granite-2 each has been represented by 15 training samples. A total of 13 pairs of rock types have been considered for discriminant function analysis in order to evaluate the spectral discrimination between different rocks. On the other hand, six pairs of spectral channels have been considered for generating the scatter plots of the different rock pairs such as TM band pairs 1-5, 1-7, 3-4, 3-7, 4-7 and 5-7. The probability of intermixing or misclassification in various rock pairs has been estimated following the same procedure as described under DFA of MSS data and are presented in Table 4.2.

4.3.7.2.1 Rock Pair : Quartzite-1 - Quartzite-2

The discriminant function analysis of the rock pair quartzite-1 - quartzite-2 shows that the field on one side of the line of division is represented by about 80-100 percent of the samples of quartzite-1 while its remaining samples are associated with all the 15 training observations of quartzite-2

le 4.2 Results of Discriminant Function Analysis for Rocks of
TM Areas

Rock Pair : Quartzite-1 - Quartzite-2

Band Pairs	Quartzite-1 misclassified as Quartzite-2 (%)	Quartzite-2 misclassified as Quartzite-1 (%)	Average degree of intermixing (%)
1-5	12	13	12.5
1-7	8	-	4
3-4	-	-	-
3-7	12	-	6
4-7	20	-	10
5-7	16	-	8

Rock Pair : Quartzites-Phyllites

Rock Pair :
Quartzite-1 - Phyllites

(b) Rock Pair :
Quartzite-2 - Phyllites

Band Pairs	Average degree of intermixing (%)	Band Pairs	Phyllites misclassi- fied as Quartzite-2 (%)	Quartzite-2 misclassified as Phyllites (%)	Average degree of intermixing (%)
1-5	40	1-5	28	6	17
1-7	72	1-7	28	-	14
3-4	56	3-4	20	-	10
3-7	56	3-7	24	13	18.5
4-7	32	4-7	28	13	20.5
5-7	38	5-7	20	-	10

Rock Pair : Quartzites (Quartzite-1 + Quartzite-2) - Phyllites

Band Pairs	Average degree of intermixing (%)
1-5	55
1-7	44
3-4	36
3-7	43.8
4-7	42.5
5-7	41

Table 4.2 (Contd.)

Table 4.2 (Contd.)

c) Rock Pair : Phyllites - Granites

Rock Pair :
Phyllites - Granite-1(b) Rock Pair :
Phyllites - Granite-2

Band Pairs	Phyllites misclassified as Granite-1 (%)	Granite-1 misclassified as Phyllites (%)	Average degree of inter-mixing (%)	Band Pairs	Phyllites misclassified as Granite-2 (%)	Average degree of inter-mixing (%)
1-5	36	36	36	1-5	20	10
1-7	28	40	34	1-7	16	8
3-4	36	44	40	3-4	16	8
3-7	32	44	38	3-7	20	16.5*
4-7	32	50	41	4-7	16	8
5-7	24	48	36	5-7	20	10

* Granite-2 is misclassified as Phyllites by 13 percent.

Rock Pair : Phyllites - Granites (Granite-1 + Granite-2)

Band Pairs	Phyllites misclassified as Granites (%)	Granites misclassified as Phyllites (%)	Average degree of intermixing (%)
1-5	20	33	26.5
1-7	20	32.5	26.25
3-4	16	42.5	29.25
3-7	24	27.5	25.75
4-7	28	33	30.5
5-7	20	27.5	23.75

(IV) Rock Pair : Quartzites - Granites
(Quartzite-1 + Quartzite-2) (Granite-1 + Granite-2)(a) Rock Pair :
Quartzite-1 - Granite-1

Band Pairs	Average degree of intermixing (%)
1-5	66
1-7	18
3-4	34
3-7	22
4-7	28
5-7	18

Table 4.2 (Contd.)

Table 4.2 (Contd.)

(b) Rock Pair : Quartzite-1 - Granite-2
No misclassification is observed
between these two litho-units
in any band pair.

(c) Rock Pair :
Quartzite-2 - Granite-1

(d) Rock Pair :
Quartzite-2 -
Granite-2

Band Pairs	Quartzite-2 misclassified as Granite-1 (%)	Granite-1 misclassified as Quartzite-2 (%)	Average degree of intermixing (%)	Band Pairs	Average degree of intermixing (%)
1-5	26.7	40	33.35	1-5	17
1-7	26.7	40	33.35	1-7	27
3-4	33.3	36	34.65	3-4	23
3-7	33.3	32	32.65	3-7	23.3
4-7	33.3	36	34.65	4-7	27
5-7	26.7	40	33.35	5-7	13.3

(e) Rock Pair : Quartzites (Quartzite-1 + Quartzite-2) -
Granites (Granite-1 + Granite-2)

Band Pairs	Average degree of intermixing (%)
1-5	33
1-7	33
3-4	32.5
3-7	27.5
4-7	38
5-7	35

(V) Rock Pair : Granite-1 - Granite-2

Band Pairs	Granite-1 misclassified as Granite-2 (%)	Granite-2 misclassified as Granite-1 (%)	Average degree of intermixing (%)
1-5	20	13.3	16.65
1-7	24	13.3	18.65
3-4	24	-	12
3-7	24	-	12
4-7	16	13.3	14.65
5-7	20	-	10

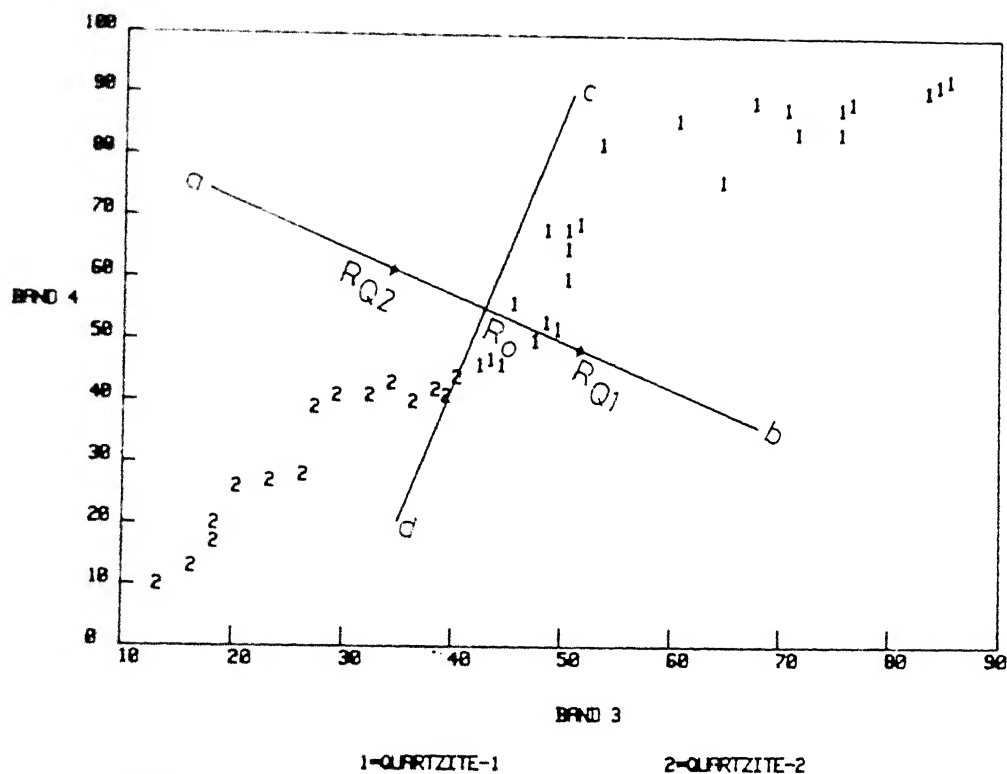


FIGURE 4.10 Scatter diagram for discriminant function analysis of Quartzite-1 (Qtz-1) and Quartzite-2 (Qtz-2). ab = discriminant function (DF) line, cd = line of division, R_{Q1} , R_{Q2} = projections of bivariate means of Qtz-1 and Qtz-2 on DF line respectively. R_0 = discriminant index, half way between R_{Q1} and R_{Q2} .

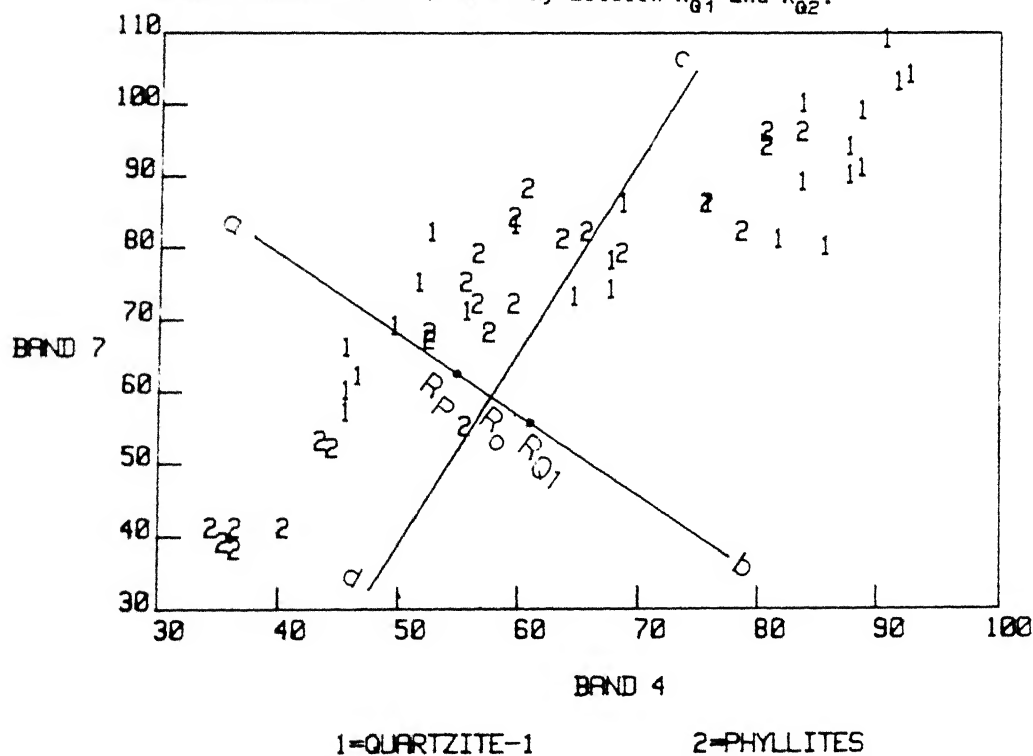


FIGURE 4.10 Scatter diagram for discriminant function analysis of Quartzite-1 (Qtz-1) and Phyllite. ab = discriminant function (DF) line, cd = line of division, R_{Q1} , R_p = projections of bivariate means of Qtz-1 and Phyllite on DF line respectively. R_0 = discriminant index, half way between R_{Q1} and R_p .

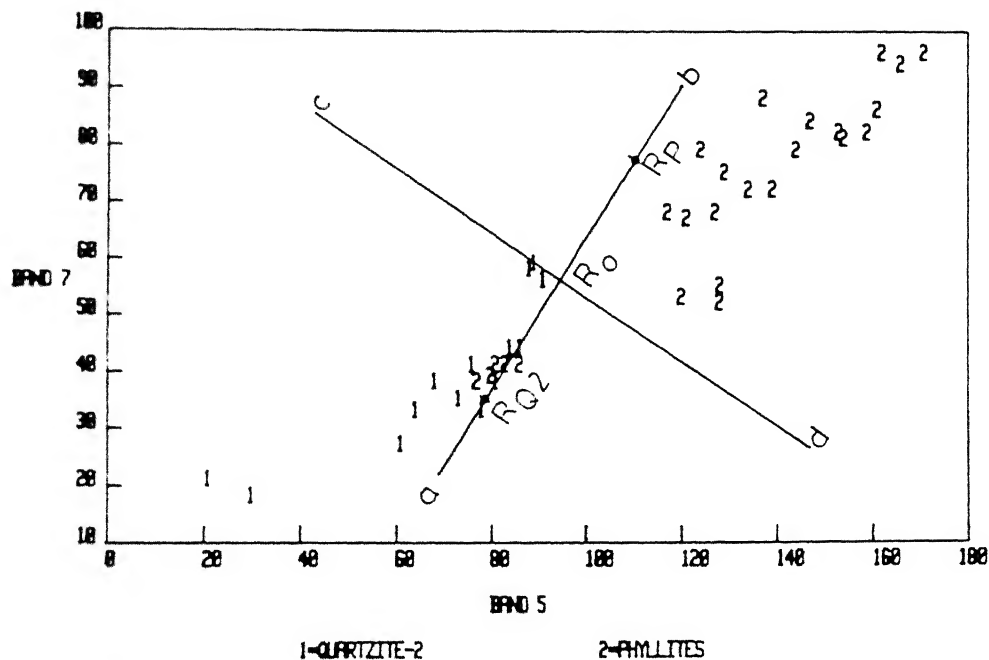


FIGURE 4.20 Scatter diagram for discriminant function analysis of Quartzite-2 (Qtz-2) and Phyllite. ab = discriminant function (DF) line, cd = line of division, R_{Q2} , R_P = projections of bivariate means of Qtz-2 and Phyllite on DF line respectively. R_0 = discriminant index, half way between R_{Q2} and R_P .

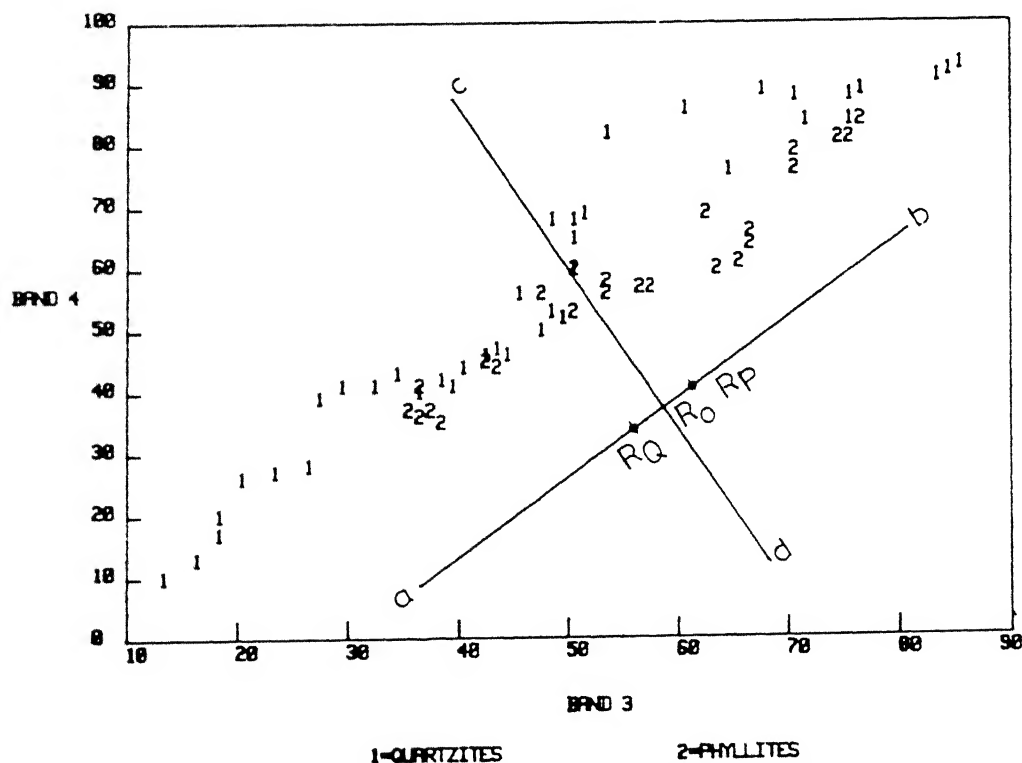


FIGURE 4.21 Scatter diagram for discriminant function analysis of Quartzite (Qtz) and Phyllite. ab = discriminant function (DF) line, cd = line of division, R_Q , R_P = projections of bivariate means of Qtz and Phyllite on DF line respectively. R_0 = discriminant index, half way between R_Q and R_P .

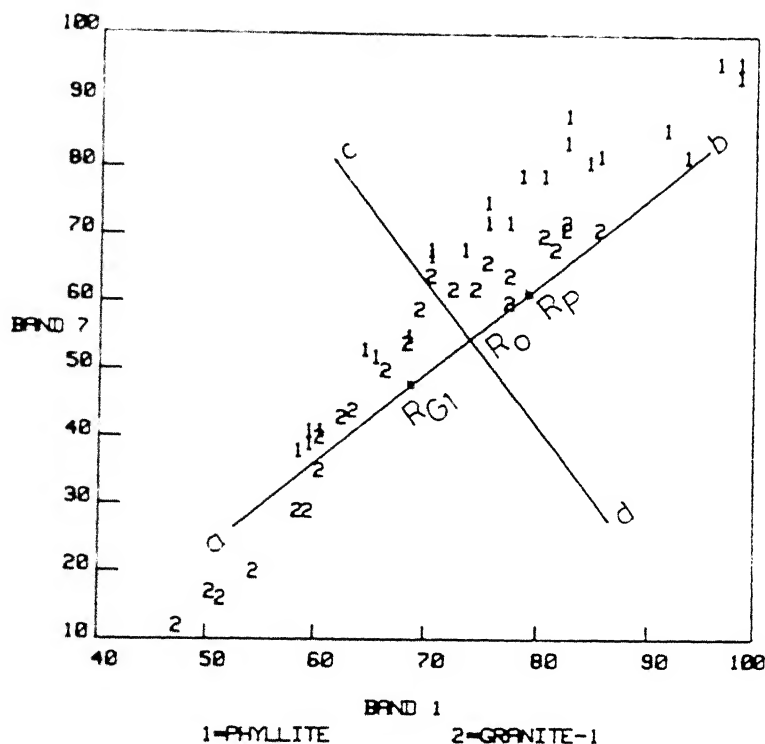


FIGURE 4.22 Scatter diagram for discriminant function analysis of Phyllite and Granite-1 (Gran-1). ab = discriminant function (DF) line, cd = line of division, R_P , R_{G1} = projections of bivariate means of Phyllite and Gran-1 on DF line respectively. R_0 = discriminant index, half way between R_P and R_{G1} .

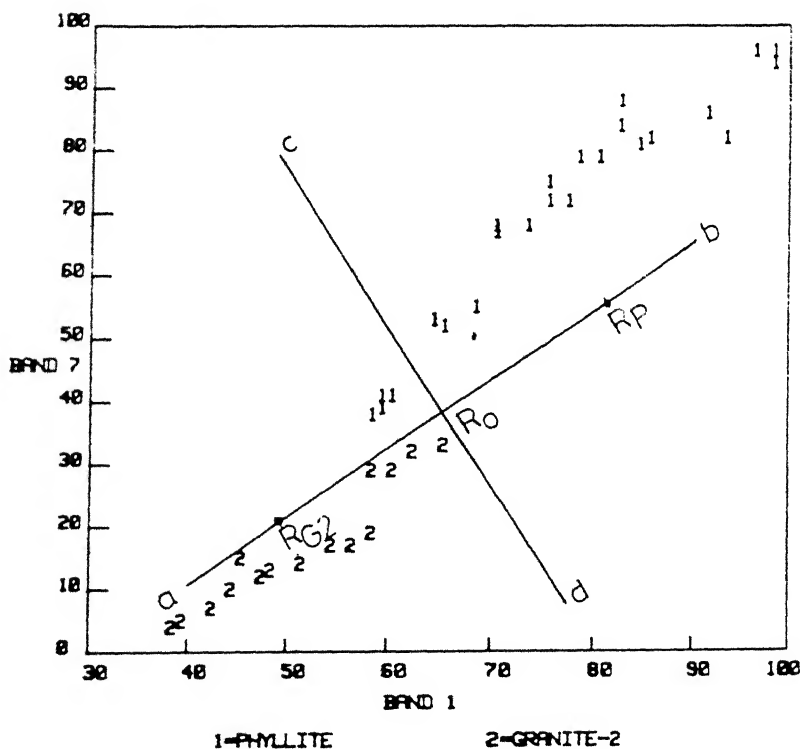
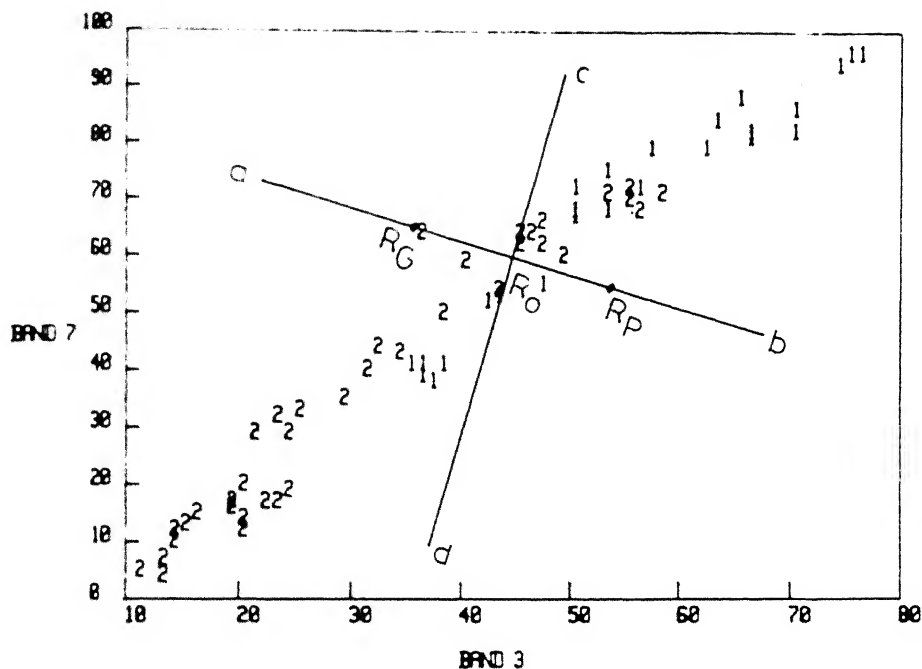


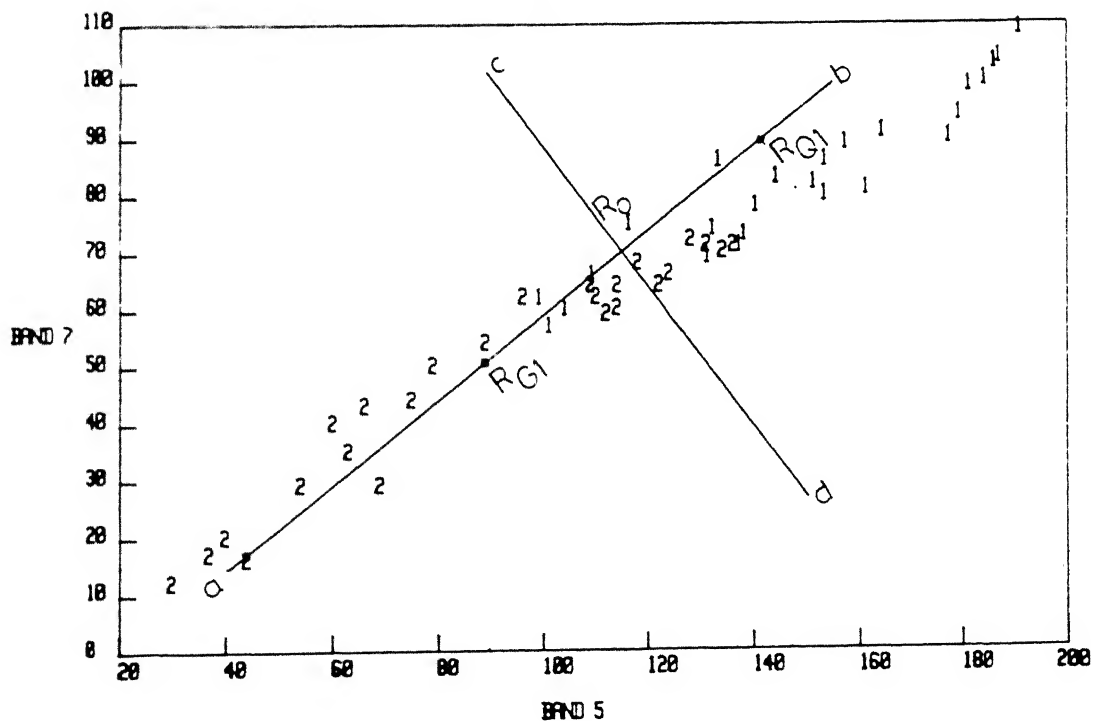
FIGURE 4.23 Scatter diagram for discriminant function analysis of Phyllite and Granite-2 (Gran-2). ab = discriminant function (DF) line, cd = line of division, R_P , R_{G2} = projections of bivariate means of Phyllite and Gran-2 on DF line respectively. R_0 = discriminant index, half way between R_P and R_{G2} .



1-PHYLLITES

2-GRANITES

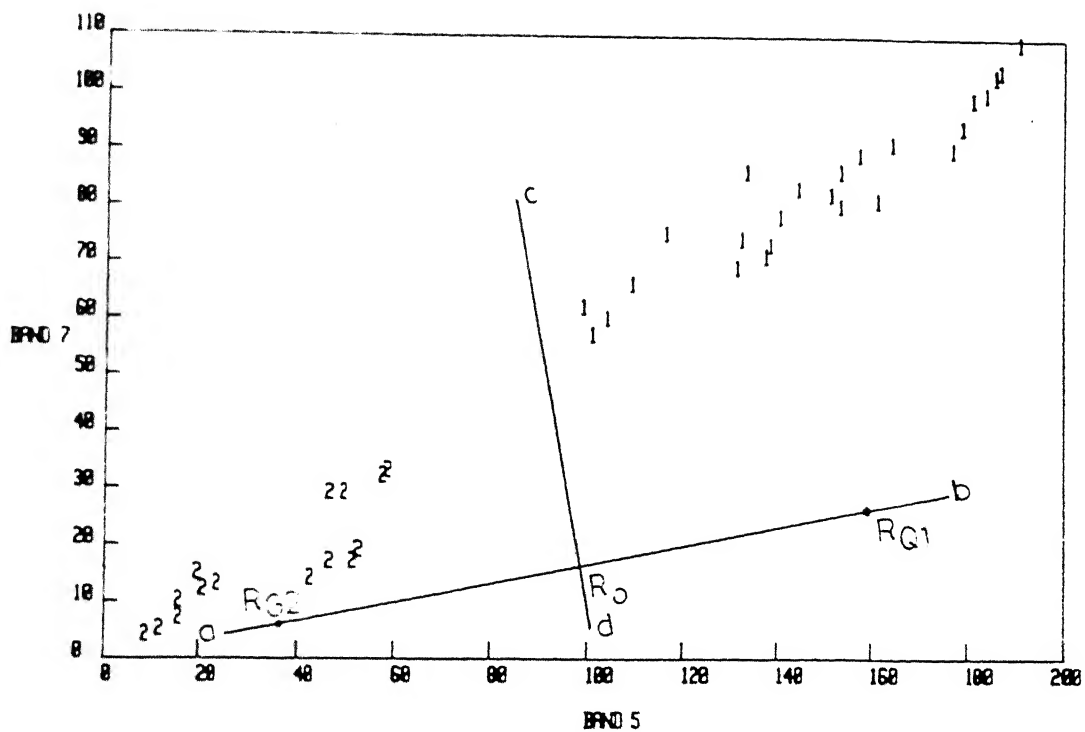
FIGURE 4.24 Scatter diagram for discriminant function analysis of Phyllite and Granite. ab = discriminant function (DF) line, cd = line of division, R_P , R_G = projections of bivariate means of Phyllite and Granite on DF line respectively. R_O = discriminant index, half way between R_P and R_G .



1-QUARTZITE-1

2-GRANITE-1

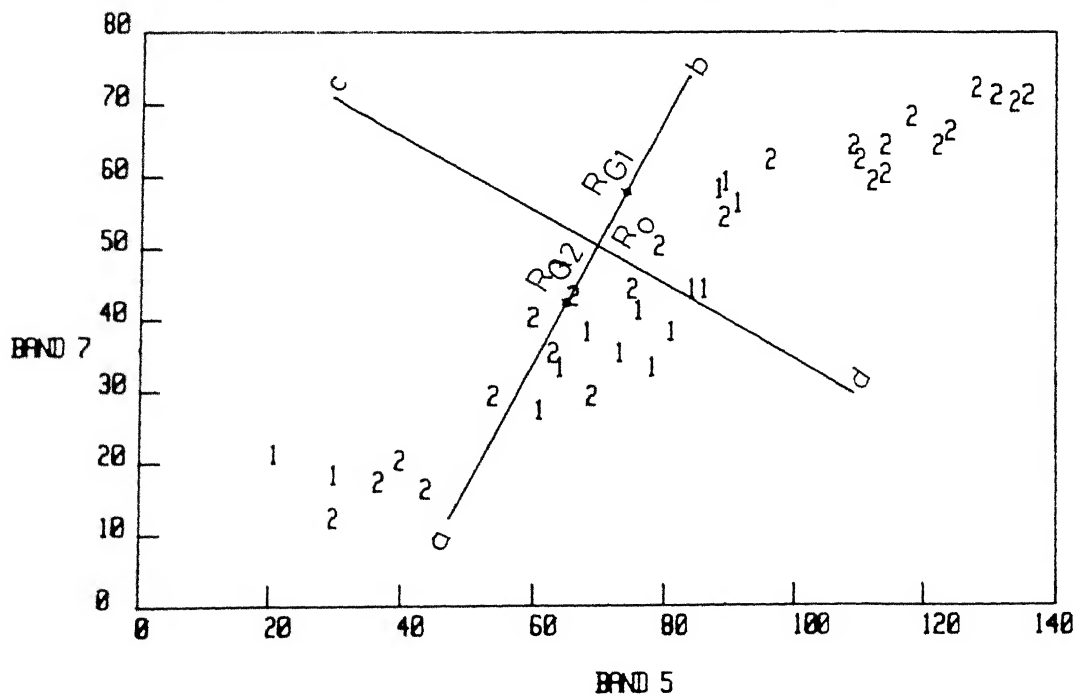
FIGURE 4.25 Scatter diagram for discriminant function analysis of Quartzite-1 (Qtz-1) and Granite-1 (Gran-1). ab = discriminant function (DF) line, cd = line of division, R_{Q1} , R_{G1} = projections of bivariate means of Qtz-1 and Gran-1 on DF line respectively. R_O = discriminant index, half way between R_{Q1} and R_{G1} .



1=QUARTZITE-1

2=GRANITE-2

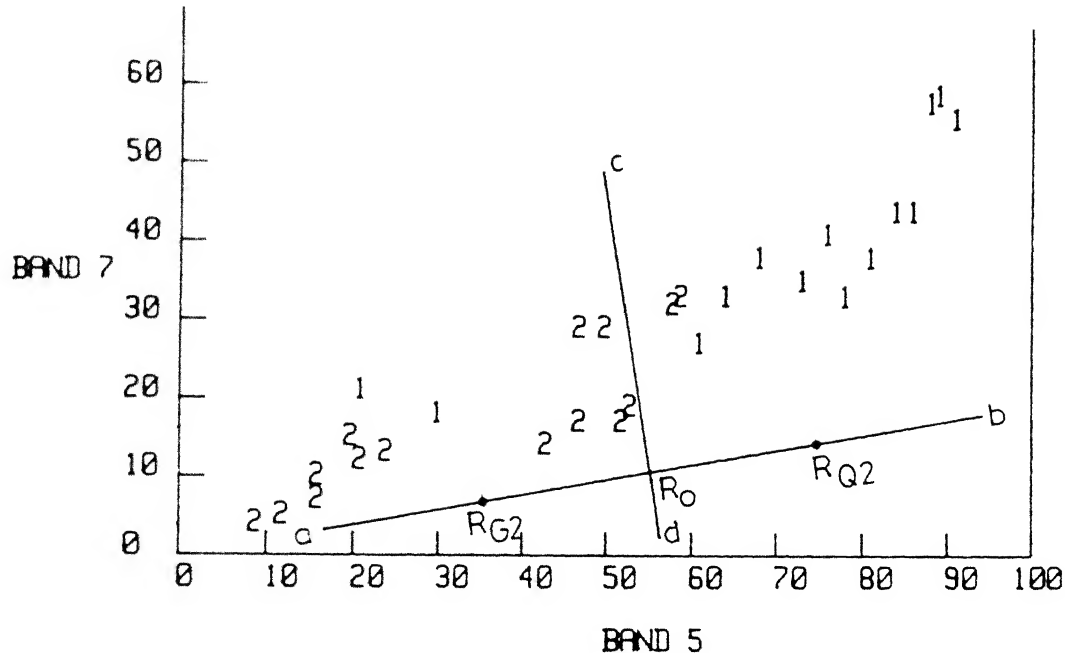
FIGURE 4.26 Scatter diagram for discriminant function analysis of Quartzite-1 (Qtz-1) and Granite-2 (Gran-2). ab = discriminant function (DF) line, cd = line of division, R_{G1} , R_{G2} = projections of bivariate means of Qtz-1 and Gran-2 on DF line respectively. R_0 = discriminant index, half way between R_{G1} and R_{G2} .



1=QUARTZITE-2

2=GRANITE-1

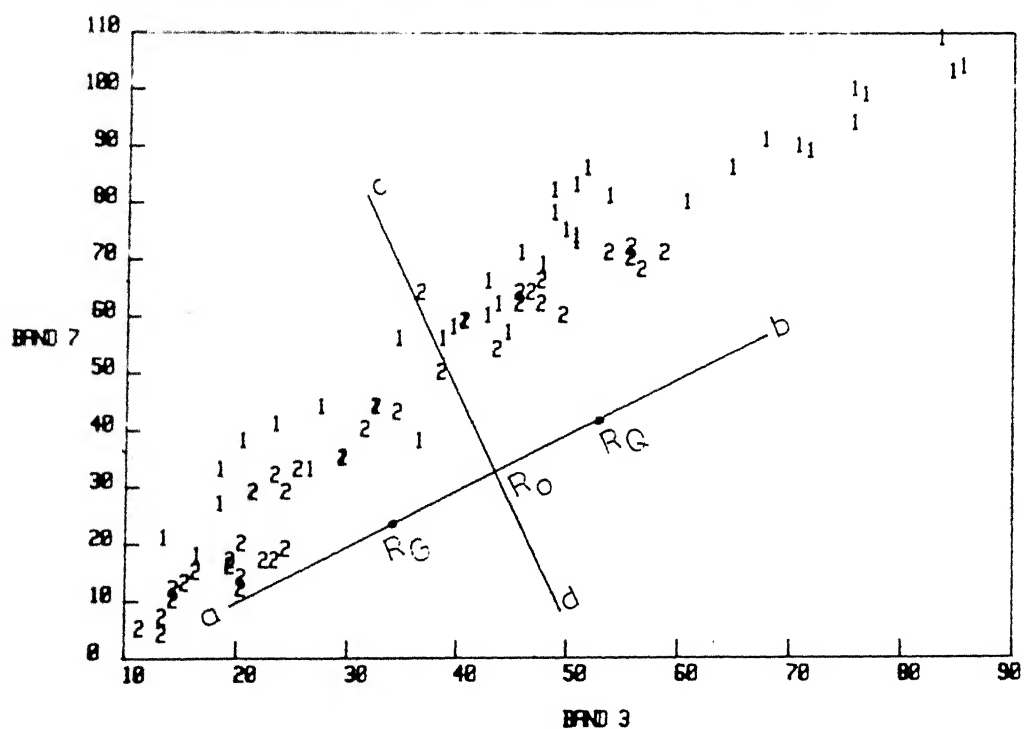
FIGURE 4.27 Scatter diagram for discriminant function analysis of Quartzite-2 (Qtz-2) and Granite-1 (Gran-1). ab = discriminant function (DF) line, cd = line of division, R_{G2} , R_{G1} = projections of bivariate means of Qtz-2 and Gran-1 on DF line respectively. R_0 = discriminant index, half way between R_{G2} and R_{G1} .



1=QUARTZITE-2

2=GRANITE-2

FIGURE 4.28 Scatter diagram for discriminant function analysis of Quartzite-2 (Qtz-2) and Granite-2 (Gran-2). ab = discriminant function (DF) line, cd = line of division, R_{Q2} , R_{G2} = projections of bivariate means of Qtz-2 and Gran-2 on DF line respectively. R_0 = discriminant index, half way between R_{Q2} and R_{G2} .



1-QUARTZITES

2=GRANITES

FIGURE 4.29 Scatter diagram for discriminant function analysis of Quartzite (Qtz) and Granite (Gran). ab = discriminant function (DF) line, cd = line of division, R_G , R_Q = projections of bivariate means of Qtz and Gran on DF line respectively. R_0 = discriminant index, half way between R_G and R_Q .

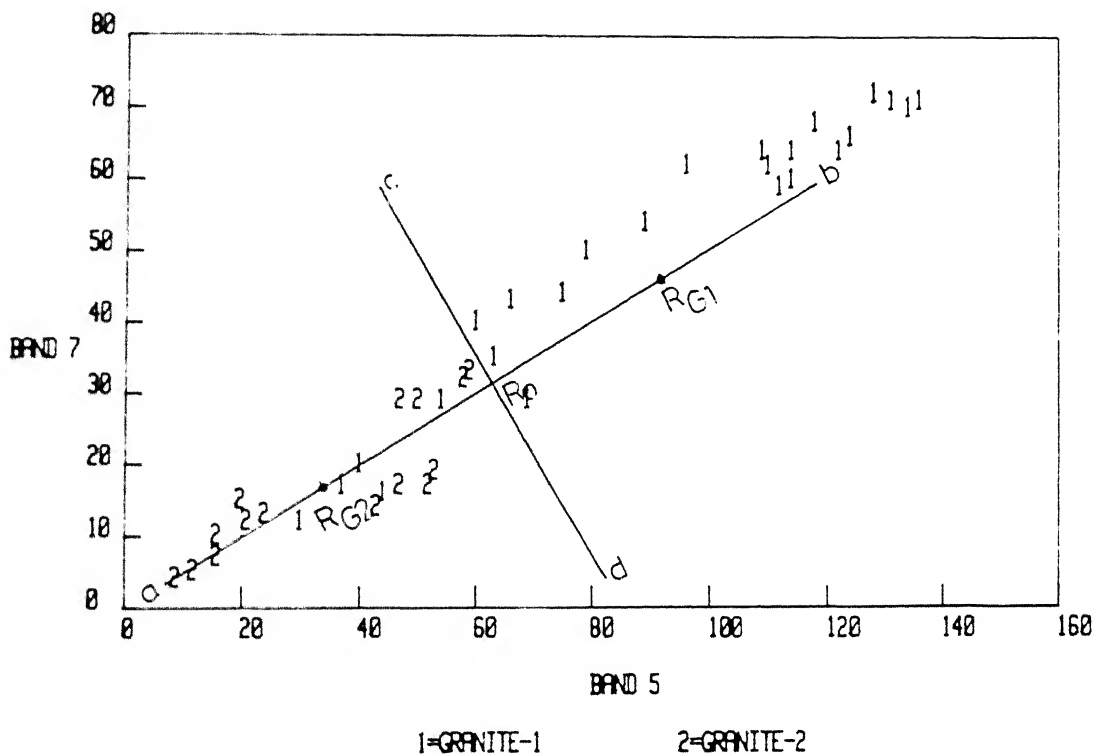


FIGURE 4.30 Scatter diagram for discriminant function analysis of Granite-1 (Gran-1) and Granite-2 (Gran-2). ab = discriminant function (DF) line, cd = line of division, R_{G1} , R_{G2} = projections of bivariate means of Gran-1 and Gran-2 on DF line respectively. R_0 = discriminant index, half way between R_{G1} and R_{G2} .

on the other side of the line of division. The absence of quartzite-2 samples in the field dominated by quartzite-1 indicates the tendency of quartzite-2 to be completely discriminated from quartzite-1. However, the presence of some training pixels of quartzite-1 in the field dominated by quartzite-2 indicates that there is some tendency of misclassification of quartzite-1 unit as quartzite-2. In the scatter plot of bands 3 and 4, both the units are completely discriminated from each other. The average degree of misclassification or intermixing of these two litho-units has been estimated to be in the order of 0 to 12.5 percent (Table 4.2).

The misclassification of quartzite-1 and quartzite-2 units is not at all in conformity with the coincident spectral plots of these rocks in different raw TM bands in the sense that the latter depict a large separation of them. This could be attributed to the change in the spectral response characteristics of the litho-units since the discriminant analysis is performed using two spectral bands. However, the coincident spectral plots for quartzite-1 - quartzite-2 in different band ratios depict complete overlap or 'intermixing' of these two rock types. Therefore, it seems reasonable to utilise the results of coincident spectral plots of band ratios for the interpretation of the ratio images only. The little intermixing of quartzite-1 and quartzite-2 as observed from the discriminant function analysis may be regarded as a meaningful situation prevailing in the field. This will be verified with the among-category

classification accuracy determined for multivariate maximum likelihood method of classification and also on the classified digital image.

4.3.7.2.2 Rock Pair : Phyllites-Quartzites

In order to facilitate comparisons among the three pairs of rocks viz. phyllites-quartzite-1, phyllites-quartzite-2 and phyllites-quartzites (i.e. quartzite-1 and quartzite-2 considered together) in terms of the degree of discrimination of the rocks in each pair,^a discriminant function analysis of each pair has been carried out separately in the six selected pairs of TM spectral channels as mentioned earlier. The results of DFA of phyllites-quartzite-1 presented in Table 4.2 show ^a/considerable misclassification of these rocks in the band pairs 1-7, 3-4 and 3-7 (i.e. 56-72% of their training observations) while in band pairs 1-5, 4-7 and 5-7, their degree of intermixing is relatively very low (i.e. 32 to 40% only). The results of discriminant function analysis of these two rocks is in close agreement with the observations made from the coincident spectral plots in different TM bands.

Discriminant function analysis of the pair phyllites-quartzite-2 shows that the phyllites are misclassified as quartzite-2 in the order of 20 to 28 percent. On the other hand, quartzite-2 is misclassified as phyllites to the extent of 6 to 13 percent of its observations in band pairs 1-5, 3-7 and 4-7 while in other band pairs, they are completely discriminated from the phyllites. Therefore, the average degree of intermixing or misclassification between the two rock types may be regarded

to vary in the range of 10 to 20.5 percent (Table 4.2). This observation is, however, in strong contrast to the coincident spectral plots generated for the training samples of the two rock types which exhibit complete separation of them. This change in the spectral discrimination between the rock types arises probably as a result of carrying out the analysis in two spectral bands in discriminant analysis. Therefore, the results of discriminant function analysis need to be verified with the between-category classification accuracy determined for maximum likelihood method of classification by using multivariate training data sets of the rock types.

Discriminant function analysis carried out for evaluating the degree of discrimination between the quartzites (i.e. quartzite-1 and quartzite-2 considered together) and phyllites reveals that there is not significant difference in the discrimination of the rocks between the pairs phyllites-quartzites (whole) and phyllites-quartzite-1 (illuminated) (Table 4.2). Scatter diagrams for phyllites-quartzite pair in different band combinations show that the phyllites dominate by the presence of 52-72 percent of its observations on one side of line of division, whereas the other side of line of division is dominated by 50-58 percent of observations of the quartzites. This results in an average misclassification of 36-55 percent of the two rocks.

4.3.7.2.3 Rock Pair : Phyllites-Granites

The discriminant function analysis of the phyllitic and the granitic rocks of the Thematic Mapper area has been carried

out exactly in the same manner as the discriminant function analysis of the phyllitic and the quartzitic rocks since like the quartzites, the granitic rocks have also been represented as two separate litho-units by the illuminated and non-illuminated portions of their exposure. Discriminant function analysis of the phyllites and the granitic rocks (illuminated) in different pairs of bands reveals that about 36.52 percent observations of granite-1 falls in the side dominated by the training samples of phyllites (64-76 percent) (Table 4.2). This is more than the number of observations of phyllites (24-36 percent) falling in association with the granitic samples on the other side of the line of division where the latter (granite-1) dominates by 48-64 percent of its training pixels. This situation implies a greater tendency of misclassification of granite-1 as phyllites than the tendency of the latter to be misclassified as the former. The average degree of intermixing of these two rocks has been estimated as 37-41 percent which is in close agreement with the coincident spectral plots of these rocks in different TM bands.

Examination of the scatter diagrams concerning the discriminant function analysis of the phyllites and granite-2 (non-illuminated) shows that 80 to 84 percent observations of the phyllites alone are present on one side of the line of division. On the other hand, except in band pair 3-7, the field on the other side of the line of division represents all the observations of granite-2 in association with the remaining observations of the phyllites. This observation indicates that

the phyllites are misclassified as granite-2 in the order of 16-20 percent while granite-2 shows absolutely no misclassification as the phyllites except in band pair 3-7 where it shows a misclassification of 13 percent. The latter part of the above observation is in conformity with the coincident spectral plots of the phyllites and granite-2 in different TM bands in the sense that they depict ^a large separation between these rocks. The average degree of misclassification between these two rocks will be therefore in the order of 8 to 16.5 percent (Table 4.2).

Discriminant function analysis of phyllites and granites (granite-1 and granite-2 considered together) in different pairs of bands reveals a misclassification in the order of 23.75 to 30.5 percent. The average degree of misclassification of phyllites and granites, however, reduces significantly by 10 percent as compared to the average degree of misclassification between the phyllites and granite-1. This decrease in the average degree of misclassification between the phyllites and granites probably results from absolutely no misclassification of granite-2 as the phyllites.

4.3.7.2.4 Rock Pair : Quartzites-Granites

It has been mentioned earlier that the quartzitic and granitic rocks of TM area have been represented each by two separate litho-units corresponding to their illuminated and non-illuminated parts in the terrain. Therefore, in order to precisely evaluate the degree of discrimination between the quartzitic and granitic terrains, their illuminated and

non-illuminated parts have been grouped into four possible different pairs of rocks. These four pairs of rocks considered for discriminant function analysis are namely quartzite-1 - granite-1, quartzite-1 - granite-2, quartzite-2 - granite-1, and quartzite-2 - granite-2. In addition, finally the discriminant function analysis of the two main litho-units (that is, considering both of their illuminated and non-illuminated parts together) has also been carried out. The results of discriminant function analysis of these rock pairs are presented in Table 4.2.

The discriminant function analysis of quartzite-1 and granite-1 reveals that except in band pair 1-5, these two rocks are misclassified in the order of 18-34 percent of their training observations. The scatter plot for bands 1 and 5, however, reveals a very high misclassification of 66 percent of the training observations of these two rocks. This observation is in agreement with the coincident spectral plots of these rocks in different TM bands.

The discriminant function analysis for quartzite-1 and granite-2 performed on the scatter plots of their training observations reveals absolutely no misclassification between these two litho-units. The result of the discriminant function analysis fully agrees with the coincident spectral plots of these rocks in different TM bands which depict ^alarge separation of these two rocks.

On the other hand, examination of the scatter diagrams used for the discriminant function analysis of quartzite-2 and granite-1 reveal that about 26.7 to 33.3 percent observations of

quartzite-2 fall in the field dominated by granite-1 on one side of the line of division, whereas on the other side of the line of division 32 to 40 percent observations of granite-1 is present in association with 67 to 73 percent observations of quartzite-2. This indicates a greater degree of misclassification of granite-1 as quartzite-2 as compared to that of quartzite-2 as granite-1, the average degree of intermixing of these two rocks being equal to about 32.65 to 34.65 percent of their training observations. This observation is also in close agreement with their coincident spectral plots in different TM bands.

The discriminant function analysis of quartzite-2 and granite-2 in the six selected band pairs reveals the presence of almost the same number of their training observations (about 73 to 87 percent) on either side of the line of division indicating a misclassification of only 13 to 27 percent of their training observations. The results obtained from the two-dimensional (that is, two band) discriminant function analysis of these two rocks show significant improvement over their one-dimensional coincident spectral plots which depict considerable overlap of them.

Finally, discriminant function analysis of the entire quartzitic rocks and the granitic rocks (that is, considering the training observations of both of their illuminated and non-illuminated parts together) revealed about 27.5 to 38 percent of intermixing of their training observations (Table 4.2).

4.3.7.2.5 Rock Pair : Granite-1 - Granite-2

The discriminant function analysis for the two varieties of the granites, that is, the illuminated portion (granite-1) and the non-illuminated portion (granite-2) gives rise to similar results obtained from the discriminant function analysis of their corresponding units of the quartzitic rocks (that is, quartzite-1 and quartzite-2) described earlier (Table 4.2). Examination of the scatter diagrams of granite-1 and granite-2 for different pairs of spectral channels reveals that about 76 to 84 percent training observations of granite-1 fall in association with only 13.3 percent observations of granite-2 on one side of the line of division. This indicates a misclassification of granite-1 as granite-2 by 16 to 24 percent, whereas granite-2 is misclassified as granite-1 to the extent of 13.3 percent in band pairs 1-5, 1-7 and 4-7 with absolutely no misclassification of the latter as the former in the other band pairs. Therefore, the average degree of misclassification of the two rocks has been estimated to be in the order of 10 to 19 percent. This observation is found not to be in conformity with the coincident spectral plots of these rocks in different TM bands in the sense that the latter depict complete separation of them.

CHAPTER 5

DIGITAL IMAGE PROCESSING OF MULTIVARIATE REMOTELY SENSED DATA FOR ROCK DISCRIMINATION

5.1 INTRODUCTION

The last two chapters have been devoted respectively to the mineralogical analysis and the laboratory derived reflectance spectra analysis of rock samples, and the graphical analysis of remotely sensed digital data for lithological discrimination. The task of lithological discrimination, however, remains incomplete without ^a detailed analysis and interpretation of the digital images. In this chapter, ^a detailed discussion is provided concerning the identification and discrimination of the rock types on the digital images generated by applying various digital image processing techniques. Besides, an attempt has also been made to evaluate the relative advantages and disadvantages of ^{the} / different image processing techniques used in this study in terms of their ability for lithological discrimination.

An attempt was made to classify the rock types of MSS Study area, that is, the area studied by using MSS data of Landsat-2 through ^a supervised classification of the principal component transformed digital data but this approach did not yield any satisfactory result. However, the discrimination of the rock types of the TM Study area, that is, the area studied by using the thematic mapper data of Landsat-5 has been performed to a satisfactory extent by employing the various image processing techniques described in Chapter 2. In the following sections, is

presented stepwise the analysis and interpretation of the statistical outputs and the digital images generated by applying these image processing techniques.

5.2 RAW BAND IMAGES

The average information content of a digital image is determined by a measure called entropy (H) which is given by

$$H = - \sum_{i=0}^k p(i) \log_2 p(i) \quad (5.1)$$

where k is the number of digital levels (for example, 256 in the case of ^{the}thematic mapper data)

and $p(i)$ is the probability of level i. This can be calculated for any given digital image with n lines and m pixels (that is, a total number of nm pixels) from

$$p(i) = \frac{F(i)}{nm} \quad (5.2)$$

where $F(i)$ is the frequency of observation of each gray level.

Similarly, the redundancy r of the digital data of an image is estimated by

$$r = b - H \quad (5.3)$$

where the quantity b represents the number of quantization bits (for example, 8 in case of TM data). The redundancy in digital remotely sensed images is due to the average information content of images (H) being less than the number of bits used to represent them.

The entropies and redundancies of the original TM images determined by using equations (5.1) and (5.2) respectively are given in Table 5.1.

Table 5.1 Entropies and Redundancies of Landsat TM Imageries of Visible and Near-infrared Range (excluding thermal band 6)

TM Bands	Entropies	Redundancies
1	5.1831	2.8169
2	4.8996	3.1004
3	5.6279	2.3721
4	5.7865	2.2135
5	7.0089	0.9911
7	6.2620	1.7380

Thus, the TM spectral bands images in order of their increasing information content and decreasing redundancy can be arranged as band 2, band 1, band 3, band 4, band 7, and band 5. This ^{inference} seems to be comparable to the information content of the black and white images of TM spectral bands in the sense that the digital images of bands 5 and 7 provide better tonal and textural contrasts than the images of the other spectral bands. However, ^a detailed examination of the images of different spectral bands ^{does} not reveal ^{any} significant difference in their overall quality from the lithological discrimination point of view because of the considerable similarity in the spectral characteristics of the rock types.

Examination of the digital image of ^{the} spectral band 5 (Figure 5.1) reveals three main litho-units on the basis of tonal and textural differences. The granitic terrain in the NW corner may be identified on the basis of its dissected appearance and dark signature. The phyllites and schists appear tonally light and comprise many structural features such as a prominent fold at the SW corner, a fault at the centre on the top of the image trending NNNW-SSE, and numerous lineaments. The quartzites are characterised by their ridge-like ^{morphological expression} _h having NNE-SSW trend which causes significant brightness variations on their exposures. For example, the sun-facing side of these ridges appears very bright while the shadowed side appears dark. This aspect leads to tremendous misclassification of the quartzites with other rock types present in the study area as discussed earlier in Chapter 4 in ^{the} discriminant function analysis of ^{the} rocks, which will also be seen on the various digital images in the following sections.

5.3 FALSE COLOUR COMPOSITES (FCCs)

False colour composites consisting of three raw band monochromatic images (displayed as red, green, and blue respectively) are the most effective means of creating a natural colour display of the terrain and hence, they facilitate ^a better identification of the surface features ^{than the} black and white pictures of raw spectral bands. Since ^{the} multispectral data often exhibit ^a high interband correlation, it is always pertinent to select all three-band combinations of the least correlated bands. In the present study, this task has been carried out with the help of a band correlation matrix, and also, by applying the

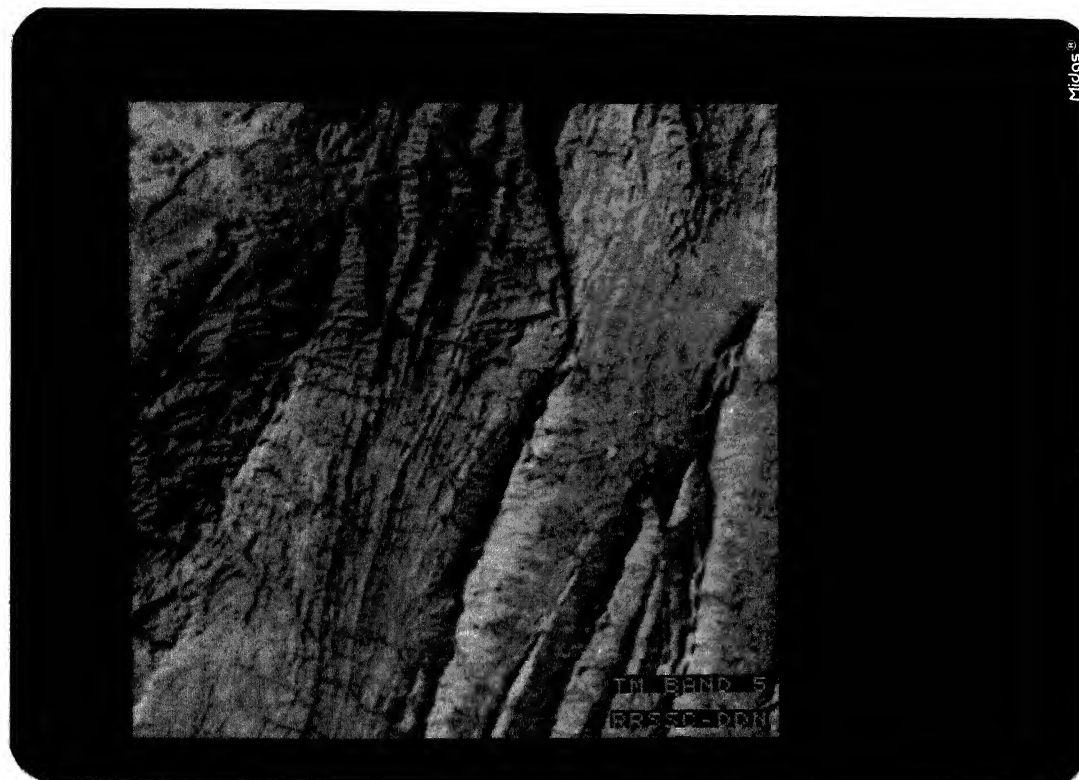


FIGURE 5.1 Black and white image of TM band 5.



FIGURE 5.2 False colour composite of TM bands 7, 5, and 4 in red, green, and blue colour combination.

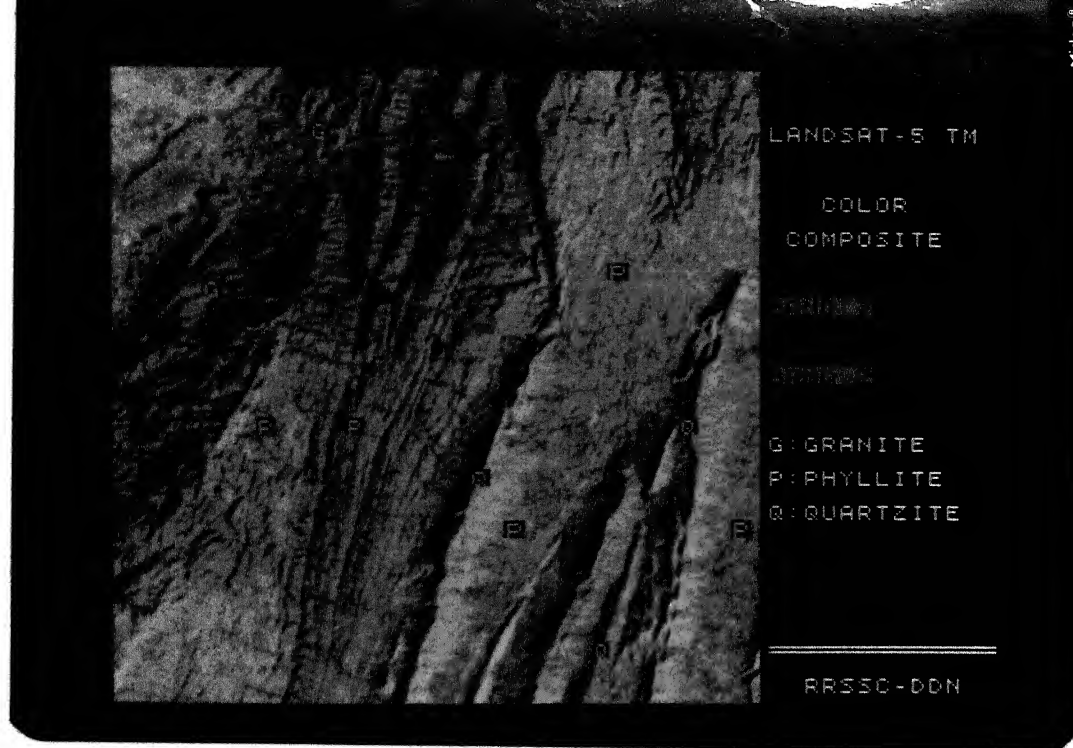


FIGURE 5.3 False colour composite of TM bands 7, 4, and 2 in red, green, and blue colour combination.

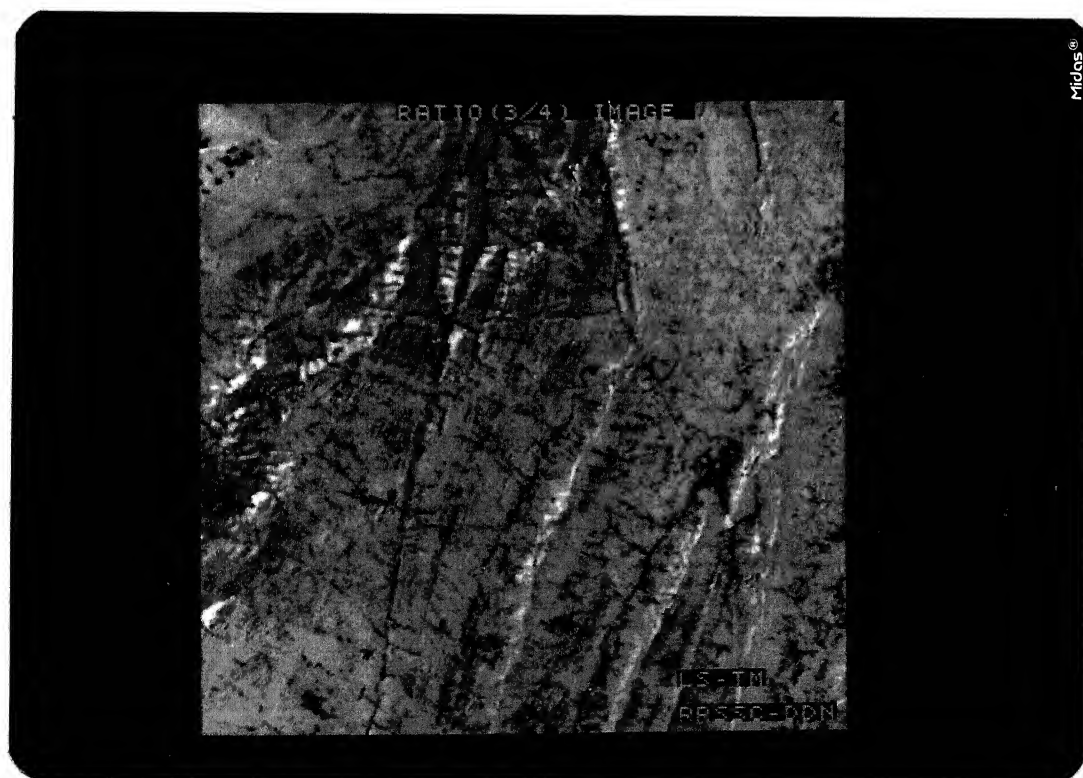


FIGURE 5.4 Black and white ratio image of TM bands 3 and 4 (3/4).

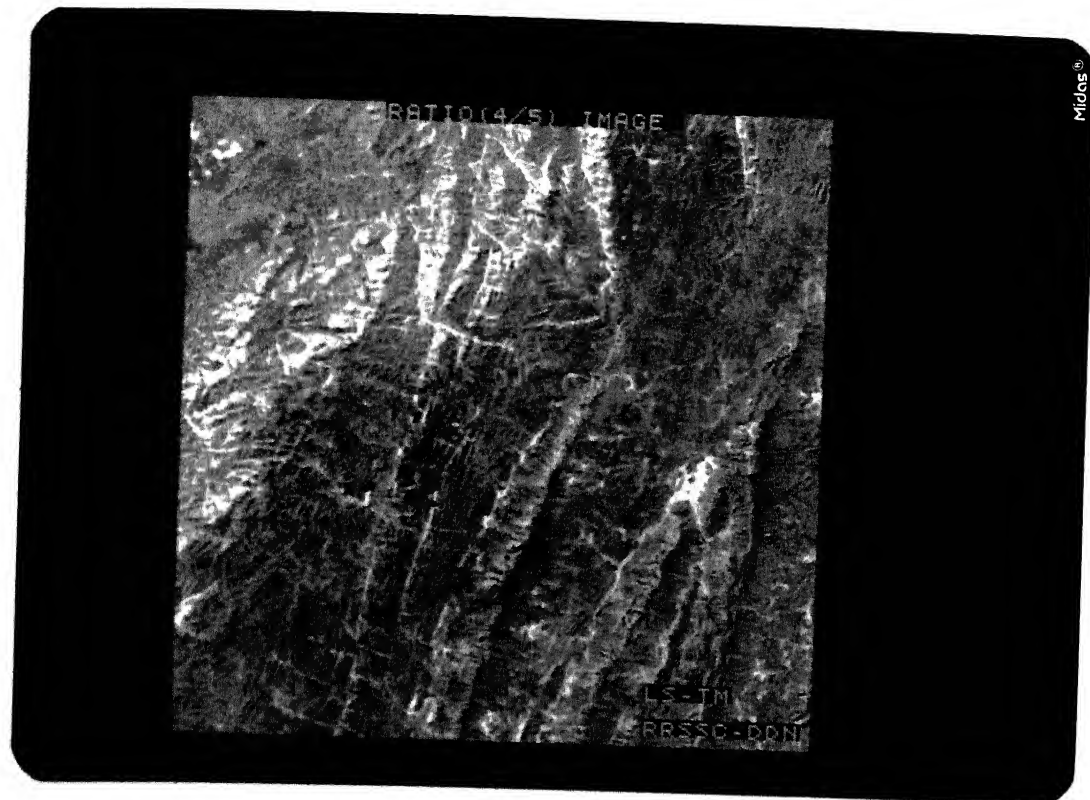


FIGURE 5.5 Black and white ratio image of TM bands 4 and 5 (4/5).

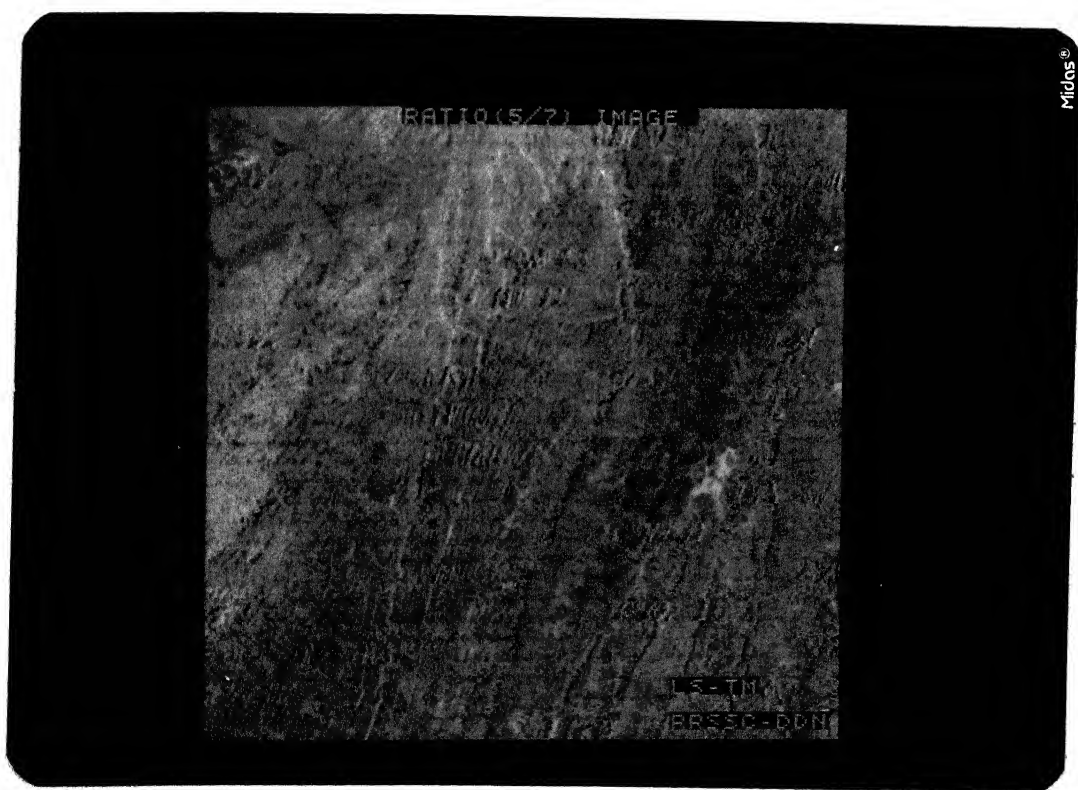


FIGURE 5.6 Black and white ratio image of TM bands 5 and 7 (5/7).



FIGURE 5.7 Colour-ratio composite of TM 2/3, 3/4, and 4/5 in red, green and blue colour combination.

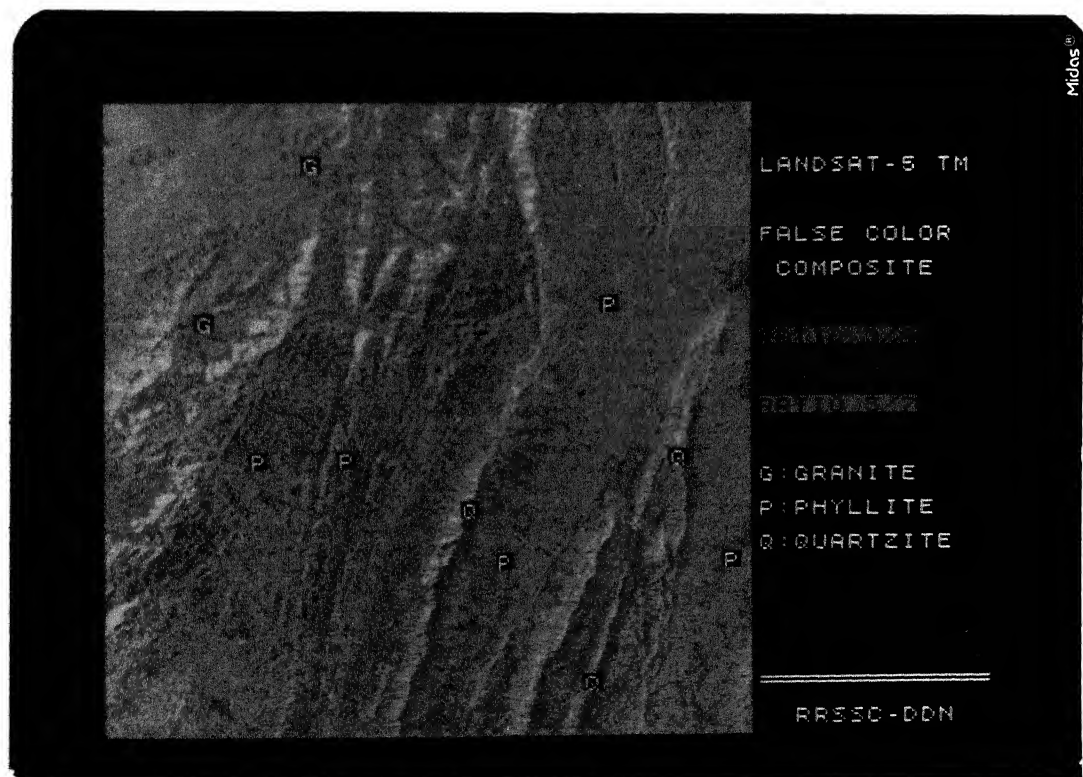


FIGURE 5.8 Colour-ratio composite of TM 3/4, 4/5, and 5/7 in red, green and blue colour combination.



FIGURE 5.9 Colour composite of brightness and greenness indices in red and green colour combination.

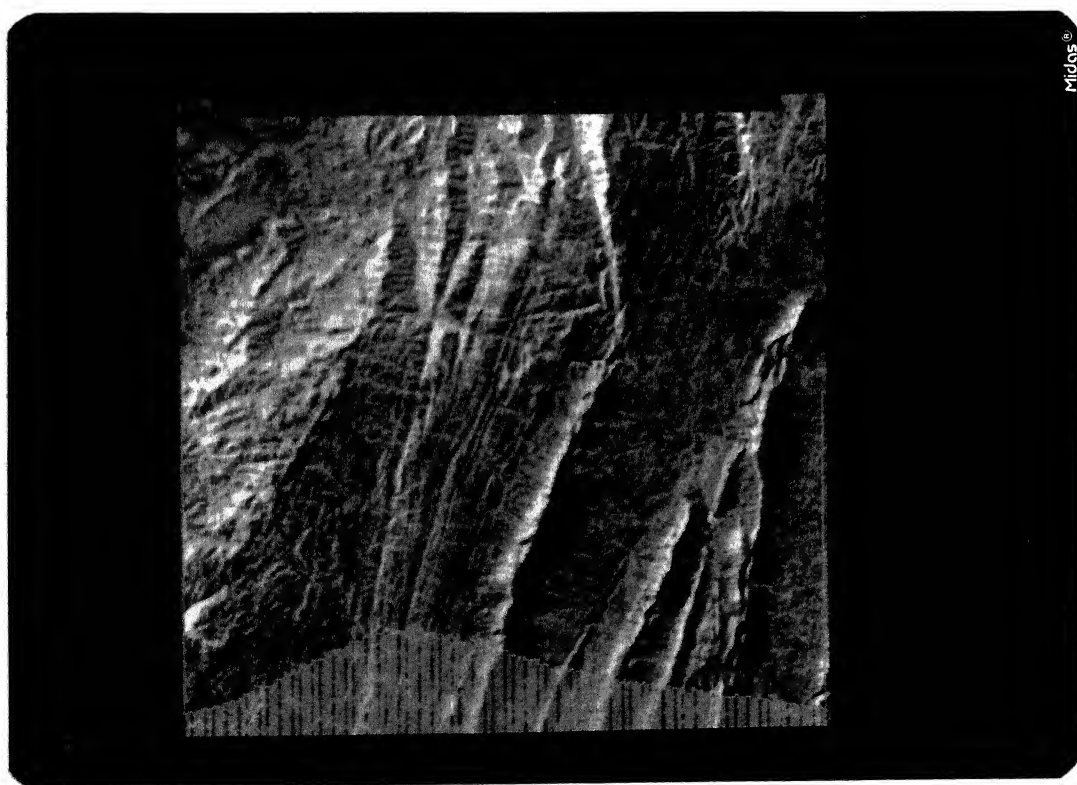


FIGURE 5.10 Black and white image of the first principal component.



FIGURE 5.11 False colour composite of the first, second and third principal components in red, green and blue colour combination. G = Erinpura Granites and Gneisses, Q = Quartzites, R1 = Biotitic Limestones and Calc Gneisses, R2 = Calc Schists, and R3 = Phyllites and Impure Limestones.

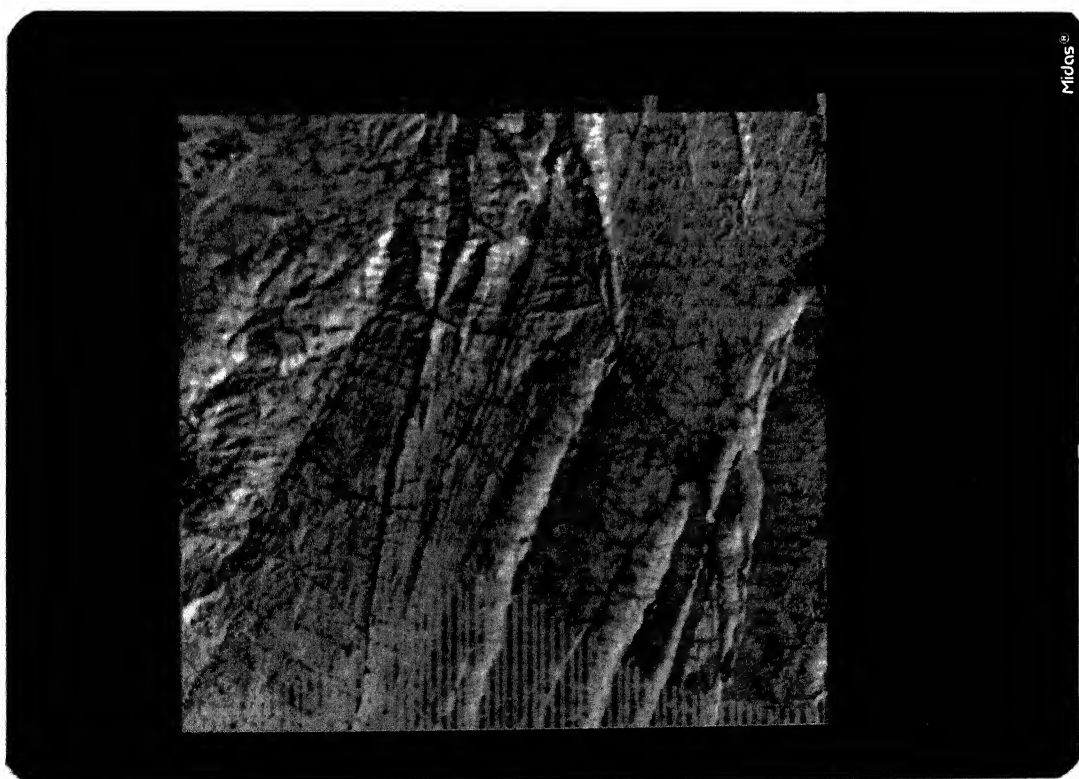


FIGURE 5.12 Black and white image of the first inverse principal component.

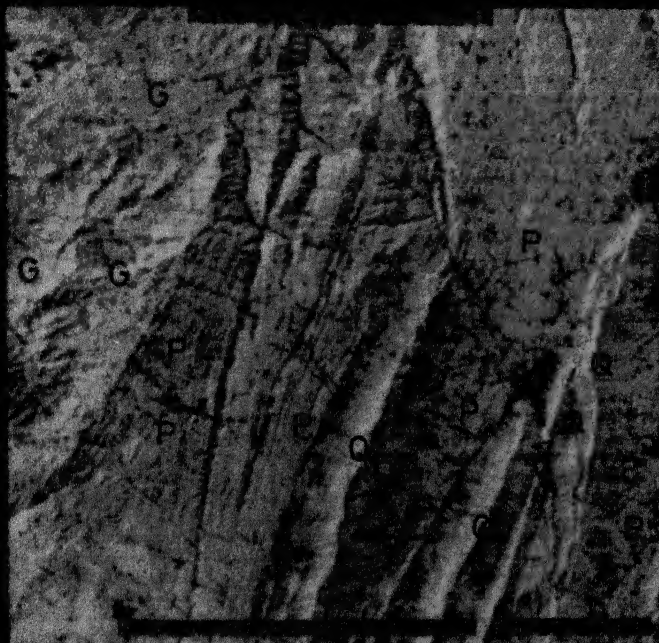
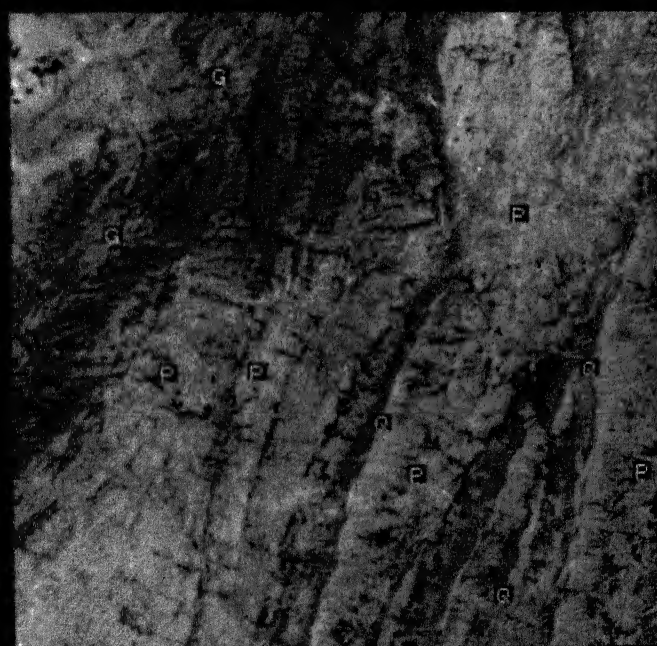


FIGURE 5.13 False colour composite of the first, second and third inverse principal components in red, green and blue colour combination. G=Granite, P=Phyllite, Q=Quartzite.



FIGURE 5.14 Black and white image of the first correspondence component.



LANDSAT-5 TM

FALSE COLOR
COMPOSITE
CORRESPONDENCE
ANALYSIS

WATER - 6

VEGETATION - 7

WATER - 6

G: GRANITE
P: PHYLLITE
Q: QUARTZITE

RRSC-DDN

Midas®

FIGURE 5.15 False colour composite of the first, second and third correspondence components in red, green and blue colour combination.

technique of Optimum Index Factor (OIF) developed by Chavez et al. (1982, 1984) that ranks all the 20 possible three-band combinations that may be made from the six bands of thematic mapper data (as the thermal band or band 6 has not been used in the study). The optimum index factor criterion is based upon the amount of total variance and correlation within and between various band combinations and is calculated for each three-band combination by dividing the sum of the standard deviations (representative of the total spectral range of the bands) by the sum of the absolute values of the correlation coefficients (providing a measure of redundancy) (Greenbaum, 1987).

That is,

$$OIF = \frac{\sum_{i=1}^3 \sigma_i}{\sum_{j=1}^3 |r_j|} \quad (5.4)$$

where σ_i is the standard deviation of band i and $|r_j|$ is the absolute value of the correlation coefficient between any two of the three bands. Thus, the three-band combination with the largest OIF will have the most information (as measured by variance) with the least amount of redundancy (as measured by correlation). The standard deviations and between band correlation coefficients used in the estimation of OIF have been taken from Table 5.2. This 20 three-band combinations of the TM data with their OIFs in decreasing order are summarized in Table 5.3.

Table 5.3 shows that a false colour composite generated by assigning blue, green, and red colours to spectral bands 4, 5,

Table 5.2 (Contd.)

ormalized Eigenvectors (Matrix A, (a_{ij}) , i = channel (row data),
 j = principal components (column data)

j (Principal Components)

		1	2	3	4	5	6
i Bands)	1	-0.1886	0.3262	-0.3060	-0.4594	0.7202	-0.1860
	2	-0.1631	0.2748	-0.2152	-0.1611	-0.1290	0.8994
	3	-0.2726	0.3844	-0.3364	-0.2709	-0.6622	-0.3909
	4	-0.2971	0.6726	0.4624	0.4811	0.1088	-4.7008×10^{-2}
	5	-0.7604	-0.4016	0.4133	-0.2973	-2.4347×10^{-2}	2.6920×10^{-2}
	7	-0.4439	-0.2380	-0.6018	0.6081	0.1170	-2.6097×10^{-2}

Band-Component Correlation Matrix (R_{ij})

(i.e. degree of correlation of each channel i with principal components j)

j (Principal Components)

		1	2	3	4	5	6
i Bands)	1	-0.8867	0.2846	-0.2032	-0.2112	0.2151	-0.0233
	2	-0.9260	0.2896	-0.1725	-0.0894	-0.0465	0.1364
	3	-0.9392	0.2458	-0.1637	-0.0912	-0.1450	-0.0360
	4	-0.8942	0.3757	0.1965	0.1416	0.0208	-3.7789×10^{-3}
	5	-0.9916	-0.0972	0.0761	-0.0379	-2.0172×10^{-3}	9.3769×10^{-4}
	7	-0.9691	-0.0964	-0.1855	0.1298	0.0162	-1.5217×10^{-3}

Table 5.3 Optimum Index Factor (OIF) for Six of the Thematic Mapper Bands for the Thematic Mapper Area

$$OIF = \frac{\sum_{k=1}^3 s_k}{\sum_{j=1}^3 |r_j|}$$
, where s_k represents standard deviation for band k and r_j represents the correlation between any two bands.

Band Combination	Σ S.D.	$\Sigma r_j $	OIF	Ranking
4-5-7	66.23	2.62	25.28	1
3-5-7	64.45	2.75	23.44	2
1-5-7	61.15	2.63	23.25	3
3-4-5	59.10	2.62	22.56	4
1-4-5	55.80	2.53	22.05	5
2-5-7	59.59	2.72	21.90	6
2-4-5	54.24	2.61	20.78	7
1-3-5	54.02	2.65	20.38	8
2-3-5	52.46	2.76	19.00	9
1-2-5	49.16	2.66	18.48	10
3-4-7	45.96	2.59	17.74	11
1-4-7	42.66	2.48	17.20	12
2-4-7	41.10	2.57	16.00	13
1-3-7	40.88	2.66	15.37	14
2-3-7	39.32	2.77	14.20	15
1-3-4	35.53	2.63	13.51	16
1-2-7	36.62	2.67	13.50	17
2-3-4	33.97	2.75	12.35	18
1-2-4	30.67	2.66	11.53	19
1-2-3	28.89	2.84	10.17	20

and 7 respectively should provide optimum information of the scene. Similarly, FCCs of the band combinations 3,5,7, and 1,5,7 each displayed in blue, green, and red combination should provide comparably ^{the} same amount of information since their optimum index factors are close to each other, and so also the band combinations 3,4,5 and 1,4,5 in B,G,R combination. The band correlation matrix presented in Table 5.2 reveals generally ^a high correlation for all band pairs (more than 80 percent correlation). Therefore, among these all those having more than 90 percent correlation have been considered very highly correlated bands such as the band pairs 1-2, 1-3, 2-3, 3-7, and 5-7 and the rest with less than 90 percent correlation may be regarded as moderately correlated bands. The band pair showing the least correlation (81 percent) consists of bands 4 and 7. The relatively low correlation of the band pairs 4-5 and 4-7 in addition to the higher variances of bands 4, 5, and 7 ^{than the} other bands (Table 5.2) results in the highest OIF for the three-band combination of 4-5-7. Moreover, it may also be observed from the band correlation matrix (Table 5.2) that band 4 is the only spectral channel which is correlated by less than 90 percent with all ^{the} other spectral bands. Since the TM spectral channel 7 is a uniquely potential band for lithological discrimination, the false colour composite incorporating bands 4 and 7 should provide ^a good contrast between ^{the} various rock types. In the present study, taking into considerations both the OIF criteria and the interband correlations of different spectral band pairs, two three-band combinations were finally selected for

generation of false colour composites. These are band combinations 4-5-7, and 2-4-7 each displayed in blue, green, and red colour combination. The false colour composites have been further linearly stretched in order to enhance the contrast between the rock types.

Examination of the false colour composites of band combinations 4-5-7 and 2-4-7 (Figures 5.2 and 5.3 respectively) shows that none of them is able to discriminate all the five litho-units present in the study area (Figure 1.3). Only three litho-units can be identified on each of the FCCs. The terrain comprising the granites and gneisses can be identified on the basis of its dissected appearance and dark greenish to greyish spectral signature. The quartzites are identifiable on the basis of their ridge like structure trending NNE-SSW. The phyllitic terrain comprising the phyllites and schists may be identified on the basis of their relatively even topography and light brownish green spectral signature. The phyllitic terrain also exhibits many structural features such as fold, fault, and lineaments. The fold may be observed distinctly at the SW corner of the composites. The FCCs reveal two sets of lineaments trending SE-NW and SEE-NW respectively and a series of faults trending NNW-SSE. The ridge structure induces variation in illumination condition on the quartzitic rocks as a result of which two different units of the same may be recognised on the FCCs, one representing the illuminated part and the other the non-illuminated or shadowed part which have been referred to as quartzite-1 and quartzite-2 respectively in the discussion elsewhere in the thesis.

Similarly, due to ^{the} brightness variations prevailing on the granitic terrain as well, these rocks have been represented by two separate litho-units namely granite-1 and granite-2 corresponding to the illuminated and the non-illuminated parts respectively.

One significant observation that may be made on the colour composite of bands 2, 4, 7 in blue, green, and red combination is that the vegetation cover and the cultivate developed on the valleys, the granitic terrain and the moisture prone areas are highlighted more prominently on composite image ^{than} the FCC of bands 4, 5, 7. This is attributable to the sensitivity of TM spectral bands 2 and the plant health and vigour resulting in the bluish reflectance of vegetation. In fact, the relatively dense vegetation on the granitic rocks and on the flanks of quartzitic ridges has been observed during the field check.

5.4 RATIO IMAGES AND FALSE COLOUR COMPOSITES OF BAND RATIO

5.4.1 Methodology

Spectral ratioing (see section 2.3.2.1) brings substantial reduction of the effect of extraneous factors related to sensor on the brightness values caused by topographic variations, shadows or seasonal changes in illumination angle and intensity that act equally at all wavelengths (Rowan, 1975; Goetz et al., 1983; Siega Gillespie, 1980). One of the main advantages of ratioing is that a material has same ratio value regardless of variation in illumination, however, this is subject to vegetation cover and not

In the present study, ratio images have been generated for the thematic mapper area only, that is, the area studied by using the thematic mapper data of Landsat-5. Three black and white ratio images of spectral ratios $3/4$, $4/5$, and $5/7$, and two false colour composites of band ratios $2/3$, $3/4$, $4/5$, and $3/4$, $4/5$, $5/7$ have been studied with a view to discriminating the litho-units on the basis of variations in the distribution of vegetation and hydroxyl content of rocks. The ratio images and their FCCs have been further rescaled to fill the dynamic range of the display medium (0-255) by contrast enhancement technique.

Since the iron content of different rocks has not been estimated owing to the nonavailability of suitable instruments, it precludes the possibility of carrying out the interpretation of the ratio images and the false colour composites of band ratios in relation to the variation in iron content. For example, ferric-iron rich rocks have relatively high $2/3$ ratio values because they exhibit a sharp fall-off in reflectance from approximately $0.8 \mu\text{m}$ to shorter wavelengths (Hunt et al, 1971; Hunt, 1977). The ratio image of TM bands 2 and 3 ($2/3$) also depicts the variation in vegetation distribution because the higher reflectance of vegetation in TM band 2 (visible green) than the TM band 3 (visible red) yields high $2/3$ ratio values for the vegetated terrain. Similarly, the ratio image of TM bands 3 and 4 ($3/4$) offers considerable potential to delineate the distribution of vegetation. Because vegetation has very low reflectance in TM band 3 (visible red) than the TM band 4 (shortwave infrared), vegetation is expected to exhibit very low

3/4 ratio values. Spectral ratio of TM bands 4 and 5 (4/5) is also useful for mapping vegetation cover. Owing to high water absorption in TM channel 5 due to vegetation, the band ratio of TM 4/5 yields high ratio values for the vegetated terrain (Segal and Merin, 1989).

The ratio of TM bands 5 and 7 (5/7) has unique potential of delineating the relative proportion of clay minerals on the ratio image. This is due to the high absorption in the $2.2 \mu\text{m}$ region (TM band 7) and high reflectance in the $1.6 \mu\text{m}$ wavelength (TM band 5) region due to clay minerals, which give rise to high 5/7 ratio values for clay-rich rocks and low 5/7 ratio values for clay-poor rocks. The absorption bands around TM band 7 wavelength region has been attributed to the presence of hydroxyl molecules in the structure of clay minerals. Similarly, vegetation, due to the abundance of molecular water in the leaves also controls the 5/7 ratio values. Vegetated areas will therefore yield very high 5/7 ratio values ^{than the} less vegetated areas.

5.4.2 Analysis and Interpretation

5.4.2.1 Black and White Ratio Images

Examination of the TM 3/4 ratio image (Figure 5.4) reveals almost uniform spectral signatures for the various rock types of the study area. By comparison to the false colour composite of the raw bands images, the non-illuminated parts of the quartzitic and granitic rocks have brighter tones ^{than} their respective illuminated parts on this ratio image. This observation, however, is in sharp contrast to the results of the

histogram analysis of the corresponding band ratio which depicts higher frequencies of training samples of the illuminated parts of these rocks (Figure 4.8b). The identical spectral signatures of the rock types could be attributed to the occurrence of same slopes in the reflectance spectra of different rock types (Figures 3.9a,b and 3.10a,b) which would give rise to identical ratio values for any band ratio. In order to ascertain the exact reason for the occurrence of brighter tone in the non-illuminated parts of the quartzitic and granitic terrains, it is pertinent to carry out detailed study of the field reflectance spectra acquired from the field. In the densely vegetated areas such as those developed along the river valleys and the moisture prone areas, the strong chlorophyll absorption of red energy (TM band 3) relative to short-wavelength infrared energy (TM band 4) results in very low $3/4$ ratio values which give rise to darker signature on this ratio image.

Examination of the TM $4/5$ ratio picture reveals contrasting difference in the tones of different litho-units (Figure 5.5). The granitic terrain is distinctive by its very bright tonal signature while the neighbouring terrain of the phyllites and schists conveys uniformly darker (greyish) signature. These observations are consistent with the results of the histogram analysis of the corresponding band ratio (Figure 4.8c). The brighter signature of the granitic terrain indicates development of healthy and dense vegetation cover which causes very intense absorption in TM channel 5 due to the water molecules present in the leaves of the plants, thereby yielding

very high 4/5 ratio values. The low 4/5 ratio values causing darker signature for the phyllitic terrain could be due to development of very sparse vegetation cover. Like the ratio image of TM 3/4, ratioing of TM bands 4 and 5 also produces brighter tone for the non-illuminated parts of the quartzites ^{than} their illuminated parts. Detailed analysis of field reflectance spectra is necessary to understand this anomaly.

Examination of the ratio picture of TM 5/7 (Figure 5.6) reveals that the spectral ratioing of bands 5 and 7 brings about complete loss of the identities of different rock types as reflected by their thoroughly identical spectral signatures. This observation also fully agrees with the results of histogram analysis of the band ratio 5/7 as discussed in section 4.3.4. The identical 5/7 ratio values of the rock types is implicative of general absence of clay minerals in the rocks and uniform density of vegetation cover throughout the study area. However, like in other ratio images, on the ratio image of TM 5/7 as well, the granitic terrain is marked by slightly brighter tone ^{than the} other litho-units.

This observation is suggestive of presence of reasonable amount of clay minerals in granites and also, development of a denser and healthy vegetation cover on them.

5.4.2.2 False Colour Composites of Band Ratios

False colour composites generated by combining three monochromatic ratio data sets have two-fold advantages of combining data from more than two bands and presenting the data in colour, which further facilitates the interpretation of subtle differences in spectral reflectances. Examination of the false

colour composite of band ratios 2/3, 3/4, and 4/5 reveals very prominently the densely vegetated cover developed on the granitic terrain, along the stream valleys, and on other moisture prone areas in red colour (Figure 5.7). The reddish signature of the vegetation cover results due to considerable contributions from the TM 2/3 component implying large 2/3 ratio values caused by very high reflection of green energy (band 2) and intense absorption of red energy (band 3). The granitic terrain appears brighter on its non-illuminated parts than on the illuminated parts. The whitish appearance of the non-illuminated parts is attributable to almost equal contributions of red, green and blue colours from the ratio images of TM 2/3, 3/4 and 4/5 respectively. Therefore, it is suggestive of a relatively dense and healthy vegetation cover on the granitic terrain. It may also be observed that the non-illuminated parts of the quartzitic rocks look brighter (pale greenish white) than the illuminated portions (green) probably due to smaller contributions from 3/4 ratio, which therefore suggest relatively thin vegetation cover on them. The terrain covering the phyllites and the schists, and the illuminated parts of the quartzite ridges convey almost identical spectral signatures, thereby appearing as a single litho-unit. This observation is also consistent with the results of discriminant function analysis of phyllite - quartzite-1. The greenish signature of these rocks in addition to the conspicuous absence of reddish signature almost throughout their terrains indicates significant amount of green contributions from 3/4 ratio, thereby suggesting a reasonably

thin vegetation cover on the phyllitic and quartzitic rocks. This may be explained by the fact that vegetation has very low reflectance in TM band 3 (visible red) ^{than in} TM band 4 (shortwave infrared); therefore, thin vegetation will exhibit relatively high 3/4 ratio values as compared to dense vegetation cover.

Examination of the false colour composite of the three monochromatic ratios 3/4, 4/5, and 5/7 displayed in red, green, and blue respectively (Figure 5.8) reveals that the rock types of the study area are resolved more distinctly on this composite as compared to the FCC of ratios 2/3, 3/4, and 4/5 (Figure 5.7). It may be easily noticed that like the colour composite of ratios 2/3, 3/4, and 4/5, the FCC of 3/4, 4/5, and 5/7 also exhibits almost identical spectral signature (brownish) for most part of the phyllitic terrain, and for the illuminated parts of the quartzites. However, these two rock types exhibit greenish blue signature on the remaining portions of their terrains which is not conspicuous on the other false colour composite of ratios 2/3, 3/4, and 4/5. These observations, no doubt, indicate considerable intermixing between these two rock types, that is, the phyllites and the quartzite-1 (illuminated) while the variation in their spectral signatures (colours) may be explained on the basis of the variation in the density of vegetation cover developed on them. For example, moderately dense vegetation cover will give rise to high 5/7 ratio and therefore, will contribute significant proportion of bluish colour to the image, whereas a

thin vegetation cover will yield reasonably high 3/4 ratio values (red), thereby imparting brown signature to the image.

The granitic terrain is identifiable on the FCC on the basis of its dissected and massive appearance, and in general, a bluish spectral signature. However, the non-illuminated parts of the quartzites and the granitic rocks exhibit almost identical spectral signatures, that is, yellow colour and pale greenish yellow colour respectively which are strikingly brighter than the spectral signatures of their respective illuminated counterparts. The nearly identical spectral signatures of the non-illuminated parts of these two rocks is also evident in their discriminant function analysis. The yellow colour of the non-illuminated parts of the quartzites results due to the combined effect of significant contributions of red colour from TM 3/4 ratio and smaller contributions of green colour from TM 4/5 ratio which indicate significantly a thin cover of vegetation on the quartzitic ridges. In contrast, the pale greenish yellow colour of the non-illuminated parts of the granitic rocks is caused by smaller contributions of red colour from TM 3/4 ratio and a larger contributions of green colour from TM 4/5 ratio, thereby suggesting a denser cover of vegetation.

As discussed above, the brighter spectral signatures of the non-illuminated parts of the granites and the quartzites relative to the respective illuminated parts of these rocks on the two FCCs of ratio images is also apparent in the coincident spectral plots of the rock types for different band ratios (Figure 4.9) which depict significantly larger confidence ranges

(intervals) and higher ratio values for the non-illuminated parts of these rocks as compared to their illuminated portions. Likewise, the identical spectral signatures of different rock types on the FCCs of ratios arise as a result of strong interband correlation and occurrence of similar slopes in the reflectance spectra of different rock types.

5.5 COLOUR COMPOSITE OF THE BRIGHTNESS AND GREENNESS INDICES

A colour composite has been generated by assigning red and green colours respectively to the monochromatic images of the brightness and greenness indices using the relevant coefficients as given in section 2.3.2.6 for Landsat Thematic Mapper data (Figure 5.9). The objective is to demarcate both the soil covered areas or the barren exposures and the vegetated areas on the same digital composite image, respectively, on the basis of the reddish and greenish spectral signatures of the image.

Examination of this composite image reveals that the entire granitic and gneissic terrain is covered by a dense vegetation cover, whereas the terrain comprising the schists and the phyllites exhibits development of vegetation only at favourable sites such as river and stream valleys owing to the occurrence of suitable surface drainage.

The composite image also very clearly delineates the sparse distribution of vegetation on the non-illuminated portions of the quartzitic ridges which is not so conspicuous on any other digital image including the false colour composites of the raw bands data. However, the presence of vegetation on the illuminated portions of the quartzites has been masked to a

significant extent by the predominant effect of the brightness component of the image. In fact, as seen on the composite image, the reddish yellow colour of the illuminated portions of the quartzitic rocks results due to relatively very large contributions of red energy from the brightness component and moderate amount of green energy contributions from the greenness component. Likewise, the almost uniform reddish signature of the phyllitic rocks indicates significantly high red contributions from the brightness component and relatively very less green contributions from the greenness component, thereby suggesting a very thin cover of vegetation on the phyllitic terrain.

On the other hand, the colour composite image of the brightness and greenness indices brings out the various structural features such as lineaments, the folds, and the faults as clearly as the false colour composites of raw bands data. Comparison of the brightness and greenness indices colour composite image and the various false colour composites of raw bands data used in the study reveals that the former provides better manifestation of the litho-units and the distribution of vegetation on different litho-units, thus facilitating effective and easier discrimination of the rock types.

5.6 MULTIVARIATE PRINCIPAL COMPONENT ANALYSIS

5.6.1 MSS Study Area

As mentioned earlier, only four major litho-units of the MSS area, that is, the area studied by using MSS data, have been considered for principal component analysis because of their

general dominance in the study area; these are namely the gneiss, schist (GNSC), quartz mica schist (QMS), intercalated calc and cherty quartzite, marble, phyllite (ICQMP), and granite. The various statistical parameters such as the mean, standard deviation, variance-covariance matrix, correlation matrix for each rock type differently and for all rocks together have been determined from the same training data sets as those used for the scatter plots of two-dimensional principal component analysis (Figure 4.10a-f) and are presented in Table 5.4. This table also contains the band-component correlation matrix. The category-wise means and the standard deviations for all four spectral bands are given in Table 5.4. It may be noted that the means and the standard deviations of training data in different channels are comparable. The sample variance for each band is shown along the main diagonal and the covariance in off-diagonal positions in the variance-covariance matrix. From the variance-covariance matrix and interband correlation matrix it may be noted that the training data are highly correlated in band pairs 5-6, 5-7, and 6-7, whereas they are poorly but inversely correlated in the other three band pairs, that is, 4-5, 4-6, and 4-7. Both of these factors, that is, strong correlation and inverse correlation pose tremendous problems in the classification of the rock types.

The variance (eigenvalues), percent variance, and the cumulative percent variance in different principal components are given in Table 5.4. It may be seen that the first principal component accounts for 67.56 percent variance, and the second, third and fourth principal components account for 24.51 percent,

Table 5.4 Principal Component Analysis Data Sheet for MSS Data
(Various parameters mentioned here have been estimated using the training sets of rock types used for 2-dimensional PCA of MSS data)

i) Global Means and Standard Deviations (S.D.) for All Spectral Channels

	Bands			
	4	5	6	7
Means	55.6033	50.0435	47.5380	38.0761
S.D.	22.6370	18.9104	17.0191	12.9300

ii) Global Variance-Covariance Matrix

	Bands			
	4	5	6	7
Bands 4	512.4374			
5	-192.4963	357.6046		
6	-159.0149	254.6486	289.6488	
7	-101.9860	185.6251	186.3140	167.1854

iii) Global Correlation Matrix

	Bands			
	4	5	6	7
Bands 4	1.0000			
5	-0.4497	1.0000		
6	-0.4127	0.7912	1.0000	
7	-0.3484	0.7591	0.8466	1.0000

iv) Eigenvalues for Global Variance-Covariance Matrix

	λ_1 (PC1)	λ_2 (PC2)	λ_3 (PC3)	λ_4 (PC4)
Variance	896.5285	325.0752	73.3312	31.9414
Percent	67.56	24.51	5.53	2.41
Variance				
Cumulative	67.56	92.07	97.60	100.00
Percent				
Variance				

Table 5.4 (Contd.)

Table 5.4 (Contd.)

v) Normalized Eigenvectors (Matrix A) a_{ij} , i = channel (row data)
 j = principal components (column data)

		j (Principal Components)			
		1	2	3	4
(Bands)	4	0.8153	-0.5773	-0.0314	-0.0306
	5	-0.3559	-0.5464	0.7564	0.0511
	6	0.2968	0.3573	0.3425	0.8167
	7	-0.3471	-0.4904	-0.5563	0.5740

vi) Band-Component Correlation Matrix (R_{ij})

		j (Principal Components)			
		1	2	3	4
(Bands)	4	1.0784	-0.4597	-0.0119	-0.0076
	5	-0.5630	-0.5212	0.3426	0.0153
	6	0.5223	0.3790	0.1724	0.2712
	7	-0.8037	-0.6838	-0.3685	0.2510

vii) Matrix of Factor Loadings

		i (Bands)			
		4	5	6	7
(Principal Components)	j 1	0.0272	-0.0197	0.0347	-0.0614
	2	-0.0193	-0.0303	0.0418	-0.0867
	3	-0.0011	0.0419	0.0400	-0.0984
	4	-0.0010	0.0028	0.0953	0.1016

viii) Category-wise Means for All Spectral Bands

		Category (Rock Types)			
		GNSC	QMS	ICCQMP	GRANITE
Bands	4	60.5085	56.4082	47.1463	56.1143
	5	47.9830	49.9796	54.1951	48.7429
	6	46.9661	49.4490	47.9756	45.3143
	7	37.7119	38.7347	37.9756	37.8857

Contd.

Table 5.4 (Contd.)

(ix) Category-wise Standard Deviations for All Spectral Bands

Category (Rock Types)

		GNSC	QMS	ICCQMP	GRANITE
Bands	4	20.2564	24.2847	19.2945	25.6593
	5	18.8401	18.7455	17.4287	20.8783
	6	18.9782	17.7436	14.7538	15.2600
	7	14.1714	12.9756	11.1119	13.1681

(x) Matrix of Category-wise Transformed Means

Category (Rock Types)

		GNSC	QMS	ICCQMP	GRANITE
Bands	4	0.0142	-0.1135	-0.4533	-0.1884
	5	-3.9302	-3.8967	-3.8416	-3.9526
	6	0.1152	0.2019	0.4043	0.0685
	7	8.3837	8.7342	8.5380	8.2506

(xi) Matrix of Category-wise Transformed Standard Deviations

Category (Rock Types)

		GNSC	QMS	ICCQMP	GRANITE
Bands	4	-0.0321	0.1101	0.0110	0.0076
	5	-1.3981	-1.4207	-1.2478	-1.6322
	6	0.1330	0.1931	0.2070	0.1629
	7	3.2820	3.0384	2.5654	2.8259

Contd.

Table 5.4 (Contd.)

i) Categorywise 95% Confidence Intervals in Different Principal Component

Rock types	Principal Component-1		Principal Component-2		Principal Component-3		Principal Component-4	
	Min	Max	Min	Max	Min	Max	Min	Max
SC	0.0772	-0.0487	-1.1900	-6.6704	-0.1455	0.3758	1.9510	14.8164
S	-0.3293	0.1022	-1.1122	-6.6813	-0.1766	0.5803	2.7789	14.6895
CCQMP	-0.4748	-0.4319	-1.3960	-6.2873	-0.0015	0.8100	3.5099	13.5662
ANITE	-0.2032	-0.1735	-0.7335	-7.1517	-0.2506	0.3877	2.7118	13.7893

NB : I. GNSC = Gneiss Schist

QMS = Quartz Mica Schist

ICCQMP = Intercalated Calc and Cherty Quartzite Marble
PhylliteII. Min (Minimum) = $\mu - 1.96\sigma$ Max (Maximum) = $\mu + 1.96\sigma$ where μ = transformed meanand σ = transformed standard deviation.

5.53 percent and 2.41 percent variance respectively. The first two principal components account for 92.07 percent of the total variance and therefore, they may be chosen for further analysis of the digital data instead of resorting to the reflectance data of all the four MSS spectral channels. The matrix of eigenvectors presented in columns for different principal components and the band-component correlation matrix show that the first principal component is accounted for mainly by contributions from band 4, and the second component from band 6 and less significantly from band 7. The third principal component is dominated by band 5 and less significantly by band 6, and the fourth component is dominated by contributions from bands 6 and 7 with small contributions from band 5.

The next step of principal component analysis is the supervised classification of the transformed data of the original reflectance values of different spectral channels. The various steps involved in the classification are explained in section 2.3.2.2.2 and the results of each step of computation are presented in Table 5.4. Here only 95 percent confidence intervals have been determined assuming that the distribution of training sets of different rock types in different spectral channels are Gaussian in nature. The confidence intervals for first principal component shows that all the rock types except QMS have distinct non-overlapping ranges. However, in other principal components only a single rock in each exhibits non-overlapping range, for example, ICCQMP in principal component-2 and -4, GNSC in principal component-3. This observation may be related with the

fact that the first principal component represents maximum amount of variance of the data set and therefore, yields optimum discrimination of the rock types. None of the principal components provides distinct non-overlapping confidence limits for QMS. Moreover, when the confidence intervals for different rock types were used for classifying the transformed reflectance data for principal component-1, it yielded extremely ambiguous results with not a single rock type being classified accurately. This observation could be attributed to the strong as well as inverse correlation of the original reflectance data among different spectral bands. The occurrence of larger values for the minimum limit and smaller values for the maximum limit in the confidence intervals of the rocks in different principal components (Table 5.4) may be explained by the inverse band correlation of the training sets of the rock types.

5.6.2 TM Study Area

The multivariate principal component analysis of the TM study area, that is, the area studied by using thematic mapper data of Landsat-5 has been performed by considering the same five litho-units used for the two-dimensional principal component analysis (section 4.3.6.). These are namely quartzite-1, quartzite-2, phyllites, granite-1, and granite-2. Table 5.5 lists the various statistical parameters for principal component transformation which have been estimated from the training data of the rock types used in the two-dimensional scatter diagrams for PCA. It may be seen that the means and the standard deviations in different bands are comparable. The

5.5 Principal Component Analysis Data Sheet for TM Data
 (Various parameters mentioned here have been estimated from the training sets of rock types used for 2-dimensional PCA of TM data)

Global Means and Standard Deviations (S.D.) for All Spectral Channels

	Bands					
	1	2	3	4	5	7
Means	69.2381	33.8952	42.7429	48.5048	101.8381	55.0952
S.D.	14.5823	11.3247	19.1251	22.7698	47.4773	27.0183

Global Variance-Covariance Matrix

	Bands					
	1	2	3	4	5	7
1	212.6447					
2	161.5444	128.2485				
3	270.0233	208.0209	365.7698			
Bands 4	321.5710	247.6688	417.6118	518.4639		
5	663.7985	508.3386	872.0253	1035.4287	2254.0985	
7	380.3233	289.4908	497.0632	587.6341	1253.0444	729.9908

Global Correlation Matrix

	Bands					
	1	2	3	4	5	7
1	1.0000					
2	0.9782	1.0000				
3	0.9682	0.9604	1.0000			
Bands 4	0.9685	0.9605	0.9590	1.0000		
5	0.9588	0.9454	0.9604	0.9578	1.0000	
7	0.9653	0.9461	0.9619	0.9552	0.9768	1.0000

Eigenvalues for Global Variance-Covariance Matrix (λ)

	λ_1 (PC1)	λ_2 (PC2)	λ_3 (PC3)	λ_4 (PC4)	λ_5 (PC5)	λ_6 (PC6)
Variance	4108.8706	47.77807	23.9086	16.2713	9.1858	3.2020
Percent	97.6	0.01	5.7×10^{-3}	3.86×10^{-3}	2.18×10^{-3}	7.6×10^{-4}
Variance						
Cumulative	97.6	97.61				100.00
Percent						
Variance						

Contd.

Table 5.5(Contd)

i) Normalized Eigenvectors (Matrix A, (a_{ij}) , i = channel (row data),
 j = principal components (column data))

j (Principal Components)

		1	2	3	4	5	6
i (Bands)	1	-0.0955	0.0115	-0.0073	0.0206	-0.7254	0.6812
	2	-0.0816	0.0464	-0.2858	-0.4599	0.5726	0.6084
	3	0.3721	-0.0729	0.4979	-0.7510	-0.1794	-0.1095
	4	0.8181	-0.2940	-0.4719	0.1255	-0.0526	0.0548
	5	-0.0571	0.6018	-0.5724	-0.3514	-0.2863	-0.3185
	7	-0.4161	-0.7375	-0.3463	-0.2912	-0.1702	-0.2221

i) Band-Component Correlation Matrix (R_{ij})

(i.e. degree of correlation of each channel i with principal components j)

j (Principal Components)

		1	2	3	4	5	6
i (Bands)	1	-0.4198	0.0055	-0.0024	0.0057	-0.1507	0.0836
	2	-0.4619	0.0283	-0.1234	-0.1638	0.1532	0.0961
	3	1.2471	-0.0263	0.1273	-0.1584	-0.0284	-0.0102
	4	2.3031	-0.0893	-0.1013	0.0222	-0.0070	0.0043
	5	-0.0771	0.0876	-0.0590	-0.0299	-0.0183	-0.0120
	7	-0.9872	-0.1887	-0.0627	-0.0435	-0.0191	-0.0147

ii) Matrix of Factor Loadings

i (Bands)

		1	2	3	4	5	7
j (Principal Components)	1	-0.0015	-0.0118	0.0761	0.2028	-0.0188	-0.2326
	2	0.0002	0.0067	-0.0149	-0.0729	0.1986	-0.4123
	3	-0.0001	-0.0413	0.1018	-0.1170	-0.1889	-0.1936
	4	0.0003	-0.0665	-0.1536	0.0311	-0.1160	-0.1628
	5	-0.0113	0.0828	-0.0367	-0.0130	-0.0945	-0.0951
	6	0.0106	0.0880	-0.0224	0.0136	-0.1051	-0.1242

Contd.

Table 5.5 (Contd.)

1) Category-wise Means for All Spectral Bands

		Category (Rock Types)				
		Quartzite-1	Quartzite-2	Phyllites	Granite-1	Granite-2
TM Bands	1	81.36	58.47	76.00	67.68	51.13
	2	43.56	25.33	39.24	32.16	20.33
	3	58.88	27.27	54.80	38.36	18.53
	4	69.72	30.47	56.84	47.40	19.13
	5	147.32	71.07	128.12	89.16	34.13
	7	81.48	39.07	68.16	48.68	16.07

Category-wise Standard Deviations for All Spectral Bands

		Category (Rock Types)				
		Quartzite-1	Quartzite-2	Phyllites	Granite-1	Granite-2
TM Bands	1	8.9157	7.5863	12.8225	10.9688	8.5929
	2	8.5736	7.1481	8.8989	7.9251	5.7776
	3	14.6011	9.0116	13.3947	13.1208	4.9261
	4	17.3674	11.9754	14.9239	17.5381	8.8871
	5	28.6687	21.2249	28.7073	34.0877	18.4463
	7	14.2920	13.0245	18.9883	19.6823	9.5951

Matrix of Category-wise Transformed Means

		Category (Rock Types)				
		Quartzite-1	Quartzite-2	Phyllites	Granite-1	Granite-2
Principal Components	1	- 3.7433	- 2.5583	- 3.1470	- 0.9513	0.5927
	2	- 9.9835	- 4.4383	- 7.3359	- 6.1590	- 1.3712
	3	-47.5768	-22.8320	-40.1003	-29.2448	-10.7564
	4	-40.0958	-19.5094	-35.1891	-24.7998	-10.1613
	5	-22.0548	-10.3942	-18.9528	-13.1840	- 4.5779
	6	-21.2754	- 9.6676	-18.1242	-12.0817	- 3.4053

Matrix of Category-wise Transformed Standard Deviations

		Category (Rock Types)				
		Quartzite-1	Quartzite-2	Phyllites	Granite-1	Granite-2
Principal Components	1	0.6553	-0.4108	-1.0374	- 0.7741	-0.4835
	2	-1.6215	-2.1105	-3.3517	- 2.7614	-0.9744
	3	-9.0836	-7.3088	-9.8517	-11.2949	-6.1220
	4	-7.9206	-6.0652	-8.6014	- 9.1501	-4.5649
	5	-4.2218	-3.2242	-4.6133	- 5.2719	-2.5720
	6	-4.0300	-3.1764	-4.5533	- 5.2688	-2.5210

Contd.

Table 5.5. (Contd.)

(xii) Category-wise 95% Confidence Intervals in Different Principal Components

Rock Types	PC 1		PC 2		PC 3		PC 4		PC 5		PC 6	
	Min	Max	Min	Max	Min	Max	Min	Max	Min	Max	Min	Max
Quartzite-1	-5.0278	-2.4589	-6.8054	-13.1616	-29.7330	-65.3806	-24.5715	-55.6201	-13.7801	-30.3296	-13.3767	-29.171
Quartzite-2	-1.7532	-3.3634	-0.3018	-8.5748	-8.5066	-37.1573	-7.6216	-31.3972	-4.0748	-16.7136	-3.4420	-15.89
Phyllites	-1.1137	-5.1803	-0.7666	-13.9052	-20.7911	-59.4096	-18.3304	-52.0478	-9.9106	-27.9949	-9.1996	-27.048
Granite-1	-0.5660	-2.4686	-0.7466	-11.5714	-7.1068	-51.3828	-6.8657	-42.7340	-2.8511	-23.5169	-1.7548	-22.408
Granite-2	-1.5404	-0.3550	0.5386	-3.2809	1.2428	-22.7556	-1.2140	-19.1086	0.4633	-9.6190	1.5358	-8.342

N.B.

PC = Principal Component

Min (Minimum) = $\mu - 1.96\sigma$ Max (Maximum) = $\mu + 1.96\sigma$ where μ = transformed meanand σ = transformed standard deviation.

variance-covariance matrix shows that the off-diagonal elements, that is, the covariances are larger by comparison to at least one of the diagonal elements (band variances) in different pairs of spectral channels indicating considerable correlation among different spectral bands. This may be verified from the band correlation matrix which exhibits more than 95 percent correlation among the training reflectance of different spectral channels. However, in contrast to the training reflectance of MSS spectral bands, there is no inverse or negative correlation among the spectral responses of different spectral channels of TM data.

The results of principal components transformation presented in Table 5.5 show that the first principal component accounts for 97.6 percent of the total variance indicating that the digital image of this component will be able to provide almost the same amount of information contained in all the six spectral channels of TM data since these together constitute the total variance of 100 percent. Moreover, the very high variance of the first principal component is also suggestive of considerable amount of correlation among spectral channels. From the matrix of normalized eigenvectors and band-component correlation matrix, it may be noted that the first principal component is strongly dominated by contributions from band 4 with relatively small contributions from band 3. Principal component-2 is dominated by large contributions from band 5 with little contributions from bands 1 and 2 but adds only 0.01 percent of the total variance. The variances of the other principal components are so negligible that they are most likely to contain significantly large amount

of noise resulting in considerable loss of the useful information.

Finally, the supervised classification of the TM reflectance data was carried out in the same manner as that for the MSS data, following the procedure outlined in section 2.3.2.2.2. The confidence limits for different principal components shown in Table 5.5 reveal highly overlapping ranges for different rock types. It may be noted that even the litho-units corresponding to the illuminated and non-illuminated portions of each of the quartzites and the granites do not have distinct spectral separation. The only rock type which exhibits relatively smaller spectral overlap with the other rock types in all the principal components except the principal component-4 is the non-illuminated portion of the granite (that is, granite-2). This may be ascribed to the contrastingly low reflectance values of granite-2 ^{than the} other rock types. The considerable overlap of the confidence limits of rock types in different principal components could be attributed to the very high interband correlation of the training reflectance values of the rock types. It may also be observed from the confidence intervals of the rocks in different principal components that the minimum limits represent larger values while the maximum limits represent the smaller values. This may be attributed to the negative angle of rotation of the original bands as discussed in section 4.3.6 due to which the first principal components in most of the scatter plots pass across the distribution of data, thereby

100

accounting for smaller variances relative to the second principal components.

Since the approach of supervised classification for the transformed training reflectance data of rock types did not yield distinct confidence limits for any of the rock types, it was decided to perform the principal component analysis by taking into consideration the whole digital data of the six TM spectral channels. The results of principal component transformation of original TM bands are shown in Table 5.2. It may be seen that the total amount of variances accounted for by different principal components are comparable to the variances of the corresponding principal components estimated from the training reflectance of the rock types. The first three principal components account for 98.7 percent of the total variance. From the matrix of normalized eigenvectors and the band-component correlation matrix, it can be noted that the first principal component is dominated strongly by contributions from spectral bands 1 and 2 and less significantly from bands 3 and 4. The second principal component having 3.22 percent variance is dominated by contributions from band 4 and less significantly from bands 1, 2 and 3. The third principal component is dominated by almost equal contributions from spectral bands 4 and 5 but adds only 1.87 percent of the total variance. The first principal component dominated by bands 1 and 2 is sensitive to plant health and vigour and hence, should be useful in vegetation mapping. In addition, contributions of infrared energy from band 4 indicates its usefulness for geobotanical studies as well. The second principal component

being dominated by spectral band 4 and less significantly from bands 1, 2, and 3 should be useful for geobotanical mapping and also for delineation of drainage network. The third principal component dominated almost equally by bands 4 and 5 should be able to discriminate rock types based upon geobotanical relationship. The remaining principal components contain significantly very less percentages of variances and hence, are likely to exhibit very high degree of noise resulting in very poor contrast and loss of significant amount of information on the principal component images.

5.6.3 Image Interpretation and Results

It is very important to realize the approximate rule of thumb as stated below while interpreting the principal component pictures (Siegal and Gillespie, 1980, p 200). Very often in PCA, the first principal component image is just a weighted average picture of all the spectral channels, while the second principal component image is the difference between the least correlated bands, the third principal component is the difference between the next correlated bands and so on. Therefore, obviously the sixth principal component image represents the difference between the most correlated bands. As expected, the first principal component image brings out most of the information contained in the six spectral channels of TM data (Figure 5.10). Examination of the first principal component image which has been further Gaussian-stretched and histogram-equalized reveals that the whole granitic and gneissic terrain appears conspicuous by its brighter tonal appearance. The non-illuminated parts of the quartzitic

ridges have identical spectral signature as that of the granites and gneisses and hence, tend to be misclassified as the latter. In contrast, the illuminated parts of the quartzites exhibit very dark signature which indicates sharp deviation from their natural colour. The phyllites and schists are identifiable on the basis of their relatively even topography and generally darker signature with occasional presence of bright tones especially along the stream valleys.

The contrastingly brighter tone of the granitic terrain is suggestive of the strong manifestation of the geobotanical relationship and occurrence of a dense and healthy vegetation cover. This inference is, in fact, ascertained by the considerable contributions of visible wavelength energy from TM bands 1, 2 and 3, and short wavelength infrared energy from TM band 4 to the first principal component image. The dark signatures of the illuminated parts of the quartzites, and the phyllitic terrain may, therefore, be ascribed to the presence of less vegetation cover on them.

Comparison of the black and white image of TM band 5 (Figure 5.1) and the first principal component image reveals that the corresponding litho-units exhibit mutual reversal of their tonal signatures on the two images. Since the spectral signatures of TM band 5 image represent the natural tones (signatures) of the litho-units, the spectral signatures of the first principal component image certainly indicate an overall departure from the natural colours of the rock types present in the study area. This aspect of the first principal component

image may be attributed to the fact that the principal component images no longer represent one to one mapping between sensor wavelength bands and colours. Rather each colour now represents a linear combination of the spectral components (bands), making photointerpretation difficult. This is true particularly in geological studies where the emphasis is laid on the colour differences to discriminate among rock types. However, there being little interest in the meanings of actual colours to the structural features, they are expressed conspicuously on the image of principal component-1 due to increase in its overall information content.

The other principal component images convey significantly very less amount of information in proportion to their variances. The second and third principal component images, for example, appear tonally homogeneous, thereby making it extremely difficult to identify any of the litho-units. Likewise, due to the high noise level of the fourth, fifth and sixth principal component images, practically all information is lost in these images.

The false colour composite of principal components-1,-2, and -3 displayed as red, green, and blue colour respectively provides better colour manifestation of the various litho-units present in the study area (Figure 5.11). The band-component correlation matrix presented in Table 5.2 indicates that these three principal components are dominated by TM bands 1,2, and 4, band 4, and band 4 respectively which further suggest that the false colour composite of the first three principal components

should magnificently express the plant health and vigour, and the geobotanical relationship of the litho-units.

The granitic and gneissic rocks appear reddish indicating significant contributions from the first principal component suggesting a dense and healthy vegetation cover. The non-illuminated parts of the quartzite ridges show identical signature as that of the granites which is consistent with the results of discriminant function analysis of these two rocks as discussed in section 4.3.7.2.4. However, the illuminated parts of the quartzites convey greenish blue signature indicating strong blue contributions from principal component-3 and less significantly from principal component-2 (green). The considerably subdued spectral signature of the illuminated parts of the quartzites *as compared to* their non-illuminated parts indicates that the departure of the spectral signatures of the litho-units from their natural colours is also prevalent on the false colour composite of the first three principal components.

An interesting and significant observation that can be made on the FCC of the first three principal components is that the three litho-units namely the calc schists, phyllites and impure limestones, and the biotitic limestones and calc gneisses as shown in Figure 1.3 are resolved to a considerable extent on this composite image. These three litho-units convey identical spectral signatures, thereby appearing as a single litho-unit on the digital images generated by other image processing techniques. This observation makes the FCC of the first three principal components the unique image for being capable of demarcating all

the five litho-units present in the study area as shown in Figure 1.3. Therefore, this composite image has been used to prepare a lithological map of the TM study area. The wedge-like portion sandwiched between the granitic terrain on the left and the calc schists on the right may be identified as the biotitic limestones and calc gneisses in comparison with Figure 1.3. The green signature of this litho-unit is attributable to significant green contributions from the second principal component which is indicative of a generally thin vegetation cover. However, the presence of shades of brown and violet colour in this terrain is suggestive of the development of a moderately dense vegetation cover at these sites due to contributions from the first and third principal components. The calc schists may be identified by its dark brown signature and ridge like elongation with a NNE-SSW trend. The dark brown signature of this litho-units results due to significant red contributions from the first principal component with relatively less green contributions from the second principal component, which is indicative of a reasonably dense vegetation cover. The phyllites and impure limestones is conspicuous by its homogeneous greenish spectral signature and flat topography. The greenish signature of this litho-unit indicates contributions from the second principal component only which is suggestive of a thin vegetation cover. The fourth litho-unit is namely the granites and gneisses identified by its reddish signature and dissected appearance while the fifth litho-unit namely the quartzites is conspicuous by its ridges.

Unlike the false colour composites of the raw spectral bands, the false colour composite of the first three principal components drastically suppresses the various structural features of the study area.

5.7 INVERSE PRINCIPAL COMPONENT ANALYSIS

Following the procedure outlined in section 2.3.2.3, an inverse principal component image was generated by using the eigenvectors of the first inverse principal component which was further linearly stretched in order to accentuate its contrast (Figure 5.12). Examination of this black and white picture reveals significant reduction of its tonal contrast as compared to the first principal component image and the black and white images of the raw spectral bands. Nevertheless, the three main litho-units such as the granites, phyllites and schists, and the quartzites can be still identified on the basis of their topography and tonal differences. However, the illuminated portions of the quartzite ridges still convey subdued spectral signature ^{than} the non-illuminated portions. This feature of the inverse principal component image arises due probably to the redistribution of the information contained in the principal component images.

Likewise, examination of the false colour composite of the first three inverse principal component images in red, green, and blue colour combination (Figure 5.13) reveals that the various litho-units appear grossly homogeneous on this image owing to their nearly identical spectral signatures (that is, greenish yellow to yellow). It may be seen that as compared to

the false colour composites of the raw bands data and the principal components, there is drastic suppression of the colour contrast between the litho-units on the composite image of the inverse principal component images. The granitic and gneissic rocks are identifiable by their bright greenish yellow colour, whereas the terrain comprising the phyllites and schists may be distinguished from others on the basis of its even topography and light yellowish to violet signature. The violet colour of the illuminated parts of the quartzites makes it conspicuous and demarcable from their non-illuminated parts. However, the subdued appearance of the illuminated parts *as compared to* the non-illuminated parts of the quartzites indicates that the inversion of the principal components fails to bring the original colours of the surface features back onto the false colour composite of the inverse principal components.

5.8 CORRESPONDENCE ANALYSIS

5.8.1 Introduction

The procedure of the correspondence analysis has been outlined in detail in section 2.3.2.5. Table 5.6 lists the correspondence matrix or the similarity matrix 'S' derived by using equation (2.35), and the eigenvalues and the eigenvectors extracted from this matrix for different components of the correspondence analysis referred to as the correspondence components.

Evaluation of the similarity matrix 'S' reveals that the elements of the second and the third columns corresponding to

5.6 Correspondence Analysis Data Sheet for Thematic Mapper Data

Correspondence Matrix or Similarity Matrix (S)

		Bands					
		1	2	3	4	5	7
Bands	1	0.2112					
	2	0.1445	0.1003				
	3	0.1590	0.1113	0.1246			
	4	0.1720	0.1203	0.1342	0.1476		
	5	0.2329	0.1638	0.1841	0.1995	0.2794	
	7	0.1721	0.1215	0.1368	0.1474	0.2068	0.1552

Eigenvalues for Different Components ('COR' denotes Correspondence Components)

	$\lambda_1(\text{COR1})$	$\lambda_2(\text{COR2})$	$\lambda_3(\text{COR3})$	$\lambda_4(\text{COR4})$	$\lambda_5(\text{COR5})$
Variance	1.3103×10^{-2}	2.8355×10^{-3}	1.5374×10^{-3}	8.0841×10^{-4}	1.0867×10^{-4}
Total Similarity (%)	71.24	15.39	8.38	4.39	0.59
Total Similarity (Cumulative %)	71.24	86.63	95.01	99.40	100.00

Eigenvectors in Columns Corresponding to Correspondence Components

		j (Correspondence Components)				
		1	2	3	4	5
i (Bands)	1	-0.7071	0.3511	-0.2562	0.2121	-0.2490
	2	-0.2358	2.4411×10^{-2}	0.2350	-0.1979	0.8660
	3	-4.0685×10^{-2}	-6.5361×10^{-2}	0.5294	-0.6386	-0.4269
	4	-5.9707×10^{-2}	-0.8502	1.8332×10^{-2}	0.3531	-5.5412×10^{-2}
	5	0.4893	6.1980×10^{-2}	-0.6260	-0.2957	4.2637×10^{-2}
	7	0.4469	0.3809	0.4546	0.5439	-2.9893×10^{-2}

the TM spectral bands 2 and 3 respectively are similar, that is, the respective row elements of these bands do not vary significantly from each other. Therefore, these two spectral bands are expected to provide similar information which is also evident from their similar application potential. The similarity between these two bands can also be verified as per the criteria suggested by Davis (1986, p 506) for similarity measurement. This states that in order for the two variables (say, any two spectral bands) to qualify as a mutually high pair or a highly correlated pair, coefficients r_{ij} and r_{ji} must be the highest coefficients in their respective columns in the intervariable (or the interband) correlation matrix, where the notation r_{ij} represents the correlation coefficients. Inspection of the interband correlation matrix presented in Table 5.2 reveals that the highest coefficients of the second and third columns corresponding to the TM spectral bands 2 and 3 respectively (i.e. 0.9792) are mutual with regard to their positions in the matrix. Therefore, these two spectral bands may be considered similar. Similarly, since the coefficients $r_{7,5}$ and $r_{5,7}$ (Table 5.2) are found to be the highest coefficients (i.e. 0.9513) in the columns corresponding to the TM spectral bands 5 and 7 respectively, these two bands may be considered similar. Here, one might consider the spectral bands 1 and 5 similar on the basis of the closer resemblance of their respective row elements in the similarity matrix 'S' as compared to the corresponding elements of the spectral bands 5 and 7; however, since the highest coefficients of spectral bands 1 and 5 in the interband

carried out using only the first correspondence component image and the false colour composite since the images of the second to fifth components appear tonally homogeneous with significant reduction in the contrast resulting in severe loss of overall information.

Examination of the first correspondence component image (Figure 5.14) which has been Gaussian-stretched and histogram-equalized reveals that the contrast between the litho-units is comparable to that shown by the black and white image of the raw spectral band (Figure 5.1). However, comparison of the first correspondence component image and the first principal component image reveals that the tones (spectral signatures) of the corresponding litho-units are mutually reversed on these two images; that is, the litho-units appearing brighter on the principal component image are darker in appearance on the correspondence component image and vice-versa. For example, the granitic terrain has a brighter tone on the first principal component image (Figure 5.10) while it appears dark on the first correspondence component image. These observations may be explained by the fact that correspondence analysis provides a measure of the correspondence or similarity between raw spectral bands and hence, maintains the relationship between the original reflectance of different wavelength bands and colours. On the other hand, as mentioned earlier in section 2.3.2.3, principal component images do not provide a one to one mapping between the sensor wavelength bands and colours and rather, each colour represents a linear combination of the raw spectral bands.

Examination of the false colour composite of the first three correspondence components (Figure 5.15) reveals better colour contrast between the various litho-units than any other digital image. The granites and gneisses are identifiable by bluish green colour. The terrain comprising the phyllites and schists are conspicuous by their greenish yellow colour. The illuminated parts of the quartzite ridges appear yellowish red while the non-illuminated parts exhibit bluish green colour, identical to the granites. The bluish green (mid-cyan) colour of the granitic terrain results due to significant green and blue contributions from correspondence components-2 and -3 respectively indicating healthy and dense vegetation cover since the third correspondence component is dominated by TM spectral bands 2 and 3. It may be observed that the granitic terrain, at places, exhibits conspicuous presence of the spectral signature closely resembling the illuminated parts of the quartzites indicating misclassification of these two rock types. This observation is also consistent with the results of discriminant function analysis of these two rocks as discussed in section 4.3.7.2.4. The greenish yellow signature of the phyllitic terrain indicates significant contributions of red colour from the first correspondence component with relatively smaller green contributions from the second correspondence component. Since the first and second correspondence components are dominated commonly by spectral band 7, it indicates that the phyllitic rocks are generally devoid of clay minerals as reflected by considerable contributions (reflectance) from band 7. Moreover, since the

third correspondence component dominated by spectral bands 2 and 3 has no contributions to the spectral signature of the phyllites, it indicates that this rock type is covered by a sparse vegetation cover. The reddish pink (magenta) colour of the illuminated parts of the quartzites indicates significant red contributions from first^{the}/correspondence component (dominated by band 7) suggesting absence of clay minerals and development of a thin vegetation cover. On the other hand, ^a/detailed field observation is essential in order to ascertain the reasons for the bluish-green spectral signature of the non-illuminated parts of the quartzites on the composite image.

The false colour composite of the first three correspondence components brings about significant loss of the structural information of the study area. It may be seen that the fold is visible very indistinctly and the lineaments have almost disappeared on the composite image.

CHAPTER 6

AUTOMATIC CLASSIFICATION OF THE REMOTELY SENSED DIGITAL DATA

6.1 INTRODUCTION

In the present study, maximum likelihood method of supervised classification has been carried out in order to classify the thematic mapper data of Landsat-5 using all the spectral bands excluding the thermal band, that is, band 6. The various computational steps for this method of classification has been dealt with in detail in section 2.4. As mentioned therein, this classification has been performed by assuming equal a-priori probability of each class.

In order to account for the brightness variation of the litho-units due to varying illumination, the quartzites and the granites have been represented each by two different litho-units corresponding to their illuminated and the non-illuminated regions as seen on the false colour composites. Similarly, in order to reduce the effect of vegetation, two classes of vegetation cover have been incorporated in this classification. Consequently, eight classes including five classes of rocks have been selected on the false colour composite of TM spectral bands 4, 3 and 2 in red, green and blue combination (Figure 6.1). These are listed in Table 6.1.

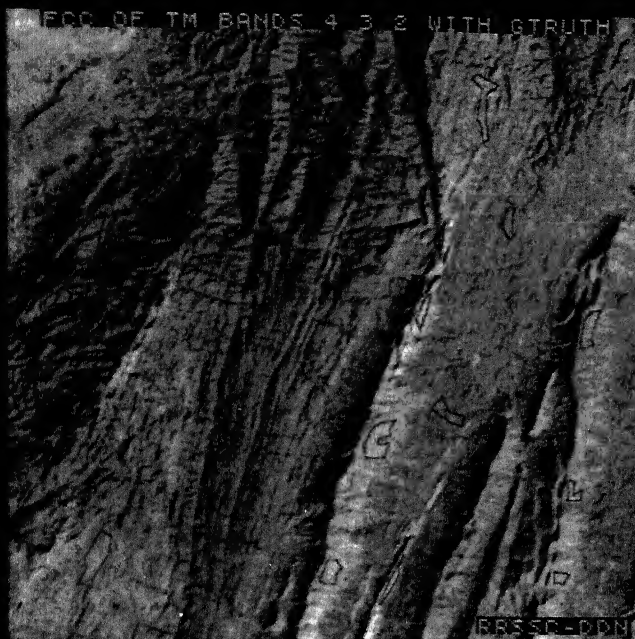


FIGURE 6.1 False colour composite of TM bands 4,3, and 2 in red, green and blue colour combination with Ground Truths.



FIGURE 6.2 Digital thematic image of TM Study area generated by using maximum likelihood classifier (using TM bands 1,2,3,4,5, and 7).

ble 6.1 Description of the Training Classes Used in Maximum Likelihood Classifier

Class Number	Class Name	Description	Colour on FCC	Number of training sets on FCC	Number of training pixels on FCC
	Vegetation-1	Forested area	Red	2	44
	Vegetation-2	Cultivated area	Light red	6	61
	Quartzite-1	Illuminated portions of quartzite ridges	Bright light green	8	1792
	Quartzite-2	Non-illuminated or shadowed portions of quartzite ridges	Dark green	5	657
	Phyllites	Even topography	Green	4	1662
	Granite-1	Illuminated portions of the granitic terrain	Light green	5	1810
	Granite-2	Non-illuminated portions of the granitic terrain	Dark green	5	354
	Water	-	Red patch	3 (points)	16

The ground truths (G-truth) for these classes were extracted through delineating polygons on their exposures in the FCC (Figure 6.1). The number of polygons delineated and the total number of training pixels for different classes are given in Table 6.1. The various statistical parameters such as the mean and variance-covariance matrix estimated for different classes from their training pixels are presented in Tables 6.2(a)-(h). These parameters are used in order to classify any unknown pixel based on the logic described in section 2.4. Also shown in the tables are the correlation matrix of each class. It has been assumed here that the training sets for each class used in the classification are normally distributed (i.e. Gaussian in nature).

In order to evaluate the spectral separability between different classes, the training set pixels of the classes were first classified. The result of this classification is presented in form of a contingency table or confusion matrix in Table 6.3. The table shows the actual categories in row and the predicted categories in columns where the actual categories are the ones already identified on the FCC of spectral bands 4, 3, and 2, and the predicted categories represent the categories chosen by the analyst. The objective is to classify the training pixels of the actual categories as one or more predicted categories on the basis of their spectral similarity determined by the maximum likelihood classifier. The diagonal elements of this table represent the number of training pixels of each category correctly classified and the off-diagonal elements represent the

Table 6.2(a) Statistical Information for the Category : Vegetation-1

Class Number : 1
No. of Pixels : 44

(i) Means and Standard Deviations (S.D.) for Different Bands

	Bands					
	1	2	3	4	5	7
Means	58.7045	26.6136	24.1591	74.5682	53.8182	21.0909
S.D.	2.9356	1.7349	3.0222	5.6141	6.6684	3.9647

(ii) Variance-Covariance Matrix

	Bands					
	1	2	3	4	5	7
1	8.6175					
2	3.6814	3.0098				
3	6.8198	4.6297	9.1338			
Bands 4	-4.9912	-1.6442	-5.5222	31.5178		
5	13.2645	7.0662	14.0063	-7.0558	44.4672	
7	8.0496	4.8760	8.9628	-5.9381	23.0166	15.7190

(iii) Correlation Matrix

	Bands					
	1	2	3	4	5	7
1	1.0000					
2	0.7228	1.0000				
Bands 3	0.7687	0.8830	1.0000			
4	-0.3028	-0.1688	-0.3255	1.0000		
5	0.6776	0.6108	0.6950	-0.1885	1.0000	
7	0.6916	0.7089	0.7480	-0.2668	0.8706	1.0000

Contd.

Table 6.2(b) Statistical Information for the Category : Vegetation-2

Class Number : 2
Number of Pixels : 61

(i) Means and Standard Deviations (S.D.) for Different Bands

	Bands					
	1	2	3	4	5	7
Means	68.5082	33.6393	37.9836	61.6721	92.5082	47.5738
S.D.	3.3761	2.6920	4.0911	7.1740	9.9912	6.4005

(ii) Variance-Covariance Matrix

	Bands					
	1	2	3	4	5	7
1	11.3979					
2	7.8885	7.2470				
3	11.9591	10.3547	16.7373			
Bands 4	8.2159	8.7672	8.8634	51.4664		
5	26.9553	21.4295	32.0247	21.5277	99.8245	
7	15.3809	12.0595	18.8126	3.7949	58.0366	40.9661

(iii) Correlation Matrix

	Bands					
	1	2	3	4	5	7
1	1.0000					
2	0.8680	1.0000				
Bands 3	0.8658	0.9402	1.0000			
4	0.3392	0.4540	0.3054	1.0000		
5	0.7991	0.7967	0.7834	0.3003	1.0000	
7	0.7118	0.6999	0.7184	0.0826	0.9075	1.0000

Contd.

Table 6.2(c) Statistical Information for the Category :
Quartzite-1 (Illuminated part)

Class Number : 3
Number of Pixels : 1792

(i) Means and Standard Deviations (S.D.) in Different Bands

	Bands					
	1	2	3	4	5	7
Means	88.8432	46.4894	64.8666	72.9570	150.8147	83.9615
S.D.	4.2961	3.5596	6.2069	6.3947	12.5030	7.7061

(ii) Variance-Covariance Matrix

	Bands					
	1	2	3	4	5	7
1	18.4567					
2	12.7245	12.6705				
3	19.3745	20.0267	38.5262			
Bands 4	14.2971	16.7006	32.2991	40.8926		
5	16.0199	19.1441	45.8297	46.5718	156.3246	
7	8.0248	9.7169	25.1220	19.9291	84.8500	59.3841

(iii) Correlation Matrix

	Bands					
	1	2	3	4	5	7
1	1.0000					
2	0.8321	1.0000				
Bands 3	0.7266	0.9064	1.0000			
4	0.5204	0.7337	0.8137	1.0000		
5	0.2982	0.4301	0.5905	0.5825	1.0000	
7	0.2424	0.3542	0.5252	0.4044	0.8806	1.0000

Contd.

Table 6.2(d) Statistical Information for the Category :
Quartzite-2 (Non-illuminated part)

Class Number : 4
Number of Pixels : 657

i) Means and Standard Deviations (S.D.) in Different Bands

	Bands					
	1	2	3	4	5	7
Means	54.0335	21.1111	21.9361	21.1020	34.4247	17.8478
S.D.	3.5327	2.9250	4.7765	6.4643	13.2071	7.0126

ii) Variance-Covariance Matrix

	Bands					
	1	2	3	4	5	7
1	12.4800					
2	8.3738	8.5554				
3	13.6886	13.0802	22.8148			
Bands 4	17.1793	16.5336	27.6230	41.7862		
5	31.5902	29.2314	49.9663	66.3997	174.4271	
7	15.2456	15.1752	24.6113	31.6076	80.1757	49.1762

(iii) Correlation Matrix

	Bands					
	1	2	3	4	5	7
1	1.0000					
2	0.8104	1.0000				
Bands 3	0.8112	0.9362	1.0000			
4	0.7523	0.8744	0.8946	1.0000		
5	0.6770	0.7567	0.7921	0.7777	1.0000	
7	0.6154	0.7398	0.7348	0.6972	0.8657	1.0000

Contd.

Table 6.2(e) Statistical Information for the Category : Phyllites

Class Number : 5

No. of Pixels : 1662

i) Means and Standard Deviations (S.D.) for Different Bands

	Bands					
	1	2	3	4	5	7
Means	77.5860	40.7750	53.4922	56.5668	118.6005	70.6432
S.D.	4.8562	3.9921	6.7580	7.0945	15.4059	9.0491

ii) Variance-Covariance Matrix

	Bands					
	1	2	3	4	5	7
1	23.5827					
2	16.0692	15.9372				
3	25.2558	25.3513	45.6709			
bands 4	25.0435	24.8538	43.7214	50.6709		
5	51.7512	45.3276	78.4474	81.6194	237.3431	
7	25.9752	25.6223	44.5057	42.9313	114.3782	81.8860

iii) Correlation Matrix

	Bands					
	1	2	3	4	5	7
1	1.0000					
2	0.8289	1.0000				
bands 3	0.7696	0.9397	1.0000			
4	0.7269	0.8775	0.9119	1.0000		
5	0.6917	0.7370	0.7535	0.7468	1.0000	
7	0.5911	0.7093	0.7278	0.6687	0.8204	1.0000

Contd.

Table 6.2(f) Statistical Information for the Category :
Granite-1 (Illuminated part)

Class Number : 6
No. of Pixels : 1810

(i) Means and Standard Deviations (S.D.) for Different Bands

	Bands					
	1	2	3	4	5	7
Means	65.0265	30.0680	36.2972	48.2541	84.9503	42.6017
S.D.	5.2117	4.3883	7.2426	10.2842	22.9273	12.8397

(ii) Variance-Covariance Matrix

	Bands					
	1	2	3	4	5	7
1	27.1617					
2	20.3154	19.2568				
3	33.4088	30.5942	52.4552			
Bands 4	45.3319	39.8402	66.8980	105.7652		
5	97.1232	82.7138	139.1694	194.9798	525.6591	
7	53.2895	45.4531	76.0283	100.9426	268.6270	164.8584

(iii) Correlation Matrix

	Bands					
	1	2	3	4	5	7
1	1.0000					
2	0.8883	1.0000				
Bands 3	0.8851	0.9626	1.0000			
4	0.8458	0.8828	0.8981	1.0000		
5	0.8128	0.8822	0.8381	0.8269	1.0000	
7	0.7963	0.8067	0.8176	0.7644	0.9125	1.0000

Contd.

Table 6.2(g) Statistical Information for the Category :
Granite-2 (Non-illuminated part)

Class Number : 7
No. of Pixels : 354

(i) Means and Standard Deviations (S.D.) for Different Bands

	Bands					
	1	2	3	4	5	7
Means	49.7768	17.2316	15.1864	13.1102	16.2232	8.1469
S.D.	3.1342	1.8754	2.9572	5.1241	8.3438	4.2194

(ii) Variance-Covariance Matrix

	Bands					
	1	2	3	4	5	7
1	9.8231					
2	4.6223	3.5170				
3	7.6009	5.0472	8.7449			
Bands 4	13.1630	8.7428	14.3072	26.2562		
5	19.7248	12.7760	21.0573	37.0150	69.6197	
7	9.2644	6.3247	10.0687	17.6646	32.5520	17.8033

(iii) Correlation Matrix

	Bands					
	1	2	3	4	5	7
1	1.0000					
2	0.7864	1.0000				
Bands 3	0.8201	0.9101	1.0000			
4	0.8196	0.9098	0.9442	1.0000		
5	0.7543	0.8165	0.8534	0.8657	1.0000	
7	0.7005	0.8993	0.8069	0.8170	0.9246	1.0000

Contd.

Table 6.2(h) Statistical Information for the Category : Water

Class Number : 8
No. of Pixels : 16

(i) Means and Standard Deviations (S.D.) for Different Bands

	Bands					
	1	2	3	4	5	7
Means	54.3750	22.3750	22.7500	21.0000	29.4375	17.8750
S.D.	3.7396	3.6379	5.8041	9.8679	13.1860	8.3955

(ii) Variance-Covariance Matrix

	Bands					
	1	2	3	4	5	7
1	13.9844					
2	12.6719	13.2344				
3	19.9063	20.0938	33.6875			
Bands 4	29.8125	27.8125	51.2500	97.3750		
5	43.7734	40.2734	67.9219	114.9375	173.8711	
7	29.1094	27.8594	45.8438	73.6250	108.3672	70.4844

(iii) Correlation Matrix

	Bands					
	1	2	3	4	5	7
1	1.0000					
2	0.9315	1.0000				
Bands 3	0.9171	0.9516	1.0000			
4	0.8079	0.7747	0.8948	1.0000		
5	0.8877	0.8396	0.8875	0.8827	1.0000	
7	0.9272	0.9122	0.9408	0.8887	0.9789	1.0000

Table 6.3 Contingency Table or Confusion Matrix of G-Truths

PREDICTED CATEGORY

	Veg-1	Veg-2	Qtz-1	Qtz-2	Phyl	Gran-1	Gran-2	Water	Other Pixel	To
Veg-1	40	0	0	0	0	0	0	0	4	
Veg-2	2	52	0	0	1	3	0	0	3	
Qtz-1	0	1	1584	0	123	6	0	0	78	1
Qtz-2	0	0	0	373	0	17	153	80	34	
Phyl	0	14	113	0	1430	32	0	0	73	1
Gran-1	0	83	1	83	29	1434	9	23	148	1
Gran-2	0	0	0	27	0	5	315	7	0	
Water	0	0	0	0	0	0	2	14	0	
Total *	42	150	1698	483	1583	1497	479	124	340	
Accu- racy** (%)	95.4	245.9	94.7	73.5	95.2	82.7	135.3	775		

I.B.: (i) Veg-1 = Vegetation-1, Veg-2 = Vegetation-2, Qtz-1 = Quartzite
Qtz-2 = Quartzite-2, Phyl = Phyllites, Gran-1 = Granite
Gran-2 = Granite-2.

(ii) '*' represents the total number of training pixels of actual categories classified as each predicted category; this is obtained by summing up the numbers in each column. For example, the number of training pixels of the various actual categories classified as the predicted category vegetation-1, is equal to 42.

(iii) '**' represents the percentage by which an actual category is represented on the digital classified image. For an actual category (say, Veg-1), this is obtained by dividing the total number of pixels of various actual categories in rows classified as the predicted category Veg-1 (i.e. the sum of the elements in the column corresponding to the predicted category, Veg-1) by the actual number of training samples extracted for that actual category, i.e. Veg-1. For example, for Vegetation class, this may be determined by dividing 42 by 44, then taking the percentage, that is, $(42/44) \times 100 = 95.4$.

number of incorrectly classified pixels of each actual category as the various predicted categories. In an ideal case, the off-diagonal elements should be equal to zero, indicating no misclassification. The numbers of correctly classified pixels and the incorrectly classified pixels in the confusion matrix can be expressed in percentages as shown in Table 6.4.

In the next step, the digital data of the entire subscene were classified in order to generate a digital classified or thematic image as shown in Figure 6.2.

6.2 INTERPRETATION OF CONFUSION MATRIX AND DIGITAL THEMATIC IMAGE

Analysis of the contingency table (Table 6.3) reveals that no class was classified upto 100 percent accuracy. The individual rock type accuracies ranged from 56.8 percent for quartzite-2 to 90 percent accuracy for granite-2. However, forested area (class 4) also exhibits very high degree of classification accuracy of 90.9 percent (Table 6.4). Overall classification accuracy was 81.96 percent. 5242 pixels correctly classified out of 6396 pixels sampled. Likewise, out of 6396 pixels sampled, 340 pixels (i.e. 5.32 percent) were unclassified, that is, they did not belong to any predicted class. Among the five predicted classes of rock types chosen, granite-2 was found to be the most misclassified class with the total number of training samples of all the actual categories misclassified as granite-2 being the largest, that is, 36.3 percent while the quartzite-2 proved to be the least misclassified class (6.85 percent). The contingency table (Table 6.4) also shows that with the exception of the water class, the cultivated cover class (class 2) was found to be the

Table 6.4 Confusion Matrix of Training Classes, in percentage

PREDICTED CATEGORY

		Veg-1	Veg-2	Qtz-1	Qtz-2	Phyl	Gran-1	Gran-2	Water	Other Pixel	Total
A	Veg-1	90.9	0	0	0	0	0	0	0	9.1	100
C	Veg-2	3.3	85.2	0	0	1.6	4.9	0	0	4.9	100
T	Qtz-1	0	0.05	88.4	0	6.9	0.33	0	0	4.35	100
A	Qtz-2	0	0	0	56.8	0	2.6	23.3	12.2	5.2	100
L	Phyl	0	0.8	6.8	0	86.0	1.9	0	0	4.4	100
C	Gran-1	0	4.6	0.05	4.6	1.6	79.2	0.5	1.3	8.2	100
A	Gran-2	0	0	0	7.6	0	1.4	90.0	2.0	0	100
T	Water	0	0	0	0	0	0	12.5	87.5	0	100
E	Total *	3.3	5.45	6.85	12.2	10.1	11.13	36.3	15.5		

N.B.: (i) Veg-1 = Vegetation-1, Veg-2 = Vegetation-2, Qtz-1= Quartzite-1, Qtz-2 = Quartzite-2, Phyl = Phyllites, Gran-1 = Granite-1, Gran-2 = Granite-2.

(ii) '*' represents the total percentage of samples of actual categories misclassified as a predicted category; obtained by summing up the off-diagonal elements in the columns for respective predicted category. For example, the various actual categories misclassified as the predicted category Granite-2 is obtained by summing up the off-diagonal elements in its column, that is, $23.3 + 0.5 + 12.5 = 36.3$. Granite-2 is the most misrepresented class on the digitized thematic image.

most dominantly represented class on the classified image since it is represented by 245.9 percent of its actual number of training pixels sampled. Quartzite-2 is the least represented class, it being correctly represented by 73.5 percent of its actual number of pixels sampled. These observations indicate that most of the rock types show greater spectral affinity towards vegetation-2 (class 2) ^{than} vegetation-1 (class 1). Besides, granite-2 is also represented by a larger percentage (135.3 percent) in terms of its actual number of training samples.

Further analysis of the contingency table (Table 6.3) reveals that out of the ten rock pairs possible, seven rock pairs exhibit distinct spectral separation of the rocks; these are namely quartzite-1 - quartzite-2, granite-1 - granite-2, phyllites - quartzite-2, phyllites - granite-1, phyllites - granite-2, quartzite-1 - granite-1, and quartzite-1 - granite-2. In fact, except the rock pairs phyllites - granite-1 and quartzite-1 - granite-1, all the other five rock pairs show very little misclassification in their respective discriminant function analysis (Table 4.2). On the other hand, quartzite-2 misclassified as granite-2 to an extent of 23.3 percent while granite-2 misclassified as quartzite-2 by only 7.6 percent. If we assign equal weightage to both these classes, that is, if the number of training pixels of both be considered equal, then also it results in a lower misclassification of granite-2 as quartzite-2. This observation indicates that quartzite-2 has greater spectral affinity towards granite-2 ^{in comparison to} what

granite-2 shows towards quartzite-2. The misclassification of these rocks has also been observed in their two-dimensional discriminant function analysis described in section 4.3.7.2. Likewise the phyllites and quartzite-1 show a mutual misclassification of 6.8 to 6.9 percent. The third pair showing misclassification is granite-1 and quartzite-2. Granite-1 misclassified as quartzite-2 by 4.6 percent while quartzite-2 misclassified as granite-1 by 2.6 percent. The degree of misclassification between various rocks as shown by the maximum likelihood classifier is significantly lower as compared to their corresponding degree of misclassification revealed by the discriminant function analysis. The generally greater misclassification of the rocks in bivariate discriminant function analysis *as compared to* the multivariate (> 2 bands) maximum likelihood method of classification results probably both due to the significantly very small number of training samples and also less number of spectral bands used in the former.

Examination of the digital thematic image (Figure 6.2) reveals that the illuminated parts of the quartzitic terrain (quartzite-1) sharply demarcate from the non-illuminated parts (quartzite-2) on the basis of the colour difference. The illuminated parts of the quartzites show occasional presence of spectral signature of illuminated parts of the granites (granite-1) but the shadowed parts of the quartzites is marked frequently by the presence of spectral signatures of the phyllites and the granite-2. The illuminated parts of the granitic rocks are conspicuous by their dark brown signature and

completely demarcate from their non-illuminated parts showing yellow colour. The granitic rocks, neither in their illuminated parts nor in the shadowed parts, exhibit presence of spectral signature of any other rock type. These observations are, in fact, consistent with the classification accuracies of the quartzites and the granites shown in the confusion matrix (Table 6.3). The phyllitic rocks can be distinguished from the other rock types on the basis of their even topography and greenish colour. The terrain comprising the phyllites and schists is also marked by the presence of spectral signatures closely resembling the granite-1 (illuminated), which is indicative of the presence of a fourth litho-unit. In fact, the presence of the fourth litho-unit has been observed more conspicuously on the false colour composite of the first three principal components (Figure 5.11) and has been identified as the calc schists with regard to its relative position on the geological map published by the Geological Survey of India (Figure 1.3).

Comparison of the digital thematic image and the published geological map (Figure 1.3) reveals that there is no sharp demarcation of different litho-units on the digital image vis-a-vis their positions on the published map. Out of the five litho-units shown on the published map only three can be clearly demarcated on the basis of the differences in their colours such as the granites, the phyllites and schists, and the quartzites. The similar spectral signatures of the Erinpura granites and gneisses, and the biotitic limestones and the calc gneisses and consequently, their occurrence as a single litho-unit on the

classified image may be attributed to their identical constituent minerals and moreover, to the confusing influence of vegetation cover developed on them. Likewise, the intermixing of the phyllites and impure limestones with the calc schists may be explained by the same factors. On account of the reasons cited above, supervised classification of rock types using remotely sensed data is not a good proposition from application point of view.

It may be seen that the digital thematic image brings about considerable suppression of the various structural features such as the lineaments and the fold at the SW corner as a result of classifying the digital reflectance values as the various predefined classes.

CHAPTER 7

SUMMARY AND CONCLUSIONS

In the present study, an attempt has been made to carry out lithological discrimination in parts of Rajasthan state (India) using satellite remote sensing data through application of various image processing techniques. The study area has been purposefully selected in the semi-arid to arid regions of the Aravalli Mountain Ranges which provide adequate rock exposures to carry out the research in a satisfactory manner. The research has been carried out in two phases in two different areas : one through the analysis of MSS data from Landsat-2 (referred to as the MSS study area situated in Sirohi District) and the other through the analysis of TM data from Landsat-5 (referred to as the TM study area, the major part of which lies in Udaipur District and a smaller part in Pali District). The MSS area comprises seven rock types belonging to the Aravalli Supergroup and Erinpura granites and gneisses. The major rock types present in the area are Gneiss, Schist (GNSC), Quartz Mica Schist (QMS), Intercalated Calc and Cherty Quartzite, Marble, Phyllite (ICCQMP), Calc Gneiss, Granite and Syenite. On the other hand, the TM study area comprises five litho-units namely Phyllites and Impure Limestones, Biotitic Limestones and Calc Gneisses, Calc Schists and Quartzites belonging to Ajabgarh Series of Delhi Supergroup, and Erinpura granites and gneisses.

Spectral discrimination among the rocks of MSS study area has been carried out resorting only to the graphical analysis of MSS digital data. However, lithological discrimination in TM study area is mainly based upon the analysis and interpretation of digital images generated by applying various image processing techniques in conjunction with statistical and graphical analyses of TM data. The MSS study area was windowed with reference to the corner coordinates of the entire MSS scene. The window data was then corrected for geometric distortion applying the nearest neighbourhood sampling method. On the other hand, the TM study area was demarcated on the digital image of the entire TM scene displayed on the colour monitor screen by matching the features of the image with those on a large scale toposheet of TM study area.

The entire operation involved in the present study has been carried out mainly in three stages. The first stage comprises a field trip including the study of the field occurrence of the litho-units present in both the MSS and TM study areas, collection of rock samples from representative sites, and mineralogical and spectroscopic analyses of rock samples in the laboratory. During field survey, it was observed that the rocks are in general unweathered in most part of their exposed cover. The mineralogical analysis performed through the microscopic and XRD studies of rock samples reveals that the rocks of MSS and TM study areas are composed mainly of silicates such as quartz, feldspars, pyroxenes, hornblende and mica. Iron impurities are common in all the rocks. The gneissic rocks (augen gneiss) of MSS

study area being partly weathered is found to consist of clay mineral (Kaolinite). In TM study area, calc gneiss and impure limestones consist of appreciable amount of calcite and dolomite. Tremolite schist being intensely weathered contains reasonable amount of kaolinite while hornblende schist shows presence of chlorite. On the other hand, the laboratory-derived visible and near infrared diffused reflectance curves of the rock samples show that the various rocks of MSS and TM study areas may be arranged as granite, phyllite and schist, gneiss, quartzite and limestone in order of their increasing reflectance. Of special significance to the present study is that different rock types have strikingly different albedos but similar reflectance spectra, that is, the slopes of their spectra are same.

The next two stages deal with the analysis and interpretation of the remotely sensed digital data for lithological discrimination. The second stage comprises graphical analysis of digital data while in the third stage, analysis and interpretation of the digital images generated by applying various image processing techniques have been carried out. Out of the seven litho-units present in MSS study area, only four have been considered for analysis such as GNSC, QMS, ICCQMP and Granite because these four units cover more than eighty percent of the study area and all other litho-units are too small in area to be resolved through the statistical and graphical analyses of digital data. Similarly, for TM study area, only three litho-units have been considered for analysis since these could be identified and demarcated on the basis of their differences in

spectral signatures on the FCCs of raw bands data. These are namely the granites and gneisses, phyllites and schists, and quartzites. In the present study, an attempt has been made to evaluate the effects of brightness variation on the discrimination of the rock types. Since digital images have been generated only for the TM study area, it was possible to identify the illuminated and non-illuminated (shadowed) parts of different rock types of only this study area on the FCCs and digital images. For example, owing to brightness variation of the two litho-units namely granites and gneisses, and the quartzites induced by topography, each of them is represented in the analysis by two separate litho-units corresponding, respectively, to the illuminated (bright) and the non-illuminated (shadowed) portions of their terrains. Training reflectances were extracted for the various litho-units of MSS and TM study areas in proportion to their areal extent.

In the graphical analysis, histograms of training data of the rocks in different bands show that each rock of MSS and TM study areas is associated with the spectral characteristics of the other rocks in the respective study areas as evident from the presence of at least 2 to 3 distinct peaks in each histogram. The coincident spectral plots depict considerable overlap between various rocks of MSS study area while the various litho-units of TM study area are fairly separable. Histograms of selected MSS band ratios plotted for the various rocks of MSS study area reveal nearly equal relative frequencies for different rock types in the highest frequency bars indicating that all the rock types

will be equally conspicuous on the ratio images. On the other hand, while the histogram of TM 2/3 reveals good discrimination of ^{both} parts of the quartzites and the illuminated part of the granites, ratio images of TM 3/4 and 4/5 each provide good discrimination of the illuminated parts of the quartzites and granites. The scatter diagrams for two-dimensional principal component analysis in different MSS band pairs depict distinct clusters of the training sets of different rock types; however, each cluster consists of almost equal number of training pixels of different rock types indicating considerable intermixing among them. The scatter diagrams for PCA of TM data show that the training data of the rock types are elliptically distributed, thereby indicating considerable interband correlation. Discriminant function analysis (DFA) for the rocks of MSS study area reveals considerable intermixing between different rocks. In TM study area, the illuminated and non-illuminated units of the quartzites are largely discriminated in their scatter diagrams for DFA. Phyllites and the illuminated unit of the quartzites show considerable extent of intermixing while there is little intermixing between the phyllites and the shadowed parts of the quartzites. Similarly, while the phyllites show considerable degree of intermixing with the illuminated parts of the granites, there is little intermixing between the former and the non-illuminated parts of the granites. DFA of various sub-pairs of the quartzitic and granitic rocks reveals little to moderate amount of intermixing; however, there is no intermixing

between the illuminated parts of the quartzites and the non-illuminated parts of the granites.

In the present study, digital images have been generated and analyzed for TM study area only, that is, the area studied by using TM data. The false colour composites generated by applying the criteria of Optimum Index Factor reveal three litho-units on the basis of differences in spectral signatures and topography. These are namely the quartzites identified by their ridges, the phyllites and schists by their even topography, and the granites and gneisses by their dissected appearance. Of the various ratio images generated, only the ratio picture of TM 4/5 provides good tonal contrast among the various litho-units which has been attributed to the varying density of vegetation cover developed on different rocks. The FCCs of band ratios, however, provide better discrimination of the various litho-units and also, clearly delineate the distribution of vegetation. The granitic terrain is densely vegetated while there is a sparse vegetation cover on the phyllitic and quartzitic terrains. The FCCs of ratio images show identical spectral signatures for the phyllites and the illuminated parts of the quartzites and similarly, for the non-illuminated parts of both of the quartzites and granites. This observation may be attributed to the brightness variation in the quartzitic and granitic rocks and also, occurrence of similar slopes in the reflectance spectra of different rock types. The observations made on the ratio images and FCCs of band ratios are found to be fairly consistent with the results of the histogram analysis of corresponding band ratios. The colour

composite image of the brightness and greenness indices highlighted the vegetated and barren areas of the TM study area. Of the five component images generated by applying the technique of correspondence analysis, only the first component image brings about significant tonal contrast between various litho-units since it accounts for more than 70 percent similarity. The FCC of the first three correspondence component images provides better colour contrast between various rock types than any other digital image. The granitic terrain, at places, exhibits spectral signatures of the illuminated parts of the quartzites indicating misclassification of these two litho-units. In the domain of multivariate PCA, supervised classification of principal components based on the 95% confidence intervals of the rock types did not yield any satisfactory result since all the rock types of both MSS and TM study areas have highly overlapping ranges in different principal components. Therefore, principal component images were generated for TM data using the whole digital data of the six TM bands (i.e. bands 1 to 5 and 7). The first PC image provides better demarcation of the various litho-units than the others since it accounts for more than 90 percent of variance.

One of the most significant findings of the present study is that the FCC of the first three principal components demarcates all the five litho-units present in the TM study area mapped earlier by the Geological Survey of India on the basis of the differences in spectral signatures and topography. The three litho-units viz. Phyllites and Impure Limestones, Biotitic

Limestones and Calc Gneisses, and Calc Schists, which appear as a single litho-unit on the other digital images owing to their nearly identical spectral signatures, are resolved to a considerable extent on the FCC of the first three principal components. Therefore, a geological map has been prepared from this composite image and is shown in Figure 7.1. The illuminated and non-illuminated portions of the quartzitic ridges have been mapped together for obvious reasons. Comparison of this geological map with the published geological map does not reveal much difference in the dispositions of the rock types. However, there being no sharp discrimination in the spectral signatures of the two litho-units viz. the granite and gneisses, and the calc schists on their northern parts on the FCC of the first three principal component images, their contact has been located approximately.

A structural map of the TM study area prepared from various digital images is shown in Figure 7.2. The structural map shows a major fault striking NNW-SSE and two minor faults striking almost eastwest. The major fault truncates the various litho-units including one of the quartzitic ridges. The minor faults have probably caused gradual narrowing of the quartzitic ridges from southwest to northeast. A fold conspicuously present at the SW corner in the terrain of biotitic limestones and calc gneisses with its axis trending NE-SW is also shown in the structural map. The map shows four sets of lineaments trending SE-NW, SEE-NWW, NNW-SSE, and SW-NE respectively. Detailed studies of the various

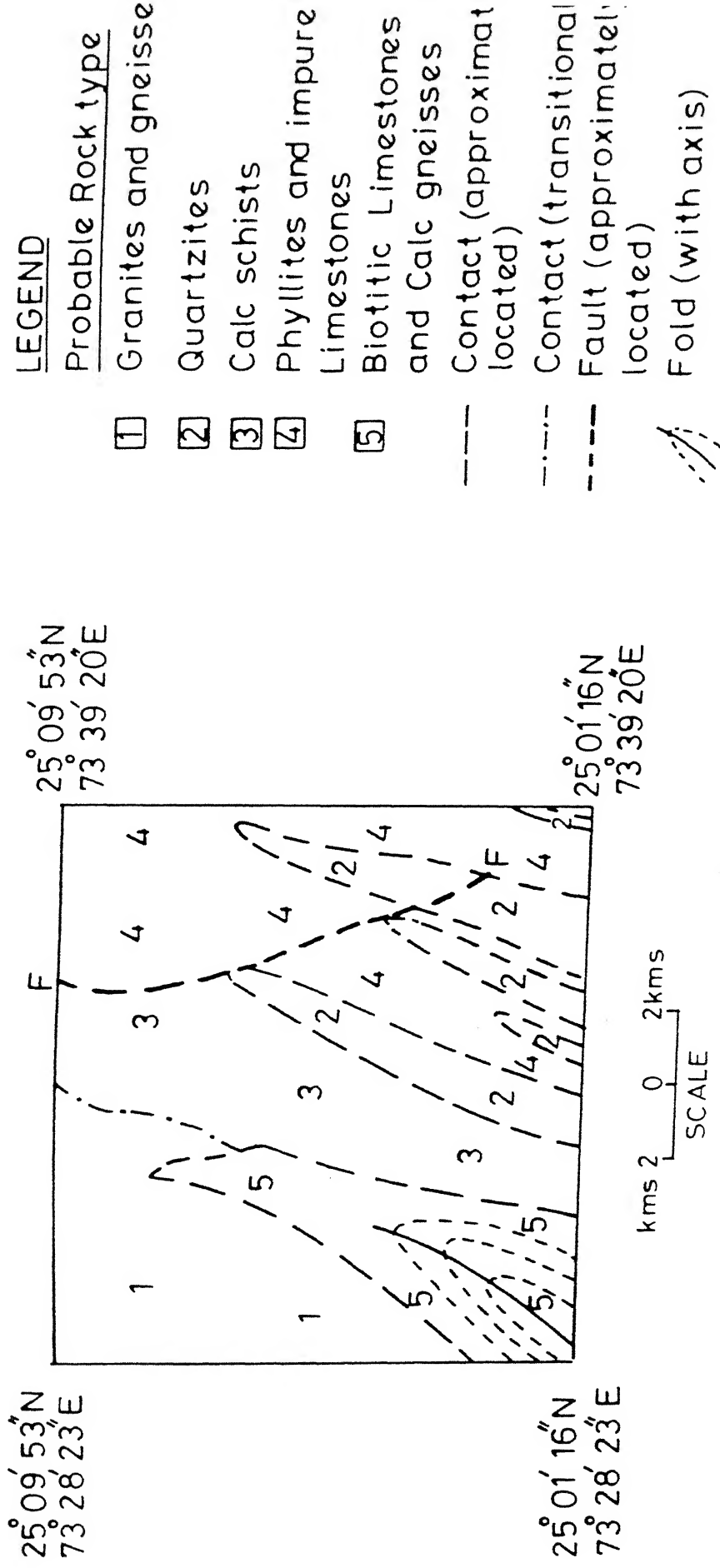


FIGURE 7.1 Geological map of the TM area prepared from the FCC of the principal components -1, -2 and -3 in red, green, and blue colour combination.

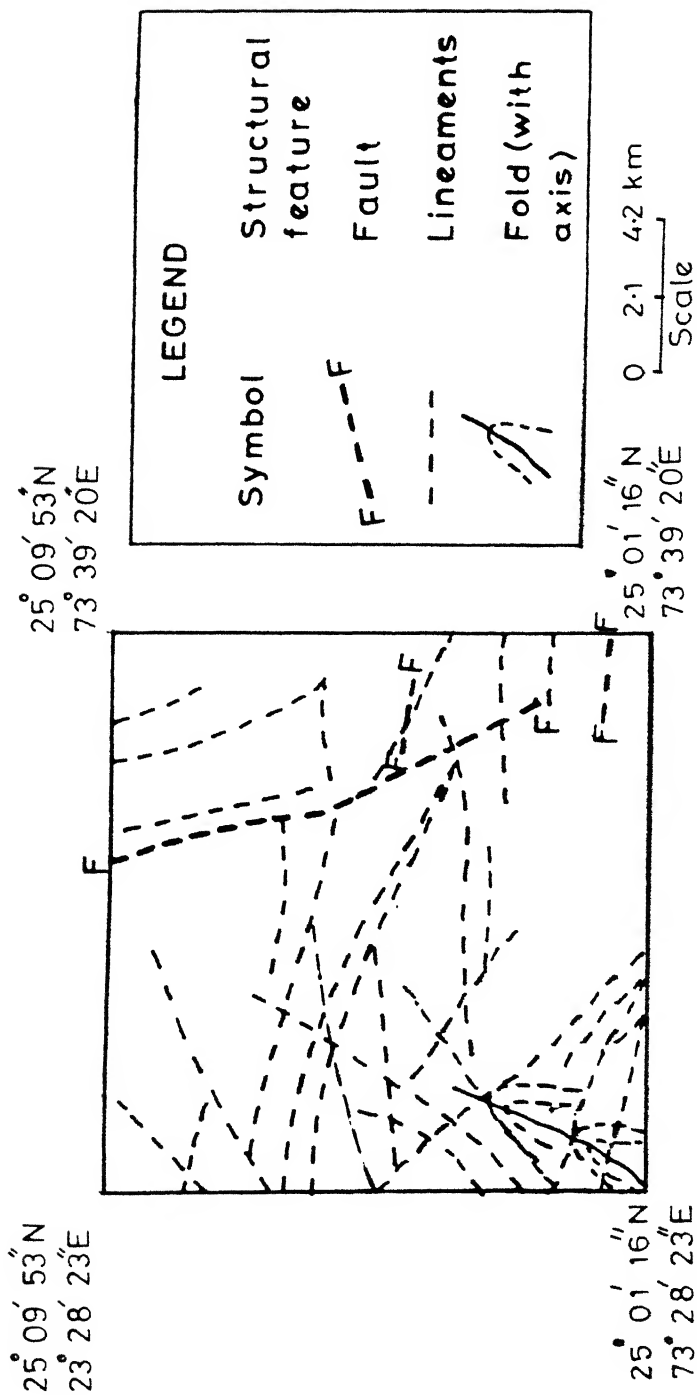


FIGURE 7.2 Structural map of the TM area prepared from the digital images.

structural features on the digital images may be carried out to reconstruct the tectonic history of the study area.

Supervised classification has been carried out for TM study area using eight classes including five litho-units (that is, the illuminated and shadowed parts of each of the quartzites and granites considered separately and the phyllites), two agriculture classes, and water applying Maximum Likelihood classifier. The classification yielded an overall accuracy of 82 percent for the training data sets of rock types. The digital thematic image, however, reveals that there is no sharp discrimination among the various litho-units.

The results obtained from the various approaches adopted in the present study have been found to fairly agree with each other. The considerably larger discriminations of the rocks of TM study area as compared to the rocks of MSS study area as revealed by the various graphical analyses of the training data of the rocks arises as a result of taking into account the brightness variation of the rocks of TM study area and consequently, considering their illuminated and non-illuminated portions separately in the analysis. The study has also shown that brightness variation can cause considerable degree of misclassification among the rock types on the digital images. The capability of the FCC of the first three principal components to resolve all the five litho-units mapped by the Geological Survey of India is attributable to the considerable interband decorrelation of the TM data. On the other hand, the misrepresentation (or misclassification) of various litho-units

on the other digital images may be attributed to the similar spectral characteristics of the rock types (as seen in their laboratory derived diffused reflectance spectra) caused due to their identical mineralogical composition and development of uniform density of vegetation cover. Finally, a ranking table has been prepared on the basis of the capabilities of the different image processing and pattern recognition techniques employed in the study for lithological discrimination in the TM study area (Table 7.1).

The present study has been carried out with limited laboratory investigations. Therefore, in order to thoroughly understand the relationship between the mineralogy and reflectance of rocks, detailed analysis of laboratory reflectance spectra is necessary. Moreover, thorough analysis of field reflectance spectra will be able to provide significant informations desired in the interpretation of the remotely sensed digital images. Since the rocks of the study areas contain mostly silicate minerals, it is suggested that analysis of thermal infrared data may be carried out in order to obtain better discrimination among rock types as reported by various workers (Bartholomew et al., 1989; Eberhardt et al., 1987; Kahle, 1987). In addition, application of fuzzy pattern recognition techniques to remotely sensed digital data might prove to be more useful for lithological discrimination.

Table 7.1 Ranking Table of Various Methods Employed in the Present Study for Lithological Discrimination.

Sl.No.	Methods Employed	Number of Rock Types Correctly Classified	Percentage of Accuracy
1.	Band Ratioing	3	66.66
2.	Principal Component Analysis	5	100
3.	Inverse Principal Component Analysis	3	66.66
4.	Correspondence Analysis	3	66.66
5.	Soil Brightness Indices and Vegetation Indices (Greenness) Image	3	66.66
6.	Supervised Maximum Likelihood Classifier	3	66.66

REFERENCES

- Abrams, M.J., Lithological mapping. In : Remote Sensing in Geology, (edited by B.S. Siegal and A.R. Gillespie), Wiley, New York (1980).
- Abrams, M.J., et al., Remote sensing for porphyry copper deposits in southern Arizona, Econ. Geol., Vol. 78, pp. 591-604 (1983).
- Arlington, V.A., Landsat Data Users Handbook, U.S. Geological Survey (1979).
- Bakliwal, P.C., et al., Possibility of locating gossans through digital enhancement of Landsat MSS data, Proc. of Seminar on Remote Sensing in Geology and Mineral Targetting, ISRO/GSI J (1985).
- Balasundaram, M.S., Geological and Mineral Map of Rajasthan, Geol. Survey of India Publication (1969).
- Bartholomew, M.J., et al., Infrared spectroscopy (2.3-20 μm) for the geological interpretation of remotely-sensed multispectral thermal infrared data, Int. J. Rem. Sens., Vol. 10, No. 3, pp. 529-544 (1989).
- Bernstein, R., Digital image processing of Earth observation sensor data, IBM J. Res. Develop., Vol. 20, pp. 40-57 (1976).
- Chavez, P.S., et al., Statistical method for selecting Landsat MSS ratios, J. Appl. Photographic Engg., Vol. 8, p. 23 (1982).
- Chavez, P.C., et al., Image processing techniques for thematic mapper data, Tech. Papers, 50th Annual Meeting of the American Society of Photogrammetry, Vol. 2, pp. 728-743 (1984).
- Crist, E.P., The tasselled cap - a preliminary formulation, Proc. of the Symposium on Machine Processing of Remotely-Sensed Data, Purdue University, West Lafayette, Indiana, pp. 357-368 (1983).
- Crist, E.P., and R.C. Cicone, A physically-based transformation of thematic mapper data - the TM Tasselled Cap, IEEE Trans. Geosci. Rem. Sens., Vol. GE-22, pp. 256-263 (1984a).
- Crist, E.P., and R.C. Cicone, Comparison of the dimensional characteristics and features of simulated Landsat-4 MSS and TM data, Rem. Sens. Env., Vol. 14, pp. 235-246 (1984b).
- Davis, J.C., (ed.), Statistics and Data Analysis in Geology, Wiley, New York (1986).

- 207
- Drury, S.A., SPOT Data as^{an} aid to structural mapping in Rajasthan, India, Proc. of the Advances in Geological Remote Sensing, One day meeting at British Geological Survey, Keyworth, Nottingham (1987).
- Eberhardt, J.E., et al., Mid-infrared remote sensing systems and their application to lithologic mapping, IEEE Trans. Geosci. Rem. Sens., Vol. GE-25, NO. 2 (1987).
- Evans D., Multisensor classification of sedimentary rocks, Rem. Sens. Env., Vol. 25, pp. 129-144 (1988).
- Fisher, R.A., The use of multiple measurements in taxonomic problems, Annals of Eugenics, Vol. 7, pp. 179-188 (1936).
- Geological Survey of India Plate No. 56, National Atlas of India (1975).
- Goetz, A.F.H., and L.C. Rowan, Geologic remote sensing, Science, Vol. 211, pp. 781-791 (1981).
- Goetz, A.H.Z., et al., Remote sensing for exploration : an overview, Econ. Geol., Vol. 78, No. 4, pp. 573-590 (1983).
- Goetz, A.F.H., et al., Optical remote sensing of the Earth, Proc. IEEE, Vol. 73, No. 6 (1985).
- Greenbaum, D., Lithological discrimination in central Snowdania using airborne multispectral scanner imagery, Int. Jl. Rem. Sens., Vol. 8, No. 6, pp. 799-816 (1987).
- Gupta, A.K., Geology, mineralization and natural resources studies of Sirohi district, Rajasthan using remote sensing imagery and CCTs, M.Tech. thesis (unpublished), I.I.T. Kanpur (1981).
- Gupta, A.K., and K. Ganesha Raj, (eds.), Use of Remote Sensing for Geological Applications in India - A Status Report : ISRO-NNRMS-TR-59-86 (1986).
- Gupta, P.K., and S. Viswanathan, Geological interpretation of southern Rajasthan through Landsat-2 MSS data, Proc. National Conference on Application of Remote sensing on Natural Resources, Environmental Landuse and Problems Relating to Training and Education, CSRE, IIT Bombay (1983).
- Heron, A.M., Synopsis of the pre-Vindyan geology of Rajputana, Trans. Nat. Inst. Sci. India, Vol. 1, pp. 1-17 (1935).
- Heron, A.M., (ed.), The Geology of Central Rajputana, Mem. Geol. Surv. India, Vol. 79(1), 389 pp. (1953).
- Hunt, G.R., Spectral signatures of particulate minerals in the visible and near-infrared, Geophysics, Vol. 42, pp. 501-511 (1977).

Oldfield, R.B., and J. Elgy, Geological mapping from remotely sensed data using tonal, textural and contextual features, Proc. 13th Annual Conference of the Remote Sensing Society, Univ. of Nottingham, pp. 533-537 (1987).

Patel, N., and K.K. Rampal, Discrimination of rock types using Landsat thematic mapper data, Advances in Space Research, Proc. of Symposium S.2, Twenty-eighth COSPAR Plenary Meeting held at the Hague, The Netherlands, June-July 1990 (Paper on print), Pergamon Press, Oxford (1990).

Ramaswamy, S.K., Proc. of the Seminar on National Natural Resources Management System, Hyderabad (Indian Space Research Organisation, Bangalore), (1983).

Ramaswamy, S.M., et al., Optimisation of digitally enhanced landsat multispectral data for geological and geomorphological mapping and evaluation of potentiality in locating basement mineralisation - A case study from Bhilwara Area, Rajasthan, Proc. Seminar on remote sensing in geology and mineral targetting, ISRO/GSI JEP (1985).

Rampal, K.K., (ed.), Textbook of Photogrammetry, Oxford and IBH, New Delhi (1982).

Rowan, L.C., Application of satellites to geologic exploration, American Scientist, Vol. 63, No. 4, pp. 393-403 (1975).

Rowan, L.C., et al., Digital classification of contact metamorphic rocks in Extremadura, Spain using Landsat thematic mapper data, Geophysics, Vol. 52, No. 7, pp. 885-897 (1987).

Roy, A.B., (ed.), Precambrian of the Aravalli Mountain, Rajasthan, India, Memoir 7, Geological Survey of India, Bangalore (1988).

Santisteban, A., and L. Munoz, Principal components of a multispectral image : Application to a geological problem, IBM J. Res. Develop., Vol. 22, No. 5, pp. 444-454 (1978).

Segal, D.B., and I.S. Merin, Successful use of Landsat thematic mapper data for mapping hydrocarbon microseepage-induced mineralogic alteration, Lisbon Valley, Utah, Photogram. Engg. and Rem. Sens., Vol. 55, No. 8, pp. 1137-1145 (1989).

Siegal, B.S., and A.R. Gillespie (eds.), Remote Sensing in Geology, Wiley, New York (1980).

Siegrist, A.W., and C.C. Schnetzler, Optimum spectral bands for rock discrimination, Photo. Engg. Rem. Sens., Vol. 46, No. 9, pp. 1207-1215 (1980).

Swain, P.H., and S.M. Davis, (eds.), Remote Sensing : The Quantitative Approach, McGraw-Hill, New York (1978).

GENERAL REFERENCES

- Bhan, S.K., and K. Krishnanunni, Applications of remote sensing in geology. In : Remote Sensing (edited by B.L. Deekshatulu and Y.S. Rajan), Indian Academy of Sciences, Bangalore (1984).
- Curran, P.J., (ed.), Principles of Remote Sensing, Longman, London (1985).
- David, M., et al., Progresses in R- and Q-mode analysis : Correspondence analysis and its applications to the study of geological processes, Canadian J. Earth Sci., Vol. 11, pp. 131-146 (1974).
- Deekshatulu, B.L., and Y.S. Rajan (eds.), Remote Sensing, Indian Academy of Sciences, Bangalore (1984).
- Gonzalez, R.C., and P. Wintz (eds.), Digital Image Processing, Addison-Wesley, Reading, Massachusetts (1977).
- Gopalan, A.K.S., and K. Krishnanunni, (eds.), Proc. of the Seminar on Remote Sensing in Geology and Mineral Targeting, ISRO-Dept. of Mines, (1985).
- Kerr, P.F., (ed.), Optical Mineralogy, McGraw-Hill, New York (1959).
- Khorram, S., et al., Comparison of Landsat MSS and TM data for urban land-use classification, IEEE Trans. Geosci. Rem. Sens., Vol. GE-25, No. 2, pp. 238-243 (1987).
- Krishnan, M.S., (ed.), Geology of India and Burma, CBS, New Delhi (1982).
- Lees, R.D., et al., Evaluation of Landsat thematic mapper imagery for geologic applications, Proc. IEEE, Vol. 73, No. 6, pp. 1108-1117 (1985).
- Lo, C.P., (ed.), Applied Remote Sensing, Longman, London (1986).
- Mitra, S., (ed.), Fundamentals of Optical, Spectroscopic and X-ray Mineralogy, Wiley Eastern, New Delhi (1989).
- Sabins, F.F., Jr., (ed.), Remote Sensing : Principles and Interpretation, 2nd Edition, Freeman, New York (1986).
- Short, N.M., (ed.), The Landsat Tutorial Workbook (Basics of Satellite Remote Sensing), Scientific and Technical Information Branch, NASA, Washington D.C. (1982).